STUDY OF STRUCTURE AND DYNAMICS OF MONOLAYERS CONTAINING PROTEINS AND LIPIDS AT THE AIR-WATER INTERFACE USING TWO DIMENSIONAL INFRARED SPECTROSCOPY METHODS

by

SARATCHANDRA SHANMUKH

(Under the Direction of Richard A. Dluhy)

ABSTRACT

Chapters 3 – 8 of this dissertation are composed of individual manuscripts which have either been published or submitted to scholarly journals.

In Chapter 3, 2D IR correlation analyses are performed on IRRAS spectra of surfactant proteins B and C containing lipid monolayers at the air-water interface. Based on the correlation plots, it was concluded that the secondary structures of SP-B and SP-C are heterogenous and change with increase in surface pressure. Chapter 4 describes an investigation using infrared spectroscopy into the change in the secondary structure of deacylated SP-C with pH.

In Chapter 5, a new model-based 2D IR method is introduced and described using simulated spectral models. This method, *kv* correlation, makes use of a set of simulated exponential curves that are mathematically cross-correlated against a set of experimental curves and the resulting correlation plot between spectral frequency and rate constant reveals temporal relationships in terms of a numerical parameter. In Chapter 6, the *kv* correlation method is used to study the

interaction between a phospholipid (DPPA) monolayer and the antibiotic Tetracycline by collecting PM-IRRAS spectra at the air-water interface.

A synthetic peptide, mSP-B_{1-25}, is characterized using PM-IRRAS at the air-water interface and *kv* correlation to determine if it can be used as an effective replacement for the native SP-B protein in lung surfactant. This study, presented in Chapter 7, revealed the changes in secondary structure of the peptide present in different concentrations in a lipid matrix of deuterated DPPC and DOPG on subphases containing sodium and calcium ions.

In Chapter 8, Ag nanorod substrates, that are prepared by vapor deposition on the substrate at an oblique angle, are characterized for their SERS activity. Nanorod samples of different lengths were characterized at 785nm using 1,2-trans(bi-pyridyl)-ethene as a probe molecule. Surface Enhancement factors of 10^8 were observed and the enhancement factor was found to increase with increase in the length of the nanorods.

INDEX WORDS: Fourier Transform Infrared Spectroscopy (FT-IR), Infrared Reflection-Absorption Spectroscopy (IRRAS), Two Dimensional Infrared Correlation Analysis (2D-IR), Air-water Interface, Polarization Modulation IRRAS, Surface Enhanced Raman Scattering, DPPC, Pulmonary Surfactant, SP-B, SP-C, Nanorods, GLAD

STUDY OF STRUCTURE AND DYNAMICS OF MONOLAYERS CONTAINING PROTEINS AND LIPIDS AT THE AIR-WATER INTERFACE USING TWO DIMENSIONAL INFRARED SPECTROSCOPY METHODS

by

SARATCHANDRA SHANMUKH

B.Sc., University of Madras, India 1998

M.Sc., Indian Institute of Technology Madras, India, 2000

A Dissertation Submitted to the Graduate Faculty of The University of Georgia in Partial Fulfillment of the Requirements for the Degree

DOCTOR OF PHILOSOPHY

ATHENS, GEORGIA

2005

© 2005

Saratchandra Shanmukh

All Rights Reserved

STUDY OF STRUCTURE AND DYNAMICS OF MONOLAYERS CONTAINING PROTEINS AND LIPIDS AT THE AIR-WATER INTERFACE USING TWO DIMENSIONAL INFRARED SPECTROSCOPY METHODS

by

SARATCHANDRA SHANMUKH

Major Professor: Richard A. Dluhy

Committee: Jonathan Amster
Geoffrey Smith

Electronic Version Approved:

Maureen Grasso
Dean of the Graduate School
The University Of Georgia
May 2005

ACKNOWLEDGEMENTS

I would first like to thank my wife, Kala, for all her love, support and help without which this work would not be possible. I would also like to thank my parents, brother and grandparents for their love and encouragement. I wish to express my deepest gratitude to my research advisor, Richard A. Dluhy, for his mentoring, support and encouragement during the course of my research. Acknowledgement is also due to my committee members, Jonathan Amster, Geoffrey Smith and Lucia Babcock for reviewing my dissertation and guidance throughout the duration of my Ph.D. I would like to thank the past and current members of the Dluhy research group for all their guidance, ideas and support throughout my Ph.D. Finally, I would like thank the University Of Georgia and the Government of the United States of America for giving me the opportunity to visit and experience this amazing country.

TABLE OF CONTENTS

Page

ACKNOWLEDGEMENTS iv

CHAPTER

1 INTRODUCTION 1

2 LITERATURE REVIEW 5

3 EFFECT OF HYDROPHOBIC SURFACTANT PROTEINS SP-B AND SP-C ON PHOSPHOLIPID MONOLAYERS: PROTEIN STRUCTURE STUDIED USING 2D IR AND $\beta\nu$ CORRELATION ANALYSIS 92

4 DE-ACYLATED PULMONARY SURFACTANT PROTEIN SP-C TRANSFORMS FROM α-HELICAL TO AMYLOID FIBRIL STRUCTURE VIA A pH DEPENDENT MECHANIMS: AN IR STRUCTURAL INVESTIGATION 153

5 $k\nu$ CORRELATION ANALYSIS: A QUANTITATIVE TWO-DIMENSIONAL IR METHOD FOR ANALYSIS OF RATE PROCESSES WITH EXPONENTIAL FUNCTIONS 209

6 2D IR ANALYSES OF RATE PROCESSES IN LIPID-ANTIBIOTIC MONOMOLECULAR FILMS 260

7 STRUCTURE AND PROPERTIES OF PHOSPHOLIPID-PEPTIDE MONOLAYERS CONTAINING MONOMERIC SP-$B_{1\text{-}25}$: PEPTIDE CONFORMATION BY INFRARED SPECTROSCOPY 303

8 RANDOMLY ALIGNED SILVER NANOROD ARRAYS PRODUCE HIGH SENSITIVITY SERS SUBSTRATES 352

9 CONCLUSIONS.....369

CHAPTER 1

INTRODUCTION

Biomembranes found in nature have complex structures and multiple components that continuously interact with each other and with other components present in the immediate environment. Pulmonary surfactant is the mixture of lipids and specific proteins produced by type II pneumocytes in the alveolar epithelium that lines the air-alveolar fluid interface of the lung and is needed to reduce alveolar surface tension to near zero at low lung volumes and prevent end-expiratory collapse. Deficiency of one or more components of this mixture has been shown to cause Respiratory Distress Syndrome (RDS) in premature infants, and has also been implicated in the Acute Respiratory Distress Syndrome (ARDS) that can result from lung injury due to a variety of causes. An insoluble monolayer film of amphipathic molecules spread at the air-water interface is commonly known to as a Langmuir monolayer. Since Langmuir monolayers are also 2-D dynamically compressed films at the A/W interface, they can be used as a model experimental system to study the structure, dynamics and the mechanism by which pulmonary surfactant lowers surface tension at the alveolar air-water interface.

Several methods have been applied to the study of the structure of biomembranes observed in nature. The work presented in this dissertation utilizes modern experimental techniques such as Polarization Modulation Infrared Absorption Spectroscopy at the air-water interface (PM-IRRAS) and Two-Dimensional Infrared Correlation spectroscopy (2D IR) to study the structure,

nature of interaction between different components and their dynamic behavior. Infrared external reflection spectroscopy, also referred to as IRRAS, has been used to study monomolecular thin films on metal surfaces for several years. The use of external reflection FT-IR spectroscopy to study monomolecular films directly at the air-water interface was originally developed in the mid 1980s and this represented a major step in the application of IRRAS to the study of biologically relevant membranes and molecules in an environment closest to what is found in nature.

IRRAS at the air-water interface is hindered by interference due to isotropic water vapor absorption and baseline dispersion effects due to the water substrate. In order to overcome these inherent limitations, polarization modulation spectroscopy has been applied to monomolecular films at the air-water interface. Polarization Modulation Infrared Reflectance Spectroscopy (PM - IRRAS) involves a fast modulation of the polarization of the incidence electric field between parallel and perpendicular linear polarization states. After electronic filtering and demodulation of the signal using a lock-in amplifier, the differential reflectivity spectrum is then computed. The Polarization Modulation Reflectance spectrum is insensitive to isotropic absorptions and reflects the difference between the parallel and perpendicular polarizations.

Two-dimensional infrared correlation spectroscopy (2D IR) is a modern analytical technique that is increasingly being used in the interpretation of complex spectra, which generally have broad, multiply overlapped spectral features. Besides functioning as a spectral resolution enhancement method similar to curve fitting or deconvolution, 2D IR possesses an additional advantage, in that it is capable of discerning temporal relationships between intensity variations within the set of spectra. $\beta\nu$ Correlation is a modified 2D IR technique that can represent temporal relationships in terms of a phase angle parameter. This method makes use of a set of simulated sinusoidal curves that are correlated against the experimental spectral set.

In Chapter 3, conventional 2D IR correlation spectroscopy and $\beta\nu$ correlation methods are applied to IRRAS spectra of Langmuir monolayers of lipid-protein mixtures of pulmonary surfactant proteins SP-B and SP-C spread at the air-water interface. This study reveals the change in secondary structure of the proteins as the monolayer film is compressed to higher pressures. A new modified 2D IR correlation method, called $k\nu$ correlation, is described and discussed with examples in Chapter 5. This method is useful in identifying underlying band components in the case of overlapped peaks and in identifying temporal relationships between molecular events in terms of a numerical parameter. The usefulness of this technique is demonstrated by applying it to the photopolymerization of ethyl-2-cyanoacrylate using metallocenes as photoinitiators. Chapter 6 describes the study of the interaction between the amphipathic molecule DPPA that is spread at the air-water interface and an antibiotic Tetracycline that is present in the subphase. $k\nu$ Correlation was applied to PM-IRRAS spectra that were obtained at the air-water interface on the above system. The change in secondary structure of a synthetic peptide mSP-$B_{1\text{-}25}$ with change in surface pressure and in the presence of a lipid matrix is investigated in Chapter 7. mSP-$B_{1\text{-}25}$ retains the surface active properties of the 79 residue long native SP-B protein. This study involved collecting PM-IRRAS spectra on monomolecular films of mixtures of mSP-$B_{1\text{-}25}$ in varying concentrations and deuterated DPPC and DOPG on subphase containg sodium and calcium ions.

Surface Enhanced Raman Spectroscopy has emerged as a routine and powerful tool for the investigation and structural characterization of interfacial thin film systems. SERS excellent sensitivity and selectivity allows for observation and elucidation of chemical information from single monolayers on planar metal surfaces. Routine enhancements of $10^4 - 10^6$ can be achieved for SERS experiments compared to the use of traditional unenhanced Raman spectroscopy. In

Chapter 8, substrates consisting of silver nanorod arrays with varying rod lengths were fabricated by an oblique angle vapor deposition method and were evaluated as potential surface-enhanced Raman spectroscopy (SERS) substrates using trans-1, 2-bis (4-pyridyl)ethene as a probe molecule. Enhancement factors of upto ~10^8 were calculated and SERS activity was shown to depend upon the length of the nanorods.

CHAPTER 2

LITERATURE REVIEW

Langmuir Monolayers

Certain organic molecules will orient themselves at the interface between a gaseous and liquid phase (or between two liquid phases) to minimize their free energy. The resulting surface film is one molecule in thickness and is commonly called a monomolecular layer or simply a monolayer. A Langmuir monolayer can be defined as a layer of amphiphilic molecules that are oriented with their hydrophilic heads on one side of the layer and their hydrophobic tails on the other. Floating films on water were known from ancient times (18^{th} century B.C.) in places as diverse as Babylon, Greece, China and Japan, though this knowledge formed a part of their spiritual and superstitious beliefs [1]. The ancient art of Japanese marbling, called '*suminagashi*', which literally means 'ink-float' or 'ink-stream', is recognized as the earliest technical application of surface films. Aristotle and his contemporaries have described sailors spreading oil on water to calm the surface. This is probably the earliest technical application of surface films [2].

In more recent times, Benjamin Franklin, with his famous Clapham pond experiment, made the first scientific investigation of this phenomenon in 1774. Lord Rayleigh was the first to measure the lowering of water surface tension quantitatively due to spreading of olive oil. During the following year, Agnes Pockels made a systematic study by compressing layers

containing different amounts of oil on the water surface with barriers, thus observing that the surface tension fell rapidly when the monolayer was compressed below a certain area. It was later speculated by Lord Rayleigh that at this area, the oil molecules were closely packed and this spectacular speculation was the basis for the subject of monomolecular films. In 1917, Irving Langmuir put forward evidence for the air-water interface. He was the first to investigate chemically pure substances instead of using oil as his forerunners. A few years later, Langmuir showed how these monomolecular films could be transferred onto solid substrates. In 1955, Katharine Blodgett demonstrated the sequential transfer of monolayers onto the solid substrate to form multilayer films, which are now referred to as Langmuir-Blodgett (LB) films.

In the generally accepted membrane model, proteins are embedded in a lipid bilayer, which consists of two weakly coupled monolayers. Investigations on monolayers indicate the state of the bilayer, and monolayer studies with phospholipids spread at the air-water interface can be performed in a well-defined way. The two dimensional molecular density and the ionic conditions of the subphase can be varied, as well as the temperature and the composition. Other useful characteristics of phospholipid monolayers are that the systems are planar over macroscopic dimensions and that at least one symmetry axis, the plane normal, is well-known

An air-water interface has a large free energy per unit area of ~72 mN/m. The addition of amphipathic molecules lowers the surface tension. This lowering, expressed as a positive number, is the force per unit length with which the monolayer tries to expand relative to a clean interface, that is, the surface pressure.

Langmuir Monolayers are produced and characterized in an apparatus that has traditionally been referred to as a Langmuir trough, which consists of a trough, usually made up of hydrophobic materials like Teflon to contain the subphase water and movable barrier(s) that span

over the water surface. In a common Langmuir film experiment, a known amount of amphiphilic material dissolved in a water-immiscible, volatile organic solvent such as chloroform is placed on a water surface. After evaporation of the solvent, the monolayer material is compressed with the movable barriers. Monolayer formation is usually monitored with the surface pressure-area isotherm. The subphase temperature is controlled by water circulation underneath the trough. The most commonly used technique to characterize a Langmuir Monolayer is the surface pressure (π) – area (A) isotherm, that is a plot of the change in surface pressure as a function of the area available to each molecule on the aqueous subphase surface (Figure 2.1). The measurement is carried out by continuously compressing the monolayer while monitoring the surface-pressure to maintain a pseudo-equilibrium condition, though it is possible to obtain equilibrium values by compressing the monolayer on a point-to-point basis. The surface pressure is measured during monolayer compression by the Wilhelmy method, in which the force acting on a plate, usually made of Platinum or filter paper that is attached to a sensitive electrobalance, partially immersed in the subphase is measured (Figure 2.2).

Impurities present in the monolayer material, the sub-phase water or the trough can cause experimental errors in accurate measurement of surface pressure. Solubility of the monolayer material and the change in the water level of the subphase as a result of evaporation can also be responsible for errors. Surface pressure-area isotherms are also dependent on experimental factors such as subphase temperature, solvent evaporation, speed of compression and the structure of the molecule.

The study of monolayers has a lot of significance in many fields of science and technology, such as in chemistry, physics, and biology and material science. Several techniques have been used to study monolayer films at the air-water interface to extract different physical or

Figure 2.1 A surface pressure – Area isotherm of a hypothetical phospholipid monolayer spread at the air-water interface at room temperature.

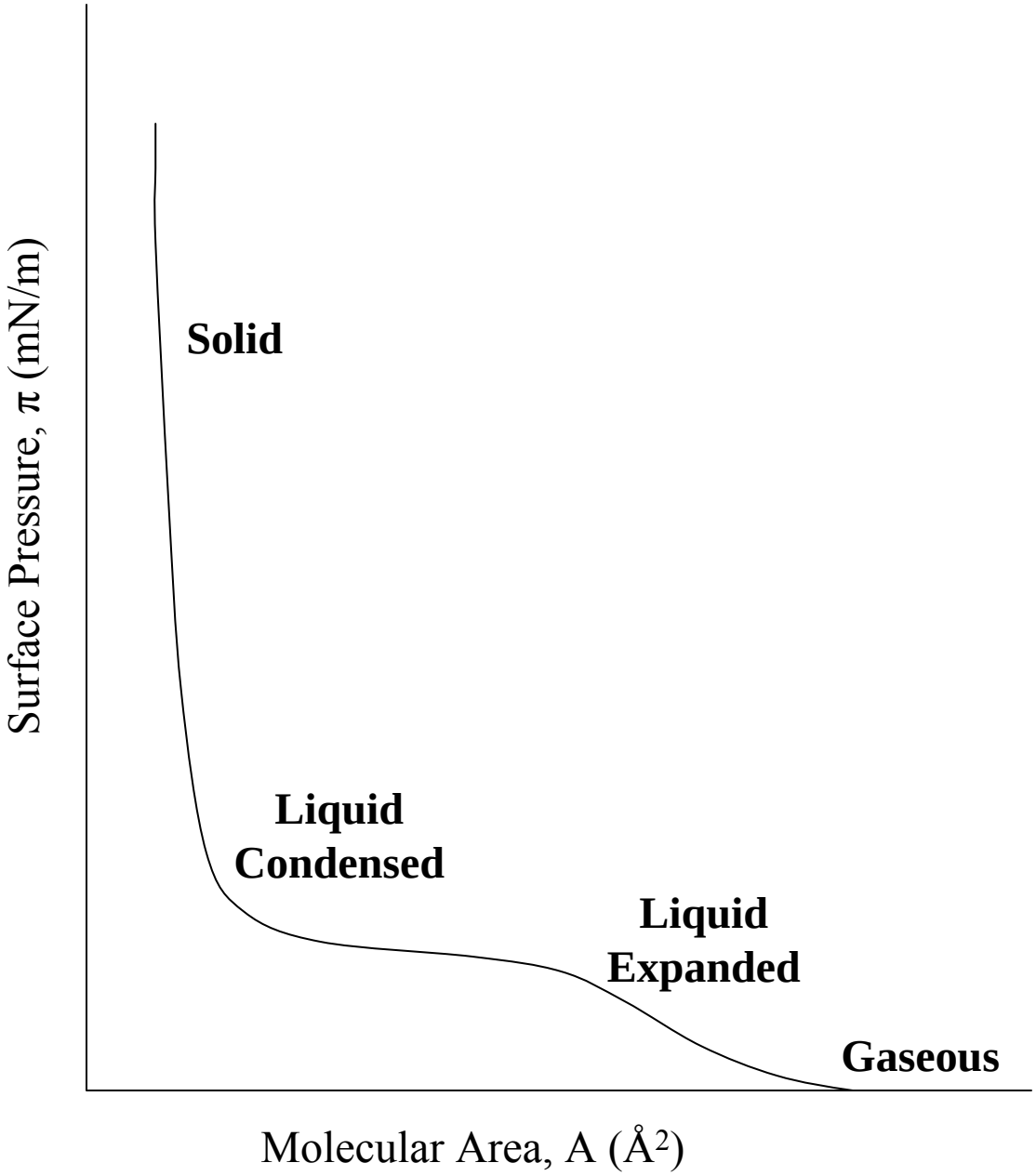
Surface Pressure, π (mN/m)
Solid
Liquid
Condensed
Liquid
Expanded
Gaseous
Molecular Area, A (Å2)

Figure 2.2 A schematic representation of a Langmuir Film Balance

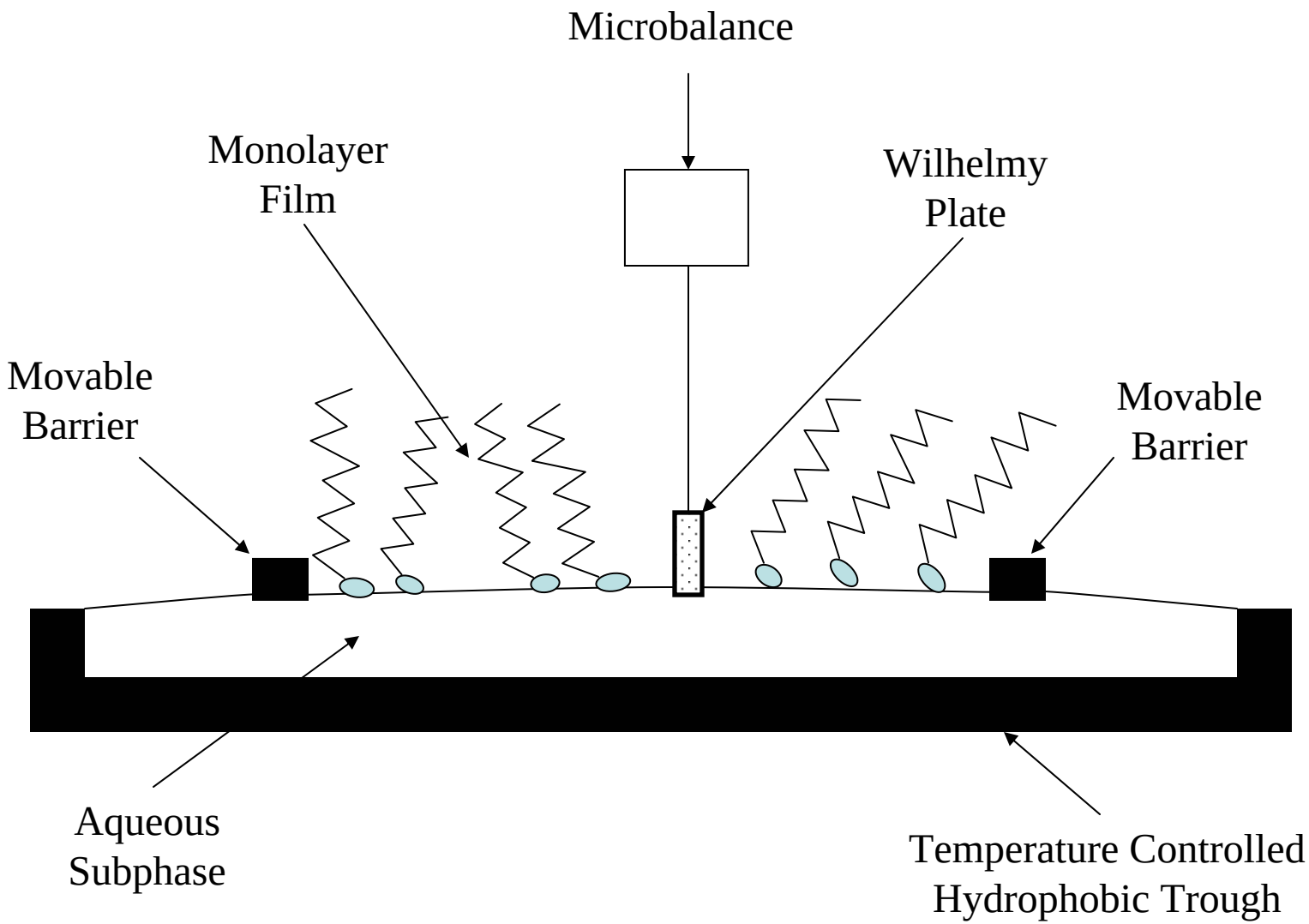
Microbalance
Monolayer
Film
Wilhelmy
Plate
Movable
Barrier
Movable
Barrier
Aqueous
Subphase
Temperature Controlled
Hydrophobic Trough

chemical properties of the film. The most common and popular technique used is the surface pressure-area isotherm technique. Using this, first hand information on monolayer formation and other properties such as molecular area, monolayer phases and the collapse behavior of the monolayer can be obtained. The extent of mixing in a mixed monolayer can be better understood by the study of the isotherms. Since amphiphilic molecules forming monolayers tend to carry charges in their headgroups, surface potential-area isotherms and conductance measurements can be used to determine the orientation of molecular dipoles in the monolayer, study the interaction of the species present in the subphase with the monolayer and study intermolecular head group interaction and hydrogen bonding among molecules. Another technique that makes use of the charges of the headgroups of the molecules is Maxwell displacement current measurements and this technique can be used to study aggregation and the course of photochemical reactions in the monolayer [3].

The physical characteristics of the film at the interface are commonly studied by optical techniques such as microscopy and spectroscopy. While Brewster angle microscopy is a very useful technique that has been used to study morphological features, domain formation, monolayer phases, aggregation and phase co-existence, fluorescence microscopy can also be used to study domain formation, formation of monolayer phases and their coexistence at different surface pressures. Inter-molecular interaction and aggregation can also be studied by the detection of chromophores by UV-VIS spectroscopy [3].

While grazing angle X-Ray diffraction can be used to obtain positional order, in-plane lattice structure and the different phases of the monolayer, X-ray and neutron reflectivity can be used to probe the nanostructures of the surface and the interface. Using these techniques, the course of

reaction in the monolayer, monolayer thickness and monolayer-counterion interactions can be studied quite in depth.

Due to their greater sensitivity to the surface/interface region, non-linear optical techniques such as Second harmonic generation can be used to study the surface density of the monolayer, pK_a and degree of ionization of head groups and orientation of molecules within the monolayer. Sum frequency generation can also be used to determine orientation and conformational changes, structure of the interface, phase transitions, surface density of the monolayer [3].

Other techniques such as quartz crystal microbalance and ellipsometry can be used to determine monomolecular nature, water incorporation into the monolayer, monolayer thickness, visco-elastic behavior, shear modulus and rheological transitions in the monolayer.

Pulmonary Surfactant

Pulmonary surfactant is the mixture of lipids and specific proteins produced by type II pneumocytes in the alveolar epithelium that lines the air-alveolar fluid interface of the lung and is needed to reduce alveolar surface tension from 72mN/m (the value at a pure A/W interface at 37C) to near zero at low lung volumes and prevent end-expiratory collapse [4]. Deficiency of one or more components of this mixture has been shown to cause Respiratory Distress Syndrome (RDS) in premature infants [5], and has also been implicated in the Acute Respiratory Distress Syndrome (ARDS) that can result from lung injury due to a variety of causes [6-8].

Since Langmuir monolayers are also 2-D dynamically compressed films at the A/W interface, they can be used as a model experimental system to study the structure, dynamics and the mechanism by which pulmonary surfactant lowers surface tension at the alveolar air-water interface.

Phospholipids are the major lipid component, approximately 90%, in pulmonary surfactant while other lipids that are found include cholesterol, triacylglycerol and free fatty acids. Of the phospholipids phosphatidylcholine (PC) is the most abundant component of surfactant and is found in a quantity of 70- 80% of the total amount of lipid [9, 10]. Nearly two-thirds of PC is saturated, especially in the dipalmitoylated form (DPPC). The anionic phosphatidylglycerol (PG) accounts for approximately 8% [11-13] while other lipids such as phosphatidylethanolamine (PE, 5%), phosphatidylinositol (PI, 3%); and phosphatidylserine (PS), lysophosphatidylcholine, and sphingomyelin make up the rest [14]. Other significant components of lung surfactant are the plasmalogen analog of PC and cholesterol, which accounts for 2.4 weight% of the total composition of surfactant [15].. Although most of surfactant consists of lipids, it comprises approximately 10% protein. Pulmonary surfactant contains atleast four distinct specific proteins which have been identified to date. These proteins can be divided into 2 groups: the hydrophilic surfactant proteins SP-A and SP-D and the hydrophobic surfactant proteins SP-B and SP-C. SP-A and SP-D may play an important role in the first line of defense against inhaled pathogens, and SP-A may have a regulatory role in the formation of the monolayer that reduces the surface tension. Phizackerley and coworkers were the first to show the presence of hydrophobic surfactant proteins. The hydrophobic proteins appear to be critical for surfactant's ability to lower surface tension by enhancing adsorption and spreading of surfactant phospholipids to the air-liquid interface.

Regulation of Phospholipid synthesis and Secretion

The lamellar bodies contain lipid and protein components of surfactant [16] and are secreted into the fluid layer lining the alveoli. After secretion, surfactant is transformed into specific

structures called tubular myelin, from which insertion of phospholipids into air-liquid interface is thought to take place. The phospholipids molecules are found with their hydrophobic fatty acid chains up in the air and the hydrophilic headgroups in the subphase. Surfactant phospholipids form stable surface films with low surface tension upon compression; adsorption of phospholipids from the subphase into the surface film is highly accelerated in the presence of hydrophobic surfactant proteins [17]. Phospholipid adsorption is required to ensure molecular occupation of the air-water interface during inflation of the lung. The composition of the monolayer is also an important factor in the adsorption of the surface-active material into the monolayer [18, 19].

During expiration the surface tension at the air-water interface of the lung is reduced. To reach a low surface tension the film gets enriched in DPPC. The process may either occur by selective insertion of DPPC during adsorption or by selective exclusion of other components of the surface film during reduction of the surface area. During the next inhalation and expansion of the surface area of the alveoli, the hydrophobic surfactant proteins improve the re-spreading of the lipids.

SP-C

Mature bovine surfactant protein C (SP-C) is secreted by type II epithelial cells into the alveoli in a complex mixture of surfactant lipids and proteins. Bovine SP-C consists of 34 amino acids and is an extremely hydrophobic, predominately α-helical protein of approximately 4.0 kD with charged amino acids (K10 and R11) near its N terminus. In bovine SP-C cysteines C4 and C5 are acylated with C-16 (palmitoyl) chains, while canine SP-C contains only one cysteine residue. The function of the acylation is not clear, but it is speculated that palmitoylation leads

to a better binding of a protein to a membrane, influences the conformation and orientation of peptides, or plays a role in membrane fusion. The NMR structure in apolar solvent describes the valine-, leucine- and isoleucine-rich region of this small protein as a rigid rod in which only a few residues near the N terminus (L1 – P7) and the C terminus are *not* helical [20]. The length of this helix (V8 – G34) is ~ 39 Å with a diameter is of ~12 Å.

SP-C is associated with enhanced re-adsorption of phospholipids to the surfactant lipid monolayer at the air-water interface during monolayer expansion (the *in-vitro* equivalent to inhalation) [10]. It also appears to play a role in the formation of three-dimensional layers of surfactant during compression of the monolayer through a mechanism whereby SP-C assists in transfer of lipids from the monolayer to form stacked multilayer structures. Using *ex-situ* microscopy methods, the SP-C - dependent formation of membrane adherent particles has been demonstrated at high surface pressures [21-23], and a model for the formation of multibilayer phospholipid reservoirs, stabilized by SP-C, has been proposed [23, 24]. SP-C has also been shown to catalyze the formation of micrometer-sized, surface-associated, 3D particles at the interface, as visualized using scattered light dark-field microscopy with grazing incidence laser illumination [25, 26].

SP-B

SP-B is a small hydrophobic protein of 79 amino acid residues, known for its high cysteine content [27]. In the species for which the sequence has been described, the primary structure (and especially the positions of the cysteine residues) is conserved (± 80% of the mature protein). The cysteine residues form a unique disulfide pattern of three intramolecular bonds and one intermolecular disulfide bond, which stabilize the protein and produce a dimeric form of SP-B

[28, 29]. Mature SP-B contains a small disulfide loop within a larger loop. The secondary structure of SP-B is mainly alpha-helical. The helices have amphipathic character [30, 31].

Definitely the most important property of SP-B is to enhance the biophysical properties of surfactant lipids. SP-B greatly enhances the formation of a stable surface film by inducing the insertion of phospholipids into the monolayer [17, 18, 32, 33]. The positive charges of the protein are essential for the activity of the protein [34] and the interaction with negatively PG enhances phospholipid adsorption [19, 35]. SP-B is, together with SP-A, necessary for the formation of tubular myelin structures [36-38]. SP-B is able to induce the calcium-dependent fusion of membranes [36, 39]. The addition of SP-B increases the inter- and intramolecular ordering of bilayer membranes, especially under the gel to fluid phase transition temperature [34, 40]. This ordering is possible the result of a specific interaction of the positively charged SP-B with the PG headgroup [19, 40, 41]. One monomeric SP-B molecule influences 50-70 molecules of phospholipid [42]. It has been suggested that SP-B reduces the surface tension by an increase of the lateral stability of the phospholipid layer [34].

IRRAS

Infrared external reflection spectroscopy, also referred to as IRRAS, has been used to study monomolecular thin films on metal surfaces for several years [43-46]. The use of external reflection FT-IR spectroscopy to study monomolecular films directly at the A/W interface was originally developed in the mid 1980s by Dluhy [47]. This represented a major step in the application of IRRAS to the study of biologically relevant membranes and molecules in an environment closest to what is found in nature. Several research groups have adopted IRRAS as a method to investigate the structure and dynamics of Langmuir monolayers at the A/W interface

and there is a huge amount of literature available in this field on a variety of films. The classes of molecules that have been studied using the IRRAS technique include alcohols [48-52], fatty acids and derivatives [53-59], phospholipids [60-65], lipid/peptide and lipid/protein [66-77], proteins and synthetic polypeptides [66, 70, 78-85], acylamino acids [53, 86, 87] and polymers[88-94].

External Reflectance: Theory

An infrared external reflection spectrum is obtained by reflecting the incoming radiation from a three phase ambient-thin film-substrate system and measuring the reflected intensity as a function of wavelength. The absorption spectrum (A) is generated by ratioing the sample reflectance (R) against the reflectance of the film-free substrate (R_0) since this is a reflection experiment.

$$A = -\log(R / R_0) \qquad (1)$$

The spectrum obtained by this process is dependent on the wavelength, polarization of the light, thickness of the film, angle of incidence and the optical constants of the three phases involved (Figure 2.3).

The substitution of a dielectric surface for a reflective metal surface in the external reflection IR experiment has profound consequences for the resulting spectra. Application of this theory to the case of monomolecular films in situ at the air-water interface has shown distinct differences between the spectra of these monolayers and those supported at an air-metal interface. Although the reflectivity of metals is always very high, it can be seen that the reflectance of IR radiation at the air-water interface is considerably weaker and approaches zero at the pseudo-Brewster angle. This difference has considerable implications for the appearance of the resulting reflectance

spectra. The main differences can be understood by considering the underlying optical theory. The theoretical description of external reflection spectroscopy is explicitly given by the Maxwell and Fresnel equations and is based on the classical electromagnetic theory for an N-phase system of parallel, optically isotropic layers.

In a N-phase stratified layer system, the optical properties of the j^{th} phase are characterized by the complex refractive index, defined as:

$$n_j = n_j + ik_j \tag{2}$$

where n_j is the real refractive index and k_j is the absorption constant of the j_{th} phase.

Dluhy compared the polarized electromagnetic properties of a hypothetical monolayer film at the A/W interface with one at the air-metal interface [47, 95]. These properties included reflectance, phase shift and mean square electric field intensities vs. angle of incidence for the monolayer covered surfaces. The works showed that the so called surface selection rule which applies to the air-metal interface does not apply to the A/W interface. The optimal angle of incidence for A/W measurements was found to be in the range of 0 - 40° based on theoretical calculations, in contrast to the optimal angle of incidence for air-metal measurements, which is near grazing incidence. For all incident angles below the Brewster angle, the calculations predicted higher reflectivities for the monolayer covered surface than for the water substrate which is manifested as negative absorption bands in the IRRAS spectra.

An additional difference between IRRAS on metals and the water surface is the polarization dependence of the spectra. On metal substrates, only parallel polarized (*p* – polarized) light can be used, since *s* – polarized light does not generate an electric field at the surface. This is the origin of the "surface selection rule", according to which only vibrational dipole moments oriented perpendicular to the surface will be observed, as this is the only orientation that the *p* –

Figure 2.3 The interaction of electromagnetic radiation with a 3-phase system of optically isotropic layers

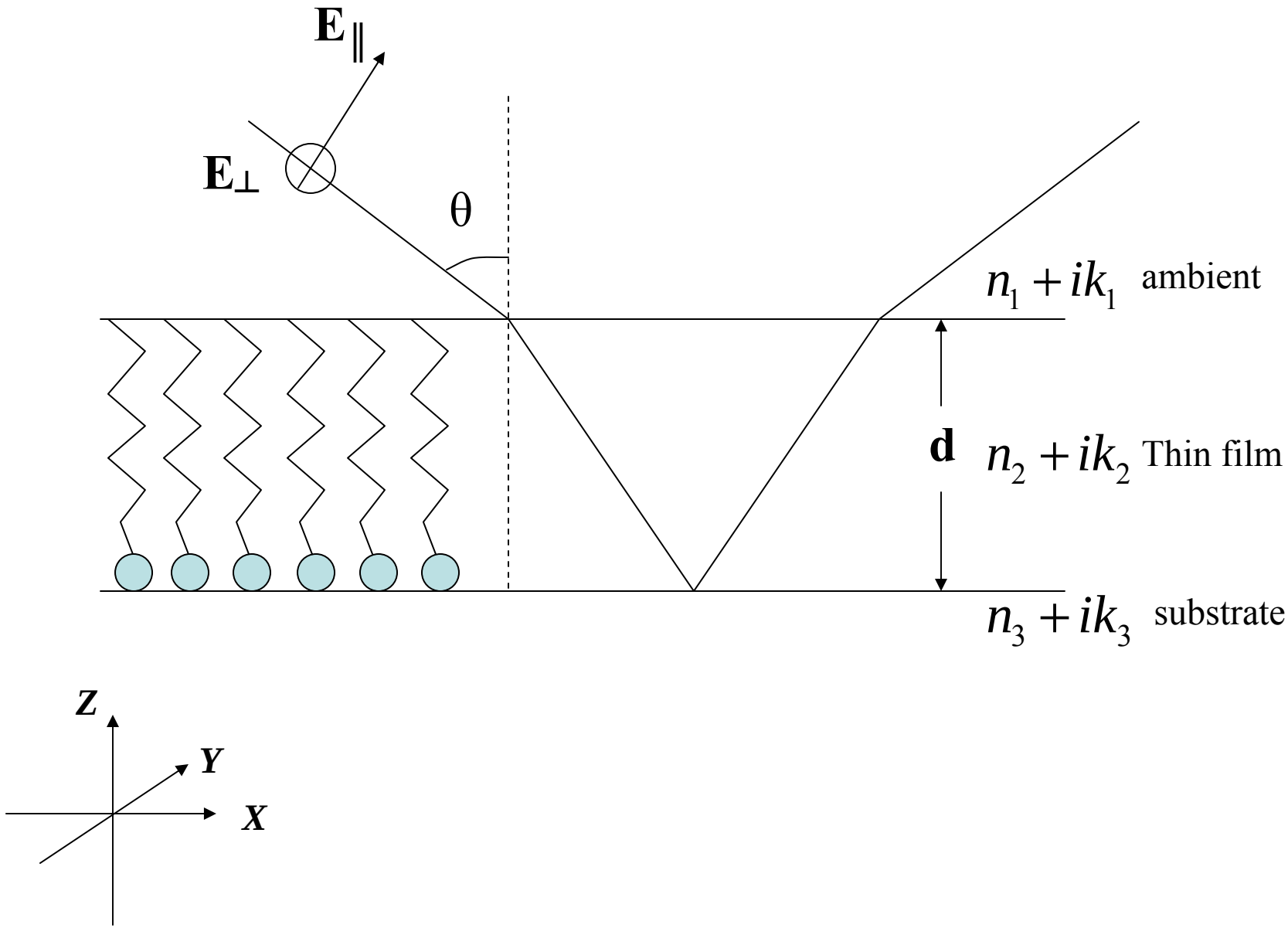
$\mathbf{E}_{\parallel}$
$\mathbf{E}_{\perp}$
θ
$n_1 + ik_1$ ambient
d
$n_2 + ik_2$ Thin film
$n_3 + ik_3$ substrate
Z
Y
X

polarized radiation will excite. Since finite values of the mean square electric fields for both *p* – and *s* – polarized radiation are present at the air-water interface, the polarized external reflectance spectra contain information about all three orthogonal geometric orientations of the monolayer film, which is unlike the case of monolayer films on metal substrates. Based on this principle, several groups have used polarization and angle dependence of the monolayer absorbance to determine thin-film orientation in Langmuir monolayers.

Despite the success of instrumental designs reported to date in studying Langmuir monolayers, there are inherent fundamental physical and spectroscopic limitations that make the IRRAS experiment difficult to perform. These major limitations are (a) very weak absolute reflectances, which restrict the possible S/N ratio in the final spectra; (b) interferences from H_2O vapor; and (c) baseline dispersion in regions of liquid water absorbance bands because of the anomalous dispersion of the water reflectance. These effects are especially pronounced in the spectral region from 1400 cm^{-1} to 1900 cm^{-1}, which contains the conformationally sensitive amide I region of the infrared spectrum.

In order to overcome several of these inherent limitations, polarization modulation spectroscopy has been applied to monomolecular films at the air-water interface. Polarization Modulation Infrared Reflectance Spectroscopy (PM - IRRAS) involves a fast modulation of the polarization of the incidence electric field between parallel and perpendicular linear polarization states [96-98]. After electronic filtering and demodulation of the signal using a lock-in amplifier, the differential reflectivity spectrum is then computed. The Polarization Modulation Reflectance spectrum is insensitive to isotropic absorptions and reflects the difference between the parallel and perpendicular polarizations.

PM-IRRAS

Since the pioneering work of Greenler [44], IRRAS using *p* - polarized light at grazing incidence has been a widely used to method to study thin films deposited on metallic substrates. Application of the "surface selection rule" to the IRRAS spectrum allows one to deduce from the intensities of the bands, the orientation of the surface transition moments.

Since *s* - polarized light does not generate a surface electric field (and hence any surface absorption) at a metal surface, it is possible to use polarization modulation to discriminate between the surface absorption and the isotropic absorption resulting from the local environment of the sample. Therefore polarization modulation of the incident light combined with a processing of the detected intensity leads to an experimental PM-IRRAS signal approaching the theoretical differential reflectivity:

$$\left(\frac{\Delta R}{R}\right) = \frac{R_p - R_s}{R_p + R_s} \tag{3}$$

In a general PM-IRRAS experiment on any sample with polarized reflectances R_p and R_s, the signal at the detector output can be electronically split into a first part carrying only the intensity modulation induced by the moving mirror if the FTIR spectrometer:

$$I_+ = C_+ \left\{ \left(R_p + R_s\right) + J_0(\phi_0)\left(R_p - R_s\right) \right\} I_0(\omega_i) \tag{4}$$

and into a second part that contains the polarization modulation induced by the PEM:

$$I_- = C_- \left\{ J_2(\phi_0)\left(R_p - R_s\right) \right\} I_0(\omega_i)\cos(2\omega_m t) \tag{5}$$

After demodulation, the ratio of these two parts gives the PM-IRRAS signal:

$$S = C\frac{J_2(\phi_0)(R_p - R_s)}{(R_p + R_s) + J_0(\phi_0)(R_p - R_s)} \tag{6}$$

where J_2 and J_0 are the second and zero order Bessel functions of the maximum dephasing, φ_0 introduced by the PEM, and C is a constant accounting for the different amplification of the two

parts during the two-channel electronic processing [96-98]. The experimental setup for the PM-IRRAS experiment is shown in Figure 2.4.

When the sample under study is an ultrathin film deposited on metallic substrates ($R_p \approx R_s$), within the spectral region where $\varphi_0 = \pi$, the above expression reduces to:

$$S = C\frac{(R_p - R_s)}{(R_p + R_s)}J_2(\phi_0) \qquad (7)$$

As a result isotropic absorption occurring in the sample environment does not contribute to *S*, and the only bands observed on the PM-IRRAS spectra are representative of the absorptions occurring in the immediate vicinity of the metallic surface. The electric field at the metal surface is maximum at incidence angles close to the grazing angle and hence optimum detection is also achieved at similar angles ($\theta \approx 80°$). Since the orientation of this electric field is normal to the metal surface, PM-IRRAS band intensities are governed by the "surface selection rule".

In the case of a dielectric substrate, such as the air-water interface, the optimization of the PM-IRRAS detection of the surface absorptions is more involved. On a dielectric substrate, depending on the angle of incidence, the reflectances due to *p* and *s* polarized light may be different, and hence the full expression should be used. Further, surface absorptions with the transition moment parallel to the substrate are also detected, since the electric field at the surface now has an intra-surface component. The water surface also has a large, specific, and spectrally dependent contribution to the PM-IRRAS signal, and consequently, comparison with the bare water surface spectrum is always necessary to extract the tiny signal of the monolayer.

$$\Delta S = S(d) - S(0) \qquad (8)$$

where *S(d)* and *S(0)* are the PM-IRRAS signals given by expression 3, respectively, for covered and uncovered substrates. The differential signal is normalized with respect to the substrate to rule out the $J_2(\varphi_0)$ dependence that contributes to the signal from the substrate.

Figure 2.4 A cartoon representation of the PM-IRRAS experimental setup

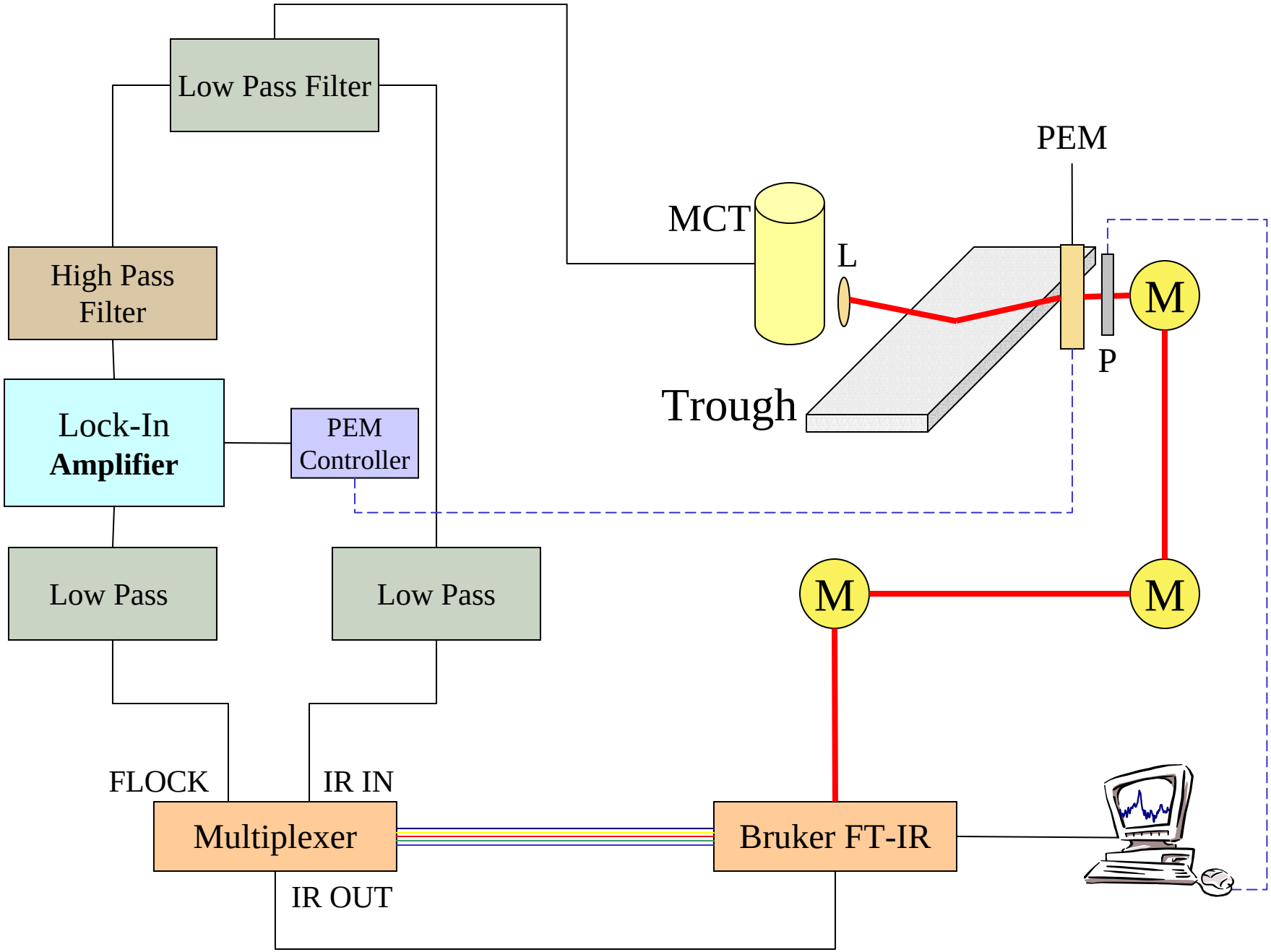
Low Pass Filter
High Pass Filter
Lock-In Amplifier
PEM Controller
Low Pass
Low Pass
FLOCK
IR IN
Multiplexer
IR OUT
Bruker FT-IR
MCT
L
PEM
M
P
Trough
M
M

$$\frac{\Delta S}{S} = \frac{S(d) - S(0)}{S(0)} \quad (9)$$

Polarization Modulation spectra obtained at the A/W interface have a few differences from those at metal surfaces. At an angle of incidence of ~80°, surface selection rules show that vibrations with transition moments in the plane of the interface yield positive going peaks, whereas those normal to the interface yield negative going peaks. Transition moments poised at ~38° to the surface normal yield no spectral features. These selection rules can be used to determine the orientation of molecules at the interface [96-98].

IRRAS: Applications

Although the use of external reflectance IR spectroscopy is a relatively new approach to the study of Langmuir monolayers, there is already a growing body of literature reporting the results of the spectroscopic study of a variety of these monomolecular films. The majority of this work has been in the conformational analysis and phase transitions of model monolayers, but there have also been several studies of naturally isolated pulmonary surfactant, cation interactions with monolayer headgroups, and peptide monolayer films.

A large number of studies have appeared in which external reflection IR spectroscopy was used to study phospholipids monolayers as models of biomembrane interfaces. Some of the earliest published IR spectra of Langmuir monolayers were of phospholipids at various surface pressures. It was shown that this IR reflectance method could identify vibrations due to the hydrocarbon acyl chains, carbonyl ester, and phosphate groups for these monolayer films at the air-water interface and that the external reflection method could differentiate between the physical conformations of phospholipid monolayer films at the air-water interface. In addition, the conformation sensitive C-H stretching bands from the lipid's hydrocarbon chains could be

used to monitor the expanded to condensed thermodynamic transition of the monolayer using this reflectance method.

Although the majority of studies published so far have focused on the hydrocarbon vibrations as indicators of monolayer phase states, it is possible to observe not only the hydrocarbon vibrations but also the vibrational modes due to the polar headgroups. The structure-function relationships in isolated and model systems that mimic pulmonary surfactant have been studied with external reflectance IR technique. Other studies have used model monolayer films composed of binary mixtures of PG and PC lipids in order to test the "squeezing-out" hypothesis of pulmonary surfactant function. In this case the PC component was composed of DPPC containing completely perdeuterated acyl chains. In this fashion, the C-H stretching function (due to the PG component) and the C-D vibrations (due to the PC component) could be simultaneously monitored. The relative intensities of these two vibrational bands as a function of surface pressure could then be used to determine the fractional concentration of each component in the mixed monolayer.

IRRAS has been used to investigate the chain orientations of fatty acids [54-56, 97, 99-101] and to study the effect of subphase pH, headgroup protonation and presence of cations in the subphase on monomolecular films of fatty acids [54, 58, 59, 97, 99, 100, 102-104].

Some of the earliest studies using IRRAS have been on the chain conformation and conformational order in different regions of phospholipid monolayers at the A/W interface [63, 64, 105]. In studies that are more relevant to the research reported in this work, the "squeeze-out" hypothesis in pulmonary surfactant has been tested using a mixture of phosphatidylcholine and phosphatidylglycerol lipids [60, 65]. The effect of Ca^{2+} ions present in the subphase on the monolayer and the acyl chain orientation in these molecules has also been investigated. Flach et

al. have investigated a the stratum corneum using a model system comprising of a mixture of ceramide, fatty acid and cholesterol using IRRAS [62].

IRRAS is ideally suited to the study of lipid-protein mixtures spread at the A/W interface. Mixtures of DPPC with lung surfactant proteins SP-B and SP-C have been investigated to study the secondary structure changes in the proteins, to test the "squeeze out" hypothesis, orientation of the helix in the protein and the effect of deacylation on the function of SP-C [68, 74, 106]. Several studies have been reported on the effect of proteins on the chain conformation of phospholipids and change in protein secondary structure due to lipid-protein interaction [66, 67, 69, 76, 77, 107-111]. The insertion of proteins into lipid monolayers from the subphase has been studied by IRRAS as well [73, 75].

Two Dimensional Infrared Correlation Spectroscopy

Two-dimensional infrared correlation spectroscopy (2D IR) is a modern analytical technique that is increasingly being used in the interpretation of complex spectra, that generally have broad, multiply overlapped spectral features. Besides functioning as a spectral resolution enhancement method similar to curve fitting or deconvolution, 2D IR possesses an additional advantage, in that it is capable of discerning temporal relationships between intensity variations within the set of spectra. 2D IR was developed in the later 1980s by Isao Noda while working at Proctor & Gamble. In a series of papers, Noda described the basic principles of this technique and its application to polymer systems. The sample is subjected to an environmental perturbation, such as concentration, temperature, pH, pressure *et cetera*, which causes any physical or chemical modification to the sample, thereby resulting in some kind of measurable change in the resulting spectrum. The variations in intensity of individual spectral frequencies

are then mathematically cross-correlated to produce contour plots that are termed "two-dimensional correlation maps". Based on the positions where these peaks occur and their signs, it is possible to identify vibrational modes that respond to the perturbation. Spectral resolution enhancement is achieved when the different vibrational modes occurring at different wavelengths respond in a different manner to the sample perturbation.

Initially, the 2D IR method required the external perturbation to posses a simple time-dependent sinusoidal waveform [112-116], however, a generalized method for obtaining two-dimensional correlation spectra was later introduced by Noda in which the external perturbations could be of any waveform that was a function of time or any other physical variable [117, 118]. The mathematical formalism for this generalized method was somewhat more complicated since it required the complex Fourier transformation of dynamic spectra, however, a modification of the generalized method was later introduced which uses the much simpler discrete Hilbert transform in place of the complex Fourier Transform[119].

Generalized 2D IR correlation spectra are characterized by two independent wavenumber axes (υ_1, υ_2) and a correlation intensity axis. In general, two types of spectra are obtained, commonly referred to as the 2D synchronous spectrum and the 2D asynchronous spectrum. Vibrational modes that are significantly coupled, or whose transition dipole moments change in-phase at similar rates in response to the external sample perturbation (i.e. modes that are synchronized) appears in the 2D synchronous spectrum. Conversely, bands that are significantly decoupled, or whose transition dipole moments respond out of phase at different rates to the external sample perturbation (i.e. modes that are asynchronized) appear in the 2D asynchronous spectrum. The correlation intensity in the 2D synchronous and asynchronous maps reflects the relative degree of in-phase or out-of-phase response, respectively.

2D synchronous spectra are symmetric with respect to the diagonal line in the correlation map. Intensity maxima appearing along the diagonal are called autopeaks (corresponding to the autocorrelation of perturbation-induced molecular vibrations), and are always positive. Intensity maxima located at off-diagonal positions are called cross peaks (corresponding to the cross-correlation of perturbation-induced molecular vibrations at two different wavenumbers). A pair of cross peaks may be positive or negative.

2D asynchronous spectra are antisymmetric with respect to the diagonal line in the correlation map. Only cross peaks located at off-diagonal positions appear in asynchronous spectra; a pair of cross peaks consists of two intensity maxima/minima, on eof which is necessarily positive and the other necessarily negative. Asynchronous cross peaks represent a lack of strong chemical interactivity, since their presence reflects the mutually independent nature of the reorientation of the dipole moments of the molecule's functional groups in response to an external perturbation.

A major advantage of 2D IR correlation spectroscopy is the possibility for enhanced resoluition observed in the asynchronous spectra. If two IR dipole transition moments change orientation independently of each other at different rates, overlapped bands appear as two cross peaks in the asynchronous spectrum. This is true even for heavily overlapped band for which the corresponding cross peaks may appear close to the diagonal. The temporal, or phase relationship, between two cross-correlated IR bands changing intensity under a time-dependent perturbation determines the sign of the cross peaks. Two positive crosspeaks (intensity maxima) are observed in the 2D synchronous spectrum when two transition-moments change orientations identically, and in-phase. Two negative crosspeaks (intensity minima) are observed in the 2D synchronous spectrum when two transition moments change orientations out-of-phase; furthermore, maximum

Figure 2.5 Examples of Synchronous and Asynchronous correlation plots resulting from the generalized 2D IR correlation method.

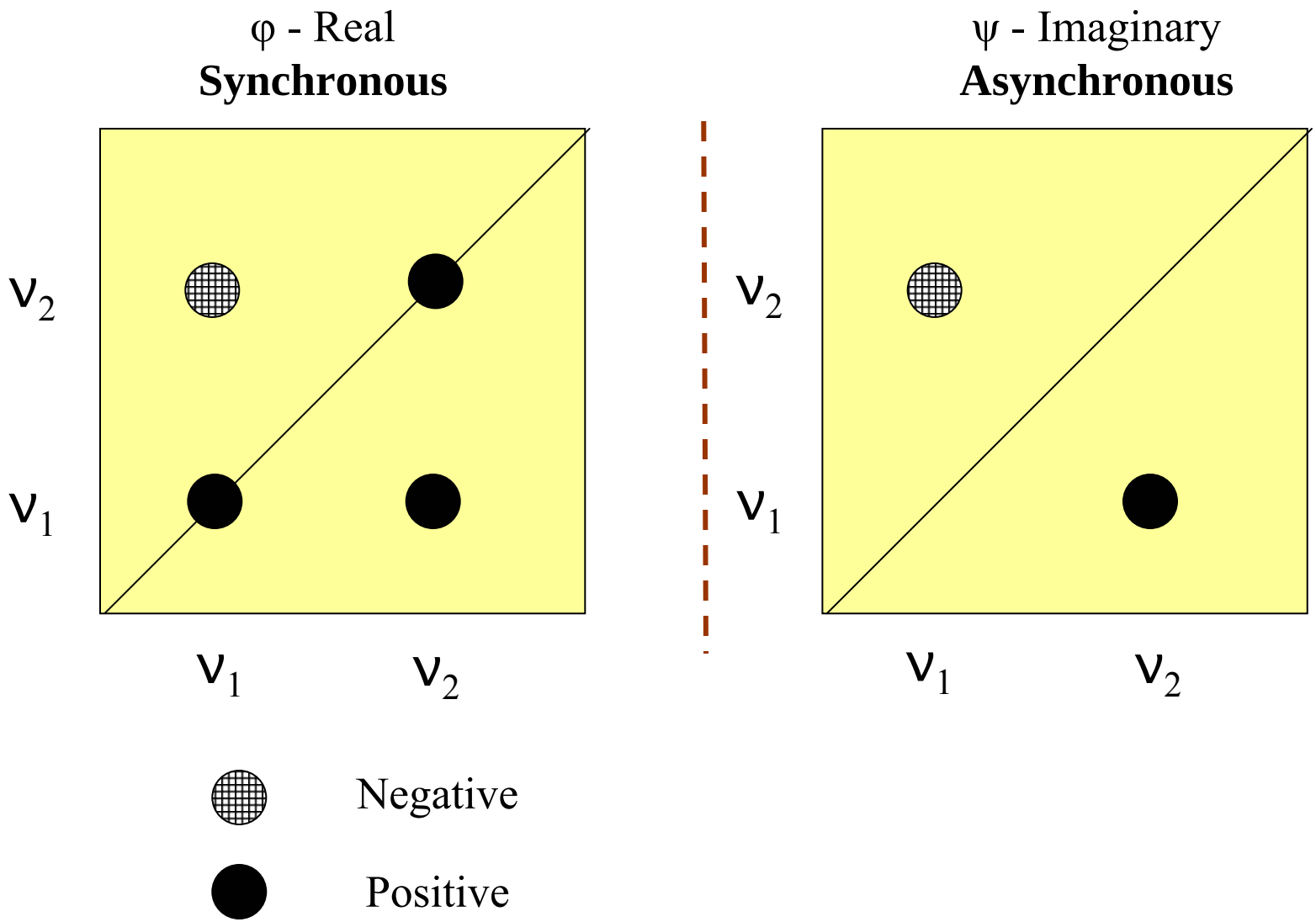
φ - Real
Synchronous
ψ - Imaginary
Asynchronous
ν2
ν1
ν1
ν2
ν2
ν1
ν1
ν2
Negative
Positive

and minimum correlation intensities are observed when the signal variations are 90 degrees out-of-phase.

The interpretation of 2D correlation maps can be difficult. The very reason that IR spectroscopy is valuable in molecular analysis, i.e. the highly sensitive nature of vibrational spectra to local environment, means that the 2D synchronous and asynchronous spectra can be complex, even for simple systems. Several articles have appeared that explore the current state-of-the-art for 2D IR spectral interpretation. The effect of commonly encountered changes in the IR band parameters, such as frequency, bandwidth, intensity changes and errors in band position have been described by Gericke et al. [120]. Other common complications encountered in spectral analysis, including the effect of noise and baseline fluctuations on 2D spectra, were investigated by Czarnecki [121, 122]. The effect of instrumental parameters such as resolution, zero-filling and apodization functions on the generalized 2D IR correlation maps has been studied [123]. The most common issue relating to the interpretation of asynchronous correlation maps has been the presence of excessive cross peaks due to noise present in the experimental infrared spectrum. The effects of noise on the evaluation of correlation coefficients has been investigated [124, 125]. Different methods have been adopted to minimize this such as wavelets and smoothing [126].

Applications of 2D IR

Since the development of 2D IR correlation spectroscopy, the interest in this field can be classified into two areas: Method development and Application. Recent reviews of generalized 2D IR correlation have appeared in the literature [127-130]. Harrington et al. published a very useful overview of the 2D IR technique with a tutorial on the use of MATLAB as the

implementation program for performing the correlation [131]. Most of the applications of 2D IR are based on collecting experimental data on systems that are subjected to environmental perturbations such as temperature, pH, concentration, pressure etc. These spectra are usually collected at even spaced intervals of the perturbation parameter since the interpretation of the 2D maps is easier if this is the case. Noda has studied the use of uneven spaced data in 2D IR correlation [132]. Yu has investigated the normalization method used when concentration is used as the perturbation parameter [133]. Several new modified new methods using 2D IR correlation as a basis have been introduced in the last few years. In a series of papers [134-137], Jung has described the use of Eigen Value Transformations in the correlation method and discussed the effect on resolution, noise, selectivity and normalization on the resulting correlation maps. A new method of 2D correlation was developed by Sasic called sample-sample correlation. This method involved cross correlating spectral sets similar to the generalized method but the correlation was between the external perturbation variables and the resulting correlation plots were between the perturbation variables and not the spectral frequencies [138-141]. Morita has developed a global phase angle description of the 2D method [142-144]. 2D IR has also been applied to self modeling curve resolution analysis of spectral sets [145]. Sasic has also investigated the use of moving windows in the 2D correlation method and determined the signal to noise threshold in correlation spectra [146]. Wu has described a technique called hybrid 2D Correlation spectroscopy [147, 148]. PCA and generalized 2D IR correlation methods have been compared by Sasic [149]. Gericke investigated the application of 2D IR to biological samples and used simulated spectra for this purpose. By varying bandshapes, frequency and intensities, Gericke was able to accomplish this [120]. The H/D exchange kinetics of proteins can be studied

using this technique, and Raussens has used model spectra to better understand this application [150].

2D IR is increasingly being used in the identification and classification of traditional Chinese medicines [151-156]. 2D IR is increasingly being used to identifying different protein conformations that are present under the broad Amide I band in the infrared spectrum [157-174]. The denaturation and unfolding of proteins in solution has also been studied using 2D IR by several researchers [171, 175-180]. Some other biological systems that have been studied using 2D IR include bacteria [181, 182], enzymes [178, 183-185], protein-antigen binding [186, 187], biopolymers [188-190] and food products [191, 192].

For example, the thermal transitions of a number of proteins has been studied using 2D IR, including cytochrome c [169, 193], CMP kinases [178], ovalbumin [171], β-lactoglobulin [194], avidin [187] and synthetic helix-forming peptides [195]. Several studies have been published that use pH gradients or H – D exchange to enhance the amide spectral region and assign conformations to the underlying band components [196-198]. Studies using 2D hetero-spectral correlations have appeared that enable comparisons to be made among a number of spectral techniques [199, 200].

Two-dimensional IR correlation analysis has also been used to analyze structure in monomolecular films. The phase behavior of phospholipid monolayers using 2D IR have been studied and it was shown how these methods could distinguish bands due to co-existing phases in a disorder-order phase transition in the monolayer [201, 202].

The original application of this correlation method was to polymerization processes [203, 204]. Some other oligomers that have been studied include ester based polymers such as phthlates, actetates and benzoates [205-216]. Liquid crystal polymers [217-222], epoxy resins

and polysilanes [223-227] are some other polymers that have investigated using 2D IR correlation. The properties of different polymer blends containing polystyrene having been investigated in details using two dimensional infrared correlation spectroscopy [228-240]. Investigations of phase transitions in Langmuir monolayers, liquid crystals, polymer thin films that are induced by pressure, temperature and pH have been performed using 2D IR [201, 202, 207, 210, 213, 221, 231, 241-243]. In a novel application, Awichi has investigated the molecular interactions between glucose anomers and carbon nanotubes using 2D IR correlation [244].

The application of two-dimensional cross correlation is not necessarily limited to infrared spectroscopy and has been applied to Raman spectroscopy [117, 163, 189, 199, 200, 229, 234, 238, 245-249], X-Ray Absorption Spectroscopy [250] and Fluorescence spectroscopy [251-254]. Recently, Izawa et al. have described the application of 2D cross correlation analysis to gel permeation chromatography in a series of papers [255-259]. The principle of generalized two dimensional cross correlation has also been applied to NMR spectra by Eads et al.. [260].

Raman Spectroscopy

Raman spectroscopy is an important vibrational spectroscopy technique in the structural characterization of molecules due to its sensitivity to internal molecular structure, the chemical nature of the molecule, and the local molecular environment. Raman also gives advantages over IR for characterization of hydrocarbon assemblies, which include sensitivity to chain backbone, sensitivity to intra and inter molecular lateral interactions and ability to detect low frequency vibrational modes [261].

The Raman Effect is produced as a result of the interaction between light and matter. Scattered light can be either of the same frequency as the incident light (elastic) or be of a

Figure 2.6 A diagrammatic representation of the Raman Scattering process.

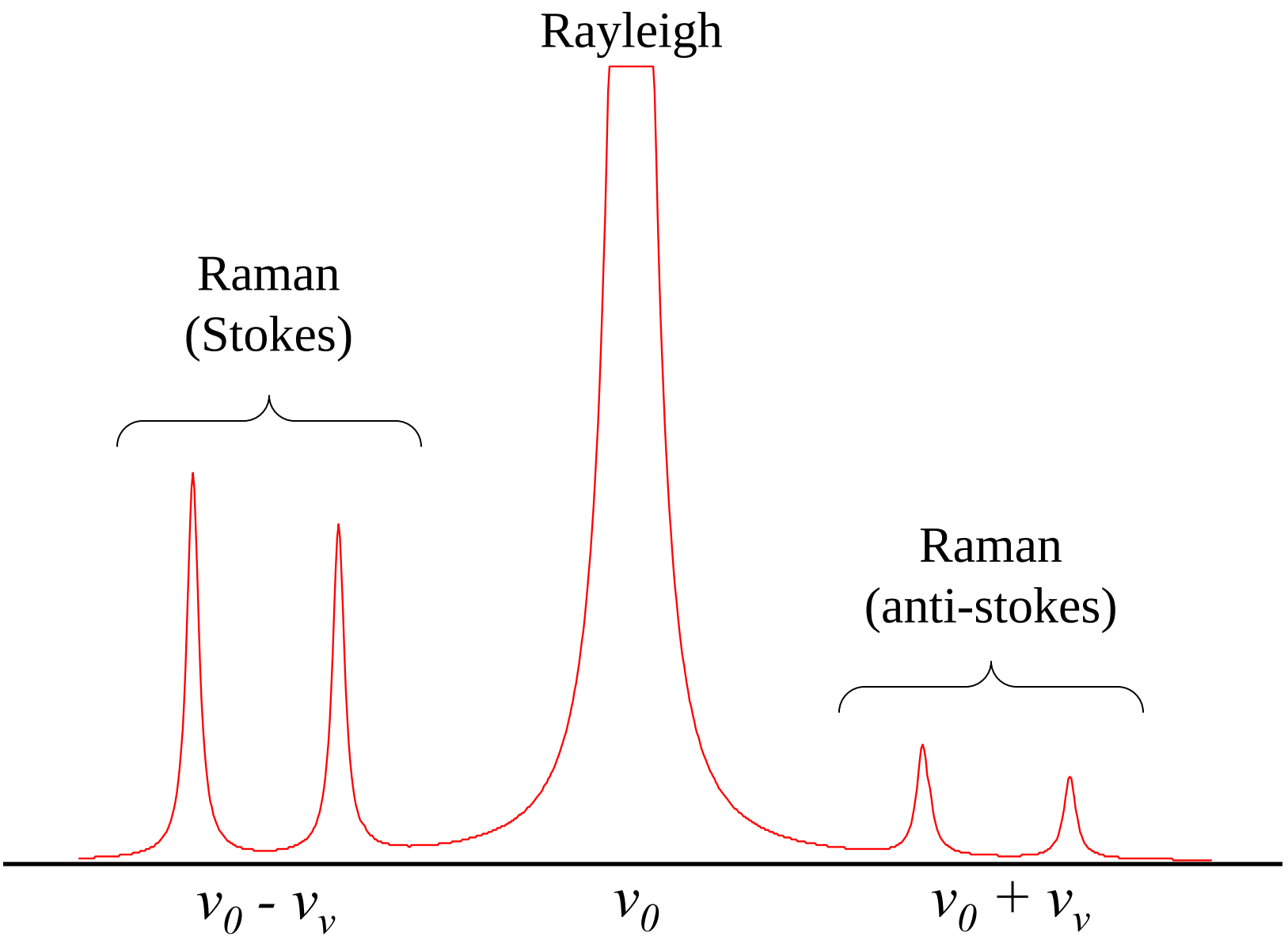
Rayleigh
Raman
(Stokes)
Raman
(anti-stokes)
$\nu_0 - \nu_v$
ν_0
$\nu_0 + \nu_v$

different frequency (inelastic). Though Brillouin (1922) [262] and Smekal (1925) [263] were the first to theoretically predict the inelastic scattering of light, the first experimental evidence of this effect was provided by Raman and Krishnan in 1928 [264, 265]. Since the Raman effect is a very weak optical phenomenon, its use was limited until the invention of the laser by Schawlow and Townes (1958) and Maiman (1960) [266, 267]. The laser proved to be the ideal source for this spectroscopic method because of the high power density and the variety of wavelengths achievable within the visible region. Further instrumental advances, such as multichannel detectors, notch filters and holographic gratings, within the past couple of decades have made Raman spectroscopy one of the most versatile methods for chemical analysis. Both routine qualitative and quantitative measurements of inorganic and organic species that exist as gases, vapors, aerosols, liquids or solids and complex analytical problems such as determining molecular structure and orientation can be performed at a wide variety of temperatures [268-271]. Modern Raman techniques and sampling geometries have not only compensated for the weak Raman Effect, but have allowed Raman spectroscopy to emerge as an effective and sensitive tool for routine analytical measurements amenable to both laboratory and remote environments. Recent thorough reviews on the theory behind the Raman scattering phenomenon can be found in literature [268, 271, 272].

Surface Enhanced Raman Scattering

Surface Enhanced Raman Scattering (SERS) was discovered nearly 30 years ago by Fleischmann in 1974 who observed intense Raman scattering from pyridine adsorbed onto a roughened silver electrode surface from an aqueous solution. This enhancement effect was also observed independently by Van Duyne and Creighton. The developments in this field were

initially in the fundamentals and later on shifted to applications and several papers have been published in diverse fields which included electrochemistry, analytical chemistry, chemical physics, solid-state physics, biophysics and even medicine.

The motivation for the original work that led to the discovery of SERS was to develop a chemically specific spectroscopic probe that could be used to study electrochemical processes in situ. It was immediately obvious that the great enhancement in intensities observed could not be accounted for simply by the increase in the number of scattering molecules present and it was proposed that the enhancement of the scattered intensity occurred in the adsorbed state. Jeanmaire and Van Duyne tentatively proposed an electric field enhancement mechanism (EM) whereas Albrecht and Creighton speculated that resonance Raman scattering from molecular electronic states, broadened by their interaction with molecular electronic states, broadened by their interaction with the metal surface, might be responsible (CHEM).

The SERS effect has been observed for a very large number of molecules adsorbed on surfaces of metals, the most common ones being silver, copper and gold, in a variety of morphologies and physical environments. The greatest enhancements have been reported for surfaces which are rough on the nanoscale (10-100nm). The different methods available to prepare SERS substrates include electrode surfaces roughened by one or more oxidation-reduction cycles, island films deposited on glass surfaces at elevated temperatures, films deposited by evaporation or sputtering in vacuum onto cold substrates, metal colloids in solution (especially aggregated colloids), single ellipsoidal nanoparticles and particle arrays prepared by lithographic techniques.

SERS differs in a number of ways from ordinary Raman spectroscopy of molecules and solids and even from unenhanced surface Raman spectroscopy. The intensities of the bands

observed generally fall off with increasing vibrational frequency; C-H stretches, for example, tend to be relatively weak in SERS. Overtones and combination bands are not common. Selection rules are relaxed resulting in the appearance of normally forbidden Raman modes in the surface spectra. The spectra tend to be completely depolarized, in contrast to solution spectra and those taken from molecules adsorbed on atomically smooth, flat surfaces, Excitation profiles differ from the ω^4 dependence of nonresonant scattering; the broad resonances observed may be characteristic of the substrate, the adsorbate or the combined system. Excitation profiles depend upon electrode potential in electrochemical experiments and may be different vibrational modes. The enhancement may be remarkably long ranged, extending tens of nanometers from the surface, depending upon the substrate morphology. Two different theories have been proposed to the phenomenon of SERS, the Electromagnetic Enhancement theory and the Chemical enhancement Theory. Both these theories have been discussed in detail in recent reviews on the subject [273][274]and hence shall be described here only briefly.

Electromagnetic Enhancement (EM)

The collective excitation of the electron gas of a conductor is called a plasmon and when the excitation is localized at the surface, it is called a surface plasmon. Surface plasmons can be localized on the surface of a spherical particle and surface roughness or curvature is required for the excitation of surface plasmons by light. The electromagnetic field of the light at the surface can be greatly enhanced under conditions of surface plasmon excitation; the amplification of both the incident laser field and the scattered Raman field through their interaction with the surface constitutes the electromagnetic SERS mechanism. The dominance of the coinage metals and the alkali metals as SERS substrates arises simply because the resonance condition is

satisfied at the visible frequencies commonly used for Raman spectroscopy. Other metals have their surface plasmon resonances in different regions of the electromagnetic spectrum and can in principle support SERS at those frequencies.

Chemical Enhancement (CHEM)

A second enhancement mechanism has been proposed that is believed to operate independently of the EM mechanism. In the case of systems in which both mechanisms are simultaneously operative the enhancement effects are multiplicative.

EM enhancement should be a non-selective amplifier for Raman scattering by all molecules adsorbed on a particular surface yet the molecules CO and N_2 differ by a factor of 200 in their SERS intensities under the same experimental conditions. This result is very hard to explain involving only EM enhancement. The large difference can not be explained by large differences in orientation since the polarizabilities of the molecules are also similar. A second line of evidence in support of a chemical mechanism comes from potential dependent electrochemical experiments. If the potential is scanned at a fixed laser frequency or the laser frequency is scanned at a fixed potential broad resonances are observed.

These observations can be explained by a resonance Raman mechanism in which either (a) the electronic states of the adsorbate are shifted and broadened by their interaction with the surface or (b) new electronic states which arise from chemisorption serve as resonant intermediate states in Raman scattering. The evidence to date supports the latter hypothesis. It is not uncommon that the highest occupied molecular orbital (HOMO) and the lowest unoccupied molecular orbital (LUMO) of the adsorbate are symmetrically disposed in energy with respect to the Fermi level of the metal. In this case charge-transfer excitations (either from the metal to the

molecule or vice versa) can occur at about half the energy of the intrinsic intramolecular excitations of the adsorbate. Molecules commonly studied by SERS typically have their lowest-lying electronic excitations in the near ultraviolet region which places the charge transfer excitations of this model in the visible region of the spectrum.

Applications

One of the main obstacles in the development of SERS as a powerful surface technique has been the lack of method to prepare stable and reproducible SERS active substrates. Among all the metals, only Ag, Au and Cu have been shown to produce significant enhancement effects and hence the number of methods available to synthesize substrates is limited by the physical and chemical properties of these metals.

It has been shown that for substrates to exhibit the SERS effect, their surface morphology should possess a roughness scale of 50nm - 200nm. The atomically flat surfaces, commonly used in fundamental research in surface science are not suitable for SERS investigations.

Over the last 20 years, the most common methods of preparation of these substrates have been electrochemical oxidation-reduction cycles, island film deposition on solid substrates (glass, quartz) at high temperatures, evaporation or sputtering of metals onto cold substrates, aggregated colloids, single ellipsoidal nanoparticles and arrays of such particles prepared by lithographic techniques [274].

Comparison of SERS substrates prepared by different methods can be made on the following factors: 1) Reproducibility 2) Stability 3) Enhancement Factors. Norrod et al. published a quantitative comparison of the sensitivity and limit of detection observed on five different SERS substrates and concluded that vapor deposited films were considerably better than

electrochemically roughened surfaces in terms of reproducibility, sensitivity and limits of detection [275]

The most popular substrates used currently for SERS experiments are colloidal solutions of silver and gold. Single molecule detection of dye molecules has been achieved using colloidal solutions of silver by several groups [276-279] and a series of papers have been published by Natan et al. [280-285] on the development of novel SERS substrates based upon the self-assembly of gold colloids. These films are prepared by successively treating a Au nanoparticle monolayer with a bi-functional cross linker and colloidal Ag or Au solutions. Some of the important characteristics of these systems include compatibility with biomolecules and the ability to tune the electromagnetic characteristics of the surface by controlling particle size and shape. Another advantage of colloidal solutions is that the degradation of the sample due to the laser is negligible as a result of Brownian motion of the colloidal particles in solution.

However, to achieve optimal signals, an elaborate and precise preparative procedure is often required, and typically the average citrate silver colloid exhibits a batch to batch %Relative Standard Deviation of 41% [286, 287] The variation of the SERS intensity with increase in age of the Ag colloid is also an issue. If the batches of colloids used are unstable, this will lead to uncertainty in the SERS signals produced at different time intervals. Further since the same colloidal solution cannot be used entirely for the same analysis, it is necessary to make a colloid that gives reproducible SERS with different batches. The preparation of colloidal solutions is dependent on several parameters such as temperature, extent of mixing and the rate of addition of the reagents. Vapor deposited silver films on solid substrates are quite popular as SERS substrates. They are relatively easy to make as the vapor deposition process is straightforward

and inexpensive. This method also affords some control over the surface morphology of the film that is deposited.

A relatively simple method for producing gold and silver island film substrates has been described by Dyer et al. where the surface plasmon frequency of the film can be tuned through the visible and the near-infrared regions of the electromagnetic spectrum [288, 289]. They achieved this by precise control of thermal evaporation deposition parameters such as substrate temperature, deposition rate and film thickness.

Constantino et al. have reported spatially resolved SERRS spectra of single dye molecules that were dispersed in a Langmuir-Blodgett monolayer of fatty acid formed on a vapor deposited silver island film. The enhancement factors obtained were similar to those obtained using colloidal solutions of silver [290].

SERS active substrates have been prepared by vapor depositing Ag films onto porous surface of zeolite nanocrystals. This substrate was found to be particularly active in the detection of extremely low concentrations of uranyl ions. The negatively charge framework of the zeolites was found to provide selectivity to the adsorption process based on static electric forces. Vapor depositing silver islands on films of silica nanospheres on a glass slide has also been shown to produce SERS active substrates. The SERS activity was observed to have a dependence on the dimensions of the silica nanospheres as well as the thickness of the Ag island films [291, 292].

Metal-coated alumina nanoparticles are the most common example due to their efficiency, low cost and less complicated preparation. Silver coated titanium dioxide nanoparticles can also be used as SERS substrates. Titanium dioxide is another material that has been used to produce SERS-active substrates. It is first deposited on glass and other substrates and then coated with a 50-100nm layer of silver by thermal evaporation [293, 294]. Silver coated silica nanoparticles

have also been synthesized and found to be SERS-active. Fumed silica particles are suspended in a water solution and coated onto a glass support followed by thermal evaporation upto a thickness of 100nm [295].

Hill et al. have reported the fabrication of single fiber surface-enhanced Raman sensors by depositing rough metal films at the tips of optical fibers [296]. Different deposition techniques such as slow evaporation of metal island films and vacuum deposition of metal films over nanoparticles were compared to identify the most efficient method. It was observed that polishing the fiber tip at an angle enhances the enhancement factor considerably.

Surface-enhanced Raman signal can also be measured using a fine metal tip, such as AFM or STM tips. Anderson [297] and Nieman et al. [298] report enhancement factors of ~10^4 using conventional silicon AFM tips that were coated with gold.

Schneider et al. have prepared SERS substrates with enhancement factors > 10^7 by deposition Au or Ag on a vapor deposited silver island film by electrocrystallization [299, 300]. The films obtained were found to be extremely stable and applicable over a broad range of analytes. To improve upon the stability and reproducibility of substrates prepared by the Electrochemical ORC method, Dick et al. have fabricated and characterized Metal Film over Nanospheres (MFON) electrodes [301]. These substrates were prepared by coating a smooth Au or Ag electrode surface with polystyrene latex nanospheres and then vapor depositing the metal over the surface.

Thin films can also be deposited on the surface of substrates by chemical reduction of silver nitrate or by photo-reduction . Chan et al. have reported the fabrication of a SERS substrate that has silver chemically deposited over a silicon porous structure [302]. The dimensions of the pores in the silicon surface in the orders of nanometers and due to the large surface area, good

enhancement factors are observed. Sailor et al. have reported detection limits 5 orders of magnitude lower than Chan et al. using a substrate made by the same method. The observed enhancement factors are approximately the same order as those obtained using colloidal solutions [303]. Ozaki et al. have developed a new SERS substrate using a novel silver enhancer and initiator mixture [304]. Aggregates of silver nanoparticles have been prepared by adding a novel silver enhancer and initiator mixture to silver colloidal nanoparticles on a quartz slide, and the resulting enlarged particles have been shown to possess greater SERS activity than the original nanoparticles themselves.

Au-Ag core-shell type bimetallic nanoparticles have also been shown to SERS-active substrates [305-308]. Mandal et al. have reported detection limits down to the single molecular level using these substrates that are prepared by a seed mediated technique in solution.

Another method to prepare SERS active substrates is to electrodeposit metal nanowires in nanopores that are created in ordered anodic alumina templates. Moskovits et al. have reported the fabrication of flat arrays of aligned Ag nanowires by electrodepositing silver in such nanopores, and then releasing the nanowires and re-depositing them on an oxidized, single crystal Si source [309]. These substrates were shown to produce enhancement factors of $\sim 10^{11}$ for Rhodamine6G. Two-dimensional arrays of metal nanowires with diameters ranging from 15-70nm were prepared by Tian et al., by electrodepositing metals like Cu, Ag, Au, Ni and Co in the nanoholes formed in anodic aluminum oxide (AAO) films, followed by partial removal of the films [310]. The observed SERS activity was found to critically depend on the length and the diameter of these nanowires.

Green et al. have reported an elaborate island lithography scheme to make Ag structures on silicon [311, 312]. This fabrication process involves formation of a randomly ordered caesium

chloride layer followed by etching, electroless plating, Ag vapor depositing and oxidation of silicon in the presence of fluoride ions. Ag structures in the shapes of toruses, pillars and spheres can be generated using this technique with fairly good enhancement factors of ~10^7 – 10^8.

Nanosphere lithography has been developed and applied by Van Duyne and coworkers to fabricate new nanoparticle structures in the last few years [313-316]. The silver metal is evaporated onto preformed arrays (masks) of polystyrene nanospheres on a glass slide, which are then removed, leaving behind the metal particles formed in the gaps in the polystyrene array. By varying the dimensions of the nanospheres used as masks, the surface plasmon resonance frequency of the Ag nanoparticles synthesized can be tuned in the 20-1000nm range. The optical properties of these size tunable Ag nanoparticles have been studied by using localized SPR spectroscopy and the effects of size, shape and inter particle spacing, nanoparticle-substrate interaction, solvent, dielectrics overlayers and molecular adsorbates have been investigated thoroughly.

To summarize, a good SERS substrate should be robust, stable over the duration of the analysis, provide strong enhancement factors, reproducible, should be easy and relatively inexpensive to prepare and easy to store. Of the different techniques discussed above, vapor deposition of island films seems to satisfy most criteria except the most important criterion of large enhancement factors.

However, vapor deposited silver nanorod films prepared using the GLAD technique are found to produce very good enhancement factors of ~10^8 that are comparable to most substrates. The enhancement factors of >10^{12} reported for colloidal solutions are for single molecules and would decrease to ~10^7 – 10^8 when averaged over all the sample molecules.

Glancing Angle Deposition is a technique for fabricating materials with a controlled structure. It is based on thin film deposition, by evaporation or sputtering, and employs oblique angle deposition flux and substrate motion to allow nanometer scale control of structure in engineered materials. The substrate is oriented at a large oblique to the incident vapor flux. This leads to an effect called atomic shadowing and results in a porous structure with isolated columns of material growing towards the vapor source. The substrate is then tilted or rotated to obtain engineer the desired microstructures [317]. Nanorod structures produced by this technique can be engineered so as to produce the right aspect ratio to achieve the greatest SERS activity.

References:

1. Tabor, D., *Babylonian Lecanomancy - An Ancient Text On The Spreading Of Oil On Water.* Journal Of Colloid And Interface Science, 1980. **75**(1): p. 240-245.
2. Fulford, G.D., *Pouring Holy Oil On Troubled Waters.* Isis, 1968. **59**(197): p. 198-199.
3. Dynarowicz-Latka, P., A. Dhanabalan, and O.N. Oliveira, *Modern physicochemical research on Langmuir monolayers.* Advances In Colloid And Interface Science, 2001. **91**(2): p. 221-293.
4. Schürch, S., *Surface tension at low lung volumes: dependence on time and alveolar size.* Respir. Physiol., 1982. **48**: p. 339-355.
5. Avery, M.E. and J. Mead, *Surface properties in relation to atelectasis and hyaline memrane disease.* Am. J. Dis. Child., 1959. **97**: p. 517-523.
6. Lewis, J.F. and A.H. Jobe, *Surfactant and the adult respiratory distress syndrome.* Am. Rev. Respir. Dis., 1993. **147**: p. 218-233.
7. Notter, R.H. and Z. Wang, *Pulmonary surfactant: physical chemistry, physiology and replacement.* Rev. Chem. Eng., 1997. **13**: p. 1-118.
8. Pison, U., et al.., *Surfactant abnormalities in patients with respiratory failure after multiple trauma.* Am. Rev. Respir. Dis., 1989. **140**: p. 1033-1039.
9. Creuwels, L.A.J.M., L.M.G. van Golde, and H.P. Haagsman, *The pulmonary surfactant system: biochemical and clinical aspects.* Lung, 1997. **175**: p. 1-39.
10. Notter, R.H., *Lung surfactants: basic science and clinical applications*. 2000, New York: Marcel Dekker, Inc.
11. Holm, B.A., et al.., *Content of dipalmitoyl phosphatidylcholine in lung surfactant: ramifications for surface activity.* Pediatr. Res., 1996. **39**: p. 805-811.

12. Hunt, A.N., F.J. Kelly, and A.D. Postle, *Developmental variation in whole human lung phosphatidylcholine molecular species: a comparision of guinea pig and rat.* Early Hum. Develop., 1991. **25**: p. 157-171.

13. Kahn, M.C., et al.., *Phosphotidylcholine molecular species of calf lung surfactant.* Am. J. Physiol., 1995. **13**: p. L567-L573.

14. Goerke, J., *Lung surfactant.* Biochim. Biophys. Acta, 1974. **344**(3-4): p. 241-61.

15. Rana, F.R., et al.., *Identification of phosphocholine plasmalogen as a lipid component in mammalian pulmonary surfactant using high-resolution phosphorus-31 NMR spectroscopy.* Biochemistry, 1993. **32**(1): p. 27-31.

16. Baritussio, A.G., et al.., *Precursor-product relationship between rabbit type II cell lamellar bodies and alveolar surface-active material. Surfactant turnover time.* Biochim. Biophys. Acta, 1981. **666**(3): p. 382-93.

17. Hawgood, S., et al.., *Nucleotide and amino acid sequences of pulmonary surfactant protein SP 18 and evidence for cooperation between SP 18 and SP 28-36 in surfactant lipid adsorption.* Proc. Natl. Acad. Sci. U. S. A., 1987. **84**(1): p. 66-70.

18. Oosterlaken-Dijksterhuis, M.A., et al.., *Characterization of lipid insertion into monomolecular layers mediated by lung surfactant pProteins SP-B and SP-C.* Biochemistry, 1991. **30**: p. 10965-10971.

19. Yu, S.-H. and F. Possmayer, *Effect of pulmonary surfactant protein B (SP-B) and calcium on phospholipid adsorption and squeeze-out of phosphatidylglycerol from binary phospholipid monolayers containing dipalmitoylphosphatidylcholine.* Biochim. Biophys. Acta, 1992. **1126**: p. 26-34.

20. Johansson, J., et al.., *The NMR structure of the pulmonary surfactant-associated polypeptide SP-C in an apolar solvent contains a valyl-rich α-helix.* Biochemistry, 1994. **33**: p. 6015-6023.

21. Amrein, M., A. von Nahmen, and M. Sieber, *A scanning force and fluorescence light microscopy study of the structure and function of a model pulmonary surfactant.* Eur. Biophys. J., 1997. **26**: p. 349-357.

22. von Nahmen, A., et al.., *The structure of a model pulmonary surfactant as revealed by scanning force microscopy.* Biophys. J., 1997. **72**: p. 463-469.

23. Kramer, A., et al.., *Distribution of the surfactant-associated protein C within a lung surfactant model film investigated by near-field optical microscopy.* Biophys. J., 2000. **78**(1): p. 458-465.

24. Galla, H.J., et al.., *The role of pulmonary surfactant protein C during the breathing cycle.* Thin Solid Films, 1998. **329**: p. 632-635.

25. Krüger, P., et al.., *Effect of hydrophobic surfactant peptides SP-B and SP-C on Binary Phospholipid Monolayers. I. Fluorescence and dark-field microscopy.* Biophys. J., 1999. **77**: p. 903-914.

26. Krüger, P., et al.., *Effect of the hydrophobic peptide SP-C on binary phospholipid monolayers. Molecular machinery at the air/water interface.* Biophys. Chem., 2002: p. In press.

27. Curstedt, T., et al.., *Low-Molecular Mass Surfactant Protein Type I: The Primary Structure of a Hydrophobic 8 kDa Polypeptide with Eight Half-Cystine Residues.* Euro. J. Biochem., 1988. **172**: p. 521-525.

28. Johansson, J., T. Curstedt, and H. Jornvall, *Surfactant Protein-B - Disulfide Bridges, Structural-Properties, And Kringle Similarities.* Biochemistry, 1991. **30**(28): p. 6917-6921.

29. Johansson, J., H. Jornvall, and T. Curstedt, *Human Surfactant Polypeptide Sp-B - Disulfide Bridges, C-Terminal End, And Peptide Analysis Of The Airway Form.* Febs Letters, 1992. **301**(2): p. 165-167.

30. Morrow, M.R., et al.., *Deuterium NMR studies of the effect of pulmonary surfactant SP-C on the 1,2-dipalmitoyl-sn-glycero-3-phosphocholine headgroup: A model for transbilayer peptides in surfactant and biological membranes.* Biochemistry, 1993. **32**(42): p. 11338-44.

31. Vandenbussche, G., et al.., *Secondary structure and orientation of the surfactant protein SP-B in a lipid environment: a Fourier transform infrared spectroscopy study.* Biochemistry, 1992. **31**: p. 9169-9176.

32. Kobayashi, T., et al.., *Activity Of Pulmonary Surfactant After Blocking The Associated Proteins Sp-A And Sp-B.* Journal Of Applied Physiology, 1991. **71**(2): p. 530-536.

33. Oosterlaken-Dijksterhuis, M.A., et al.., *Interaction of lipid vesicles with monomolecular layers containing lung surfactant proteins SP-B or SP-C.* Biochemistry, 1991. **30**: p. 8276-8281.

34. Cochrane, C.G. and S.D. Revak, *Pulmonary surfactant protein B (SP-B): structure-function relationships.* Science, 1991. **254**: p. 566-568.

35. Camacho, L., et al.., *Effect of pH on the interfacial adsorption activity of pulmonary surfactant.* Colloids And Surfaces B-Biointerfaces, 1996. **5**(6): p. 271-277.

36. Poulain, F.R., et al.., *Effects Of Surfactant Apolipoproteins On Liposome Structure - Implications For Tubular Myelin Formation.* American Journal Of Physiology, 1992. **262**(6): p. L730-L739.

37. Suzuki, Y., Y. Fujita, and K. Kogishi, *Reconstitution Of Tubular Myelin From Synthetic Lipids And Proteins Associated With Pig Pulmonary Surfactant.* American Review Of Respiratory Disease, 1989. **140**(1): p. 75-81.

38. Williams, M.C., S. Hawgood, and R.L. Hamilton, *Changes In Lipid Structure Produced By Surfactant Proteins Sp-A, Sp-B, And Sp-C.* American Journal Of Respiratory Cell And Molecular Biology, 1991. **5**(1): p. 41-50.

39. Oosterlaken-Dijksterhuis, M.A., et al.., *Lipid mixing is mediated by the hydrophobic surfactant protein SP-B but not by SP-C.* Biochim. Biophys. Acta, 1992. **1110**: p. 45-50.

40. Vincent, J.S., et al.., *Raman-Spectroscopic Studies Of Model Human Pulmonary Surfactant Systems - Phospholipid Interactions With Peptide Paradigms For The Surfactant Protein Sp-B.* Biochemistry, 1991. **30**(34): p. 8395-8401.

41. Baatz, J.E., B. Elledge, and J.A. Whitsett, *Surfactant protein SP-B induces ordering at the surface of model membrane bilayers.* Biochemistry, 1990. **29**: p. 6714-6720.

42. Shiffer, K., et al.., *Lung surfactant proteins, SP-B and SP-C, alter the thermodynamic properties of phospholipid membranes: a differential calorimetry study.* Biochemistry, 1993. **32**(2): p. 590-7.

43. Allara, D.L., A. Baca, and C.A. Pryde, *Distortions Of Band Shapes In External Reflection Infrared-Spectra Of Thin Polymer-Films On Metal Substrates.* Macromolecules, 1978. **11**(6): p. 1215-1220.

44. Greenler, R.G., *Infrared Study Of Adsorbed Molecules On Metal Surfaces By Reflection Techniques.* Journal Of Chemical Physics, 1966. **44**(1): p. 310-&.

45. Harrick, N.J., *Transmission Spectra Without Interference-Fringes.* Applied Spectroscopy, 1977. **31**(6): p. 548-549.

46. Ishino, Y. and H. Ishida, *Ft-Ir External Reflection Spectroscopy At Brewster-Angle.* Applied Spectroscopy, 1992. **46**(3): p. 504-509.

47. Dluhy, R.A., *Quantitative External Reflection Infrared Spectroscopic Analysis Of Insoluble Monolayers Spread At The Air-Water-Interface.* Journal Of Physical Chemistry, 1986. **90**(7): p. 1373-1379.

48. Alonso, C., et al.., *Characterization of the melting-crystallization transition of alcohol monolayers at the air/water interface by polarization modulation infrared reflection absorption spectroscopy.* Chemical Physics Letters, 1998. **284**(5-6): p. 446-451.

49. Buontempo, J.T. and S.A. Rice, *Infrared External Reflection Spectroscopic Studies Of Phase-Transitions In Langmuir Monolayers Of Stearyl Alcohol.* Journal Of Chemical Physics, 1993. **99**(9): p. 7030-7037.

50. Buontempo, J.T. and S.A. Rice, *Infrared External Reflection Spectroscopic Studies Of Phase-Transitions In Langmuir Monolayers Of Heneicosanol.* Journal Of Chemical Physics, 1993. **98**(7): p. 5835-5846.

51. Ren, Y., et al.., *Reflectance Infrared Spectroscopic Analysis Of Monolayer Films At The Air-Water-Interface.* Journal Of Physical Chemistry, 1994. **98**(34): p. 8424-8430.

52. Ren, Y., et al.., *Spectroscopic Characterization Of Polymer Adsorption At The Air Solution Interface.* Macromolecules, 1995. **28**(1): p. 358-364.

53. Gericke, A. and H. Huhnerfuss, *Infrared Spectroscopic Comparison Of Enantiomeric And Racemic N-Octadecanoylserine Methyl-Ester Monolayers At The Air/Water Interface.* Langmuir, 1994. **10**(10): p. 3782-3786.

54. Sakai, H. and J. Umemura, *Structure disordering during surface pressure relaxation of Langmuir films of stearic acid as studied by infrared external reflection spectroscopy.* Chemistry Letters, 1996(6): p. 465-466.

55. Sakai, H. and J. Umemura, *Molecular-orientation change in Langmuir films of stearic acid and cadmium stearate upon surface compression, as studied by infrared external-reflection spectroscopy.* Bulletin Of The Chemical Society Of Japan, 1997. **70**(5): p. 1027-1032.

56. Sakai, H. and J. Umemura, *Molecular orientation in Langmuir films of 12-hydroxystearic acid studied by infrared external-reflection spectroscopy.* Langmuir, 1998. **14**(21): p. 6249-6255.

57. SimonKutscher, J., A. Gericke, and H. Huhnerfuss, *Effect of bivalent Ba, Cu, Ni, and Zn cations on the structure of octadecanoic acid monolayers at the air-water interface as determined by external infrared reflection-absorption spectroscopy.* Langmuir, 1996. **12**(4): p. 1027-1034.

58. Sinnamon, B.F., R.A. Dluhy, and G.T. Barnes, *Reflection-absorption FT-IR spectroscopy of vinyl octadecanoate at the air/water interface.* Colloids And Surfaces A-Physicochemical And Engineering Aspects, 1999. **156**(1-3): p. 215-222.

59. Sinnamon, B.F., R.A. Dluhy, and G.T. Barnes, *Reflection-absorption FT-IR spectroscopy of pentadecanoic acid at the air/water interface.* Colloids And Surfaces A-Physicochemical And Engineering Aspects, 1999. **146**(1-3): p. 49-61.

60. Dicko, A., H. Bourque, and M. Pezolet, *Study by infrared spectroscopy of the conformation of dipalmitoylphosphatidylglycerol monolayers at the air-water interface and transferred on solid substrates.* Chemistry And Physics Of Lipids, 1998. **96**(1-2): p. 125-139.

61. Dluhy, R.A., N.A. Wright, and P.R. Griffiths, *Insitu Measurement Of The Ft-Ir Spectra Of Phospholipid Monolayers At The Air Water Interface.* Applied Spectroscopy, 1988. **42**(1): p. 138-141.

62. Flach, C.R., et al.., *Biophysical studies of model stratum corneum lipid monolayers by infrared reflection-absorption spectroscopy and Brewster angle microscopy.* Journal Of Physical Chemistry B, 2000. **104**(9): p. 2159-2165.

63. Gericke, A., et al.., *Partially deuterated phospholipids as IR structure probes of conformational order in bulk and monolayer phases.* Journal Of Molecular Structure, 1996. **379**: p. 227-239.

64. Mitchell, M.L. and R.A. Dluhy, *Insitu Ft-Ir Investigation Of Phospholipid Monolayer Phase-Transitions At The Air Water Interface.* Journal Of The American Chemical Society, 1988. **110**(3): p. 712-718.

65. Pastranarios, B., et al.., *A Direct Test Of The Squeeze-Out Hypothesis Of Lung Surfactant Function - External Reflection Ft-Ir At The Air/Water Interface.* Biochemistry, 1994. **33**(17): p. 5121-5127.

66. Dieudonne, D., et al.., *Propensity for helix formation in the hydrophobic peptides K-2(LA)(x) (x = 6, 8, 10, 12) in monolayer, bulk, and lipid-containing phases. Infrared and circular dichroism studies.* Journal Of The American Chemical Society, 1998. **120**(4): p. 792-799.

67. Dluhy, R.A., et al.., *Infrared spectroscopy of aqueous biophysical monolayers.* Thin Solid Films, 1998. **329**: p. 308-314.

68. Flach, C.R., et al.., *Palmitoylation of lung surfactant protein SP-C alters surface thermodynamics, but not protein secondary structure or orientation in 1,2-dipalmitoylphosphatidylcholine Langmuir films.* Biochimica Et Biophysica Acta-Biomembranes, 1999. **1416**(1-2): p. 11-20.

69. Flach, C.R., F.G. Prendergast, and R. Mendelsohn, *Infrared reflection-absorption of melittin interaction with phospholipid monolayers at the air/water interface.* Biophysical Journal, 1996. **70**(1): p. 539-546.

70. Gallant, J., et al.., *Polarization-modulated infrared spectroscopy and X-ray reflectivity of photosystem II core complex at the gas-water interface.* Biophysical Journal, 1998. **75**(6): p. 2888-2899.

71. Gericke, A. and H. Huhnerfuss, *Ir Reflection-Absorption Spectroscopy - A Versatile Tool For Studying Interfacial Enzymatic Processes.* Chemistry And Physics Of Lipids, 1994. **74**(2): p. 205-210.

72. Grandbois, M., et al.., *Polarization-modulated infrared reflection absorption spectroscopy measurement of phospholipid monolayer hydrolysis by phospholipase C.* Langmuir, 1999. **15**(19): p. 6594-6597.

73. Lewis, R., et al.., *Fourier transform infrared spectroscopic studies of the interaction of the antimicrobial peptide gramicidin S with lipid micelles and with lipid monolayer and bilayer membranes.* Biochemistry, 1999. **38**(46): p. 15193-15203.

74. PastranaRios, B., et al.., *External reflection absorption infrared spectroscopy study of lung surfactant proteins SP-B and SP-C in phospholipid monolayers at the air/water interface.* Biophysical Journal, 1995. **69**(6): p. 2531-2540.

75. Weygand, M., et al.., *Coupling of protein sheet crystals (S-layers) to phospholipid monolayers.* Journal Of Materials Chemistry, 2000. **10**(1): p. 141-148.

76. Wu, F.J., et al.., *Stability of annexin v in ternary complexes with ca(2+) and anionic phospholipids: IR studies of monolayer and bulk phases.* Biochemistry, 1999. **38**(2): p. 792-799.

77. Wu, F.J., et al.., *Domain structure and molecular conformation in annexin V/1,2-dimyristoyl-sn-glycero-3-phosphate/Ca2+ aqueous monolayers: A brewster angle microscopy/infrared reflection-absorption spectroscopy study.* Biophysical Journal, 1998. **74**(6): p. 3273-3281.

78. Blaudez, D., et al.., *Anisotropic optical constants of bacteriorhodopsin in the mid-infrared: Consequence on the determination of alpha-helix orientation.* Applied Spectroscopy, 1999. **53**(10): p. 1299-1304.

79. Chen, H.J., et al.., *A pH dependent coil-to-sheet transition in a periodic artificial protein adsorbed at the air-water interface.* Langmuir, 1997. **13**(18): p. 4775-4778.

80. Lavoie, H., et al.., *The behavior of membrane proteins in monolayers at the gas-water interface: comparison between photosystem II, rhodopsin and bacteriorhodopsin.* Materials Science & Engineering C-Biomimetic And Supramolecular Systems, 1999. **10**(1-2): p. 147-154.

81. Riou, S.A., S.L. Hsu, and H.D. Stidham, *Structural study of poly(beta-benzyl-L-aspartate) monolayers at air-liquid interfaces.* Biophysical Journal, 1998. **75**(5): p. 2451-2460.

82. Riou, S.A., S.L. Hsu, and H.D. Stidham, *Characterization of helical sense transition for poly(beta P-benzyl L-aspartate) constrained to the air-water interface.* Langmuir, 1998. **14**(11): p. 3062-3066.

83. Schladitz, C., et al.., *Amyloid-beta-sheet formation at the air-water interface.* Biophysical Journal, 1999. **77**(6): p. 3305-3310.

84. Boncheva, M. and H. Vogel, *Formation of stable polypeptide monolayers at interfaces: Controlling molecular conformation and orientation.* Biophysical Journal, 1997. **73**(2): p. 1056-1072.

85. Castano, S., B. Desbat, and J. Dufourcq, *Ideally amphipathic beta-sheeted peptides at interfaces: structure, orientation, affinities for lipids and hemolytic activity of (KL)(m)K peptides.* Biochimica Et Biophysica Acta-Biomembranes, 2000. **1463**(1): p. 65-80.

86. Hoffmann, F., H. Huhnerfuss, and K.J. Stine, *Temperature dependence of chiral discrimination in Langmuir monolayers of N-acyl amino acids as inferred from II/A measurements and infrared reflection-absorption spectroscopy.* Langmuir, 1998. **14**(16): p. 4525-4534.

87. Huhnerfuss, H., V. Neumann, and K.J. Stine, *Role of hydrogen bond and metal complex formation for chiral discrimination in amino acid monolayers studied by infrared reflection - Absorption spectroscopy.* Langmuir, 1996. **12**(10): p. 2561-2569.

88. Baekmark, T.R., et al.., *A systematic infrared reflection-absorption spectroscopy and film balance study of the phase behavior of lipopolymer monolayers at the air-water interface.* Langmuir, 1999. **15**(10): p. 3616-3626.

89. Baekmark, T.R., et al.., *New insights into the phase behavior of lipopolymer monolayers at the air/water interface. IRRAS study of a polyoxazoline lipopolymer.* Langmuir, 1997. **13**(21): p. 5521-5523.

90. Fujita, K., et al.., *Monolayer Formation And Molecular-Orientation Of Various Helical Peptides At The Air/Water Interface.* Langmuir, 1995. **11**(5): p. 1675-1679.

91. Hagting, J.G., et al.., *Langmuir-Blodgett mono- and multilayers of (di)alkoxy-substituted poly(p-phenylenevinylene) precursor polymers. 1. Langmuir monolayers of homo- and copolymers of (di)alkoxy-substituted precursor PPVs.* Macromolecules, 1999. **32**(12): p. 3930-3938.

92. Huo, Q., et al.., *Polarization-modulated infrared reflection absorption spectroscopic studies of a hydrogen-bonding network at the air-water interface.* Journal Of Physical Chemistry B, 1999. **103**(15): p. 2929-2934.

93. Mao, L.J., A.M. Ritcey, and B. Desbat, *Evaluation of molecular orientation in a polymeric monolayer at the air-water interface by polarization-modulated infrared spectroscopy.* Langmuir, 1996. **12**(20): p. 4754-4759.

94. Weck, M., R. Fink, and H. Ringsdorf, *Molecular recognition via hydrogen bonding at the air-water interface: An isotherm and Fourier transform infrared reflection spectroscopy study.* Langmuir, 1997. **13**(13): p. 3515-3522.

95. Dluhy, R.A., *Infrared Reflection Spectroscopy - Insitu Measurement Of The Spectra Of Phospholipid Monolayers At The Air-Water-Interface.* Biophysical Journal, 1986. **49**(2): p. A322-A322.

96. Blaudez, D., et al.., *Polarization-Modulated Ft-Ir Spectroscopy Of A Spread Monolayer At The Air-Water-Interface.* Applied Spectroscopy, 1993. **47**(7): p. 869-874.

97. Blaudez, D., et al.., *Polarization Modulation Ftir Spectroscopy At The Air-Water-Interface.* Thin Solid Films, 1994. **242**(1-2): p. 146-150.

98. Blaudez, D., et al.., *Investigations at the air/water interface using polarization modulation IR spectroscopy.* Journal Of The Chemical Society-Faraday Transactions, 1996. **92**(4): p. 525-530.

99. Blaudez, D., et al.., *Organization in pure and alternate deuterated cadmium arachidate monolayers on solid substrates and at the air/water interface studied by conventional and differential Fourier transform infrared spectroscopies.* Journal Of Chemical Physics, 1996. **104**(24): p. 9983-9993.

100. Buffeteau, T., et al.., *Optical constant determination in the infrared of uniaxially oriented monolayers from transmittance and reflectance measurements.* Journal Of Physical Chemistry B, 1999. **103**(24): p. 5020-5027.

101. Flach, C.R., A. Gericke, and R. Mendelsohn, *Quantitative determination of molecular chain tilt angles in monolayer films at the air/water interface: Infrared reflection/absorption spectroscopy of behenic acid methyl ester.* Journal Of Physical Chemistry B, 1997. **101**(1): p. 58-65.

102. Gericke, A. and H. Huhnerfuss, *Investigation Of Z-Unsaturated And E-Unsaturated Fatty-Acids, Fatty-Acid Esters, And Fatty Alcohols At The Air-Water-Interface By Infrared-Spectroscopy.* Langmuir, 1995. **11**(1): p. 225-230.

103. Gericke, A. and R. Mendelsohn, *Partial chain deuteration as an IRRAS probe of conformational order of different regions in hexadecanoic acid monolayers at the air/water interface.* Langmuir, 1996. **12**(3): p. 758-762.

104. Neumann, V., A. Gericke, and H. Huhnerfuss, *Comparison Of Enantiomeric And Racemic Monolayers Of 2-Hydroxyhexadecanoic Acid By External Infrared Reflection-Absorption Spectroscopy.* Langmuir, 1995. **11**(6): p. 2206-2212.

105. Dluhy, R.A., et al.., *Design And Interfacing Of An Automated Langmuir-Type Film Balance To An Ft-Ir Spectrometer.* Applied Spectroscopy, 1988. **42**(7): p. 1289-1293.

106. Gericke, A., C.R. Flach, and R. Mendelsohn, *Structure and orientation of lung surfactant SP-C and L-alpha-dipalmitoylphosphatidylcholine in aqueous monolayers.* Biophysical Journal, 1997. **73**(1): p. 492-499.

107. Castano, S., et al.., *Secondary structure of spiralin in solution, at the air/water interface, and in interaction with lipid monolayers.* Biochimica Et Biophysica Acta-Biomembranes, 2002. **1562**(1-2): p. 45-56.

108. Castano, S., et al.., *Structure, orientation and affinity for interfaces and lipids of ideally amphipathic lytic LiKj(i=2j) peptides.* Biochimica Et Biophysica Acta-Biomembranes, 1999. **1416**(1-2): p. 176-194.

109. Cornut, I., et al.., *In situ study by polarization modulated Fourier transform infrared spectroscopy of the structure and orientation of lipids and amphipathic peptides at the air-water interface.* Biophysical Journal, 1996. **70**(1): p. 305-312.

110. Ulrich, W.P. and H. Vogel, *Polarization-modulated FTIR spectroscopy of lipid/gramicidin monolayers at the water interface.* Biophysical Journal, 1999. **76**(3): p. 1639-1647.

111. Wu, F., et al.., *Deletion of the helical motif in the intestinal fatty acid-binding protein reduces its interactions with membrane monolayers: Brewster angle microscopy, IR reflection-absorption spectroscopy, and surface pressure studies.* Biochemistry, 2001. **40**(7): p. 1976-1983.

112. Noda, I., Bull. Am. Phys. Soc., 1986. **31**: p. 520-524.

113. Noda, I., *2-Dimensional Infrared (2d Ir) Spectroscopy - Theory and Applications.* Applied Spectroscopy, 1990. **44**(4): p. 550-561.

114. Noda, I., *Two-dimensional infrared (2D IR) spectroscopy: theory and applications.* Appl. Spectrosc., 1990. **44**: p. 550-554.

115. Noda, I., *Two-dimensional infrared spectroscopy.* J. Am. Chem. Soc., 1989. **111**: p. 8116-8118.

116. Noda, I., A.E. Dowrey, and C. Marcott, *2-Dimensional Infrared (2d Ir) Spectroscopy.* Abstracts of Papers of the American Chemical Society, 1991. **202**: p. 117-PHYS.

117. Noda, I., *Generalized two-dimensional correlation method applicable to infrared, Raman, and other types of spectroscopy.* Appl. Spectrosc., 1993. **47**: p. 1329-1336.

118. Noda, I., A.E. Dowrey, and C. Marcott, *Recent Developments In 2-Dimensional Infrared (2d-Ir) Correlation Spectroscopy.* Applied Spectroscopy, 1993. **47**(9): p. 1317-1323.

119. Noda, I., *Determination of two-dimensional correlation spectra using the Hilbert Transform.* Appl. Spectrosc., 2000. **54**(7): p. 994-999.

120. Gericke, A., et al.., *Characterization of biological samples by two-dimensional infrared spectroscopy: simulation of frequency, bandwidth, and intensity changes.* Biospectroscopy, 1996. **2**: p. 341-351.

121. Czarnecki, M.A., *Interpretation of two-dimensional correlation spectra: science or art?* Appl. Spectrosc., 1998. **52**: p. 1583-1590.

122. Czarnecki, M.A., *Two-dimensional correlation spectroscopy: Effect of normalization of the dynamic spectra.* Appl. Spectrosc., 1999. **53**: p. 1392-1397.

123. Berry, R.J. and Y. Ozaki, *Investigation into the effect of instrumental parameters in two-dimensional correlation spectrometry.* Applied Spectroscopy, 2001. **55**(8): p. 1092-1098.

124. Tandler, P.J., P.D. Harrington, and H. Richardson, *Effects of static spectrum removal and noise on 2D-correlation spectra of kinetic data.* Anal. Chim. Acta, 1998. **368**: p. 45-57.

125. Yu, Z.W., J. Liu, and I. Noda, *Effect of noise on the evaluation of correlation coefficients in two-dimensional correlation spectroscopy.* Applied Spectroscopy, 2003. **57**(12): p. 1605-1609.

126. Berry, R.J. and Y. Ozaki, *Comparison of wavelets and smoothing for denoising spectra for two-dimensional correlation spectroscopy.* Applied Spectroscopy, 2002. **56**(11): p. 1462-1469.

127. Isaksson, T., et al.., *Synchronicity and linearity in generalized two-dimensional correlation spectroscopy: Concepts relevant to the analysis of nonperiodic, monotonically increasing or decreasing spectroscopic signals.* Applied Spectroscopy, 2002. **56**(10): p. 1289-1297.

128. Noda, I., et al.., *Generalized two-dimensional correlation spectroscopy.* Appl. Spectrosc., 2000. **54**(7): p. 236A-248A.

129. Ozaki, Y. and S. Noda, *Two-dimensional correlation spectroscopy.* Applied Spectroscopy, 2000. **54**(7): p. 230A-231A.

130. Ozaki, Y., et al.., *Two-dimensional correlation spectroscopy: Principle and recent theoretical development.* Bulletin of the Chemical Society of Japan, 2001. **74**(1): p. 1-17.

131. Harrington, P.D., A. Urbas, and P.J. Tandler, *Two-dimensional correlation analysis.* Chemometrics And Intelligent Laboratory Systems, 2000. **50**(2): p. 149-174.

132. Noda, I., *Two-dimensional correlation analysis of unevenly spaced spectral data.* Applied Spectroscopy, 2003. **57**(8): p. 1049-1051.

133. Yu, Z.W. and I. Noda, *On the normalization method in two-dimensional correlation spectra when concentration is used as a perturbation parameter.* Applied Spectroscopy, 2003. **57**(2): p. 164-167.

134. Jung, Y.M., S. Bin Kim, and I. Noda, *New approach to generalized two-dimensional correlation spectroscopy. IV: Eigenvalue manipulation transformation (EMT) for partial attenuation of dominant factors.* Applied Spectroscopy, 2003. **57**(7): p. 850-857.

135. Jung, Y.M., S.B. Kim, and I. Noda, *New approach to generalized two-dimensional correlation spectroscopy. II: Eigenvalue manipulation transformation (EMT) for noise suppression.* Applied Spectroscopy, 2003. **57**(5): p. 557-563.

136. Jung, Y.M., S.B. Kim, and I. Noda, *New approach to generalized two-dimensional correlation spectroscopy. III: Eigenvalue (EMT) for spectral selectivity manipulation transformation enhancement.* Applied Spectroscopy, 2003. **57**(5): p. 564-570.

137. Jung, Y.M., et al.., *New approach to generalized two-dimensional correlation spectroscopy. 1: Combination of principal component analysis and two-dimensional correlation spectroscopy.* Applied Spectroscopy, 2002. **56**(12): p. 1562-1567.

138. Sasic, S., T. Amari, and Y. Ozaki, *Sample-sample and wavenumber-wavenumber two-dimensional correlation analyses of attenuated total reflection infrared spectra of polycondensation reaction of bis(hydroxyethylterephthalate).* Analytical Chemistry, 2001. **73**(21): p. 5184-5190.

139. Sasic, S., J.H. Jiang, and Y. Ozaki, *Potentials of variable-variable and sample-sample, generalized and statistical, two-dimensional correlation spectroscopies in investigations of chemical reactions.* Chemometrics and Intelligent Laboratory Systems, 2003. **65**(1): p. 1-15.

140. Sasic, S., A. Muszynski, and Y. Ozaki, *A new possibility of the generalized two-dimensional correlation spectroscopy. 1. Sample-sample correlation spectroscopy.* Journal of Physical Chemistry A, 2000. **104**(27): p. 6380-6387.

141. Sasic, S., A. Muszynski, and Y. Ozaki, *A new possibility of the generalized two-dimensional correlation spectroscopy. 2. Sample-sample and wavenumber-wavenumber correlations of temperature-dependent near-infrared spectra of oleic acid in the pure liquid state.* Journal of Physical Chemistry A, 2000. **104**(27): p. 6388-6394.

142. Morita, S. and Y. Ozaki, *Pattern recognitions of band shifting, overlapping, and broadening using global phase description derived from generalized two-dimensional correlation spectroscopy.* Applied Spectroscopy, 2002. **56**(4): p. 502-508.

143. Morita, S., Y. Ozaki, and I. Noda, *Global phase angle description of generalized two-dimensional correlation spectroscopy: 1. Theory and its simulation for practical use.* Applied Spectroscopy, 2001. **55**(12): p. 1618-1621.

144. Morita, S., Y. Ozaki, and I. Noda, *Global phase angle description of generalized two-dimensional correlation spectroscopy: 2. Its application to temperature-dependent*

infrared spectra of a Langmuir-Blodgett film of 2-dodecyl-7,7,8,8-tetracyanoquinodimethane. Applied Spectroscopy, 2001. **55**(12): p. 1622-1627.

145. Jung, Y.M., S.B. Kim, and I. Noda, *Application of two-dimensional correlation spectroscopy to chemometrics: Self-modeling curve resolution analysis of spectral data sets.* Applied Spectroscopy, 2003. **57**(11): p. 1376-1380.

146. Sasic, S. and Y. Ozaki, *Moving window two-dimensional correlation spectroscopy and determination of signal-to-noise threshold in correlation spectra.* Applied Spectroscopy, 2003. **57**(8): p. 996-1006.

147. Wu, Y.Q., J.H. Jiang, and Y. Ozaki, *A new possibility of generalized two-dimensional correlation spectroscopy: Hybrid two-dimensional correlation spectroscopy.* Journal of Physical Chemistry A, 2002. **106**(11): p. 2422-2429.

148. Wu, Y.Q., et al.., *Hybrid two-dimensional correlation and parallel factor studies on the switching dynamics of a surface-stabilized ferroelectric liquid crystal.* Journal of Physical Chemistry B, 2003. **107**(31): p. 7706-7715.

149. Sasic, S. and Y. Ozaki, *Comparison of principal component analysis and generalized two-dimensional correlation spectroscopy: Spectral analysis of synthetic model system and near-infrared spectra of milk.* Applied Spectroscopy, 2001. **55**(1): p. 29-38.

150. Raussens, V., J.M. Ruysschaert, and E. Goormaghtigh, *Analysis of H-1/H-2 exchange kinetics using model infrared spectra.* Applied Spectroscopy, 2004. **58**(1): p. 68-82.

151. Lu, G.H., et al.., *Study on the identification of Dangguitou and Dangguiwei by two-dimensional infrared correlation spectroscopy.* Spectroscopy And Spectral Analysis, 2004. **24**(3): p. 311-314.

152. Sun, S.Q., Q. Zhou, and H.W. Leung, *Study on Paofupian, Heishunpian and Baifupian by two-dimensional infrared correlation spectroscopy.* Spectroscopy And Spectral Analysis, 2003. **23**(6): p. 1082-1085.

153. Sun, S.Q., et al.., *Study on the identification of standard and false BanXia by two-dimensional infrared correlation spectroscopy.* Spectroscopy And Spectral Analysis, 2004. **24**(4): p. 427-430.

154. Zhou, Q., et al.., *Two-dimensional correlation infrared spectroscopy of standard and false Dahuang.* Chinese Journal Of Analytical Chemistry, 2003. **31**(9): p. 1058-1061.

155. Zhou, Q., S.Q. Sun, and L. Zuo, *Study on traditional Chinese medicine 'Qing Kai Ling' injections from different manufactures by 2D IR correlation spectroscopy.* Vibrational Spectroscopy, 2004. **36**(2): p. 207-212.

156. Zuo, L., et al.., *2D-IR correlation analysis of deteriorative process of traditional Chinese medicine 'Qing Kai Ling' injection.* Journal of Pharmaceutical and Biomedical Analysis, 2003. **30**(5): p. 1491-1498.

157. Arrondo, J.L.R., et al.., *A two-dimensional IR spectroscopic (2D-IR) simulation of protein conformational changes.* Spectroscopy-An International Journal, 2004. **18**(1): p. 49-58.

158. Arrondo, J.L.R., et al.., *A 2D-IR simulation of protein conformational changes.* Biophysical Journal, 2003. **84**(2): p. 5A-6A.

159. Czarnik-Matusewicz, B., et al.., *Analysis of near-infrared spectra of complicated biological fluids by two-dimensional correlation spectroscopy: Protein and fat concentration-dependent spectral changes of milk.* Applied Spectroscopy, 1999. **53**(12): p. 1582-1594.

160. Czarnik-Matusewicz, B., et al.., *Two-dimensional attenuated total reflection/infrared correlation spectroscopy of adsorption-induced and concentration-dependent spectral variations of beta-lactoglobulin in aqueous solutions.* Journal of Physical Chemistry B, 2000. **104**(32): p. 7803-7811.

161. Dzwolak, W., et al.., *Comparative two-dimensional Fourier transform infrared correlation spectroscopic study on the spontaneous, pressure-, and temperature-enhanced H/D exchange in alpha-lactalbumin.* Applied Spectroscopy, 2000. **54**(7): p. 963-967.

162. Gadaleta, S.J., et al.., *Two-dimensional infrared correlation spectroscopy of synthetic and biological apatites.* Biospectroscopy, 1996. **2**: p. 353-364.

163. Jung, Y.M., B. Czarnik-Matusewicz, and Y. Ozaki, *Two-dimensional infrared, two-dimensional Raman, and two-dimensional infrared and Raman heterospectral correlation studies of secondary structure of beta-lactoglobulin in buffer solutions.* Journal Of Physical Chemistry B, 2000. **104**(32): p. 7812-7817.

164. Muller, M., R. Buchet, and U.P. Fringeli, *2D-FTIR ATR spectroscopy of thermo-induced periodic secondary structural changes of poly-(L)-lysine: A cross-correlation analysis of phase-resolved temperature modulation spectra.* Journal Of Physical Chemistry, 1996. **100**(25): p. 10810-10825.

165. Murayama, K. and Y. Ozaki, *Two-dimensional near-IR correlation spectroscopy study of molten globule-like state of ovalbumin in acidic pH region: Simultaneous changes in hydration and secondary structure.* Biopolymers, 2002. **67**(6): p. 394-405.

166. Murayama, K., et al.., *Two-dimensional/attenuated total reflection infrared correlation spectroscopy studies on secondary structural changes in human serum albumin in*

aqueous solutions: pH-dependent structural changes in the secondary structures and in the hydrogen bondings of side chains. J. Phys. Chem. B, 2001. **105**: p. 4763-4769.

167. Ozaki, Y., K. Murayama, and Y. Wang, *Application of two-dimensional near-infrared correlation spectroscopy to protein research.* Vibrational Spectroscopy, 1999. **20**(2): p. 127-132.

168. Ozaki, Y., et al.., *Two-dimensional infrared correlation spectroscopy studies on secondary structures and hydrogen bondings of side chains of proteins.* Spectroscopy-An International Journal, 2003. **17**(2-3): p. 79-100.

169. Paquet, M.-J., et al.., *Two-dimensional infrared correlation spectroscopy study of the aggregation of cytochrome c in the presence of dimyristoylphosphatidylglycerol.* Biophys. J., 2001. **81**: p. 305-312.

170. Richard, J.A., et al.., *Structure of beta-purothionin in membranes: A two-dimensional infrared correlation spectroscopy study.* Biochemistry, 2005. **44**(1): p. 52-61.

171. Wang, Y., et al.., *Two-dimensional Fourier transform near-infrared spectroscopy study of heat denaturation of ovalbumin in aqueous solutions.* Journal of Physical Chemistry B, 1998. **102**(34): p. 6655-6662.

172. Wu, Y.Q., et al.., *Two-dimensional near-infrared spectroscopy study of human serum albumin in aqueous solutions: Using overtones and combination modes to monitor temperature-dependent changes in the secondary structure.* Journal of Physical Chemistry B, 2000. **104**(24): p. 5840-5847.

173. Wu, Y.Q., et al.., *Two-dimensional attenuated total reflection/infrared correlation spectroscopy studies on concentration and heat-induced structural changes of human serum albumin in aqueous solutions.* Applied Spectroscopy, 2002. **56**(9): p. 1186-1193.

174. Wu, Y.Q., K. Murayama, and Y. Ozaki, *Two-dimensional infrared spectroscopy and principle component analysis studies of the secondary structure and kinetics of hydrogen-deuterium exchange of human serum albumin.* Journal Of Physical Chemistry B, 2001. **105**(26): p. 6251-6259.

175. Fabian, H., H.H. Mantsch, and C.P. Schultz, *Two-dimensional IR correlation spectroscopy: Sequential events in the unfolding process of the lambda Cro-V55C repressor protein.* Proceedings Of The National Academy Of Sciences Of The United States Of America, 1999. **96**(23): p. 13153-13158.

176. Lefevre, T., K. Arseneault, and M. Pezolet, *Study of protein aggregation using two-dimensional correlation infrared spectroscopy and spectral simulations.* Biopolymers, 2004. **73**(6): p. 705-715.

177. Murayama, K., et al.., *Two-dimensional near-infrared correlation spectroscopy studies on protein denaturation.* Nippon Kagaku Kaishi, 1999(10): p. 637-647.

178. Schultz, C.P., O. Barzu, and H.H. Mantsch, *Two-dimensional infrared correlation analysis of protein unfolding: use of spectral simulations to validate structural changes during thermal denaturation of bacterial CMP kinases.* Appl. Spectrosc., 2000. **54**: p. 931-938.

179. Yan, Y.B., et al.., *Two-dimensional infrared correlation spectroscopy study of sequential events in the heat-induced unfolding and aggregation process of myoglobin.* Biophysical Journal, 2003. **85**(3): p. 1959-1967.

180. Yan, Y.B., et al.., *Protein thermal aggregation involves distinct regions: Sequential events in the heat-induced unfolding and aggregation of hemoglobin.* Biophysical Journal, 2004. **86**(3): p. 1682-1690.

181. Ausili, A., et al.., *Two-dimensional IR correlation spectroscopy of mutants of the beta-glycosidase from the hyperthermophilic archaeon Sultolobus soltataricus identifies the mechanism of quaternary structure stabilization and unravels the sequence of thermal unfolding events.* Biochemical Journal, 2004. **384**: p. 69-78.

182. D'Auria, S., et al.., *Binding of glutamine to glutamine-binding protein from Escherichia coli induces changes in protein structure and increases protein stability.* Proteins-Structure Function And Bioinformatics, 2005. **58**(1): p. 80-87.

183. Iloro, I., et al.., *Methionine adenosyltransferase alpha-helix structure unfolds at lower temperatures than beta-sheet: A 2D-IR study.* Biophysical Journal, 2004. **86**(6): p. 3951-3958.

184. Torrecillas, A., S. Corbalan-Garcia, and J.C. Gomez-Fernandez, *An infrared spectroscopic study of the secondary structure of protein kinase C alpha and its thermal denaturation.* Biochemistry, 2004. **43**(8): p. 2332-2344.

185. Torrecillas, A., S. Corbalan-Garcia, and J.C. Gomez-Fernandez, *Structural study of the C2 domains of the classical PKC isoenzymes using infrared spectroscopy and two-dimensional infrared correlation spectroscopy.* Biochemistry, 2003. **42**(40): p. 11669-11681.

186. Buchet, R., et al.., *Probing nucleotide binding site of annexin A6.* Vibrational Spectroscopy, 2004. **36**(2): p. 233-236.

187. Ismoyo, F., Y. Wang, and A.A. Ismail, *Examination of the effect of heating on the secondary structure of avidin and avidin-biotin complex by resolution-enhanced two-dimensional infrared correlation spectroscopy.* Appl. Spectrosc., 2000. **54**: p. 939-947.

188. Kokot, S., B. Czarnik-Matusewicz, and Y. Ozaki, *Two-dimensional correlation spectroscopy and principal component analysis studies of temperature-dependent IR spectra of cotton-cellulose.* Biopolymers, 2002. **67**(6): p. 456-469.

189. McClure, W.F., et al.., *Two-dimensional correlation of Fourier transform near-infrared and Fourier transform Raman spectra. I. Mixture of Sugar and Protein.* Appl. Spectrosc., 1996. **50**(4): p. 467-475.

190. Peng, X.N., et al.., *Further investigation on potassium-induced conformation transition of Nephila spidroin film with two-dimensional infrared correlation spectroscopy.* Biomacromolecules, 2005. **6**(1): p. 302-308.

191. Liu, Y., Y.R. Chen, and Y. Ozaki, *Two-dimensional visible/near-infrared correlation spectroscopy study of thermal treatment of chicken meats.* Journal of Agricultural and Food Chemistry, 2000. **48**(3): p. 901-908.

192. Liu, Y.L., Y.R. Chen, and Y. Ozaki, *Characterization of visible spectral intensity variations of wholesome and unwholesome chicken meats with two-dimensional correlation spectroscopy.* Applied Spectroscopy, 2000. **54**(4): p. 587-594.

193. Filosa, A., et al.., *Two-dimensional infrared correlation spectroscopy as a probe of sequential events in the thermal unfolding of cytochromes c.* Biochemistry, 2001. **40**(28): p. 8256-8263.

194. Sefara, N., N.P. Magtoto, and H.H. Richardson, *Structural characterization of β-lactoglobulin in solution using two-dimensional FT mid-infrared and FT near-infrared correlation spectroscopy.* Appl. Spectrosc., 1997. **51**(4): p. 536-540.

195. Graff, D.K., et al.., *The effects of chain length and thermal denaturation on helix-forming peptides: A mode-specific analysis using 2D FT-IR.* Journal Of The American Chemical Society, 1997. **119**(46): p. 11282-11294.

196. Murayama, K., et al.., *Two-dimensional/attenuated total reflection infrared correlation spectroscopy studies on secondary structural changes in human serum albumin in aqueous solutions: pH-dependent structural changes in the secondary structures and in the hydrogen bondings of side chains.* Journal of Physical Chemistry B, 2001. **105**(20): p. 4763-4769.

197. Nabet, A., M. Auger, and M. Pezolet, *Investigation of the temperature behavior of the bands due to the methylene stretching vibration of phospholipid acyl chains by two-dimensional infrared correlation spectroscopy.* Applied Spectroscopy, 2000. **54**(7): p. 948-955.

198. Wu, T., K. Murayama, and Y. Ozaki, *Two-dimensional infrared spectroscopy and principle component analysis studies of the secondary structure and kinetics of hydrogen-deuterium exchange of human serum albumin.* J. Phys. Chem. B, 2001. **105**: p. 6251-6259.

199. Kubelka, J., P. Pancoska, and T.A. Keiderling, *Novel use of a static modification of two-dimensional correlation analysis. Part II: Hetero-spectral correlations of protein Raman, FT-IR and circular dichroism spectra.* Appl. Spectrosc., 1999. **53**: p. 666-671.

200. Pancoska, P., J. Kubelka, and T.A. Keiderling, *Novel use of a static modification of two-dimensional correlation analysis. Part I: comparision of the secondary structure sensitivity of electronic circular dichroism, FT-IR and Raman spectra of proteins.* Appl. Spectrosc., 1999. **53**: p. 655-665.

201. Elmore, D.L. and R.A. Dluhy, *Application of 2D IR correlation analysis to phase transitions in Langmuir monolayer films.* Colloids and Surfaces A, 2000. **171**(1-3): p. 225-239.

202. Elmore, D.L. and R.A. Dluhy, *Pressure-dependent changes in the infrared C-H vibrations of monolayer films at the air/water interface revealed by two- dimensional infrared correlation spectroscopy.* Appl. Spectrosc., 2000. **54**(7): p. 956-962.

203. Noda, I., *Two-dimensional correlation approach to the dynamic rheo-optical characterization of polymers.* Chemtracts Macromol. Chem., 1990. **1**: p. 89-106.

204. Noda, I., A.E. Dowrey, and C. Marcott, *2-Dimensional Infrared (2d-Ir) Analysis of Poly(Methyl Methacrylate).* Abstracts of Papers of the American Chemical Society, 1990. **199**: p. 273-POLY.

205. Amari, T. and Y. Ozaki, *Generalized two-dimensional attenuated total reflection/infrared and near-infrared correlation spectroscopy studies of real-time monitoring of the initial oligomerization of bis(hydroxyethyl terephthalate).* Macromolecules, 2002. **35**(21): p. 8020-8028.

206. Padermshoke, A., et al.., *Melting behavior of poly(3-hydroxybutyrate) investigated by two-dimensional infrared correlation spectroscopy.* Spectrochimica Acta Part A-Molecular And Biomolecular Spectroscopy, 2005. **61**(4): p. 541-550.

207. Padermshoke, A., et al.., *Surface melting and crystallization behavior of polyhydroxyalkanoates studied by attenuated total reflection infrared spectroscopy.* Polymer, 2004. **45**(19): p. 6547-6554.

208. Padermshoke, A., et al.., *Crystallization behavior of poly(3-hydroxybutyrate-co-3-hydroxyhexanoate) studied by 2D IR correlation spectroscopy.* Polymer, 2004. **45**(21): p. 7159-7165.

209. Padermshoke, A., et al.., *Thermally induced phase transition of poly (3-hydroxybutyrate-co-3-hydroxyhexanoate) investigated by two-dimensional infrared correlation spectroscopy.* Vibrational Spectroscopy, 2004. **36**(2): p. 241-249.

210. Shin, H.S., et al.., *Characterization of beta-transition of poly(tert-butyl methacrylate) thin films by two-dimensional infrared correlation spectral analysis.* Vibrational Spectroscopy, 2002. **29**(1-2): p. 73-77.

211. Shin, H.S., et al.., *Structural comparison of Langmuir-Blodgett and spin-coated films of poly(tert-butyl methacrylate) by external reflection FTIR spectroscopy and two-dimensional correlation analysis.* Langmuir, 2002. **18**(14): p. 5523-5528.

212. Tian, G., et al.., *Studies on pre-melting and crystallization process of biosynthesized poly(3-hydroxybutyrate) using two-dimensional Fourier-transform infrared spectroscopy.* Chemical Journal of Chinese Universities-Chinese, 2002. **23**(8): p. 1627-1631.

213. Tian, G., et al.., *Study of thermal melting behavior of microbial polyhydroxyalkanoate using two-dimensional Fourier transform infrared correlation spectroscopy.* Applied Spectroscopy, 2001. **55**(7): p. 888-893.

214. Tian, G., et al.., *Two-dimensional Fourier transform infrared spectroscopy study of biosynthesized poly(hydroxybutyrate-co-hydroxyhexanoate) and poly(hydroxybutyrate-co-hydroxyvalerate).* Journal of Polymer Science Part B-Polymer Physics, 2002. **40**(7): p. 649-656.

215. Zhang, J.M., et al.., *Structural changes and crystallization dynamics of poly(L-lactide) during the cold-crystallization process investigated by infrared and two-dimensional infrared correlation spectroscopy.* Macromolecules, 2004. **37**(17): p. 6433-6439.

216. Zhang, J.M., et al.., *Weak intermolecular interactions during the melt crystallization of Poly(L-lactide) investigated by two-dimensional infrared correlation spectroscopy.* Journal Of Physical Chemistry B, 2004. **108**(31): p. 11514-11520.

217. Gregoriou, V.G., et al.., *Time-resolved vibrational spectroscopy of an electric field-induced transition in a nematic liquid crystal by use of step-scan 2D FT-IR.* Chem. Phys. Lett., 1991. **179**: p. 491-496.

218. Gregoriou, V.G., et al.., *Two dimensional infrared (2D-IR) spectroscopic studies of the viscoelastic behavior of liquid crystalline polyurethanes.* Macromolecular Symposia, 2002. **184**: p. 183-192.

219. Gregoriou, V.G., et al.., *Two-dimensional correlation infared analysis (2D-IR) based on dynamic infrared spectroscopy used as a probe of the viscoelastic behavior of side chain liquid crystalline polyurethanes.* Journal Of Physical Chemistry B, 2002. **106**(43): p. 11108-11113.

220. Shilov, S.V., et al.., *Ordering and mobility of ferroelectric liquid crystal dimer as studied by FT-IR spectroscopy with 2D-IR correlation analysis.* Macromolecular Symposia, 1997. **119**: p. 261-268.

221. Thomas, M. and H.H. Richardson, *Two-dimensional FT-IR correlation analysis of the phase transitions in a liquid crystal, 4'-n-octyl-4-cyanobiphenyl (8CB).* Vib. Spectrosc., 2000. **24**: p. 137-146.

222. Zhao, J.G., et al.., *Dynamics of a ferroelectric liquid crystal with a naphthalene ring during electric-field-induced switching studied by time-resolved infrared spectroscopy combined with two-dimensional correlation spectroscopy.* Applied Spectroscopy, 2003. **57**(9): p. 1063-1069.

223. Izawa, K., et al.., *Growth process of polymer aggregates formed by perfluorooctyltriethoxysilane. Time-resolved near-IR and two-dimensional near-IR correlation studies.* Colloid and Polymer Science, 2002. **280**(4): p. 380-388.

224. Li, W.Z., et al.., *Two-dimensional (2D) ATR-FTIR spectroscopic study on glycol diffusion in cured epoxy resins.* Acta Chimica Sinica, 2004. **62**(17): p. 1641-1644.

225. Liu, M.J., et al.., *Two-dimensional (2D) ATR-FTIR spectroscopic study on water diffusion in cured epoxy resins.* Macromolecules, 2002. **35**(14): p. 5500-5507.

226. Liu, M.J., et al.., *Study on diffusion behavior of water in epoxy resins cured by active ester.* Physical Chemistry Chemical Physics, 2003. **5**(9): p. 1848-1852.

227. Musto, P., *Two-dimensional FTIR spectroscopy studies on the thermal-oxidative degradation of epoxy and epoxy-bis(maleimide) networks.* Macromolecules, 2003. **36**(9): p. 3210-3221.

228. Huang, H., et al.., *Application of generalized two-dimensional infrared correlation spectroscopy to the study of a hydrogen-bonded blend.* Applied Spectroscopy, 2004. **58**(9): p. 1074-1081.

229. Matsushita, A., et al.., *Two-dimensional Fourier-transform Raman and near-infrared correlation spectroscopy studies of poly (methyl methacrylate) blends 1. Immiscible blends of poly(methyl methacrylate) and atactic polystyrene.* Vibrational Spectroscopy, 2000. **24**(2): p. 171-180.

230. Nakashima, K., et al.., *Two-dimensional infrared correlation spectroscopy studies of polymer blends: Conformational changes and specific interactions in blends of atactic polystyrene and poly(2,6-dimethyl-1,4-phenylene ether).* Journal Of Physical Chemistry B, 1999. **103**(32): p. 6704-6712.

231. Noda, I., G.M. Story, and C. Marcott, *Pressure-induced transitions of polyethylene studied by two-dimensional infrared correlation spectroscopy.* Vib. Spectrosc., 1999. **19**(2): p. 461-465.

232. Peng, Y. and P.Y. Wu, *A two dimensional infrared correlation spectroscopic study on the structure changes of PVDF during the melting process.* Polymer, 2004. **45**(15): p. 5295-5299.

233. Peng, Y., P.Y. Wu, and Y.L. Yang, *Two-dimensional infrared correlation spectroscopy as a probe of sequential events in the diffusion process of water in poly(epsilon-caprolactone).* Journal Of Chemical Physics, 2003. **119**(15): p. 8075-8079.

234. Ren, Y.Z., et al.., *Two-dimensional Fourier transform Raman correlation spectroscopy studies of polymer blends: Conformational changes and specific interactions in blends of atactic polystyrene and poly(2,6-dimethyl-1,4-phenylene ether).* Macromolecules, 1999. **32**(19): p. 6307-6318.

235. Ren, Y.Z., et al.., *Two-dimensional near-infrared correlation spectroscopy studies of compatible polymer blends: Composition-dependent spectral variations of blends of atactic polystyrene and poly(2,6-dimethyl-1,4-phenylene ether).* Journal of Physical Chemistry B, 2000. **104**(4): p. 679-690.

236. Ren, Y.Z., et al.., *Two-dimensional near-infrared correlation spectroscopy studies of polymer blends I: Composition-dependent spectral variations of blends of atactic*

polystyrene and poly 2,6-dimethyl-1,4-phenylene ether. Macromolecular Symposia, 1999. **141**: p. 167-183.

237. Ren, Y.Z., et al.., *Two-dimensional near-infrared correlation spectroscopy studies on composition-dependent spectral variations in ethylene/vinyl acetate copolymers: Assignments of bands due to ethylene units in amorphous, disordered, and orthorhombic crystalline phases.* Applied Spectroscopy, 1999. **53**(8): p. 919-926.

238. Ren, Y.Z., et al.., *Two-dimensional Fourier transform Raman correlation spectroscopy study of composition-induced structural changes in a series of ethylene/vinyl acetate copolymers.* Journal of Physical Chemistry B, 1999. **103**(31): p. 6475-6483.

239. Ren, Y.Z., et al.., *Two-dimensional near-infrared correlation spectroscopy studies on composition-dependent spectral variations in ethylene/vinyl acetate copolymers. Assignment of bands due to ethylene units in amorphous, disordered, and orthorhombic cyrstalline phases.* Applied Spectroscopy, 1999. **53**(8): p. 919-926.

240. Sano, A., et al.., *Spectroscopic analysis of miscibility of ethylene-vinyl acetate copolymer and tackifier using generalized two-dimensional correlation spectroscopy.* Mokuzai Gakkaishi, 2002. **48**(3): p. 191-198.

241. Jung, Y.M., et al.., *Characterization of transition temperatures of a Langmuir-Blodgett film of poly(tert-butyl methacrylate) by two-dimensional correlation spectroscopy and principal component analysis.* Applied Spectroscopy, 2002. **56**(12): p. 1568-1574.

242. Wu, Q., et al.., *Two-dimensional infrared correlation spectroscopy on dodecyloxy benzoic acid phase transition.* Spectroscopy And Spectral Analysis, 2001. **21**(6): p. 778-782.

243. Wu, Y.Q., S.M. Jiang, and Y. Ozaki, *Two-dimensional infrared spectroscopy study on phase transition and structural variations of a hydrogen-bonded liquid crystal.* Spectrochimica Acta Part a-Molecular and Biomolecular Spectroscopy, 2004. **60**(8-9): p. 1931-1939.

244. Awichi, A., et al.., *Molecular interactions between glucose anomers and carbon nanotubes probed by 2D IR correlation spectroscopy.* Abstracts Of Papers Of The American Chemical Society, 2002. **223**: p. U79-U80.

245. Noda, I. and C. Marcott, *Two-dimensional Raman (2D Raman) correlation spectroscopy study of non-oxidative photodegradation of beta-carotene.* Journal of Physical Chemistry A, 2002. **106**(14): p. 3371-3376.

246. Ren, Y.Z., et al.., *Two-dimensional Fourier-transform Raman and near-infrared correlation spectroscopy studies of poly(methyl methacrylate) blends. 2. Partially miscible blends of poly(methyl methacrylate) and poly(4-vinylphenol).* Vibrational Spectroscopy, 2000. **23**: p. 207-218.

247. Sasic, S., et al.., *Analyzing Raman images of polymer blends by sample-sample two-dimensional correlation spectroscopy.* Analyst, 2003. **128**(8): p. 1097-1103.

248. Sato, H., et al.., *Raman spectra of high-density, low-density, and linear low-density polyethylene pellets and prediction of their physical properties by multivariate data analysis.* Journal of Applied Polymer Science, 2002. **86**(2): p. 443-448.

249. Takayanagi, M., et al.., *Intermolecular interactions of merocyanine dyes studied by visible absorption, resonance Raman and infrared spectroscopies.* Journal of Molecular Structure, 1997. **407**(2-3): p. 85-92.

250. Choi, H.C., et al.., *A study of the mechanism of the electrochemical reaction of lithium with CoO by two-dimensional soft X-ray absorption spectroscopy (2D XAS), 2D Raman, and 2D heterospectral XAS-Raman correlation analysis.* Journal of Physical Chemistry B, 2003. **107**(24): p. 5806-5811.

251. Nakashima, K., et al.., *Two-dimensional fluorescence correlation spectroscopy. I. Analysis of polynuclear aromatic hydrocarbons in cyclohexane solutions.* Journal of Physical Chemistry A, 2000. **104**(40): p. 9113-9120.

252. Nakashima, K., et al.., *Two-dimensional fluorescence correlation spectroscopy II: spectral analysis of derivatives of anthracene and pyrene in micellar solutions.* Spectrochimica Acta Part a-Molecular and Biomolecular Spectroscopy, 2004. **60**(8-9): p. 1783-1791.

253. Nakashima, K., et al.., *Two-dimensional fluorescence correlation spectroscopy: Resolution of fluorescence of tryptophan residues in horse heart myoglobin.* Applied Spectroscopy, 2003. **57**(11): p. 1381-1385.

254. Roselli, C., et al.., *Two-dimensional correlation method applied to Yb^{3+} vibronic sideband spectroscopy: discrimination of fluorescence spectral features arising from different Yb^{3+} binding sites.* Biospectroscopy, 1995. **1**: p. 329-339.

255. Izawa, K., et al.., *Application of generalized two-dimensional correlation theory to gel permeation chromatographic analysis.* Physchemcomm, 2001(12): p. art. no.-12.

256. Izawa, K., et al.., *Two-dimensional correlation gel permeation chromatography study of octyltriethoxysilane sol-gel polymerization process.* Macromolecules, 2002. **35**(1): p. 92-96.

257. Izawa, K., et al.., *2D gel permeation chromatography (2D GPC) correlation studies of the growth process for perfluoro-octyltriethoxysilane polymer aggregates.* Physical Chemistry Chemical Physics, 2002. **4**(6): p. 1053-1061.

258. Izawa, K., et al.., *Two-dimensional correlation gel permeation chromatography (2D correlation GPC) study of the sol-gel polymerization of octyltriethoxysilane. HCl-concentration dependence.* Physchemcomm, 2002(2): p. 12-16.

259. Izawa, K., et al.., *Two-dimensional correlation gel permeation chromatography (2D GPC) study of 1H,1H,2H,2H-perfluorooctyltriethoxysilane sol-gel polymerization process.* Journal of Physical Chemistry B, 2002. **106**(11): p. 2867-2874.

260. Eads, C.D. and I. Noda, *Generalized correlation NMR spectroscopy.* Journal of the American Chemical Society, 2002. **124**(6): p. 1111-1118.

261. Levin, I.W., *Vibrational spectroscopy of membrane assemblies*, in *Advances in Infrared and Raman Spectroscopy*, R.J.H. Clark and R.E. Hester, Editors. 1984, Wiley: Heyden. p. 1-48.

262. Brillouin, L., *Diffusion de la lumiere et des rayonnes X par un corps transparent homogene; influence del'agitation thermique.* Annalen de Physik, 1922. **17**: p. 88-122.

263. Smekal, A., Naturwissenschaften, 1923. **11**: p. 873.

264. Raman, C.V.a.K., K.S., Nature, 1928. **121**: p. 50.

265. Raman, C.V.a.K., K.S., Proceedings of the Royal Society (London), 1929. **122**: p. 23.

266. Maiman, T.H., Nature, 1960. **187**: p. 493.

267. Schawlow, A.a.T., C. H., Phys. Rev., 1958. **122**: p. 1940.

268. Laserna, J.J., 1996.

269. Dluhy, R.A., et al.., *Vibrational spectroscopy of biomembrane model systems. Applications of infrared and raman spectroscopy to ultrathin membranes at interfaces.* Spectrochim. Acta, 1995. **51A**: p. 1413-1447.

270. Dluhy, R.A., et al.., *Vibrational Spectroscopy Of Biophysical Monolayers - Applications Of Ir And Raman-Spectroscopy To Biomembrane Model Systems At Interfaces.* Spectrochimica Acta Part A-Molecular And Biomolecular Spectroscopy, 1995. **51**(8): p. 1413-1447.

271. Ulman, A., *Characterization of Organic Thin Films*, in *Materials Characterization Series: Surfaces Interfaces, Thin Films*, C.R. Brundle and C.A. Evans, Editors. 1995, Butterworth-Heinemann: Stoneham, MA.

272. Turrell, G. and J. Corset, *Raman Microscopy. Developments and Applications*. 1996, London: Academic Press. 463.

273. Moskovits, M., *Surface Enhanced Spectroscopy.* Rev. Mod. Phys., 1985. **57**: p. 783-826.

274. Tian, Z.Q., B. Ren, and D.Y. Wu, *Surface-enhanced Raman scattering: From noble to transition metals and from rough surfaces to ordered nanostructures.* Journal of Physical Chemistry B, 2002. **106**(37): p. 9463-9483.

275. Norrod, K.L., et al.., *Quantitative comparison of five SERS substrates: Sensitivity and limit of detection.* Applied Spectroscopy, 1997. **51**(7): p. 994-1001.

276. Kneipp, K., et al.., *Ultrasensitive chemical analysis by Raman spectroscopy.* Chemical Reviews, 1999. **99**(10): p. 2957-+.

277. Kneipp, K., et al.., *Nonlinear Raman probe of single molecules attached to colloidal silver and gold clusters*, in *Optical Properties of Nanostructured Random Media*. 2002. p. 227-247.

278. Kneipp, K., et al.., *Single molecule detection using surface-enhanced Raman scattering (SERS).* Physical Review Letters, 1997. **78**(9): p. 1667-1670.

279. Nie, S.M. and S.R. Emery, *Probing single molecules and single nanoparticles by surface-enhanced Raman scattering.* Science, 1997. **275**(5303): p. 1102-1106.

280. Brown, K.R., D.G. Walter, and M.J. Natan, *Seeding of colloidal Au nanoparticle solutions. 2. Improved control of particle size and shape.* Chemistry of Materials, 2000. **12**(2): p. 306-313.

281. Freeman, R.G., et al.., *Size selection of colloidal gold aggregates by filtration: Effect on surface-enhanced Raman scattering intensities.* Journal of Raman Spectroscopy, 1999. **30**(8): p. 733-738.

282. Lyon, L.A., et al.., *Surface plasmon resonance of colloidal Au-modified gold films.* Sensors and Actuators B-Chemical, 1999. **54**(1-2): p. 118-124.

283. Lyon, L.A., D.J. Pena, and M.J. Natan, *Surface plasmon resonance of Au colloid-modified Au films: Particle size dependence.* Journal of Physical Chemistry B, 1999. **103**(28): p. 5826-5831.

284. Musick, M.D., et al.., *Electrochemical properties of colloidal Au-based surfaces: Multilayer assemblies and seeded colloid films.* Langmuir, 1999. **15**(3): p. 844-850.

285. Richardson, J.N., et al.., *A fractal analysis of colloidal Au nanoparticle electrodes.* Abstracts of Papers of the American Chemical Society, 1999. **217**: p. U115-U115.

286. Fleischmann, M., P.J. Hendra, and J. McQuillan, *Raman-Spectra of Pyridine Adsorbed at a Silver Electrode.* Chemical Physics Letters, 1974. **26**(2): p. 163-166.

287. Sudnik, L.M., K.L. Norrod, and K.L. Rowlen, *SERS-active Ag films from photoreduction of Ag+ on TiO2.* Applied Spectroscopy, 1996. **50**(3): p. 422-424.

288. Gupta, R., M.J. Dyer, and W.A. Weimer, *Preparation and characterization of surface plasmon resonance tunable gold and silver films.* Journal of Applied Physics, 2002. **92**(9): p. 5264-5271.

289. Weimer, W.A. and M.J. Dyer, *Tunable surface plasmon resonance silver films.* Applied Physics Letters, 2001. **79**(19): p. 3164-3166.

290. Constantino, C.J.L., et al.., *Single-molecule detection using surface-enhanced resonance Raman scattering and Langmuir-Blodgett monolayers.* Analytical Chemistry, 2001. **73**(15): p. 3674-3678.

291. Bao, L.L., et al.., *Study of silver films over silica beads as a surface-enhanced Raman scattering (SERS) substrate for detection of benzoic acid.* Journal of Raman Spectroscopy, 2003. **34**(5): p. 394-398.

292. Yan, W.F., et al.., *Silver-coated zeolite crystal films as surface-enhanced Raman scattering substrates.* Applied Spectroscopy, 2004. **58**(1): p. 18-25.

293. Bello, J.M., D.L. Stokes, and T. Vodinh, *Silver-Coated Alumina as a New Medium for Surfaced-Enhanced Raman-Scattering Analysis.* Applied Spectroscopy, 1989. **43**(8): p. 1325-1330.

294. Bello, J.M., D.L. Stokes, and T. Vodinh, *Titanium-Dioxide Based Substrate for Optical Monitors in Surface-Enhanced Raman-Scattering Analysis.* Analytical Chemistry, 1989. **61**(15): p. 1779-1783.

295. Alak, A.M., N. Contolini, and T. Vodinh, *Studies of Cyclodextrin-Enhanced Room-Temperature Phosphorescence.* Analytica Chimica Acta, 1989. **217**(1): p. 171-176.

296. Viets, C. and W. Hill, *Single-fibre surface-enhanced Raman sensors with angled tips.* Journal of Raman Spectroscopy, 2000. **31**(7): p. 625-631.

297. Anderson, M.S., *Locally enhanced Raman spectroscopy with an atomic force microscope.* Applied Physics Letters, 2000. **76**(21): p. 3130-3132.

298. Nieman, L.T., G.M. Krampert, and R.E. Martinez, *An apertureless near-field scanning optical microscope and its application to surface-enhanced Raman spectroscopy and multiphoton fluorescence imaging.* Review of Scientific Instruments, 2001. **72**(3): p. 1691-1699.

299. Sauer, G., G. Brehm, and S. Schneider, *Preparation of SERS-active gold film electrodes via electrocrystallization: their characterization and application with NIR excitation.* Journal of Raman Spectroscopy, 2004. **35**(7): p. 568-576.

300. Sauer, G., U. Nickel, and S. Schneider, *Preparation of SERS-active silver film electrodes via electrocrystallization of silver.* Journal of Raman Spectroscopy, 2000. **31**(5): p. 359-363.

301. Dick, L.A., et al.., *Metal film over nanosphere (MFON) electrodes for surface-enhanced Raman spectroscopy (SERS): Improvements in surface nanostructure stability and suppression of irreversible loss.* Journal of Physical Chemistry B, 2002. **106**(4): p. 853-860.

302. Chan, S., et al.., *Surface-enhanced Raman scattering of small molecules from silver-coated silicon nanopores.* Advanced Materials, 2003. **15**(19): p. 1595-+.

303. Lin, H.H., et al.., *Surface-enhanced Raman scattering from silver-plated porous silicon.* Journal of Physical Chemistry B, 2004. **108**(31): p. 11654-11659.

304. Li, X.L., et al.., *Novel method for preparing controllable and stable silver particle films for surface-enhanced Raman scattering spectroscopy.* Applied Spectroscopy, 2004. **58**(1): p. 26-32.

305. Ji, X.H., et al.., *Preparation of Au/Ag core-shell nanoparticles and its surface-enhanced Raman scattering effect.* Chemical Journal of Chinese Universities-Chinese, 2002. **23**(12): p. 2357-2359.

306. Liu, Y.C. and T.C. Chuang, *Synthesis and characterization of Gold/Polypyrrole core-shell nanocomposites and elemental gold nanoparticles based on the gold-containing nanocomplexes prepared by electrochemical methods in aqueous solutions.* Journal of Physical Chemistry B, 2003. **107**(45): p. 12383-12386.

307. Mandal, M., et al.., *Synthesis of Au-core-Ag-shell type bimetallic nanoparticles for single molecule detection in solution by SERS method.* Journal of Nanoparticle Research, 2004. **6**(1): p. 53-61.

308. Mandal, M., et al.., *Sniffing a single molecule through SERS using AU(core)-Ag-shell bimetallic nanoparticles.* Current Science, 2004. **86**(4): p. 556-559.

309. Jeong, D.H., Y.X. Zhang, and M. Moskovits, *Polarized surface enhanced Raman scattering from aligned silver nanowire rafts.* Journal of Physical Chemistry B, 2004. **108**(34): p. 12724-12728.

310. Yao, J.L., et al.., *A complementary study of surface-enhanced Raman scattering and metal nanorod arrays.* Pure and Applied Chemistry, 2000. **72**(1-2): p. 221-228.

311. Green, M. and F.M. Liu, *SERS substrates fabricated by island lithography: The silver/pyridine system.* Journal of Physical Chemistry B, 2003. **107**(47): p. 13015-13021.

312. Liu, F.M. and M. Green, *Efficient SERS substrates made by electroless silver deposition into patterned silicon structures.* Journal of Materials Chemistry, 2004. **14**(10): p. 1526-1532.

313. Jensen, T.R., et al.., *Nanosphere lithography: Effect of the external dielectric medium on the surface plasmon resonance spectrum of a periodic array of sliver nanoparticles.* Journal of Physical Chemistry B, 1999. **103**(45): p. 9846-9853.

314. Jensen, T.R., et al.., *Nanosphere lithography: Tunable localized surface plasmon resonance spectra of silver nanoparticles.* Journal of Physical Chemistry B, 2000. **104**(45): p. 10549-10556.

315. Jensen, T.R., G.C. Schatz, and R.P. Van Duyne, *Nanosphere lithography: Surface plasmon resonance spectrum of a periodic array of silver nanoparticles by ultraviolet-visible extinction spectroscopy and electrodynamic modeling.* Journal of Physical Chemistry B, 1999. **103**(13): p. 2394-2401.

316. Malinsky, M.D., et al.., *Chain length dependence and sensing capabilities of the localized surface plasmon resonance of silver nanoparticles chemically modified with alkanethiol self-assembled monolayers.* Journal of the American Chemical Society, 2001. **123**(7): p. 1471-1482.

317. Robbie, K., et al.., *Ultrahigh vacuum glancing angle deposition system for thin films with controlled three-dimensional nanoscale structure.* Review of Scientific Instruments, 2004. **75**(4): p. 1089-1097.

CHAPTER 3

EFFECT OF HYDROPHOBIC SURFACTANT PROTEINS SP-B AND SP-C ON PHOSPHOLIPID MONOLAYERS.

PROTEIN STRUCTURE STUDIED USING 2D IR AND βν CORRELATION ANALYSIS[1]

[1] Shanmukh, S., Howell, P., Baatz, J.E. and Dluhy, R.A. 2002. *Biophysical Journal*. 83 (4): 2126-2141
Reprinted here with the Permission of the publisher

Abstract

We have applied two-dimensional infrared (2D IR) and $\beta\nu$ correlation spectroscopy to *in-situ* IR spectroscopy of pulmonary surfactant proteins SP-B and SP-C in lipid-protein monolayers at the A/W interface. For both SP-B and SP-C, a statistical windowed autocorrelation method identified two separate surface pressure regions that contained maximum amide I intensity changes: 4 – 25 mN/m and 25 – 40 mN/m. For SP-C, 2D IR and $\beta\nu$ correlation analyses of these regions indicated that SP-C adopts a variety of secondary structure conformations, including α-helix, β-sheet, and an intermolecular aggregation of extended β-sheet structure. The main α-helix band split into two peaks at high surface pressures, indicative of two different helix conformations. At low surface pressures, all conformations of the SP-C molecule reacted identically to increasing surface pressure and reoriented in-phase with each other. Above 25 mN/m, however, the increasing surface pressure selectively affected the co-existing protein conformations, leading to an independent reorientation of the protein conformations. The asynchronous 2D IR spectrum of SP-B showed the presence of two α-helix components, consistent with two separate populations of α-helix in SP-B – a hydrophobic fraction associated with the lipid chains and a hydrophilic fraction parallel to the membrane surface. The distribution of correlation intensity between the two α-helix cross peaks indicated that the more hydrophobic helix fraction predominates at low surface pressures while the more hydrophilic helix fraction predominates at high surface pressures. The different SP-B secondary structures reacted identically to increasing surface pressure, leading to a reorientation of all SP-B subunits in-phase with one another.

Introduction

Mammalian pulmonary surfactant is a highly specialized substance that contains approximately 85% phospholipid, 7-10% protein, and 4-8% neutral lipid [1, 2]. The most abundant phospholipid class is phosphocholine, while anionic phospholipids including phosphoglycerols make up about 10-15% of lung surfactant phospholipids [3-5]. Lung surfactant also contains four apoproteins, including two small hydrophobic proteins (SP-B and SP-C) that are known to enhance the adsorption and dynamic film behavior of phospholipids [1, 2, 6, 7]. The lack of surfactant in the under-developed lungs of premature infants is the root cause of Respiratory Distress Syndrome (RDS) [8], while disruption of surfactant activity is linked to the pathophysiology of clinical lung damage seen in Acute Respiratory Distress Syndrome (ARDS) [9-11].

Researchers have long used insoluble, monomolecular films spread at the air/water interface as models for pulmonary surfactant [1, 12]. Surface balance techniques have been used to study the monolayer properties of the hydrophobic proteins SP-B and SP-C and their mixtures with lipids at the air/water interface [13-17]. In addition, a variety of biophysical techniques have been employed to surfactant model systems, including electron microscopy [18], Brewster angle microscopy [19], fluorescence microscopy [20-22], near-field microscopy [23], as well as scanning probe microscopy [24]. While these microscopic techniques provide important biophysical information, they cannot give the same detailed molecular-level information about lipid-protein interactions that can be obtained using vibrational spectroscopic methods.

The use of external reflection Fourier transform infrared spectroscopy to study the structure of monomolecular films directly at the air/water interface was originally developed in the mid-1980's and progress in this field has recently been reviewed [25, 26]. This infrared reflection-

absorption spectroscopy (IRRAS) technique has been applied to the study of monolayer films of extracted lung surfactant preparations [27] and more recently, to investigate the roles that SP-B and SP-C play in the function of lung surfactant [28-30]. In addition to lipid phase information, it has been shown that amide vibrations can be observed in pure or highly enriched lipid-protein films and that structural information concerning the surfactant proteins can be obtained. Although these studies have contributed significant information to the study of surfactant systems, including the nature of surfactant protein structure and orientation, difficulties remain. In particular, the low band intensities inherent in IRRAS at the A/W interface, as well as the highly overlapping nature of the amide region makes assignment of protein conformational intermediates problematic.

Recently, an approach using statistical correlation analysis known as two-dimensional infrared spectroscopy (2D IR) has been described to uncover spectral features not readily observable using traditional IR spectroscopy [31-34]. Two-dimensional IR spectroscopy is based on the correlation of dynamic spectral variations induced by an external sample perturbation. The effect of these perturbation-induced changes in the local molecular environment is manifested as pseudo time-dependent changes in IR spectral parameters. These resulting dynamic spectra are subject to a cross-correlation analysis that produces two-dimensional maps that can enhance spectral information by spreading out the IR band intensities along two orthogonal axes. 2D IR spectroscopy has particular advantages in simplifying complex spectra, identifying inter- and intramolecular interactions, and facilitating band assignments [35]. Literature references to 2D IR correlation analysis have predominately been in the area of polymer structure, an application for which the method was first developed [36]. However, the last few years has seen increasing application of this methodology to biological

problems, in particular, the use of 2D-IR for the study of macroscopic properties of proteins in aqueous solutions. For example, the thermal transitions of a number of proteins has been studied using 2D IR, including cytochrome c [37, 38], CMP kinases [39], ovalbumin [40], β-lactoglobulin [41], avidin [42] and synthetic helix-forming peptides [43]. Several studies have been published that use pH gradients or H – D exchange to enhance the amide spectral region and assign conformations to the underlying band components [44-46]. Studies using 2D hetero-spectral correlations have appeared that enable comparisons to be made among a number of spectral techniques [47, 48].

Two-dimensional IR correlation analysis has also been used to analyze structure in monomolecular films. The phase behavior of phospholipid monolayers using 2D IR have been studied and it was shown how these methods could distinguish bands due to co-existing phases in a disorder-order phase transition in the monolayer [49, 50].

While 2D IR has successfully been used to study structural changes and to make band assignments in proteins, it can also be used in determining the temporal order of events that occur during the external sample perturbation, albeit qualitatively. In order to more quantitatively describe the degree of coherence between spectral intensity changes and the sequence of molecular events in a set of dynamic spectra, we have recently developed a modified 2D IR correlation method called $\beta\nu$ correlation analysis [51]. This method is a variation of asynchronous cross-correlation, in which dynamically varying spectra are correlated against a mathematical function with varying phase angle. We recently applied $\beta\nu$ correlation analysis to surface pressure-induced changes in the IRRAS spectra of phospholipid monolayers at the A/W interface, and showed how the relative rates of acyl chain and methyl group reorientation could be quantitatively determined [52].

The research described in this paper represents the first study that uses $\beta\nu$ correlation analysis for the study of protein structure. We use this method to probe the conformational intermediates in the surface pressure-resolved IRRAS spectra of two lipid-protein samples: DPPG/SP-C and DPPG/SP-B at the A/W interface. While these proteins have been previously studied using IRRAS at the A/W interface, the detailed study of their conformational intermediates and reorientation in response to increasing surface pressure has not been completely described.

Materials and Methods

Surface Chemistry

The synthetic phospholipid 1,2-dipalmitoyl-*sn*-glycero-3-phosphoglycerol (DPPG), was purchased from Avanti Polar Lipids (Alabaster, AL) and was used as received. ACS grade NaCl and HPLC grade methanol and chloroform were obtained from J.T. Baker. Subphase H_2O was obtained from a Barnstead (Dubuque, IA) ROpure/Nanopure reverse osmosis/deionization system having a nominal resistivity of 18.3 MΩ cm.

Purification of Surfactant Proteins B (SP-B) and C (SP-C)

SP-B and SP-C were purified from calf lung surfactant extract (CLSE) by isocratic normal phase liquid chromatography on Silica C8 as described elsewhere [53]. Briefly, approximately 700 mg CLSE (total lipid plus protein) was initially reduced in volume by evaporation under nitrogen to approximately 4 ml (~1% of column bed volume). Small amounts of chloroform were added to the concentrated CLSE if the solution became cloudy. The concentrated CLSE was then applied to a 450 ml bed volume LC column that had been pre-equilibrated with 7:1:0.4 MeOH/$CHCl_3$/5% 0.1M HCl. The added CLSE was allowed to completely adsorb to the column, and was then eluted with 7:1:0.4 MeOH/$CHCl_3$/5% 0.1M HCl at a flow rate of 0.4

ml/min and UV detection at 254 nm. SP-B eluted from the column as the first peak, while SP-C eluted as the second peak as determined by SDS PAGE and protein sequencing (see below). SP-B fractions were combined and, as determined by the method of Shin, the final SP-B solution was free of phospholipid [54], while SDS PAGE and protein sequencing indicated the absence of SP-C (see below). Fractions containing SP-C were combined, concentrated via N_2 gas stream and run on a second C8 LC column. Fractions containing purified SP-C from this second column were combined. Phospholipid content of purified SP-C using the method of Shin [54] was determined to be less than 4 mole lipid/mole SP-C. Protein sequencing analysis (see below) indicated that the purified SP-C was free of SP-B.

SDS PAGE and amino acid analysis

For SDS PAGE, 20 microliters of the appropriate column fractions were suspended in NuPage sample buffer (Invitrogen, Carlsbad, CA) and applied to 4-10 % gradient acrylamide Tris/Bis gels (NuPage gels, Invitrogen) under non-reducing conditions. Electrophoresis was performed at a constant voltage of 200 V for 40 minutes with a morpholinoethanesulphonic acid (MES) buffer containing 50 mM MES/50 mM Tris Base/3.5 mM SDS/1 mM EDTA, pH 7.7 as the running buffer. Silver staining for detection of protein bands was performed according to Morrissey [55]. N-terminal amino acid sequence analysis was performed for seven to ten cycles using an Applied Biosystem Procise sequence analyzer. SP-B and SP-C were identified by the N- terminal sequences of Phe-Pro-Ile-Pro-Ile-Pro and Leu-Ile-Pro-???-???-Pro-Val, respectively, where positions 4 and 5 in the SP-C sequence were both assumed to be Cys. The concentrations of SP-B and SP-C were determined by the BCA total protein assay (Sigma Chemical Co., St. Louis, MO).

Preparation of Samples

Stock solutions of DPPG (~2.5 mg/ml in 4:1 $CHCl_3$:MeOH) were prepared and concentrations verified by inorganic phosphorus assay [56]. Solutions of the lipid and proteins containing 20:1 lipid-protein mol:mol (for SP-C) or 40:1 lipid-protein mol:mol (for SP-B) – *i.e.* app. 22 wt% for both SP-B and SP-C – were prepared by mixing the appropriate amounts of the phospholipid stock solution together with the stock solutions of SP-B or SP-C in 1:1 $CHCl_3$:MeOH. The subphase used for all experiments was 150 mM NaCl in deionized H_2O (pH 5.6).

FTIR External Reflectance Measurements

Infrared external reflection-absorbance spectra of monolayers at the A/W interface were acquired using a Perkin Elmer Spectrum 2000 FTIR spectrometer equipped with an external sample beam. A sixty-degree, gold-coated, off-axis parabolic mirror (Janos Technology Inc., Townshend, VT) reflected the beam coming from the spectrometer onto the surface of a Nima 601M film balance (Coventry, England) at an incidence angle of 30 degrees to the surface normal. The beam reflects off of the subphase, sampling the film, and a second parabolic mirror collects the beam and directs it into a collection mirror and then onto the sensing chip of a liquid N_2-cooled HgCdTe detector. The film balance, optical components, and detector are housed in a sealed, plexiglas chamber that allows humidity control of the local trough environment, thus improving water vapor background subtraction. A schematic diagram of the experimental set-up has been previously published [26].

The subphase was first cleaned by aspiration and a single beam spectrum was collected for use as the IR background spectrum. The subphase temperature was held constant at 22 ± 1 °C by flowing thermostatted water through the hollow body of the trough. The temperature in the

enclosed chamber was typically 24°C and the relative humidity remained fairly constant at 70%. Typically 5-10 μl of sample was spread via syringe onto the trough surface. The film was allowed to equilibrate for a period of 30 minutes and then was compressed intermittently and spectra collected over a range of surface pressures from ~5 mN/m to a maximum of 45-65 mN/m depending on the nature of the film.

External reflection-absorption spectra were collected with 1024 scans at 16 cm^{-1} resolution, apodized with a Norton-Beer (medium) function, and were Fourier transformed with one level of zero filling. A resolution of 16 cm^{-1} was chosen for several reasons: 1) time of collection is minimized and SNR is maximized when spectra are collected at lower resolution, 2) residual water vapor bands are easier to subtract at low resolution when the relative humidity varies slightly during the course of the experiment, and 3) valid statistical correlation analyses can be constructed for IR spectra collected at lower resolutions, as has recently been discussed [57].

All monolayer spectra are presented as reflection-absorption spectra, *i.e.*, $A = -\log\left(\frac{R}{R_0}\right)$, where R is the IR reflectivity of the monolayer surface and R_o is the IR reflectivity of the bare water subphase background. The reflectance IR spectra used in the analyses presented here were baseline corrected using the GRAMS/32 (Galactic Industries, Salem, NH) software package prior to determination of peak positions and band intensities; in addition, residual water vapor bands have been subtracted. Adjustments for changes in surface density (*i.e.* intensity normalization) were also performed using GRAMS/32. Other than baseline correction and intensity normalization, the spectra have not been smoothed or further processed. Vibrational frequencies were calculated using a 5-point center of gravity algorithm [58] written in our laboratory for the Grams/32 environment.

Calculation of 2D IR Correlation Spectra.

The 2D IR synchronous spectrum, $\Phi(\nu_1,\nu_2)$, and the asynchronous spectrum, $\Psi(\nu_1,\nu_2)$, were calculated using Equations 1 and 2. These algorithms use the most recent mathematical formalism in which a Hilbert transform is utilized for calculating the asynchronous spectrum rather than the more commonly employed Fourier transform [59]. In all cases the average spectrum was subtracted from each sequentially obtained surface pressure-dependent IRRAS spectrum to produce a set of dynamic IR spectra. The dynamic spectra were then used in the correlation analysis.

$$\Phi(\nu_1,\nu_2)=\frac{1}{N-1}\sum_{j=0}^{N-1}y(\nu_1,n_j)\cdot y(\nu_2,n_j) \tag{1}$$

$$\Psi(\nu_1,\nu_2)=\frac{1}{N-1}\sum_{j=0}^{N-1}y(\nu_1,n_j)\cdot\sum_{k=0}^{N-1}M_{jk}\cdot y(\nu_2,n_k) \tag{2}$$

In Equations 1 and 2, ν_1 and ν_2 represent two independent frequencies, n_j represents the number of the spectrum in the ordered sequence where the first spectrum number is zero, N represents the total number of spectra used in the calculation, and M_{jk} is the Hilbert transform matrix, which is defined in Equation 3.

$$M_{jk}=\begin{cases}0 & \text{if } j = k\\ 1/\pi(k-j) & \text{otherwise}\end{cases} \tag{3}$$

The 2D plots presented in this article were calculated using 2D IR correlation analysis algorithms written in our laboratory for the MATLAB programming environment (Version 6, The MathWorks, Inc., Natick, MA).

βν Correlation Analysis.

A $\beta\nu$ correlation analysis is a mathematical asynchronous cross correlation performed on a set of dynamically varying IR spectra against a set of sinusoidal functions that differ only by their phase angle β. A full description of the details of the $\beta\nu$ correlation analysis has been presented elsewhere [51]. This type of correlation analysis is mathematically described using Equation 4.

$$\Psi(\nu,\beta) = \frac{1}{N-1}\sum_{j=0}^{N-1} y(\nu,n_j)\cdot\sum_{k=0}^{N-1} M_{jk}\cdot\sin(k\phi+\beta) \qquad (4)$$

The correlation intensity Ψ at some point (ν, β) represents the correlation of the measured IR spectral intensity y (ν, n_j) with the mathematical function $\sin(k\phi + \beta)$. In Equation 4, y is the IR intensity; ν is the frequency or wavenumber; n_j is the number of the spectrum in the ordered sequence where the first spectrum number is zero; β is the phase angle of the respective sine function; N is the total number of spectra used in the calculation; ϕ is a constant value in degrees (or radians) chosen based upon the total number of dynamic spectra used in the calculation, and M_{jk} is the Hilbert transform matrix previously defined in Equation 3.

In this study all $\beta\nu$ correlations were performed with $\phi = 10^{o}$, so that $\sin(k10° + \beta)$ describes approximately ¼ of the cycle of a sine function, or the approximate form of a commonly observed variation in spectral band intensities upon sample perturbation. Only the asynchronous correlation algorithm is used in the $\beta\nu$ correlation analysis presented here, since asynchronous 2D IR correlations are more sensitive to differences in the form of the signal variation than are

synchronous correlations [32]. Note also that the computational algorithm for the $\beta\nu$ correlation analysis uses the most recent mathematical formalism, in which a Hilbert transform is used for calculating the asynchronous spectrum, rather than the more computationally cumbersome Fourier transform [59]. The effective phase angle, β_e , is defined by Equation 5.

$$\beta_e = \beta + 90^o \tag{5}$$

In Equation 5, β is the point of maximum positive correlation intensity in the plot of β *vs.* ν as defined by Equation 4. The value of β_e is defined in this fashion so that the phase angle β and the effective phase angle β_e are the same for a sinusoidal signal variation with constant frequency. In this article, the contour levels are evenly spaced in the $\beta\nu$ plots from 0 to the maximum value for positive correlations. Negative correlations are not displayed since they simply differ from the positive correlations by 180^o.

The $\beta\nu$ plots of effective phase angles *vs.* wavenumber were calculated using $\beta\nu$ correlation analysis algorithms written in our laboratory for the MATLAB programming environment.

Results and Discussion

IRRAS Spectra of Lipid:Protein Monolayer Films

Infrared external reflectance-absorption spectra were obtained at the air-water interface for monolayer films of DPPG plus the surfactant proteins SP-B and SP-C; these spectra are shown in Figure 3.1. These IR spectra were acquired while the monolayer was held at specific surface pressure values from 4.0 mN/m to 40.0 mN/m during step-wise compression of the film balance. External reflection-absorption IR spectra of monomolecular films at the air-water interface differ substantially from spectra obtained by conventional transmission IR spectroscopy. In particular, the complex refractive indices of both sample and substrate contribute to the observed IRRAS spectra of A/W monolayers. Therefore, these spectra are functions of the wavelength, state of

polarization, thin film thickness, angle of incidence of the incoming light, and the optical constants of the three phases involved [60]. The physical basis for the method as well as the use of IR spectroscopy to study monolayer films at the A/W interface has recently been reviewed [25, 26].

Monolayer IRRAS spectra were collected using an unpolarized incident IR source and have been normalized to account for changes in trough area. Normalization refers to the adjustment of IR spectral intensities to take into account changes in surface density as the trough area available to the monomolecular film decreases during compression. Intensity changes in area-normalized monolayer spectra more accurately reflect conformational changes in the monolayer, as apposed to merely reflecting an increase in number density. We have previously shown that intensity normalization is important for understanding 2D IR correlation maps calculated from IRRAS monolayer spectra [50]. In addition, the spectra used in these analyses were collected at 16 cm^{-1} resolution. The issue of resolution is particularly relevant to monolayer IRRAS at the air-water interface, since it is a low-intensity reflectance technique with inherently weak (10^{-3} – 10^{-4} AU) band intensities. Due to the very broad amide I proteins bands (bandwidths greater than 30 cm^{-1}), a spectral resolution of 16 cm^{-1} was used to minimize collection time and maximize S/N. A recently published paper has addressed instrumental issues in the calculation of 2D IR spectra and has shown that lower resolution spectra may be appropriate for use in 2D calculations under certain circumstances [57].

The overlaid spectra in Figure 3.1 are reflection-absorbance spectra displaying the amide I (1700 – 1600 cm^{-1}) and amide II (1600 – 1500 cm^{-1}) regions of the surfactant proteins. Also observed is the C=O vibration from the phospholipid between 1750 – 1700 cm^{-1}. These IRRAS absorption bands exhibit negative IR intensities, in agreement with the experimental conditions

[60]. Figure 3.1A illustrates IRRAS spectra at the A/W interface for a DPPG/SP-C monolayer at a protein concentration of ~22 wt%. Clearly evident in the spectra are the lipid C=O band at 1738 cm^{-1}, two protein amide I bands at ~1654 and 1625 cm^{-1}, and the protein amide II band at ~1550 cm^{-1}. Figure 3.1B illustrates the same spectral regions as in Figure 3.1A, for a DPPG/SP-B monolayer also at a protein concentration of ~22 wt%. The identical carbonyl and amide bands are evident in the spectra of the SP-B monolayer as in the spectra of the SP-C monolayer, although relative band heights for the amide vibrations differ.

Identification of Unique Surface Pressure Regimes Using Windowed Autocorrelation Analysis

Prior to analysis of the lipid-protein monolayer spectra using 2D IR correlation spectroscopy, we employed a windowed autocorrelation method to identify the surface pressure regimes that encompass the greatest variation in amide spectral intensity. These regions can be located by adapting a dynamic filtering technique that auto correlates IR intensities within a defined surface pressure window and plots them against the average surface pressure, thereby locating the regions of maximal spectral variation. This technique has been previously applied to the temperature-dependent 2D IR spectra of liquid crystals [61].

The windowed autocorrelation analysis method begins by separating the monolayer IRRAS spectra into a smaller data set containing only the first four spectra of lowest surface pressure (*e.g.* P_1 through P_4). An average spectrum is calculated from the spectra in this window; the individual spectra in the window are mean-centered by subtraction of the average. Next, 2D IR analysis is used to calculate the correlation intensities for each spectral frequency in this windowed, mean-centered data set. The resulting autocorrelation intensities represent the

Figure 3.1 IR external reflection-absorption spectra of a lipid:protein monolayer showing the amide I and amide II spectral regions collected at surface pressures from 4.0 to 40.0 mN/m. The spectra were collected as a function of increasing monolayer surface pressure and have been normalized for changes in surface density. (A) DPPG / SP-C (20:1, mol:mol, ~22 wt% SP-C). (B) DPPG / SP-B (40:1 mol:mol, ~22 wt% SP-B).

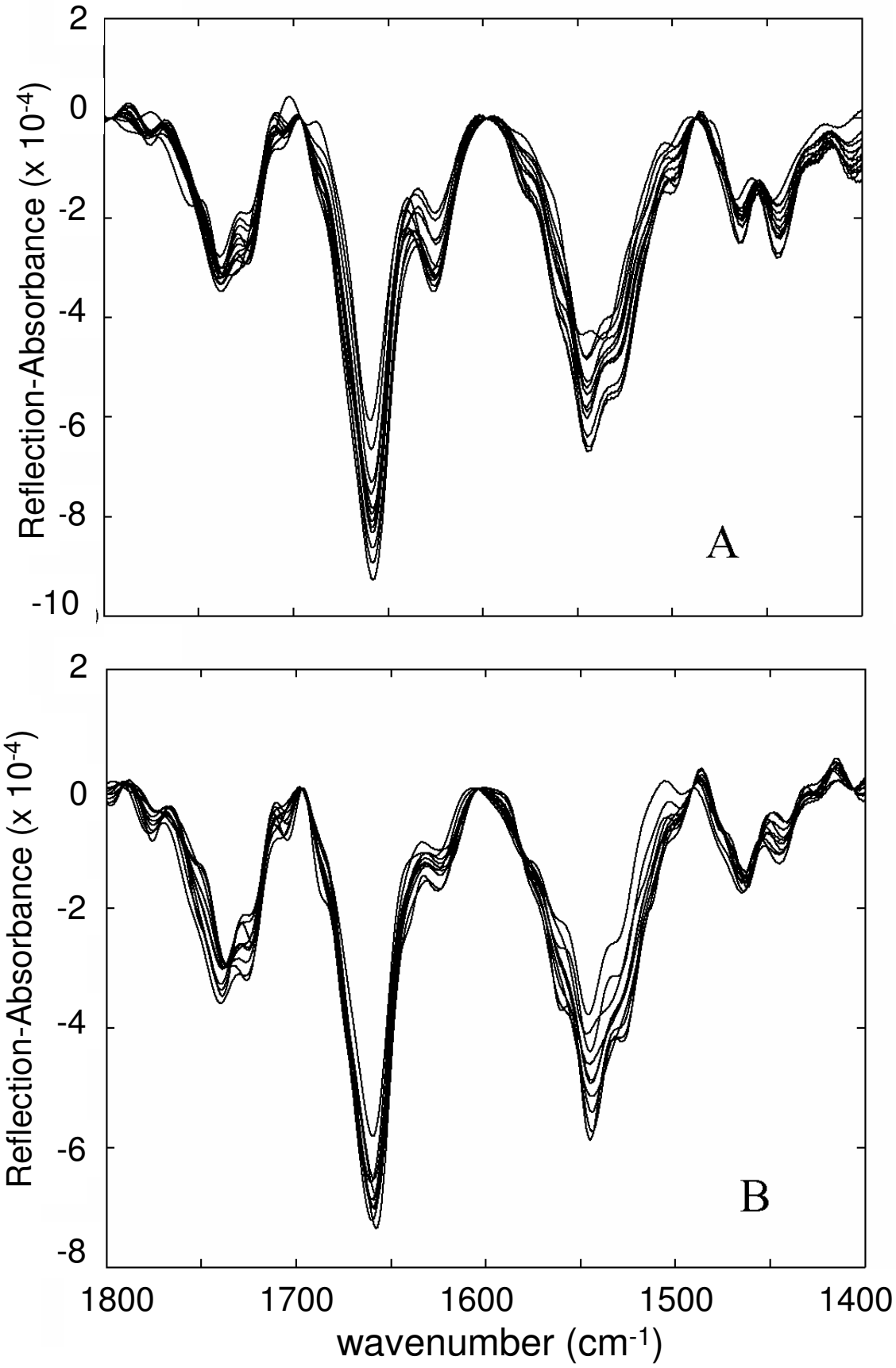
2
0
-2
-4
-6
-8
-10
Reflection-Absorbance (x 10-4)
A
2
0
-2
-4
-6
-8
Reflection-Absorbance (x 10-4)
B
1800
1700
1600
1500
1400
wavenumber (cm-1)

amount of spectral variation that occurs at each frequency as a function of the average surface pressure of the windowed data set. This autocorrelation window is then swept over the entire data set translating it one surface pressure-resolved spectrum at a time (*i.e.* the second window contains P_2 through P_5, *etc.*).

The autocorrelation spectrum that results from this process is plotted as a function of the average surface pressure of the autocorrelation window. The spectral frequencies that have the largest autocorrelation intensities will be those frequencies at which the largest spectral variations occur. In this manner, surface pressure regions that contain maximal spectral variations may be identified. With this information at hand, 2D IR or $\beta\nu$ correlation analysis can be performed solely within these regions to establish the structural or temporal relationships that contribute to the spectral variations.

We have applied this windowed autocorrelation analysis method to the monolayer IRRAS spectra of DPPG/SP-C and DPPG/SP-B. The results are shown in Figure 3.2. In analyzing these spectra, we were particularly concerned with the protein structural components, hence we concentrated on autocorrelation of the amide I spectral region. Figure 3.2A shows a contour plot of the autocorrelation spectra for the DPPG/SP-C sample. This contour plot is dominated by a large band at ~1650 cm^{-1} that shows two intensity maxima: one between ~12 – 18 mN/m and one above ~27 mN/m. Based on these autocorrelation spectra, we can reliably partition the surface pressure-resolved spectra of the DPPG/SP-C monolayer into two pressure regions, low (4 – 25 mN/m) and high (25 – 40 mN/m). A similar contour plot of the autocorrelation intensities for the DPPG/SP-B spectra is shown in Figure 3.2B. In this case, an intense autocorrelation maxima at ~1650 cm^{-1} is observed at high surface pressure (> 25 mN/m), however, lower intensity contours occur below 25 mN/m. Therefore, we have also divided the surface pressure-resolved spectra of

the DPPG/SP-B monolayer into two pressure regimes: low (4 – 25 mN/m) and high (25 – 40 mN/m). The approach that we have taken here isolates the surface pressure regions that contain maximal spectral variations. Using these newly defined surface pressure regimes, we have performed 2D IR and $\beta\nu$ correlation analyses on the IRRAS spectra of both the SP-C – and SP-B – containing monolayers in order to better understand the surface pressure-induced protein rearrangements in the monolayer.

2D IR Correlation Analysis of the SP-C Amide I Region

Synchronous and asynchronous 2D IR correlation maps were calculated for the SP-C – containing monolayer to investigate protein conformational changes that occur upon monolayer compression. Figure 3.3 shows the 2D contour map for the synchronous correlation of the DPPG/SP-C IRRAS spectra, in both the low surface pressure regime below 25 mN/m (Figure 3.3A) as well as the high surface pressure region above 25 mN/m (Figure 3.3B). Synchronous 2D spectra are characterized by on-diagonal auto peaks as well as off-diagonal, symmetric cross peaks. Synchronous 2D auto peaks simply reflect how the spectral intensity responds to the external perturbation; synchronous cross peaks, on the other hand, develop when two separate transition dipole moments are significantly coupled, or if they reorient in-phase to the external perturbation [62].

Note that due to the symmetric properties of synchronous correlation cross peaks with respect to the diagonal, it is necessary to describe only the cross peaks above the diagonal line. This property also holds for the antisymmetric properties of the cross peaks in the asynchronous correlation plots (see below). In this article correlation peaks are described as ν_1 *vs*. ν_2, where ν_1 refers to the wavenumber value of the *x*-axis and ν_2 refers to the wavenumber value of the *y*-axis.

Figure 3.2 Surface pressure-wavenumber contour plot of autocorrelation intensities based on a dynamic filtering technique using a windowed autocorrelation analysis method. Contours result from the autocorrelation intensities calculated as a function of a translating surface pressure window. (A) DPPG / SP-C (20:1, mol:mol, ~22 wt% SP-C). (B) DPPG / SP-B (40:1 mol:mol, ~22 wt% SP-B).

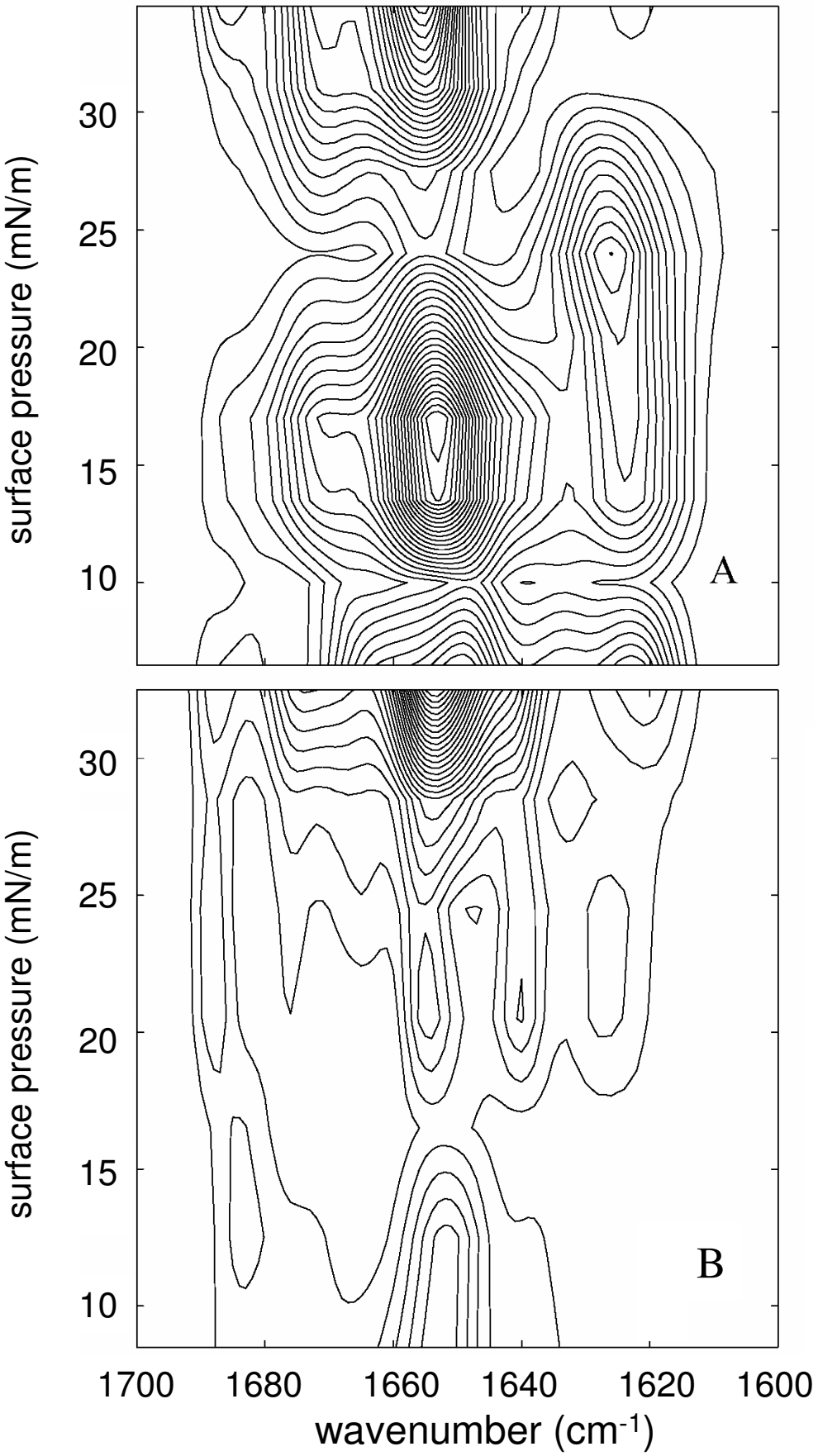
surface pressure (mN/m)
30
25
20
15
10
A
surface pressure (mN/m)
30
25
20
15
10
B
1700
1680
1660
1640
1620
1600
wavenumber (cm-1)

Mature SP-C consists of 35 amino acids and is an extremely hydrophobic, predominately α-helical protein of approximately 4.2 kD with charged amino acids (K10 and R11) near its N terminus. The cysteines C4 and C5 are acylated in bovine SP-C. The NMR structure of SP-C in apolar solvent essentially describes the protein as a rigid rod in which only a few residues near the N terminus (L1 – P7) and the C terminus itself are *not* helical [63]. The length of this helix (V8 – G34) is ~ 39 Å with a diameter is of ~ 12 Å.

The 2D IR synchronous map of the low-pressure region of the DPPG/SP-C monolayer (Figure 3.3A) is dominated by a strong auto peak at 1652 cm^{-1} with less intense auto peaks at 1672 cm^{-1} and 1625 cm^{-1}. Positive cross peaks are observed at 1652 *vs*. 1625 cm^{-1} and 1685 *vs*. 1625 cm^{-1}. Positive synchronous cross peaks indicate a coordinated spectral response in which the functional groups are reorienting in the same direction. In addition, there is a negative cross peak between the 1676 cm^{-1} *vs*. 1630 cm^{-1} bands. Negative synchronous cross peaks also indicate significantly coupled molecular reorientation, albeit one where the spectral intensity of one component increases while the second decreases.

The high surface pressure region (>25 mN/m) of the DPPG/SP-C monolayer is also dominated by the major auto peak at 1656 cm^{-1} (Figure 3.3B) with additional auto peaks observable at 1685, 1671, 1666 and 1622 cm^{-1}. Cross peaks associated with the 1622 cm^{-1} band can be observed at wavenumber values 1656 *vs*. 1622 cm^{-1}, 1671 *vs*. 1622 cm^{-1} and 1685 *vs*. 1622 cm^{-1}. Additional cross peaks at 1671 *vs*. 1654 cm^{-1} and 1685 *vs*. 1654 cm^{-1} are also observed.

The wavenumber location of the cross peaks in the 2D IR synchronous map can be identified with protein secondary structure conformations (*e.g.* α-helices, β-sheets & turns, unordered structure, *etc.*) using previously published IR correlations, see *e.g.* [64-67]. Caution is

Figure 3.3 Synchronous 2D IR correlation plots of the monolayer IRRAS spectra of DPPG / SP-C (20:1, mol:mol, ~22 wt% SP-C). Solid lines indicate regions of positive correlation intensity; dashed lines indicate regions of negative correlation intensity. Spectra were divided into two pressure regions based on their autocorrelation intensities. 2D IR synchronous correlations were calculated on spectra contained within the pressure region. The one-dimensional spectrum shown in this figure is the calculated average of the spectra used in the 2D analysis. (A) 4.0 mN/m – 25.0 mN/m. (B) 25.0 mN/m – 40.0 mN/m.

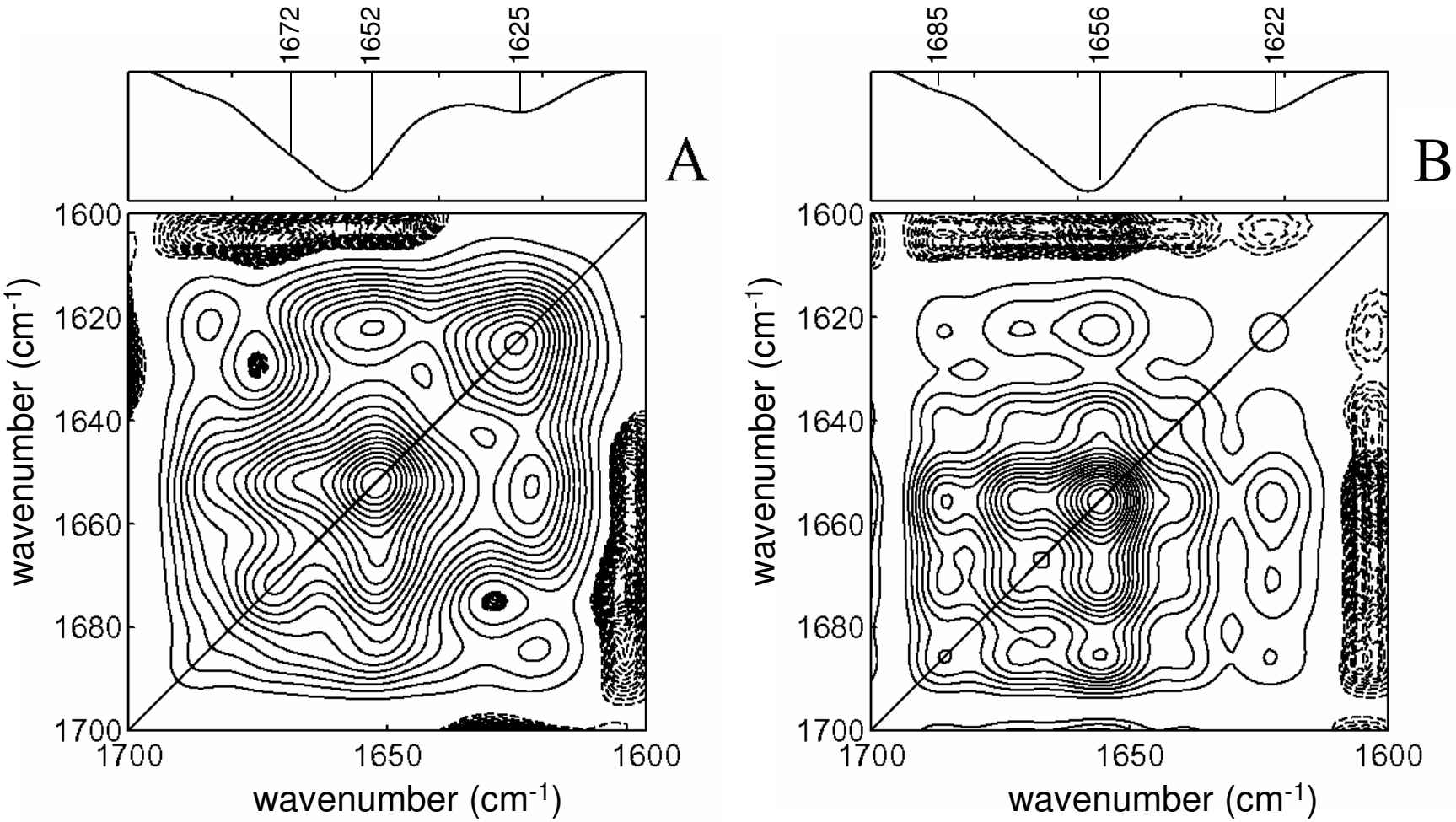
1672
1652
1625
A
1600
1620
1640
1660
1680
1700
wavenumber (cm-1)
1700
1650
1600
wavenumber (cm-1)
1685
1656
1622
B
1600
1620
1640
1660
1680
1700
wavenumber (cm-1)
1700
1650
1600
wavenumber (cm-1)

advisable when making conformational assignments using IR amide I spectra since secondary structure correlations with a specific wavenumber are not unique and a wavenumber range exists in the amide I region for any particular protein conformation. Nevertheless, using the most well-established associations, the cross peak at 1654 cm^{-1} can be considered characteristic of α-helices, while the bands at 1630 and 1676 cm^{-1} are assigned to β-sheet and β-turn/loop structures, respectively.

In both the raw spectra (Figure 3.1) and the synchronous and asynchronous (see below) 2D maps for DPPG/SP-C, we also observe bands and cross peaks at wavenumber values both high (1687 cm^{-1}) and low (1620 cm^{-1}) in the amide I range. Using *ab initio* calculations, this pair of peaks has been assigned to a structure of extended, multistranded, antiparallel β-sheet aggregates [68]; these peaks have also been experimentally observed for a model β-sheet peptide [69]. This association is strengthened in the case of SP-C, since the 2D synchronous maps for both low and high pressures show a cross peak between 1687 and 1620 cm^{-1}, indicating a coordinated response between the two bands. The implication for SP-C, a predominately α-helical protein [63], is that some portion of the molecule undergoes intermolecular hydrogen-bonding resulting from aggregation of unfolded protein segments.

Taking these structural assignments into account, the synchronous 2D map for SP-C shows that the α-helix is the predominate structural motif in both the low and high pressure regions, as expected. However, the cross peaks at 1625, 1630, 1672 and 1685 cm^{-1} also demonstrate that SP-C contains a more varied secondary structure containing a higher degree of aggregated β-strands than previously reported.

Asynchronous 2D IR correlation maps were also calculated from the DPPG/SP-C IRRAS monolayer spectra. In a similar fashion to the synchronous plots of Figure 3.3, Figure 3.4 shows

the 2D contour map for the asynchronous correlation of the DPPG/SP-C spectra, in both the low surface pressure regime below 25 mN/m (Figure 3.4A) as well as the high surface pressure region above 25 mN/m (Figure 3.4B). Asynchronous 2D spectra are antisymmetric with respect to the diagonal in the correlation map and contain no auto peaks; the spectrum consists only of off-diagonal cross peaks with two intensity maxima – one positive and one negative. Peaks appear in asynchronous 2D correlation maps if the transition dipole moments are significantly decoupled, or if the dipole moments reorient out-of-phase or at different rates in response to the external perturbation. This attribute is used to unmask the differential response of functional groups in the molecule, and makes asynchronous 2D correlation plots particularly useful for resolution enhancement [62].

The asynchronous 2D IR map of SP-C also indicates the presence of a varied, heterogeneous secondary structure for SP-C, in agreement with the synchronous correlation spectra. Four prominent cross peaks are observed in the low-pressure region (Figure 3.4A) at 1652 *vs*. 1634 cm^{-1} (-), 1663 *vs*. 1652 cm^{-1} (+), 1675 *vs*. 1663 cm^{-1} (-) and 1685 *vs*. 1675 cm^{-1} (+). Less intense, broad cross peaks are observed for the association of the band attributed to a β-sheet intermolecular aggregation (~1615 cm^{-1}) with the bands 1634, 1652 and 1663 cm^{-1}. The presence of asynchronous cross peaks at 1615, 1634, 1675 and 1685 cm^{-1} confirms the presence of these bands in the synchronous spectrum, and indicates that the SP-C protein conformation is comprised of extended β-sheet structure.

In the high pressure region above 25 mN/m, the asynchronous 2D correlation plot for DPPG/SP-C is characterized by a number of different cross peaks (Figure 3.4B), with a more complicated cross peak structure than is observed in the asynchronous spectrum of the low pressure region. Major positive asynchronous correlations are observed between 1654 *vs*. 1647

cm^{-1}, 1675 *vs*. 1647 and 1665 cm^{-1}, with an elongated correlation intensity band at 1688 *vs*. 1647, 1665 and 1680 cm^{-1}. Major negative asynchronous correlations are observed between 1665 *vs*. 1654 cm^{-1} and 1680 *vs*. 1654 and 1675 cm^{-1}. In addition, there is an elongated negative correlation intensity band between app. 1647 to 1680 *vs*. 1625 cm^{-1}.

The most relevant features of the asynchronous spectrum for the high pressure region are the split α-helix peak at 1654 / 1647 cm^{-1}, the elongated correlation intensity maxima associated with the 1680 cm^{-1} band, and the elongated correlation intensity minima associated with the 1625 cm^{-1} band. The ability of asynchronous 2D IR to resolve overlapped peaks is demonstrated in Figure 3.4B as the low pressure asynchronous α-helix cross peak at 1652 cm^{-1} has divided into two components at high pressure, one at 1654 cm^{-1} and one at 1647 cm^{-1}. This is the first report of two co-existing α-helix conformations in SP-C lipid-protein monolayers at high surface pressure. The 1647 cm^{-1} helix band, in particular, shows asynchronous cross peaks with a number of other bands, including 1654, 1675 and 1680 cm^{-1}, indicating an out-of-phase response of this conformation with the other protein conformations. These large elongated asynchronous correlation features at 1620 and 1680 cm^{-1} indicate that the motion of the extended β-structure is also significantly decoupled from the rest of the protein and reorients independently of the main helix structure at high surface pressures.

The asynchronous correlation spectrum for SP-C (Figure 3.4) presents a more complex band structure than does the synchronous correlation spectrum (Figure 3.3). The multiple cross peaks observed in the asynchronous correlation plot demonstrate that SP-C is comprised of a varied secondary structure. The major result of the asynchronous 2D correlation analysis is that the main α-helix band splits into two peaks at high surface pressures, indicating two different co-existing helix conformations for SP-C. The peaks at ~1634 and 1675 cm^{-1} indicate a β-sheet

Figure 3.4 Asynchronous 2D IR correlation plots of the monolayer IRRAS spectra of DPPG / SP-C (20:1, mol:mol, ~22 wt% SP-C). Solid lines indicate regions of positive correlation intensity; dashed lines indicate regions of negative correlation intensity. Spectra were divided into two pressure regions based on their autocorrelation intensities. 2D IR asynchronous correlations were calculated on spectra contained within the pressure region. The one-dimensional spectrum shown in this figure is the calculated average of the spectra used in the 2D analysis. (A) 4.0 mN/m – 25.0 mN/m. (B) 25.0 mN/m – 40.0 mN/m.

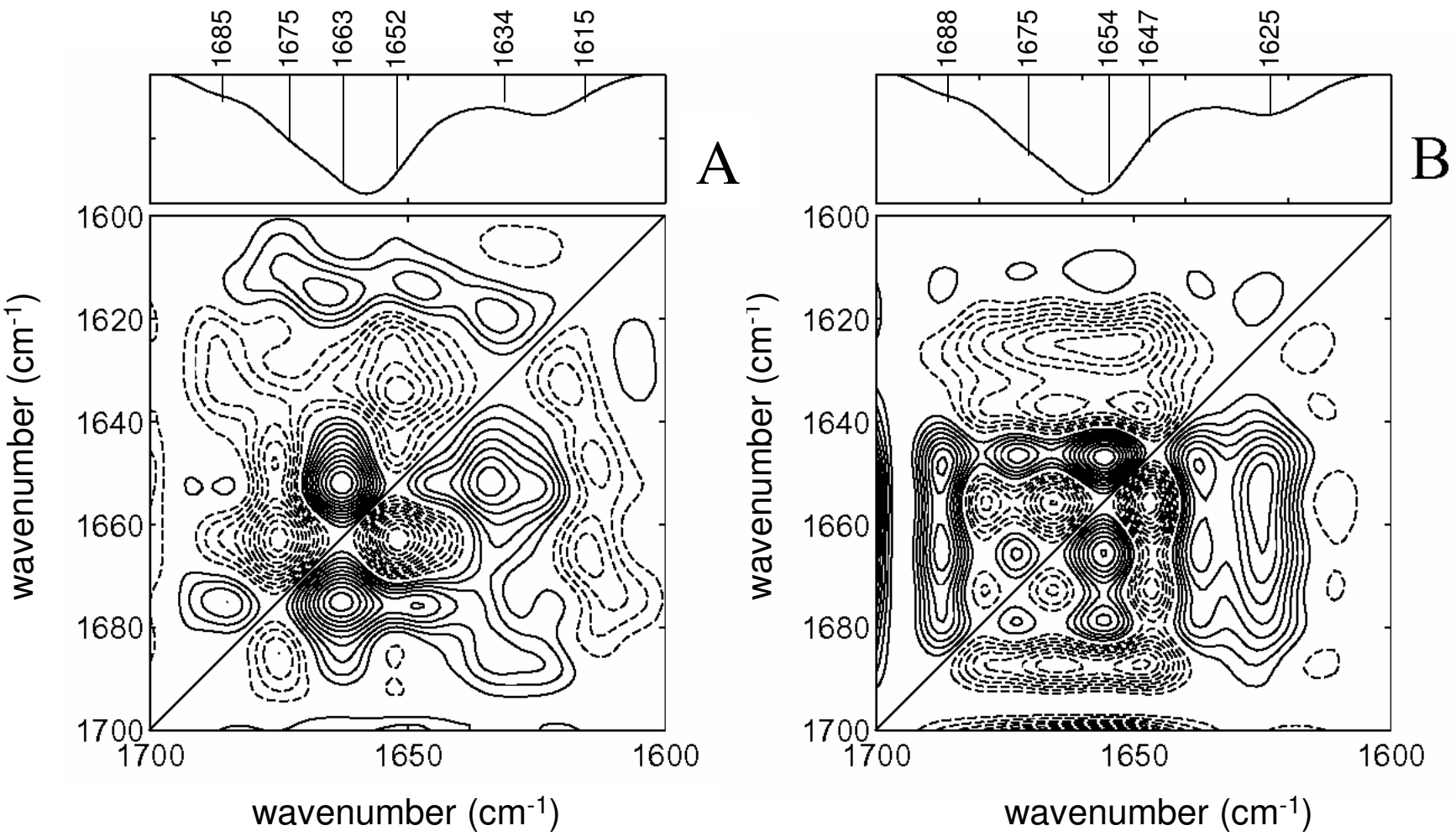
1685
1675
1663
1652
1634
1615
A
1600
1620
1640
1660
1680
1700
wavenumber (cm-1)
1700
1650
1600
wavenumber (cm-1)
1688
1675
1654
1647
1625
B
1600
1620
1640
1660
1680
1700
wavenumber (cm-1)
1700
1650
1600
wavenumber (cm-1)

structure exists at both low and high surface pressures. Also, the cross peaks at ~1620 and 1680 cm^{-1} demonstrate that an intermolecular aggregation of extended β-sheet structure exists in the monolayer. This is possibly due to the relatively high amount of SP-C in the monolayer (~22 wt%), as compared to the physiologically relevant concentration of ~1 wt%. A previous IRRAS study has documented the presence of protein aggregation in highly enriched lipid/SP-C monolayers [28]. However, other more recent research suggests that monomeric α-helical SP-C is thermodynamically metastable, with the peptide irreversibly forming β-sheet aggregates resembling amyloid fibrils which may be implicated in pulmonary alveolar proteinosis [70, 71]. Therefore, the presence of several α-helix conformations as well as the β-aggregate bands in the 2D spectra may indicate an intermediate in the α to β conversion, which is known to be a slow, kinetically controlled process. This is the first time that specific IR evidence has demonstrated that multiple α-helix conformations as well as β-structure conformational intermediates exist for SP-C – containing monolayers at the A/W interface.

$\beta\nu$ Correlation Analysis of the SP-C Amide I Region

In addition its use in studying structural changes and making band assignments, 2D IR correlation spectroscopy has also been used to determine the temporal order of events that occur during the external sample perturbation. The basis for this determination is the relative signs of the asynchronous and synchronous cross peaks [62]. A positive asynchronous cross peak at (ν_1, ν_2) indicates that the intensity change at ν_1 occurs before ν_2; a negative cross peak at ν_1 is observed if the change occurs after ν_2. This rule, however, is reversed if the corresponding synchronous peak at (ν_1, ν_2) has a negative sign, *i.e.* $\Phi(\nu_1,\nu_2)<0$. While it is possible to determine the relative sequence of molecular rearrangements based on comparison of the signs of the cross peaks in the asynchronous *vs.* synchronous correlation maps, this procedure is

somewhat cumbersome, inherently qualitative in nature and leads to uncertainties for highly overlapped spectra.

In order to more quantitatively describe the degree of coherence between the observed spectral intensity changes and the sequence of molecular events in a discrete set of dynamic spectra, we have recently developed a modified 2D IR correlation method called $\beta\nu$ correlation analysis [51]. In this method an asynchronous cross-correlation is performed using a set of dynamically varying spectra, *i.e.* $y(\nu, n_j)$, against a mathematical function that approximates the functional form that the external perturbation induces on the IR spectral intensities. To date, we have employed a sin function, *e.g.* $\sin(k\phi + \beta)$. The resulting correlation intensities are a function of the spectral frequency (ν) and the phase angle (β) of the mathematical function. The maximum correlation intensity will be observed at one point (ν, β) in the correlation plot for the range $360 > \beta > 0$; this point is used to define a new parameter – the effective phase angle β_e of $f(\nu, \beta)$. The β_e value quantitatively reveals the degree of coherence between the experimental intensities and the sequence of molecular events in a discrete set of dynamic spectra. We recently applied $\beta\nu$ correlation analysis to surface pressure-induced changes in the IRRAS spectra of phospholipid monolayers at the A/W interface, and showed how the relative rates of acyl chain and methyl group reorientation could be quantitatively determined [52].

The $\beta\nu$ correlation plot for the amide I region of SP-C at low surface pressure (< 25 mN/m) is shown in Figure 3.5A. In addition, the values for the effective phase angle (β_e) and the band assignments for the peaks in this plot are presented in Table 3.1. It is immediately obvious from Figure 3.5A that the most intense peak in the $\beta\nu$ plot is observed at 1650 cm^{-1} and corresponds to the α-helix of SP-C. However, peaks due to β strands (1663 cm^{-1}) as well as to extended, aggregated β structures (1620 and 1682 cm^{-1}) are also apparent. (The peak at 1606 cm^{-1} is likely

due to a side chain vibration and is not included in this analysis.) It is also apparent from Figure 3.5A and Table 3.1 that each of the amide I peaks for SP-C at low surface pressures have nearly identical β_e values, with a standard error of less than 1% relative to the mean. These data confirm that all segments of the SP-C protein reorient at the identical relative rate when the surface pressure is increased up to 25 mN/m. The relative reorientation of SP-C secondary structure becomes more complicated at high surface pressures (25 – 40 mN/m), as illustrated in Figure 3.5B. As seen in Table 3.1, the β_e values at high pressures divide into three identifiable groups. The largest effective phase angle (indicative of the most rapid reorientation) is that of the 1656 cm^{-1} peak with β_e = 341.9, attributable to the high wavenumber α-helix conformation. The second group to reorient includes the peaks at 1687 cm^{-1} (β_e = 273.4), 1636 cm^{-1} (β_e = 270.9), and 1625 cm^{-1} (β_e = 263.5), all of which can be attributed to extended β sheet structures. Lastly, the third group to reorient at a much slower relative rate includes the peaks at 1678 cm^{-1} (β_e = 40.5), 1665 cm^{-1} (β_e = 43.0), and 1647 cm^{-1} (β_e = 53.2). The cross peaks in this group are associated with β turn/loop structures as well as the low wavenumber α-helix conformation. The $\beta\nu$ plot at high surface pressures (Figure 3.5B) shows that most of the correlation intensity of the two α-helix peaks is concentrated in the lower wavenumber peak at 1647 cm^{-1}, which is also the helix conformation that reorients the slowest.

A consideration of the 2D IR and β_e values for SP-C leads to the following model for protein reorientation. At low surface pressures, the protein exists in a variety of secondary structure conformations, most noticeably the predominate α-helix, but also including extended β-sheet structures. All conformations of the SP-C molecule react identically to increasing surface pressure and reorient in-phase with each other. Above 25 mN/m, however, the increasing surface pressure selectively affects the co-existing protein conformations and leads to an

Figure 3.5 $\beta\nu$ correlation plots derived from the monolayer IRRAS spectra of DPPG / SP-C (20:1, mol:mol, ~22 wt% SP-C). Spectra were divided into two pressure regions based on their autocorrelation intensities. $\beta\nu$ correlations were calculated on spectra contained within the pressure region. (A) 4.0 mN/m – 25.0 mN/m. (B) 25.0 mN/m – 40.0 mN/m.

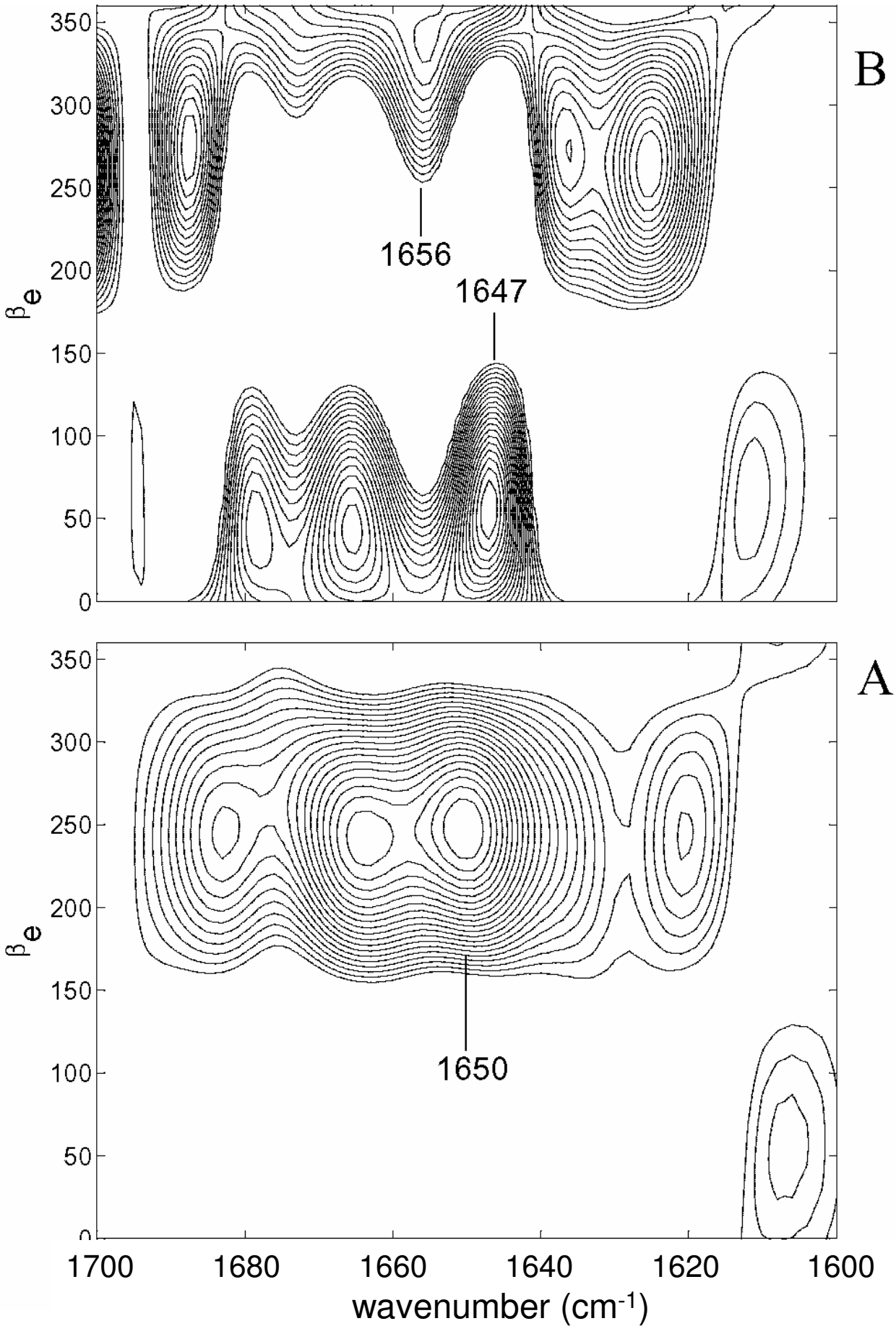
B
A
1656
1647
1650
β_e
350
300
250
200
150
100
50
0
1700
1680
1660
1640
1620
1600
wavenumber (cm^{-1})

Table 3.1

Effective phase angle, β_e, values calculated for DPPG/SP-C monolayer IRRAS spectra in amide I region. β_e values taken from the $\beta\nu$ 2D correlation plots for the DPPG/SP-C monolayer (Figure 3.5).

Wavenumber, cm^{-1}	β_e Value	Assignment
	Region A: 4.0 mN/m – 25.0 mN/m	
1682.8	244.8	β strand (aggregated)
1663.4	243.5	β turn/loop
1650.2	247.3	α helix
1620.4	244.8	β strands (aggregated)
1606.3	54.2	Side chain
	Region B: 25.0 – 40.0 mN/m	
1687.4	273.4	β strand (aggregated)
1678.3	40.5	β turn/loop
1665.4	43.0	β turn/loop
1655.9	341.9	α helix
1647.1	53.2	α helix
1636.0	270.9	β sheet
1625.1	263.5	β strand (aggregated)
1611.0	60.4	Side chain

independent reorientation of these protein subunits. The high wavenumber α-helix conformation reorients first, closely followed by the reorientation of the extended β structures, including that of the aggregated protein strands. The last protein reorientational motion to occur originates from the low wavenumber α-helix conformation as well as from β turn/loop and unordered structures, which are most likely due to very short protein fragments that link together the more ordered protein segments. The reorientation motion of this second helix conformation and the β turn/loop fragments lags significantly behind the reorientation rates of the other ordered (α and β) protein segments. As the majority of the $\beta\nu$ correlation intensity is concentrated in this second helix conformation, it is presumably this conformation that orients its helix axis towards the surface normal, as previously described [29].

It is possible that the selective reorientation of the two α-helix conformations plays a role in the SP-C – mediated formation of three-dimensional, surface-associated, lipid-protein structures at high surface pressures. Using microscopic techniques methods, these structures have been observed to be formed at high surface pressures when human recombinant or synthetic SP-C is incorporated in lipid monolayers [23, 72, 73]. While models have been proposed for the formation of these structures, the details of how SP-C facilitates their development is still unknown. However, reorientation of the α-helix is postulated to play a pivotal role.

2D IR Correlation Analysis of the SP-B Amide I Region

We have also used 2D correlation methods to study protein conformational changes in monolayers of DPPG/SP-B. In contrast to the DPPG/SP-C monolayers, the DPPG/SP-B samples were prepared at a 40:1 ratio (lipid:protein, mol:mol). Due to the higher molecular weight of SP-B, however, this mol ratio still equates to approximately 22 wt% protein in the monolayer. As described above, we have used a windowed autocorrelation method to divide the DPPG/SP-B

monolayer spectra into two separate regions for detailed analysis (Figure 3.2B). The autocorrelation method defines a low pressure regime (4 – 25 mN/m) and a high pressure regime (25 – 40 mN/m) for DPPG/SP-B monolayers, similar to the case of DPPG/SP-C.

The mature form of SP-B is a highly charged protein composed containing 79 amino acids of approximately 18 kD. A high percentage of these amino acids are cysteine, basic or hydrophobic residues. The protein exists as a disulfide-linked homodimer [74] and is expected to have several amphipathic α-helical segments on both the amino and carboxy-terminal ends [71]. In addition, each SP-B monomer contains three intramolecular disulfide bridges linking cysteines residues; a fourth disulfide bridge is responsible for the intermolecular dimerization. Evidence suggests that SP-B is not a transmembrane or trans-monolayer protein. IR results of lipid-protein vesicles [75] demonstrated that domains of SP-B are associated with the phospholipid headgroups while other domains are located inside the bilayer. Fluorescence anisotropy also determined that SP-B was not a transmembrane protein, but was associated with the membrane surface [76]. The polypeptide motif of the SP-B monomer is characterized by amphiphatic α-helices with solvent-associated hydrophilic side chains, while other hydrophobic conformations form a protein core stabilized by intramolecular disulfide bonds [77].

Figure 3.6 shows the 2D contour map for the synchronous correlation of the DPPG/SP-B IRRAS spectra, in both the low surface pressure regime below 25 mN/m (Figure 3.6A) as well as the high surface pressure region above 25 mN/m (Figure 3.6B). The synchronous map of the low pressure region (Figure 3.6A) is dominated by strong auto peaks at 1653 cm^{-1} and 1686 cm^{-1} with less intense auto peaks at 1640 cm^{-1} and 1625 cm^{-1}. Positive cross peaks are formed between the α-helix band at 1653 *vs*. 1640 and 1625 cm^{-1}. In addition, a number of positive cross peaks are formed between the β-structure bands at 1685 and 1676 cm^{-1} *vs*. 1653, 1640 and

1625 cm^{-1}. Negative cross peaks occur with the band at 1611 cm^{-1}. However, as in the case of SP-C, the peak at this wavenumber is most likely due to side chain vibrations unrelated to protein secondary structure.

The high surface pressure region (>25 mN/m) of the DPPG/SP-B monolayer presents a simpler correlation map than does the low pressure region since it is dominated by the major α-helical auto peak at 1653 cm^{-1} (Figure 3.6B). There are additional auto peaks at 1686, 1672 and 1621 cm^{-1} while positive cross peaks can be observed at wavenumber values 1653 *vs*. 1621 cm^{-1}, 1676 *vs*. 1653 and 1621 cm^{-1}, and 1685 *vs*. 1653 cm^{-1}.

The cross peaks seen in the 2D synchronous spectra of DPPG/SP-B are very similar in wavenumber to the synchronous cross peaks calculated for SP-C, indicating a high helical content for SP-B with contributions from β-sheet and unordered structure. These types of secondary structures have previously been observed in bulk phase IR studies of SP-B or the truncated N-terminal peptide of SP-B [75, 78]. Also evident in the 2D spectra are the 1620 / 1685 cm^{-1} bands attributable to extended β-aggregated structures. These extended β-structures bands have not been seen in either the previous bulk phase studies or the IRRAS studies of SP-B mentioned above. The synchronous 2D IR spectrum of SP-B mainly differs from that of SP-C in that for SP-B the 2D correlations become less numerous at high surface pressures and are dominated by the α-helix band at 1653 cm^{-1}.

Asynchronous 2D IR correlation maps were also calculated from the DPPG/SP-B IRRAS monolayer spectra. Figure 3.7 shows the 2D contour map for the asynchronous correlation of the DPPG/SP-B spectra, in both the low surface pressure regime below 25 mN/m (Figure 3.7A) as well as the high surface pressure region above 25 mN/m (Figure 3.7B). The asynchronous 2D IR

map of SP-B also indicates the presence of a heterogeneous secondary structure for this protein in the DPPG/SP-B monolayer film.

In the low pressure region (Figure 3.7A) several prominent cross peaks are observed that demonstrate the ability of asynchronous 2D IR to resolve overlapped peaks. Most noticeable is the fact that the prominent α-helix peak that occurs at 1653 cm^{-1} in the low pressure synchronous spectrum of SP-B (Figure 3.6A) splits into two components in the low pressure asynchronous spectrum (Figure 3.7A), one at 1656 and one at 1649 cm^{-1}. Both of these α-helix components generate asynchronous cross peaks at wavenumber values characteristic of other secondary structure conformations. For example, asynchronous cross peaks are seen between 1649 cm^{-1} and (1640, 1628, 1690, 1676 and 1656 cm^{-1}). The higher wavenumber α-helix component at 1656 cm^{-1} also generates cross peaks with (1682 and 1615 cm^{-1}). In addition, the extended β-sheet band observed at 1686 cm^{-1} in the low pressure synchronous spectrum also splits into lower and higher frequency components in the asynchronous spectrum (at 1682 and 1690 cm^{-1}, respectively). A number of additional prominent cross peaks are seen at 1640 cm^{-1}, characteristic of unordered structures. Cross peaks are observed between the extended β-sheet split components and other bands, including 1682 cm^{-1} and (1676, 1640, 1628 and 1690 cm^{-1}) and between 1690 cm^{-1} and (1615, 1624 and 1637 cm^{-1}).

The presence of two α-helix components in the 2D IR correlation spectrum for SP-B is consistent with previous IR results based on curve-fitting of the amide I region in the ATR spectra of bulk phase lipid / SP-B vesicles [75]. This previous study attributed two amide I band components to two separate populations of α-helix in SP-B – a hydrophobic fraction associated with the lipid chains and a hydrophilic fraction parallel to the membrane surface. Presumably, the more hydrophilic fraction would encounter stronger H-bond potential with the aqueous

Figure 3.6 Synchronous 2D IR correlation plots of the monolayer IRRAS spectra of DPPG / SP-B (20:1, mol:mol, ~22 wt% SP-B). Solid lines indicate regions of positive correlation intensity; dashed lines indicate regions of negative correlation intensity. Spectra were divided into two pressure regions based on their autocorrelation intensities. 2D IR synchronous correlations were calculated on spectra contained within the pressure region. The one-dimensional spectrum shown in this figure is the calculated average of the spectra used in the 2D analysis. (A) 4.0 mN/m – 25.0 mN/m. (B) 25.0 mN/m – 40.0 mN/m.

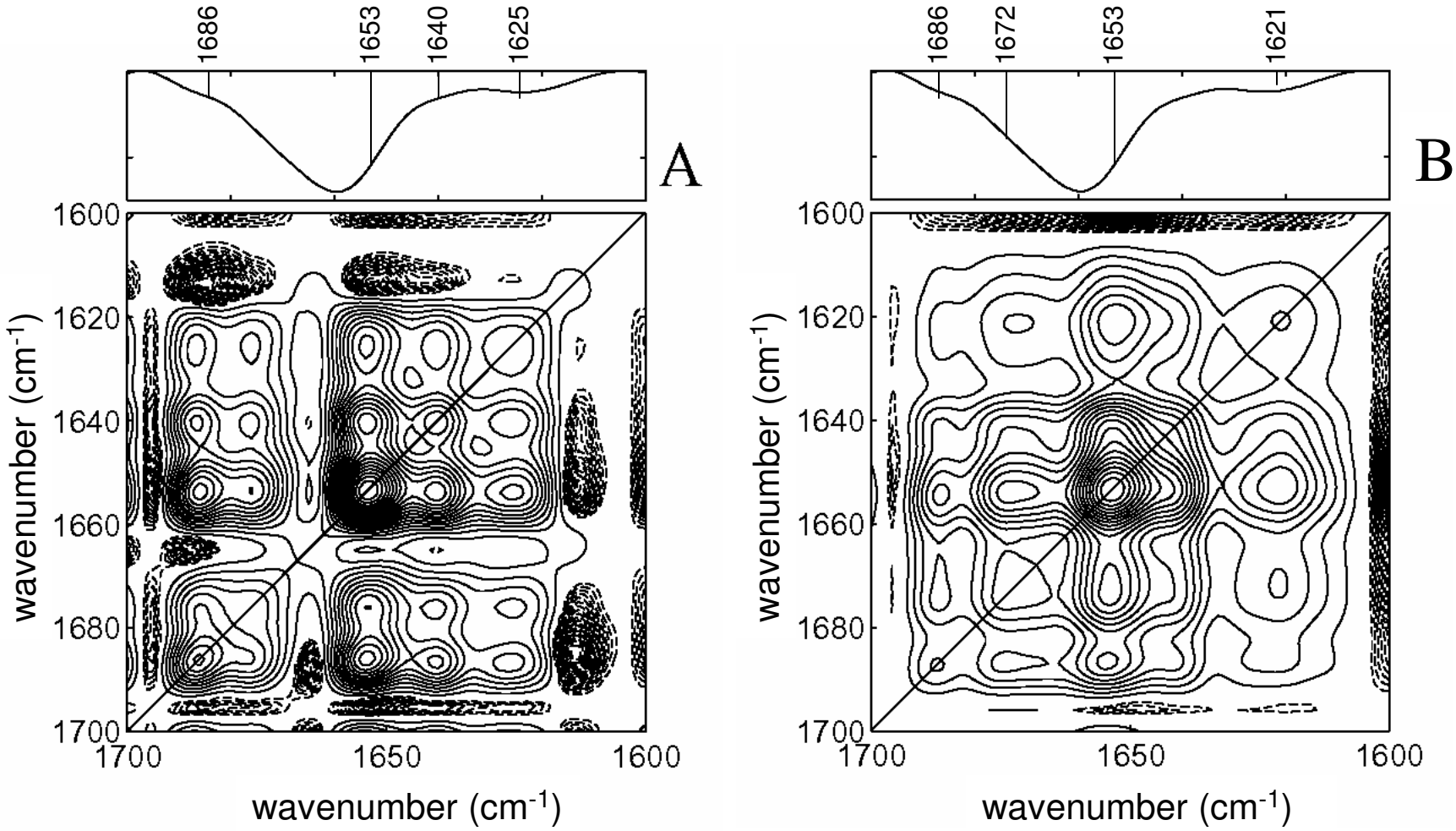
1686
1653
1640
1625
A
1600
1620
1640
1660
1680
1700
wavenumber (cm-1)
1700
1650
1600
wavenumber (cm-1)
1686
1672
1653
1621
B
1600
1620
1640
1660
1680
1700
wavenumber (cm-1)
1700
1650
1600
wavenumber (cm-1)

solvent thus slightly reducing its amide I frequency (*i.e.* the 1649 cm^{-1} peak is likely associated with the hydrophilic fraction). In Figure 3.7A, the distribution of correlation intensity between the two α-helix cross peaks indicates that the protein exists primarily in the 1656 cm^{-1} hydrophobic fraction at low surface pressures. This current study is the first time that two α-helix fractions have been observed for SP-B in monomolecular films at the A/W interface.

The asynchronous map for DPPG/SP-B reveals that the splitting of the α-helix band into two cross peaks persists in the high-pressure region above 25 mN/m (Figure 3.7B). However, the distribution of correlation intensity is reversed at high surface pressures. Above 25 mN/m, the main correlation intensity (as well as the sign of this cross peak) has shifted and is now concentrated in the 1649 cm^{-1} component. The asynchronous correlation of the two amide I components results in a number of cross peaks. The 1649 cm^{-1} α-helix band results in cross peaks with (1640 and 1628 cm^{-1}) while the 1656 cm^{-1} helix component shows cross peaks with 1649, 1634 and 1620 cm^{-1}. The extended β-sheet structure at 1690 cm^{-1} results in a long correlation intensity minimum with cross peaks at 1670, 1648 and 1620 cm^{-1}. Other prominent cross peaks are seen between 1676 cm^{-1} and (1670, 1648, 1634 and 1620 cm^{-1}) and between 1682 cm^{-1} and (1676, 1656 and 1640 cm^{-1}).

$\beta\nu$ Correlation Analysis of the SP-B Amide I Region

In order to quantitatively address how the different secondary structural components in SP-B respond with respect to increasing monolayer surface pressure, we have calculated the $\beta\nu$ correlation map for the IRRAS spectra of the DPPG/SP-B monolayer. The $\beta\nu$ plot for the amide I region of SP-B at low surface pressure (< 25 mN/m) is shown in Figure 3.8A with the band assignments for these peaks and the values for their effective phase angle (β_e) presented in Table 3.2. Figure 3.8A shows that the most intense peak in the low pressure $\beta\nu$ plot for SP-B is

observed at 1655 cm^{-1} and corresponds to the α-helix. The wavenumber value for this peak in the $\beta\nu$ plot indicates that it corresponds to the 1656 cm^{-1} α-helix cross peak seen in the asynchronous 2D IR correlation plot for SP-B (Figure 3.7); this α-helix asynchronous cross peak may be assigned to the hydrophobic helix fraction of SP-B. Peaks due to β structure (1628, 1676 and 1688 cm^{-1}) as well as to unordered structure (1640 cm^{-1}) are also apparent in the $\beta\nu$ plot. As was the case with SP-C at low pressure (Figure 3.5A and Table 3.1), it is clear from Figure 3.8A and Table 3.2 that each of the amide I peaks for SP-B at low surface pressures have nearly identical β_e values, in this case with a standard error of less than 3% relative to the mean. Thus, the same interpretation holds for SP-B as for SP-C at low surface pressure: all conformations of the SP-B protein reorient at the identical relative rate as the surface pressure is increased to 25 mN/m.

Figure 3.8B illustrates the relative reorientation of SP-B secondary structure at high surface pressures (25 – 40 mN/m). As detailed in Table 3.2, the $\beta\nu$ correlation peaks due to different SP-B secondary structures have nearly identical β_e values at high pressures, similar to the situation at low surface pressure. The most intense correlation peak for SP-B at high surface pressures is that of the 1648 cm^{-1} peak with β_e = 270.9, attributable to the α-helix. The wavenumber value for this peak in the $\beta\nu$ plot indicates that it corresponds to the 1649 cm^{-1} α-helix cross peak seen in the asynchronous 2D IR correlation plot for SP-B (Figure 3.7); this α-helix asynchronous cross peak may be assigned to the hydrophilic helix fraction of SP-B. Four other secondary structure $\beta\nu$ correlation peaks for SP-B at high surface pressures have nearly identical effective phase angles with the 1648 cm^{-1} helix peak (a standard error of less than 1% relative to the mean), indicating a nearly simultaneous reorientation for all protein segments. Theses peaks include 1682 cm^{-1} (β_e = 277.2), 1670 cm^{-1} (β_e = 274.7), 1634 cm^{-1} (β_e = 266.0), and

Figure 3.7 Asynchronous 2D IR correlation plots of the monolayer IRRAS spectra of DPPG / SP-B (40:1, mol:mol, ~22 wt% SP-B). Solid lines indicate regions of positive correlation intensity; dashed lines indicate regions of negative correlation intensity. Spectra were divided into two pressure regions based on their autocorrelation intensities. 2D IR asynchronous correlations were calculated on spectra contained within the pressure region. The one-dimensional spectrum shown in this figure is the calculated average of the spectra used in the 2D analysis. (A) 4.0 mN/m – 25.0 mN/m. (B) 25.0 mN/m – 40.0 mN/m.

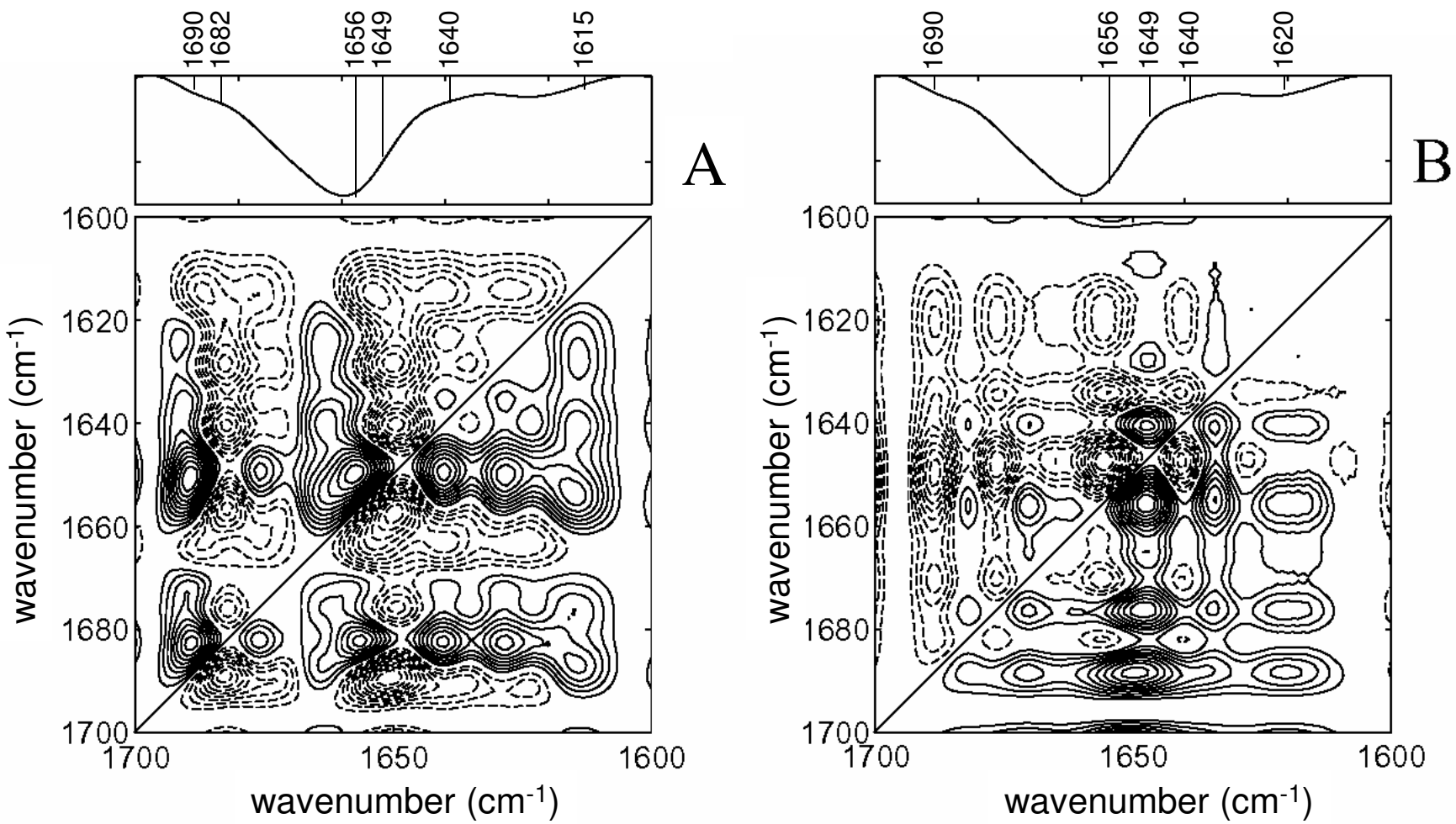
1690
1682
1656
1649
1640
1615
A
1600
1620
1640
1660
1680
1700
wavenumber (cm-1)
1700
1650
1600
wavenumber (cm-1)
1690
1656
1649
1640
1620
B
1600
1620
1640
1660
1680
1700
wavenumber (cm-1)
1700
1650
1600
wavenumber (cm-1)

Figure 3.8 $\beta\nu$ correlation plots derived from the monolayer IRRAS spectra of DPPG / SP-B (40:1, mol:mol, ~22 wt% SP-B). Spectra were divided into two pressure regions based on their autocorrelation intensities. $\beta\nu$ correlations were calculated on spectra contained within the pressure region. (A) 4.0 mN/m – 25.0 mN/m. (B) 25.0 mN/m – 40.0 mN/m.

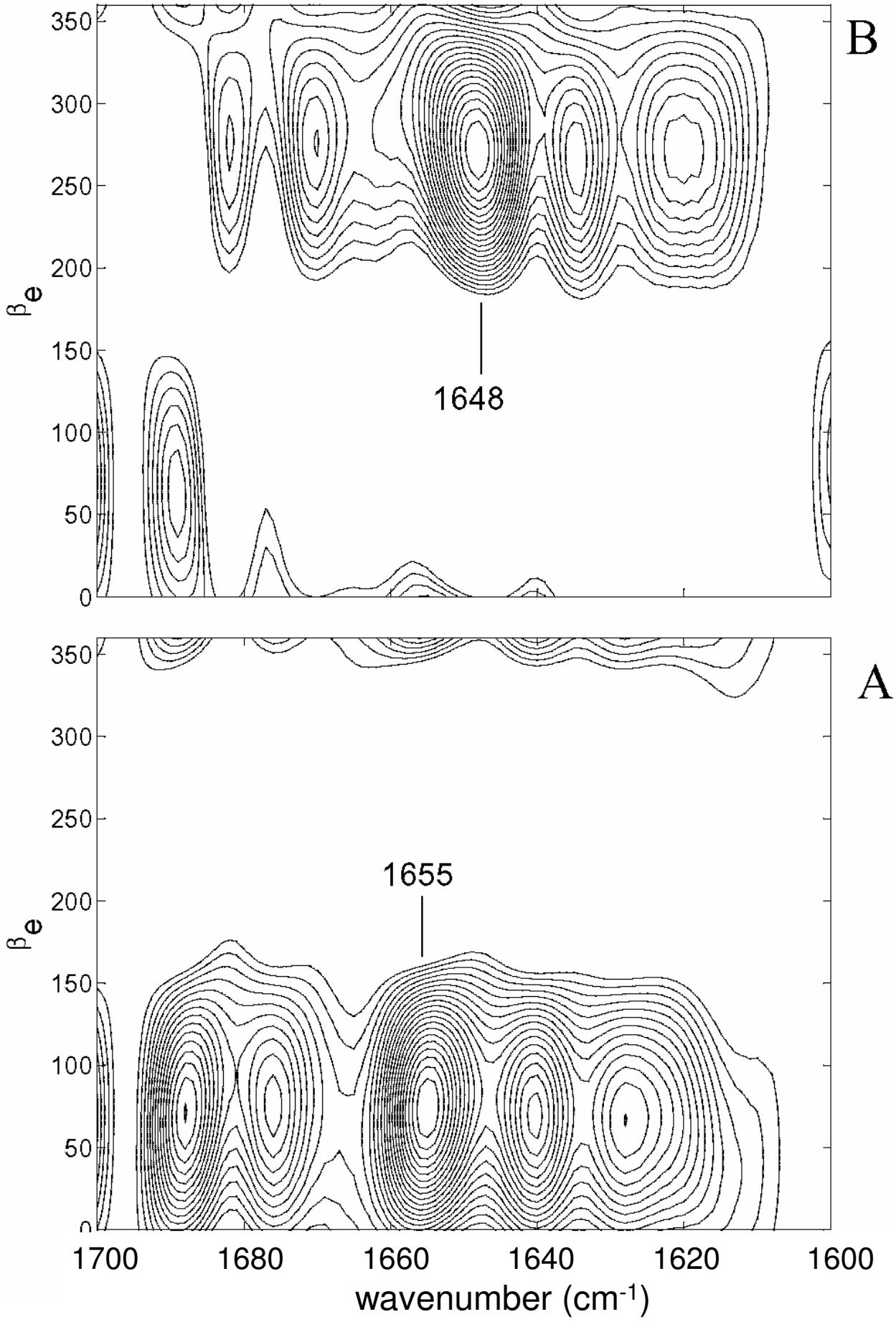
B
A
1648
1655
β_e
β_e
350
300
250
200
150
100
50
0
1700
1680
1660
1640
1620
1600
wavenumber (cm^{-1})

Table 3.2

Effective phase angle, β_e, values calculated for DPPG/SP-B monolayer IRRAS spectra in amide I region. β_e values taken from the $\beta\nu$ 2D correlation plots for the DPPG/SP-B monolayer (Figure 3.8).

Wavenumber, cm^{-1}	β_e Value	Assignment
	Region A: 4.0 mN/m – 25.0 mN/m	
1688.0	69.1	β strand (aggregated)
1676.2	75.4	β turn/loop
1654.8	74.1	α helix
1640.4	69.1	Unordered
1627.7	65.4	β strand (aggregated)
	Region B: 25.0 – 40.0 mN/m	
1689.1	62.9	β strand (aggregated)
1681.8	277.2	β turn/loop
1670.0	274.7	β turn/loop
1648.0	270.9	α helix
1634.5	266.0	β sheet
1620.0	272.2	β strands (aggregated)

1620 cm^{-1} (β_e = 272.2), all of which can be attributed to β sheet structures. A correlation peak at 1689 cm^{-1} (β_e = 62.9) is the only peak that does not fit this pattern; it reflects an extended β structure that reorients at a much slower relative rate than all the other protein segments in SP-B.

The 2D IR and $\beta\nu$ correlation methods lead to the following model for SP-B reorientation. At low surface pressures, SP-B is dominated by an α-helix secondary structure, however, the helix exists in two separate but co-existing conformations, one hydrophobic and one hydrophilic. While both helix conformations co-exist at low surface pressure, the hydrophobic conformation predominates. SP-B also has significant contributions from extended β-sheet and unordered structures. With increasing surface pressure, all conformations of the SP-B protein react identically and reorient in-phase with each other. Above 25 mN/m, however, the intensity of the helix bands shifts and the correlations are dominated by the α-helix band characteristic of the hydrophilic helix conformation. Both the 2D and $\beta\nu$ correlations detect the change in correlation intensity of the SP-B helix fractions with increasing surface pressure. Above 25 mN/m, β-sheet and unordered structures persist, but their correlation intensities decrease, leaving the hydrophilic α-helix as the dominant conformation. All SP-B conformations react identically to increasing surface pressure, leading to a reorientation of the protein subunits in-phase with one another. The one exception to this concerted reorientation is that of an isolated extended β structure peak, which lags significantly behind the reorientation rates of the other protein segments. The conservation of secondary structure and in-phase reorientation of the entire protein throughout all surface pressures is likely due to the stabilization of the SP-B protein core by its intramolecular disulfide bonds [77].

Conclusions

Using *in-situ* IR spectroscopy at the A/W interface, we have investigated the conformational intermediates that exist in the hydrophobic surfactant proteins SP-B and SP-C in lipid-protein monolayers. To accomplish this, we have applied 2D IR and $\beta\nu$ correlation spectroscopy to the analysis of the protein amide I vibrations. The results described here have identified specific protein conformations and followed the reorientation of these protein conformations as a function of increasing surface pressure. Our conclusions are as follows.

- The surface pressure regimes that encompassed the greatest variation in amide I spectral intensity were identified using a statistical approach based on a windowed autocorrelation method. These regions were located by adapting a dynamic filtering technique that auto correlates IR intensities within a defined surface pressure window and plots them against the average surface pressure, thereby locating the regions of maximal spectral variation. For both SP-B and SP-C, this autocorrelation method defined two separate surface pressure regions that produced maximum amide I intensity changes: 4 – 25 mN/m and 25 – 40 mN/m. 2D IR and $\beta\nu$ correlation analyses were performed solely within these regions to establish the structural or temporal relationships that contributed to the spectral variations.

- Multiple cross peaks observed in the 2D IR correlation spectra demonstrate that SP-C is comprised of a heterogeneous secondary structure, including α-helix, β-sheet, and an intermolecular aggregation of extended β-sheet structure. The asynchronous spectrum shows that the main α-helix band splits into two peaks at high surface pressures, indicating two different helix conformations exist for SP-C. This is the first IR evidence that multiple α-helix conformations as well as β-structure conformational

intermediates exist for SP-C – containing monolayers at the A/W interface. At low surface pressures, SP-C exists in a variety of secondary structure conformations, most noticeably the predominate α-helix, but also including extended β-sheet structures. All conformations of the SP-C molecule react identically to increasing surface pressure and reorient in-phase with each other. Above 25 mN/m, however, the increasing surface pressure selectively affects the co-existing protein conformations and leads to an independent reorientation of the protein subunits. The higher wavenumber α-helix conformation reorients first, closely followed by that of the extended β structures, including that of the aggregated protein strands. The slowest protein motion originates from the dominant α-helix conformation as well as from β turn/loop structures. It is possible that the independent reorientation of the two α-helix conformations plays a role in the SP-C – mediated formation of three-dimensional, surface-associated, lipid-protein structures.

- The 2D synchronous spectra of DPPG/SP-B indicate a high α-helical content for SP-B with contributions from β-sheet and unordered structure. The asynchronous 2D IR spectrum of SP-B shows that the prominent α-helix peak occuring at 1653 cm^{-1} in the synchronous spectrum splits into two components, one at 1656 and one at 1649 cm^{-1}. The presence of two α-helix components in the 2D IR correlation spectrum for SP-B is consistent with two separate populations of α-helix in SP-B – a hydrophobic fraction associated with the lipid chains and a hydrophilic fraction parallel to the membrane surface. This is the first study to demonstrate the presence of two α-helical components of SP-B in monomolecular films in monomolecular films at the A/W interface. The distribution of correlation intensity between the two α-helix cross peaks indicates that the

protein exists primarily in the hydrophobic fraction at low surface pressures. The splitting of the α-helix band into two cross peaks persists in the high-pressure region above 25 mN/m. However, at high surface pressures the correlation intensity of the helix bands reverses and the 2D spectra are dominated by the α-helix band characteristic of the hydrophilic helix conformation. Both the 2D and $\beta\nu$ correlations detect the change in correlation intensity of the amide I α-helix bands with increasing surface pressure. With increasing surface pressure, all conformations of the SP-B protein react identically and reorient in-phase with each other. Above 25 mN/m, β-sheet and unordered structures persist, but their correlation intensities decrease, leaving the hydrophilic α-helix as the dominant conformation. The conservation of protein secondary structure and in-phase reorientation of the entire protein throughout all surface pressures is likely due to the stabilization of the protein core by intramolecular disulfide bonds.

Acknowledgements

The work described here was supported by the U.S. Public Health Service through National Institutes of Health grant GM40117 (R.A.D.).

References:

1. Notter, R.H., *Lung surfactants: basic science and clinical applications*. 2000, New York: Marcel Dekker, Inc.
2. Creuwels, L.A.J.M., L.M.G. van Golde, and H.P. Haagsman, *The pulmonary surfactant system: biochemical and clinical aspects.* Lung, 1997. **175**: p. 1-39.
3. Hunt, A.N., F.J. Kelly, and A.D. Postle, *Developmental variation in whole human lung phosphatidylcholine molecular species: a comparision of guinea pig and rat.* Early Hum. Develop., 1991. **25**: p. 157-171.
4. Kahn, M.C., et al., *Phosphotidylcholine molecular species of calf lung surfactant.* Am. J. Physiol., 1995. **13**: p. L567-L573.
5. Holm, B.A., et al., *Content of dipalmitoyl phosphatidylcholine in lung surfactant: ramifications for surface activity.* Pediatr. Res., 1996. **39**: p. 805-811.
6. Hawgood, S. and K. Schiffer, *Structures and properties of the surfactant-associated proteins.* Annu. Rev. Physiol., 1991. **53**: p. 375-394.
7. Johansson, J., T. Curstedt, and B. Robertson, *The proteins of the surfactant system.* Eur. Respir. J., 1994. **7**: p. 372-391.
8. Avery, M.E. and J. Mead, *Surface properties in relation to atelectasis and hyaline memrane disease.* Am. J. Dis. Child., 1959. **97**: p. 517-523.
9. Pison, U., et al., *Surfactant abnormalities in patients with respiratory failure after multiple trauma.* Am. Rev. Respir. Dis., 1989. **140**: p. 1033-1039.
10. Notter, R.H. and Z. Wang, *Pulmonary surfactant: physical chemistry, physiology and replacement.* Rev. Chem. Eng., 1997. **13**: p. 1-118.

11. Lewis, J.F. and A.H. Jobe, *Surfactant and the adult respiratory distress syndrome.* Am. Rev. Respir. Dis., 1993. **147**: p. 218-233.

12. Notter, R.H., *Surface chemistry of pulmonary surfactant: The role of individual components,* in *Pulmonary Surfactant*, B. Robertson, L.G.M. van Golde, and J.J. Battenburg, Editors. 1984, Elsevier: Amsterdam. p. 17-53.

13. Oosterlaken-Dijksterhuis, M.A., et al., *Characterization of lipid insertion into monomolecular layers mediated by lung surfactant pProteins SP-B and SP-C.* Biochemistry, 1991. **30**: p. 10965-10971.

14. Taneva, S. and K.M.W. Keough, *Pulmonary surfactant proteins SP-B and SP-C in spread monolayers at the air-water interface: III. Proteins SP-B plus SP-C with phospholipids in spread monolayers.* Biophys. J., 1994. **66**(4): p. 1158-66.

15. Taneva, S. and K.M.W. Keough, *Pulmonary surfactant proteins SP-B and SP-C in spread monolayers at the air-water interface: II. Monolayers of pulmonary surfactant protein SP-C and phospholipids.* Biophys. J., 1994. **66**(4): p. 1149-57.

16. Taneva, S. and K.M.W. Keough, *Pulmonary surfactant proteins SP-B and SP-C in spread monolayers at the air-water interface: I. Monolayers of pulmonary surfactant protein SP-B and phospholipids.* Biophys. J., 1994. **66**(4): p. 1137-48.

17. Wang, Z., et al., *Differential activity and lack of synergy of lung surfactant proteins SP-B and SP-C in interactions with phospholipids.* J. Lipid Res., 1996. **37**: p. 1749-1760.

18. Tchoreloff, P., et al., *A structural study of interfacial phospholipid and lung surfactant layers by transmission electron microscopy after Blodgett sampling: influence of surface pressure and temperature.* Chem. Phys. Lipids, 1991. **59**: p. 151-165.

19. Discher, B.M., et al., *Phase separation in monolayers of pulmonary surfactant phospholipids at the air-water interface: composition and structure.* Biophys. J., 1999. **77**: p. 2051-2061.

20. Krüger, P., et al., *Effect of hydrophobic surfactant peptides SP-B and SP-C on Binary Phospholipid Monolayers. I. Fluorescence and dark-field microscopy.* Biophys. J., 1999. **77**: p. 903-914.

21. Ding, J., et al., *Effects of lung surfactant proteins, SP-B and SP-C, and palmitic acid on monolayer stability.* Biophys. J., 2001. **80**: p. 2262-2272.

22. Takamoto, D.Y., et al., *Interaction of lung surfactant proteins with anioinic phospholipids.* Biophys. J., 2001. **81**: p. 153-169.

23. Kramer, A., et al., *Distribution of the surfactant-associated protein C within a lung surfactant model film investigated by near-field optical microscopy.* Biophys. J., 2000. **78**(1): p. 458-465.

24. Krol, S., et al., *Structure and function of surfactant protein B and C in lipid monolayers: a scanning force microscopy study.* Physi. Chem. Chem. Phys., 2000. **2**(20): p. 4586-4593.

25. Mendelsohn, R., J.W. Brauner, and A. Gericke, *External infrared reflection-absorption spectrometry. Monolayer films at the air-water interface.* Ann. Rev. Phys. Chem., 1995. **46**: p. 305-334.

26. Dluhy, R.A., *Infrared spectroscopy of biophysical monolayer filims at interfaces. Theory and applications*, in *Physical Chemistry of Biological Interfaces*, A. Baszkin and W. Norde, Editors. 2000, Marcel Deker: New York. p. 711-747.

27. Dluhy, R.A., et al., *Infrared spectroscopic investigations of pulmonary surfactant. Surface film transitions at the air-water interface and bulk phase thermotropism.* Biophys. J., 1989. **56**(6): p. 1173-1181.

28. Pastrana-Rios, B., et al., *External reflection absorption infrared spectroscopy study of lung surfactant proteins SP-B and SP-C in phospholipid monolayers at the air/water interface.* Biophys. J., 1995. **69**(6): p. 2531-2540.

29. Gericke, A., C.R. Flach, and R. Mendelsohn, *Structure and orientation of lung surfactant SP-C and L-α-dipalmitoylphosphatidylcholine in aqueous monolayers.* Biophys. J., 1997. **73**(1): p. 492-499.

30. Flach, C.R., et al., *Palmitoylation of lung surfactant protein SP-C alters surface thermodynamics, but not protein secondary structure or orientation in 1,2-dipalmitoylphosphatidylcholine Langmuir films.* Biochim. Biophys. Acta, 1999. **1416**(1-2): p. 11-20.

31. Noda, I., *Recent developments in two-dimensional infrared (2D IR) correlation spectroscopy.* Appl. Spectrosc., 1993. **47**(9): p. 1317-1323.

32. Noda, I., *Two-dimensional infrared (2D IR) spectroscopy: theory and applications.* Appl. Spectrosc., 1990. **44**: p. 550-554.

33. Harrington, P.d.B., A. Urbas, and P.J. Tandler, *Two-dimensional correlation analysis.* Chemometrics and Intelligent Laboratory Systems, 2000. **50**(2): p. 149-174.

34. Noda, I., et al., *Generalized two-dimensional correlation spectroscopy.* Appl. Spectrosc., 2000. **54**(7): p. 236A-248A.

35. Ozaki, Y. and I. Noda, eds. *Two-Dimensional Correlation Spectroscopy*. AIP Conference Proceedings. Vol. 503. 2000, American Institute of Physics: New York.

36. Noda, I., G.M. Story, and C. Marcott, *Pressure-induced transitions of polyethylene studied by two-dimensional infrared correlation spectroscopy.* Vib. Spectrosc., 1999. **19**(2): p. 461-465.

37. Filosa, A., et al., *Two-Dimensional Infrared Correlation Spectroscopy as a Probe of Sequential events in the Thermal Unfolding of Cytochromes C.* Biochemistry, 2001. **40**(28): p. 8256-8263.

38. Paquet, M.J., et al., *Two-dimensional infrared correlation spectroscopy study of the aggregation of cytochrome C in the presence of dimyristoylphosphatidylglycerol.* Biophys. J., 2001. **81**(1): p. 305-312.

39. Schultz, C.P., O. Barzu, and H.H. Mantsch, *Two-dimensional infrared correlation analysis of protein unfolding: use of spectral simulation to validate structural changes during thermal denaturation of bacterial CMP kinases.* Appl. Spectrosc., 2000. **54**(7): p. 931-938.

40. Wang, Y., et al., *Two-dimensional Fourier transform near-infrared spectroscopy study of heat denaturation of ovalbumin in aqueous solution.* J. Phys. Chem. B, 1998. **102**: p. 6655-6662.

41. Sefara, N.L., N.P. Magtoto, and H.H. Richardson, *Structural characterization of β-lactoglobulin in solution using two-dimensional FT mid-infrared and FT near-infrared correlation spectroscopy.* Appl. Spectrosc., 1997. **51**(4): p. 536-540.

42. Ismoyo, F., Y. Wang, and A.A. Ismail, *Examination of the effect of heating on the secondary structure of avidin and avidin-biotin complex by resolution-enhanced two-dimensional infrared correlation spectroscopy.* Appl. Spectrosc., 2000. **54**(7): p. 939-947.

43. Graff, D.K., et al., *The effects of chain length and thermal denaturation on helix-forming peptides: a mode-specific analysis using 2D FT-IR.* J. Am. Chem. Soc., 1997. **119**: p. 11282-11294.

44. Nabet, A. and M. Pezolet, *Two-dimensional FT-IR spectroscopy: a powerful method to study secondary structure of proteins using H-D exchange.* Appl. Spectrosc., 1997. **51**(4): p. 466-469.

45. Murayama, K., et al., *Two-dimensional/attenuated total reflection infrared correlation spectroscopy studies on secondary structural changes in human serum albumin in aqueous solutions: pH-dependent structural changes in the secondary structures and in the hydrogen bondings of side chains.* J. Phys. Chem. B, 2001. **105**: p. 4763-4769.

46. Murayama, K., et al., *Two-dimensional/attenuated total reflection infrared correlation spectroscopy studies on secondary structural changes in human serum albumin in aqueous solutions: pH-dependent structural changes in the secondary structures and in the hydrogen bondings of side chains.* J. Phys. Chem. B, 2001. **105**(20): p. 4763-4769.

47. Pancoska, P., J. Kubelka, and T.A. Keiderling, *Novel use of a static modification of two-dimensional correlation analysis. Part I. Comparision of the secondary structure sensitivity of electronic circular dichroism, FT-IR, and Raman spectra of proteins.* Appl. Spectrosc., 1999. **53**(6): p. 655-665.

48. Kubelka, J., P. Pancoska, and T.A. Keiderling, *Novel use of a static modification of two-dimensional correlation analysis. Part II: Heterospectral correlations of protein, Raman, FT-IR and circular dichroism spectra.* Appl. Spectrosc., 1999. **53**(6): p. 666-671.

49. Elmore, D.L. and R.A. Dluhy, *Application of 2D IR correlation analysis to phase transitions in Langmuir monolayer films.* Colloids and Surfaces A, 2000. **171**(1-3): p. 225-239.

50. Elmore, D.L. and R.A. Dluhy, *Pressure-dependent changes in the infrared C-H vibrations of monolayer films at the air/water interface revealed by two- dimensional infrared correlation spectroscopy.* Appl. Spectrosc., 2000. **54**(7): p. 956-962.

51. Elmore, D.L. and R.A. Dluhy, *$\beta\nu$ correlation analysis: a modified two-dimensional infrared correlation method for determining relative rates of intensity change.* J. Phys. Chem. B, 2001. **105**: p. 11377-11386.

52. Elmore, D.L., S. Shanmukh, and R.A. Dluhy, *A study of binary phospholipid mixtures at the air-water interface using infrared reflection-absorption spectroscopy and 2D-IR $\beta\nu$ correlation analysis.* J. Phys. Chem. A, 2002: p. In Press.

53. Baatz, J.E., et al., *High yield purification of lung surfactant proteins SP-B and SP-C and the effects on surface activity.* Protein Express. Purificat., 2001. **23**(1): p. 180-190.

54. Shin, Y.S., *Spectrophotometric ultramicrodetermination of inorganic phosphorus and lipid phosphorus in serum.* Anal. Chem., 1962. **34**(9): p. 1164-1166.

55. Morrissey, J.H., *Silver stain for proteins in polyacrylamide gels: a modified procedure with enhanced uniform sensitivity.* Anal. Biochem., 1981. **117**: p. 307-310.

56. Chen, P.S., T.Y. Toriba, and H. Warner, *Microdetermination of phosphorous.* Anal. Chem., 1956. **28**: p. 1756-1758.

57. Berry, R.J. and Y. Ozaki, *Investigation into the effect of instrumental parameters in two-dimensional correlation spectroscopy.* Appl. Spectrosc., 2001. **55**(8): p. 1092-1098.

58. Cameron, D.G., J.K. Kauppinen, and D. Moffatt, *Precision in condensed phase vibrational spectroscopy.* Appl. Spectrosc., 1982. **36**(3): p. 245-50.

59. Noda, I., *Determination of two-dimensional correlation spectra using the Hilbert Transform.* Appl. Spectrosc., 2000. **54**(7): p. 994-999.

60. Dluhy, R.A., *Quantitative external reflection infrared spectroscopic analysis of insoluble monolayers spread at the air-water interface.* J. Phys. Chem., 1986. **90**: p. 1373-1379.

61. Thomas, M. and H.H. Richardson, *Two-dimensional FT-IR correlation analysis of the phase transition in a liquid crystal, 4'-n-octyl-4-cyanobiphenyl (8CB).* Vib. Spectrosc., 2000. **24**: p. 137-146.

62. Noda, I., *Generalized two-dimensional correlation method applicable to infrared, Raman, and other types of spectroscopy.* Appl. Spectrosc., 1993. **47**: p. 1329-1336.

63. Johansson, J., et al., *The NMR structure of the pulmonary surfactant-associated polypeptide SP-C in an apolar solvent contains a valyl-rich α-helix.* Biochemistry, 1994. **33**: p. 6015-6023.

64. Surewicz, W.K., H.H. Mantsch, and D. Chapman, *Determination of protein secondary structure by Fourier transform infrared spectroscopy: a critical assessment.* Biochemistry, 1993. **32**: p. 7720-7726.

65. Goormaghtigh, E., V. Cabiaux, and J.-M. Ruysschaert, *Determination of soluble and membrane protein structure by Fourier transform infrared spectroscopy. I. Assignments and model compounds*, in *Physiochemical Methods in the Study of Biomembranes*, H.J. Hilderson and G.B. Ralston, Editors. 1994, Plenum Press: New York. p. 329-362.

66. Jackson, M. and H.H. Mantsch, *The use and misuse of FTIR spectroscopy in the determination of protein structure.* Crit. Rev. Biochem. Mol. Biol., 1995. **30**: p. 95-120.

67. Byler, D.M. and H. Susi, *Examination of the secondary structure of proteins by deconvolved FTIR spectra.* Biopolymers, 1986. **25**: p. 469-487.

68. Kubelka, J. and T.A. Keiderling, *Differentiation of β-sheet-forming structures: ab initio-based simulations of IR absorption and vibrational CD for model peptides and protein β-sheets.* J. Am. Chem. Soc., 2001. **123**: p. 12048-12058.

69. Khurana, R. and A.L. Fink, *Do parallel b-helix proteins have a unique Fourier transform infrared spectrum?* Biophys. J., 2000. **78**: p. 994-1000.

70. Szyperski, T., et al., *Pulmonary surfactant-associated polypeptide C in a mixed organic solvent transforms from a monomeric a-helical state into insoluble b-sheet aggregates.* Protein Sci., 1998. **7**: p. 2533-2540.

71. Gustafsson, M., et al., *Amyloid fibril formation by pulmonary surfactant protein C.* FEBS Letters, 1999. **464**: p. 138-142.

72. Galla, H.J., et al., *The role of pulmonary surfactant protein C during the breathing cycle.* Thin Solid Films, 1998. **329**: p. 632-635.

73. Bourdos, N., et al., *Analysis of lung surfactant model systems with time-of-flight secondary ion mass spectrometry.* Biophys. J., 2000. **79**(1): p. 357-369.

74. Hawgood, S., et al., *Nucleotide and amino acid sequences of pulmonary surfactant protein SP 18 and evidence for cooperation between SP 18 and SP 28-36 in surfactant lipid adsorption.* Proc. Natl. Acad. Sci. U. S. A., 1987. **84**(1): p. 66-70.

75. Vandenbussche, G., et al., *Secondary structure and orientation of the surfactant protein SP-B in a lipid environment: a Fourier transform infrared spectroscopy study.* Biochemistry, 1992. **31**: p. 9169-9176.

76. Baatz, J.E., B. Elledge, and J.A. Whitsett, *Surfactant protein SP-B induces ordering at the surface of model membrane bilayers.* Biochemistry, 1990. **29**: p. 6714-6720.

77. Hawgood, S., M. Derrick, and P. Poulain, *Structure and properties of surfactant protein B.* Biochim. Biophys. Acta, 1998. **1408**: p. 150-160.

78. Gordon, L.M., et al., *Conformational mapping of the N-terminal segment of surfactant protein B in lipid using ^{13}C-enhanced Fourier transform infrared spectroscopy.* J. Peptide Res., 2000. **55**(4): p. 330-347.

CHAPTER 4

DEACYLATED PULMONARY SURFACTANT PROTEIN SP-C TRANSFORMS FROM α-HELICAL TO AMYLOID FIBRIL STRUCTURE VIA A pH-DEPENDENT MECHANISM. AN IR STRUCTURAL INVESTIGATION.[†]

[†] Shanmukh, S. (co-author), Dluhy R.A., Leapard, B.L., Kruger, P. and Baatz, J.E. 2003. Biophysical Journal. 85(4): 2417-2429
Reprinted here with the permission of the publisher

Abstract

Bovine pulmonary surfactant protein C (SP-C) is a hydrophobic, α-helical membrane-associated lipoprotein in which cysteines C4 and C5 are acylated with palmitoyl chains. Recently, it has been found that the α-helix form of SP-C is metastable, and under certain circumstances may transform from an α-helix to a β-strand conformation that resembles amyloid fibrils. This transformation is accelerated when the protein is in its deacylated form (dSP-C). We have used IR spectroscopy to study the structure of dSP-C in solution and at membrane interfaces. Our results show that dSP-C transforms from an α-helical to an β-type amyloid fibril structure via a pH-dependent mechanism. In solution at low pH, dSP-C is α-helical in nature, but converts to an amyloid fibril structure composed of short β-strands or β-hairpins at neutral pH. The α-helix structure of dSP-C is fully recoverable from the amyloid β-structure when the pH is once again lowered. Attenuated total reflectance (ATR) IR spectroscopy of lipid-protein monomolecular films showed that the fibril β-form of dSP-C is not surface-associated at the air-water interface. In addition, the lipid-associated α-helix form of dSP-C is only retained at the surface at low surface pressures and dissociates from the membrane at higher surface pressures. *In-situ* polarization modulation infrared spectroscopy (PM-IRRAS) of protein and lipid-protein monolayers at the air-water interface confirmed that the residual dSP-C helix conformation observed in the ATR-IR spectra of transferred films is randomly or isotropically oriented prior to exclusion from the membrane interface. This work identifies pH as one of the mechanistic causes of amyloid fibril formation for dSP-C, and a possible contributor to the pathogenesis of pulmonary alveolar proteinosis.

Introduction

Mammalian pulmonary surfactant is a highly specialized substance that contains approximately 85% phospholipid, 7-10% protein, and 4-8% neutral lipid [1, 2]. The most abundant phospholipid class is phosphocholine, while anionic phospholipids including phosphoglycerols make up about 10-15% of lung surfactant phospholipids [3-5]. Lung surfactant also contains four apoproteins, including two small hydrophobic proteins (SP-B and SP-C) that are known to enhance the adsorption and dynamic film behavior of phospholipids [1, 2, 6, 7]. The lack of surfactant in the under-developed lungs of premature infants is the root cause of neonatal respiratory distress syndrome (RDS) [8], while disruption of surfactant activity is linked to the pathophysiology of clinical lung damage seen in acute respiratory distress Syndrome (ARDS) [9-11].

Mature bovine surfactant protein C (SP-C) is secreted by type II epithelial cells into the alveoli in a complex mixture of surfactant lipids and proteins. Bovine SP-C consists of 34 amino acids and is an extremely hydrophobic, predominately α-helical protein of approximately 4.0 kD with charged amino acids (K10 and R11) near its N terminus. The cysteines C4 and C5 are acylated with C-16 (palmitoyl) chains in bovine SP-C. The NMR structure in apolar solvent describes the valine-, leucine- and isoleucine-rich region of this small protein as a rigid rod in which only a few residues near the N terminus (L1 – P7) and the C terminus are *not* helical [12]. The length of this helix (V8 – G34) is ~ 39 Å with a diameter is of ~ 12 Å.

SP-C is associated with enhanced readsorption of phospholipids to the surfactant lipid monolayer at the air-water interface during monolayer expansion (the *in-vitro* equivalent to inhalation) [1]. It also appears to play a role in the formation of three-dimensional layers of surfactant during compression of the monolayer through a mechanism whereby SP-C assists in

transfer of lipids from the monolayer to form stacked multilayer structures. Using *ex-situ* microscopy methods, the SP-C - dependent formation of membrane adherent particles has been demonstrated at high surface pressures [13-15], and a model for the formation of multibilayer phospholipid reservoirs, stabilized by SP-C, has been proposed [15, 16]. Research from this laboratory has demonstrated that SP-C also catalyzes the formation of micrometer-sized, surface-associated, 3D particles at the interface, as visualized using scattered light dark-field microscopy with grazing incidence laser illumination [17, 18].

These microscopy studies have been complemented by IR spectroscopic studies at the air-water interface that are able to study the secondary structure of proteins in monolayers and thin films [19, 20]. External reflectance IR has the sensitivity required to observe the amide I vibration of the SP-C protein in pure or highly enriched lipid-protein films and obtain protein structural information. This reflection IR technique has been applied to the study of monolayer films of extracted lung preparations [21] and more recently, to investigate the structure-function relationships of the lung surfactant proteins SP-B and SP-C in lipid monolayers [22-27].

These previous IR studies have confirmed the predominately α-helical nature of fully acylated SP-C at the air-water interface, and showed how this structural motif is optimized to interact with the monolayer phospholipids. Lately, however, a different picture has emerged that suggests that the α-helix is not the final, stable structure previously described for SP-C, and that other structural intermediates are available to the SP-C molecule. For example, under certain conditions, SP-C has been shown to transform from a monomeric α-helix to an aggregated β-sheet conformation [28]. This $\alpha \rightarrow \beta$ conversion results in protein aggregates that visually resemble amyloid fibrils [29]. It has previously been reported that amyloid fibrils composed of SP-C occur in pulmonary alveolar proteinosis (PAP), a disease in which lipid-protein aggregates

accumulate in the alveoli [30]. In particular, the deacylation of SP-C has been shown to increase the rate of peptide aggregation and fibril formation, presumably by destabilization of the α-helix with a concomitant increase in β-aggregation [31]. These studies suggest that α-helical SP-C is actually a metastable intermediate that may convert to β-aggregate and fibril forms, depending upon the kinetics of the particular pathways available and the milieu in which it resides. Unfortunately, the specific pathways and causes of amyloid fibril formation for proteins in general, and SP-C in particular, are not well understood [32].

In contrast to the fully acylated form of SP-C, which IR spectroscopy studies have uniformly shown to be α-helical, the previously published IR spectra of deacylated SP-C (dSP-C) show no consistent trend. In a mixed organic solvent, dSP-C was shown to fully transform from a monomeric α-helix to aggregated β-sheet [28]. Other studies of dSP-C associated with lipids report that after nucleophilic cleavage of the palmitoyl groups, the α-helical content of dSP-C decreased (and the β-strand content increased), but the protein still retained significantly helical content [33, 34]. In contrast, an IR external reflection study of dSP-C at the A/W interface showed that deacylation did not alter the protein secondary structure [22].

In the current work we report that deacylated SP-C exhibits a reversible pH-dependent conformational change from an α-helical to an extended β-strand amyloid fibril-like conformation. Multiple IR spectroscopic techniques were employed to assess the secondary structure of dSP-C in solution, bulk liposomes, lipid-protein films, and in lipid-protein monolayers at the A/W interface. IR methods used in this study include transmission IR spectroscopy of solutions and bulk liposomes, attenuated total reflectance (ATR) spectroscopy of transferred thin films, and photoelastic modulation IR external reflection spectroscopy (PM-IRRAS) of monolayers at the A/W interface. This work identifies pH as one of the mechanistic

causes of amyloid fibril formation for dSP-C, and a possible contributor to the pathogenesis of pulmonary alveolar proteinosis.

Materials and Methods

Surface Chemistry

The synthetic phospholipids 1,2-dipalmitoyl-*sn*-glycero-3-phosphoglycerol (DPPC) and 1,2-dipalmitoyl-*sn*-glycero-3-phosphoglycerol (DPPG), were purchased from Avanti Polar Lipids (Alabaster, AL) and used as received. ACS grade NaCl and HPLC grade methanol and chloroform were obtained from J.T. Baker. Ultrapure H_2O was obtained from a Barnstead (Dubuque, IA) ROpure/Nanopure reverse osmosis/deionization system and had a nominal resistivity of 18.3 MΩ cm. The subphase used in these experiments was 120 mM NaCl adjusted to pH 7 with a phosphate buffer.

Purification of Surfactant Protein C (SP-C)

SP-C was purified from calf lung surfactant extract (CLSE) by isocratic normal phase liquid chromatography on Silica C8 as described elsewhere [35]. Briefly, approximately 700 mg CLSE (total lipid plus protein) was initially reduced in volume by evaporation under nitrogen to approximately 4 ml (~1% of column bed volume). Small amounts of chloroform were added to the concentrated CLSE if the solution became cloudy. The concentrated CLSE was then applied to a 450 ml bed volume LC column that had been pre-equilibrated with 7:1:0.4 MeOH/$CHCl_3$/5% 0.1 N HCl. The added CLSE was allowed to completely adsorb to the column, and was then eluted with 7:1:0.4 MeOH/$CHCl_3$/5% 0.1 N HCl at a flow rate of 0.4 ml/min and UV detection at 254 nm. SP-C eluted from the column as the second peak as determined by SDS PAGE and protein sequencing (see below). Fractions containing SP-C were combined, concentrated via N_2 gas stream and run on a second C8 LC column. Fractions

containing purified SP-C from this second column were combined and concentrated by N_2 gas stream. Purified SP-C was then dialyzed against $CHCl_3$:MeOH (7:1) + 5.0% 0.1 N HCl, Phospholipid content of purified SP-C using the method of Shin [36] was determined to be less than 4 mole lipid/mole SP-C. Protein sequencing analysis (see below) indicated that the purified SP-C was free of SP-B.

SDS PAGE and amino acid analysis

For SDS PAGE, 20 microliters of the appropriate column fractions were dried, resuspended in NuPage sample buffer (Invitrogen, Carlsbad, CA) and applied to 4-10 % gradient acrylamide Tris/Bis gels (NuPage gels, Invitrogen) under non-reducing conditions. Electrophoresis was performed at a constant voltage of 200 V for 40 minutes with a morpholinoethanesulphonic acid (MES) buffer containing 50 mM MES/50 mM Tris Base/3.5 mM SDS/1 mM EDTA, pH 7.7 as the running buffer. Silver staining for detection of protein bands was performed according to Morrissey [37]. N-terminal amino acid sequence analysis was performed for seven to ten cycles using an Applied Biosystem Procise sequence analyzer. SP-C was identified by the N- terminal sequences of Leu-Ile-Pro-???-???-Pro-Val, where positions 4 and 5 in the SP-C sequence were both assumed to be Cys. The concentration of SP-C in solution was determined by the BCA total protein assay (Sigma Chemical Co., St. Louis, MO).

Deacylation of SP-C

Deacylation of SP-C was achieved by acid hydrolysis of the SP-C thioester groups. Hydrolysis was carried out by incubation of SP-C in a solution of 7:1 methanol/chloroform + 5% 0.1 N HCl at 20 ^{o}C for 72 days. Mass spectrometry, as described below, was used to verify deacylation of the SP-C.

Mass Spectrometry

Mass spectral data was obtained on a Bruker Reflex time-of-flight (TOF) instrument using matrix assisted laser desorption ionization (MALDI) in the Chemical/Biological Mass Spectrometry Facility at the University of Georgia. Protein samples were mixed with sinapinic acid in H_2O:CH_3CN:TFA and spotted onto a MALDI plate and allowed to dry. The dried sample plates were introduced into the spectrometer under high vacuum where a pulsed nitrogen laser (337 nm wavelength) is used to desorb and ionize the sample. The instrument was run in reflector (electrostatic mirror) mode to spatially collimate the ion beam and to produce time/energy focusing. The sample was ionized using ~120 pulses from the N_2 laser and a 10 microsecond delay. After the >3 meter flight tube, ions were detected using ultra fast dual microchannel plates. Mass accuracy for this instrument is ~4 m/z units.

Preparation of Samples

Stock lipid solutions of DPPC and DPPG (~2.5 mg/ml) were prepared in 4:1 $CHCl_3$:MeOH. Solutions of the lipid and proteins containing DPPC, DPPG and dSP-C were prepared by mixing the appropriate amounts of the phospholipid stock solution together with the stock solutions of dSP-C in 1:1 $CHCl_3$:MeOH.

Transmission IR Experiments

To follow the structure of dSP-C with increasing pH, an aliquot (150 μL) of the dSP-C stock solution was obtained having an initial pH of 1.8. This sample was progressively neutralized with 0.01 N NaOH. This low concentration of NaOH was chosen so as to finely adjust the pH of the stock solution. The pH of the protein solutions was measured using a 12 cm long Glass Micro-pH combination electrode (Thermo-Orion), connected to a Beckman 'Phi' 40 pH meter. The electrode was standardized using pH=4.0 and pH=7.0 buffer solutions.

At different pH's during the neutralization process, 10 μL aliquots of the sample solution were withdrawn and deposited on a CaF_2 crystal. After the evaporation of the solvent, transmission IR spectra of the samples were collected using a Perkin-Elmer 2000 (Norwalk, CT) FT IR spectrometer equipped with a DTGS detector. Spectra were recorded using 100 scans at 8 cm^{-1} resolution with triangular apodization and one level of zero filling. The transmission IR spectra were baseline corrected using the Grams/AI spectral software package (Ver. 6.0, Galactic Industries Inc., Salem, NH). Otherwise, the spectra have not been smoothed or further processed.

To illustrate the reversibility of the structure of dSP-C with decreasing pH, the stock solution of dSP-C (initial pH of 1.8) was neutralized using 0.1 N NaOH to a pH of 8.7. The pH of the solution was then reduced using 0.01 N HCl. At different points as the solution decreased in pH, 10 μL aliquots of the sample were withdrawn and placed on CaF_2 windows. After evaporation of the solvent, transmission IR spectra of these aliquots were obtained using the parameters described above.

Langmuir-Blodgett Monolayer Transfers

Lipid-protein monolayers were deposited onto monocrystalline, trapezoidal germanium (Ge) attenuated total reflectance (ATR) elements. The Ge ATR elements (Spectral Systems, Hopewell Junction, NY) had dimensions of 50 x 10 x 2 mm with 45° face angles, and a total surface area of 12.6 cm^2. Ge crystals were cleaned prior to Langmuir-Blodgett (L-B) film deposition by sonication for 15 minutes in a 6:4:1 chloroform:methanol:water solution, followed by sonication twice for 15 minute each in ultrapure water.

Monomolecular films were transferred onto the Ge ATR crystals using a fully programmable Joyce-Loebl Ltd. (Gateshead, England) Langmuir-Blodgett trough equipped with and a constant-

perimeter PTFE-coated fiberglass tape to control the size of the trough area. The subphase temperature was held constant to 21 ± 1 ^{o}C by flowing thermostatted water through the hollow body of the PTFE coated aluminum trough. Surface pressure measurements were recorded by differential weight measurements with a filter paper (Whatman No. 1) Wilhelmy plate suspended from a microbalance. The surface of the L-B trough was determined to be clean if the surface pressure did not increased by more than 0.2 mN/m while compressing to minimum area at full speed.

To prepare a transfer, a Ge crystal was fully immersed into the subphase through a clean surface. The lipid-protein sample was applied to the trough surface via a micro-syringe and allowed to equilibrate for 15 min. The monolayer was compressed at 5.5 cm^2/min to the final surface pressure (*e.g.* 30, 45 or 60 mN/m). The Ge crystal was vertically raised from the subphase through the monolayer film at a linear rate of 4 mm/min while the surface pressure was held constant to ± 1.0 mN/m. Transfer ratios were calculated for each sample and were always between 0.9 and 1.1.

Attenuated Total Reflectance IR Experiments

Attenuated total reflectance infrared spectra were acquired using a BioRad/Digilab (Cambridge, MA) FTS-40 spectrometer equipped with a narrow band, LN_2-cooled HgCdTe detector. Spectra were recorded with 1024 co-added scans at 4 cm^{-1} resolution using triangular apodization and one level of zero filling. The Ge ATR crystal was mounted into a horizontal ATR accessory (CIC Photonics, Inc., Albuquerque, NM); the system was purged with dry air for 15 minutes before data collection. ATR spectra were acquired using a background spectrum of the Ge crystal at room temperature just prior to L-B film deposition. ATR-IR spectra were baseline corrected using the Grams/AI spectral software package. Otherwise, the spectra have

not been smoothed or further processed. Vibrational band heights, wavenumber peak positions, and integrated intensities were calculated using a 5-point center-of-gravity algorithm [38], written in our laboratory for the Grams environment.

Polarization Modulation-IRRAS Measurements

Polarization-modulation IR reflection-absorption (PM-IRRAS) measurements at the A/W interface were performed using a Bruker Instruments (Billerica, MA) Equinox 55 Fourier transform infrared spectrometer optically interfaced to a variable angle external reflection accessory (Bruker model XA511-A). The external reflection accessory was equipped with a custom-designed Langmuir trough (Riegler & Kirstein, Berlin, Germany) containing a micro-balance Wilhelmy sensor for surface pressure readings. PM-IRRAS measurements were performed using previously described protocols [39-42], with changes adapted for our particular experimental design. The IR beam from the interferometer was directed through its external beam port and steered using mirrors into the excitation arm of the reflectance accessory. This IR beam is singly modulated at frequencies $f = 2V\tilde{\nu}$, where V is the scan speed of the interferometer and $\tilde{\nu}$ is the wavenumber of the IR radiation, resulting in a spectral bandwidth of approximately 0.4 – 6.5 kHz.

The excitation arm of the external reflection accessory was rotated using computer-driven stepper motors to achieve an angle of incidence of 74 degrees. Before reflection from the A/W interface, a wire grid polarizer (IGP225, Molectron Detector, Portland, OR) passed *p*-polarized light through a ZnSe photoelastic modulator (PEM-90, Hinds Instruments, Hillsboro, OR) operating at its resonance frequency f_m of 50 kHz. The application of a sinusoidal input voltage to the PEM crystal induced a linear modulation of the IR beam between *p*- and *s*-polarization states at a 2 f_m frequency of 100 kHz, resulting in a second, high frequency modulation of the IR

radiation. After reflection from the A/W interface, the doubly modulated IR radiation was collected by an *f*/1 ZnSe lens and focused onto the 1 mm^2 sensing chip of a liquid N_2-cooled photovoltaic HgCdTe detector (KMPV11, Kolmar Technologies, Newburyport, MA).

Due to the fact that the spectral frequencies from the interferometer are more than an order of magnitude removed from the modulation frequencies added by the PEM, the signal from the HgCdTe detector preamplifier may be separated into sum (I_{dc} – resulting from the IR spectrometer) and difference (I_{ac} – resulting from PEM modulation) components using dual-channel electronics with lock-in detection, as previously described [39, 41]. The I_{ac} difference signal was demodulated at 2 f_m with a digital lock-in amplifier (Stanford Research Systems, Model SR830) using a 100 μs time constant. The I_{ac} difference signal from the output of the lock-in, as well as the I_{dc} sum signal, was filtered using low-pass filters; electronic filtering was achieved using dual-channel electronics (Stanford Research System, Model SR650). At the output of the electronic filters, both I_{ac} and I_{dc} signals were combined using a multiplexer and sent to the 16-bit ADC of the Bruker IR spectrometer. The combined signal was deconstructed and Fourier-transformed using spectrometer software. The ratio of the resulting I_{ac} and I_{dc} single beam spectra provides the PM-IRRAS signal *S* [39].

$$S = \frac{I_{ac}}{I_{dc}} = C\,\frac{J_2(\phi)\left(R_p - R_s\right)}{\left(R_p + R_s\right) + J_0(\phi)\left(R_p - R_s\right)}$$

In this equation *c* is a constant that is the ratio of the slightly different electronic amplification of the two signal channels, and $J_n(\phi_0)$ is the n^{th} – order Bessel function of maximum dephasing ϕ_0 introduced by the PEM. In our case, the PEM was set to introduce maximum dephasing ($\phi_0 = \pi$) at 2000 cm^{-1}. The PM-IRRAS spectra shown here are presented as

normalized difference spectra, where ΔS reflects the difference in signal intensity between the film-covered surface (S) and the bare water surface (S_0).

$$\Delta S = \frac{S - S_0}{S_0}$$

PM-IRRAS spectra were recorded at a resolution of 4 cm^{-1} using a scan speed/sampling frequency of 13 kHz. The total acquisition time for each spectrum was 20 minutes, resulting in 800 interferograms per spectrum.

Results and Discussion

Mass Spectrometry of dSP-C

Figure 4.1 presents the MALDI-TOF spectrum of the deacylated SP-C protein after acidic hydrolysis of the thioester-linked palmitoyl groups at cysteines C4 and C5. Bovine SP-C in its fully acylated form has an expected molecular mass of 4058 Da. This particular mass is absent from the mass spectrum of dSP-C shown in Figure 4.1 indicating that little, if any, fully acylated SP-C exists in the sample. The major peak at 3596 m/z in the mass spectrum of dSP-C (labeled with an asterisk in Figure 4.1) corresponds to the mass of the fully acylated SP-C protein minus both covalently linked palmitoyl chains. The Na^{2+} adduct of this base peak also occurs at the expected value of 3620 m/z. A truncated form of the polypeptide appears at 3483 m/z indicating the loss of the N-terminal leucine from the amino acid chain. The peak at 3880 m/z is the intact (nontruncated) monopalmitoylated form of the protein. The N-terminus truncated one chain peptide and its Na^{2+} adduct are observed at 3719 m/z and 3733 m/z respectively. The mass peaks shown in Figure 4.1 demonstrate the successful acidic hydrolysis of the acyl chains of SP-C.

Visible Microscopy of dSP-C Amyloid Fibrils

Using visible light microscopy, we have observed the formation of amyloid fibrils from solutions of deacylated bovine SP-C (dSP-C). Approximately 150 μL of the stock solution of dSP-C in 7:1 methanol/chloroform + 5% 0.1N HCl was pipetted onto a clean glass microscope slide. The solvent was permitted to partially evaporate prior to image acquisition. Images were obtained using an Olympus BX41 microscope at 40 × magnification, fitted with an Olympus DP11 digital camera. Figure 4.2 shows the image of the fibrils formed from the dSP-C solution. The image of the fibrils presented in Figure 4.2 are consistent with previously published images of amyloid fibrils of deacylated SP-C isolated from the bronchoalveolar lavage of a clinical patient suffering from pulmonary alveolar proteinosis (PAP) [29].

pH-dependence of dSP-C Secondary Structure in Solution

Figure 4.3 illustrates the amide I region (1720 – 1580 cm^{-1}) of dSP-C solutions obtained by transmission IR spectroscopy. These spectra were obtained by pH titration of the stock dSP-C solution (7:1 MeOH:$CHCl_3$ + 5% 0.1N HCl) with 0.01 N NaOH. Ten microliter aliquots were removed from the titrated solution at the pH values indicated on the figure. The aliquots were deposited on CaF_2 windows and the solvent was allowed to evaporate prior to data collection.

The transmission IR spectra of dSP-C shown in Figure 4.3 are presented as a function of increasing pH, beginning with the acidic pH samples at the bottom of the figure. The spectra of dSP-C at pH 1.8 shows two main peaks for the protein amide vibration, one at 1656 cm^{-1} and one at 1626 cm^{-1}. These two vibrations have been previously observed in the IR spectra of fully acylated SP-C at the A/W interface [27]. The wavenumber values of these amide I bands may be associated with specific protein secondary structure conformations using previously published IR

Figure 4.1 Matrix-assisted laser desorption ionization – time of flight (MALDI-TOF) mass spectrum of deacylated SP-C. The major peak in the spectrum at 3596 m/z (labeled with asterisk) represents the mass of the completely deacylated SP-C protein minus both palmitoyl chains. There is no peak present at 4058 Da, which corresponds to the mass of native, diacylated bovine SP-C, indicating acid hydrolysis of SP-C thioester groups was complete.

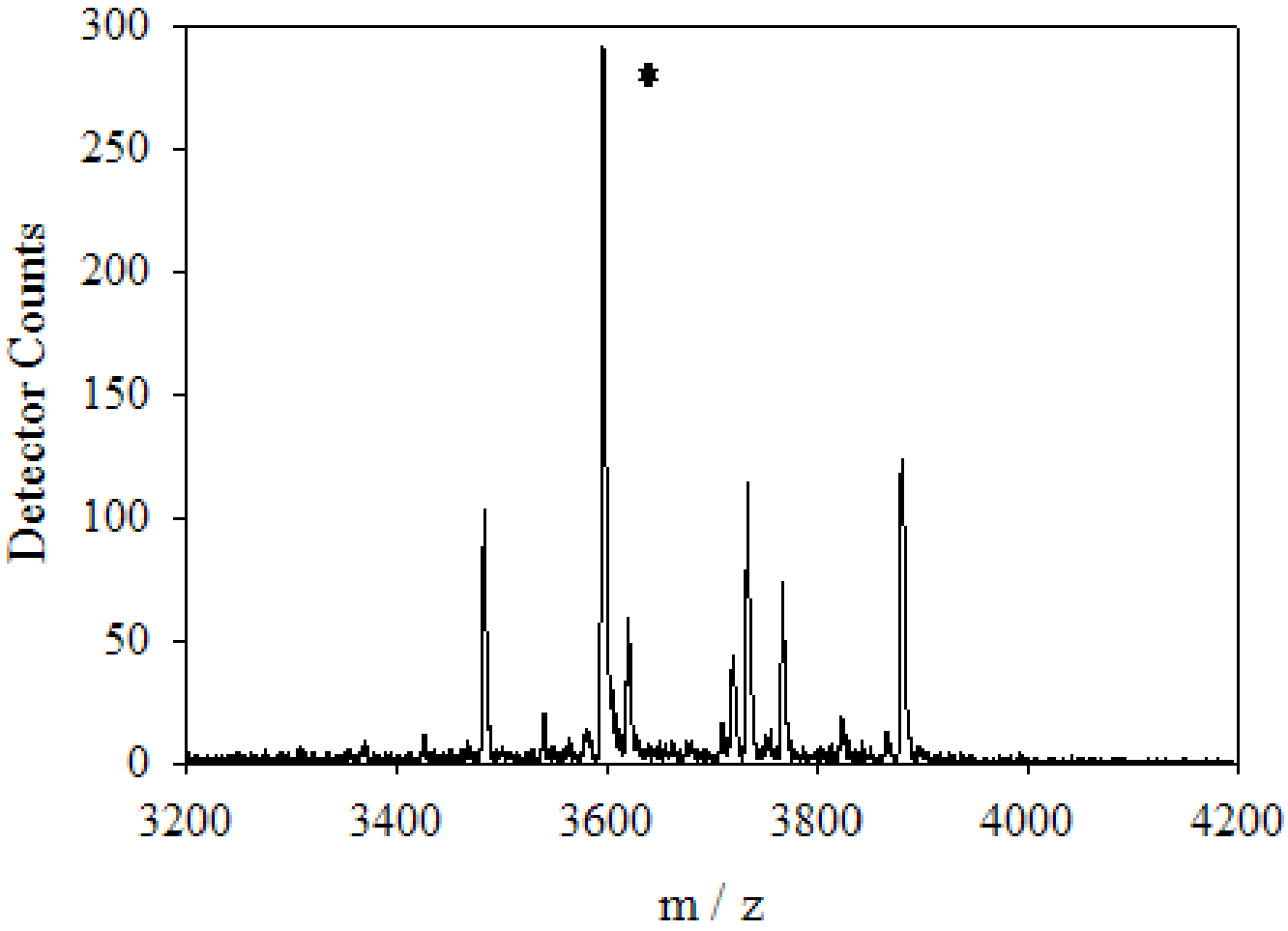
300
250
200
150
100
50
0
Detector Counts
*
3200
3400
3600
3800
4000
4200
m / z

Figure 4.2 Amyloid-like aggregates of deacylated bovine SP-C (dSP-C) detected by visible light microscopy, 40 × magnification. Approximately 150 μL dSP-C in 7:1 methanol/chloroform + 5% 0.1N HCl was pipetted onto a clean glass microscope slide. Solvent was permitted to partially evaporate prior to image acquisition using an Olympus DP11 digital camera coupled to an Olympus BX41 microscope. The bar in the figure represents a distance of 10 μm.

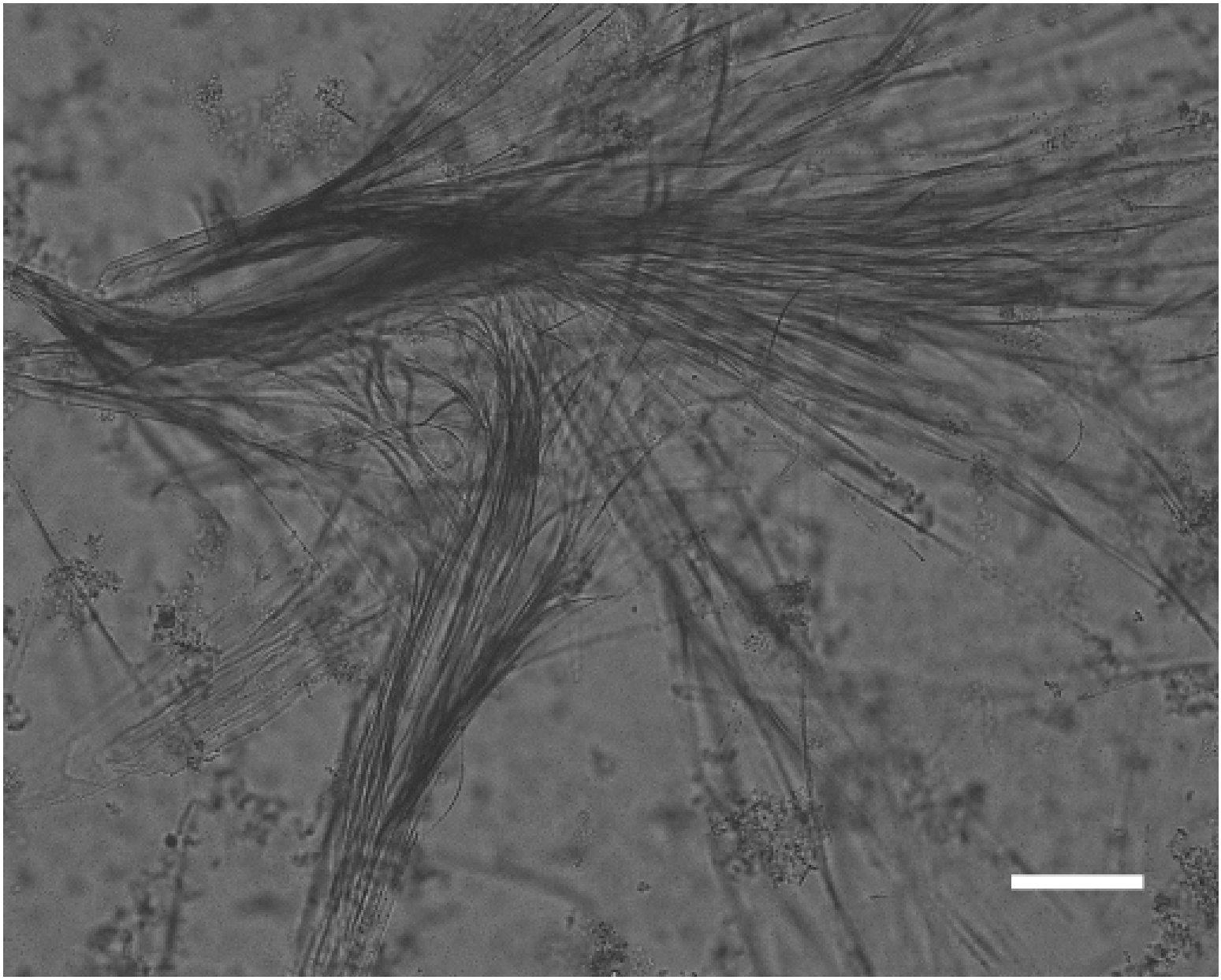

spectra-structure correlations [43, 44]. The band at 1656 cm^{-1} in the spectrum of SP-C is most commonly associated with this protein's α-helical secondary structure [24]. However, the band at 1626 cm^{-1} is not commonly identified with a specific protein conformation. Rather, it is assigned to a structure of extended, multistrand aggregates [45]. The 1626 cm^{-1} vibration has also been previously observed in the IR spectra of fully acylated SP-C, and has been attributed to protein aggregation in these samples [24, 27]. The spectra of dSP-C presented here suggest that the deacylated protein at low pH adopts a primarily α-helical secondary structure similar to that of the fully acylated protein at neutral pH.

As seen in Figure 4.3, the IR spectra of dSP-C change markedly as the pH of the solution is increased. Between pH values of 2.7 and 3.3, the α-helical band at 1656 cm^{-1} as well as the aggregation band at 1626 cm^{-1} band gradually decrease in intensity while a new band at approximately 1680 cm^{-1} grows in intensity, finally becoming predominate at pH's above 4.9.

The commonly accepted interpretation of β-sheet structure in IR spectroscopy features a characteristically split spectral signature: a prominent band at ~1630 cm^{-1} and a smaller feature at higher wavenumber, ~1680 - 1690 cm^{-1} [46]. This split IR pattern for β-sheet proteins is usually attributed to aggregated strands stabilized by intermolecular hydrogen bonds [44]; however, this particular split amide I band profile may only be characteristic for large extended anti-parallel β-sheet structures [47]. Recent research has indicated that a different IR spectral pattern may exist for smaller peptides containing short twisted β-sheet strands or β-hairpins [48]. In addition, *ab initio* calculations for short model β-sheet peptide strands reveal that coiled or twisted forms of β-structures have much less amide I splitting than is observed in multi-kD proteins containing aggregated, extended β-strands [45, 49].

Figure 4.3 Transmission IR spectra of dSP-C in the amide I spectral region. Samples were prepared by titration of stock dSP-C solution (dissolved in 7:1 MeOH:CHCl3 + 5% 0.1N HCl) with 0.01 N NaOH. Aliquots were obtained at the pH values indicated in the figure and placed on CaF2 disks. Spectra were obtained after solvent evaporation.

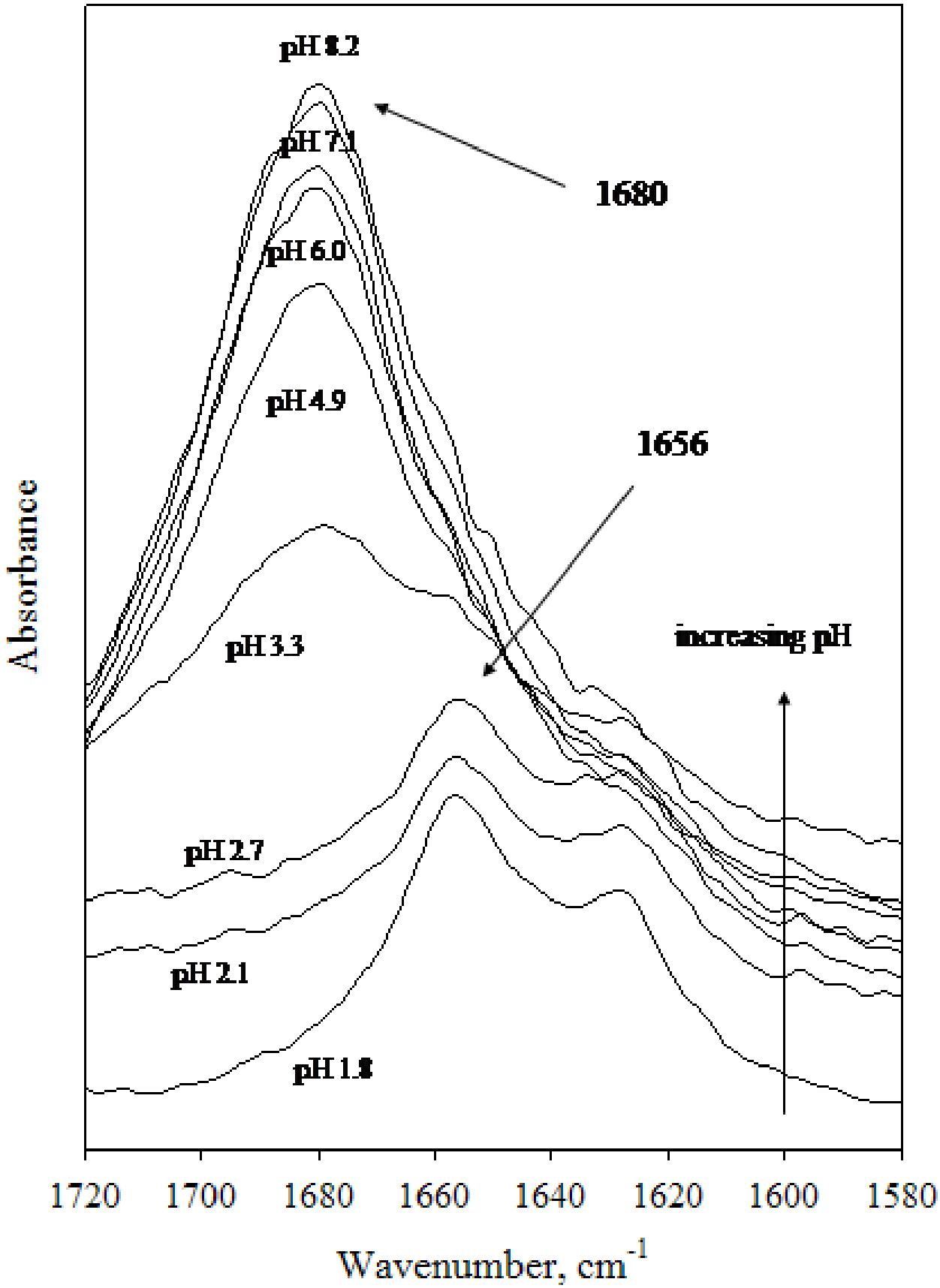
pH 8.2
pH 7.1
pH 6.0
pH 4.9
pH 3.3
pH 2.7
pH 2.1
pH 1.8
1680
1656
increasing pH
Absorbance
1720
1700
1680
1660
1640
1620
1600
1580
Wavenumber, cm-1

The main amide I band observed at 1680 cm^{-1} in the pH-dependent IR spectra at greater than pH 4 (Figure 4.3) does not correlate with the classical picture of an extended, anti-parallel β-sheet. Rather, a primary amide I vibration at 1680 cm^{-1} is consistent with short segments of twisted or coiled β-sheet strands or β-hairpins in the amyloid fibril structure of dSP-C that have not aggregated into a supramolecular structure. In support of this interpretation, computer simulations of coiled or twisted β-strands predict that a single intense amide I band should occur at a higher wavenumber value than that of a regular planar β-sheet [45]. (Note, however, that due to the constraints of the computational methods, the wavenumber values resulting from the *ab initio* calculations are not directly comparable to the experimentally determined wavenumbers.) Other IR studies of β-amyloid proteins have also documented the presence of an amide I vibration at ~1680 cm^{-1}, including the lipid association of amyloid β protein from brain [50] and an early study of deacylated SP-C [28]. In both these studies, however, a strong amide I vibration also occurs at ~1620 cm^{-1}, indicating that extensive protein aggregation has occurred in these samples.

Figure 4.4 illustrates the extent to which each dSP-C conformation contributes to the overall band profile as a function of pH. This figure was generated by first curve-fitting the pH-dependent transmission spectra from Figure 4.3. Three bands were used for the curve fitting, one at 1680 cm^{-1} (β-amyloid conformation), one at 1656 cm^{-1} (α-helix), and one at 1625 cm^{-1} (protein aggregation). In the curve-fitting procedure, the frequencies of the bands were fixed while the bandwidths were allowed to vary. The integrated intensities of each curve-fit band were then used to calculate the percentage of the amide I band area attributable to each conformation. It is clear from the curve-fitting results in Figure 4.4 that the β-amyloid band at 1680 cm^{-1} is the major contributor to protein structure above pH 3, with ~55% of the amide I

Figure 4.4 Percent of the entire amide I band intensity attributable to the major IR bands observed in the transmission IR spectra of dSP-C (Figure 4.3) plotted as a function of pH. Peaks at 1680 cm^{-1} correspond to amyloid β-structure, 1656 cm^{-1} to α-helix, and 1626 cm^{-1} to aggregated protein.

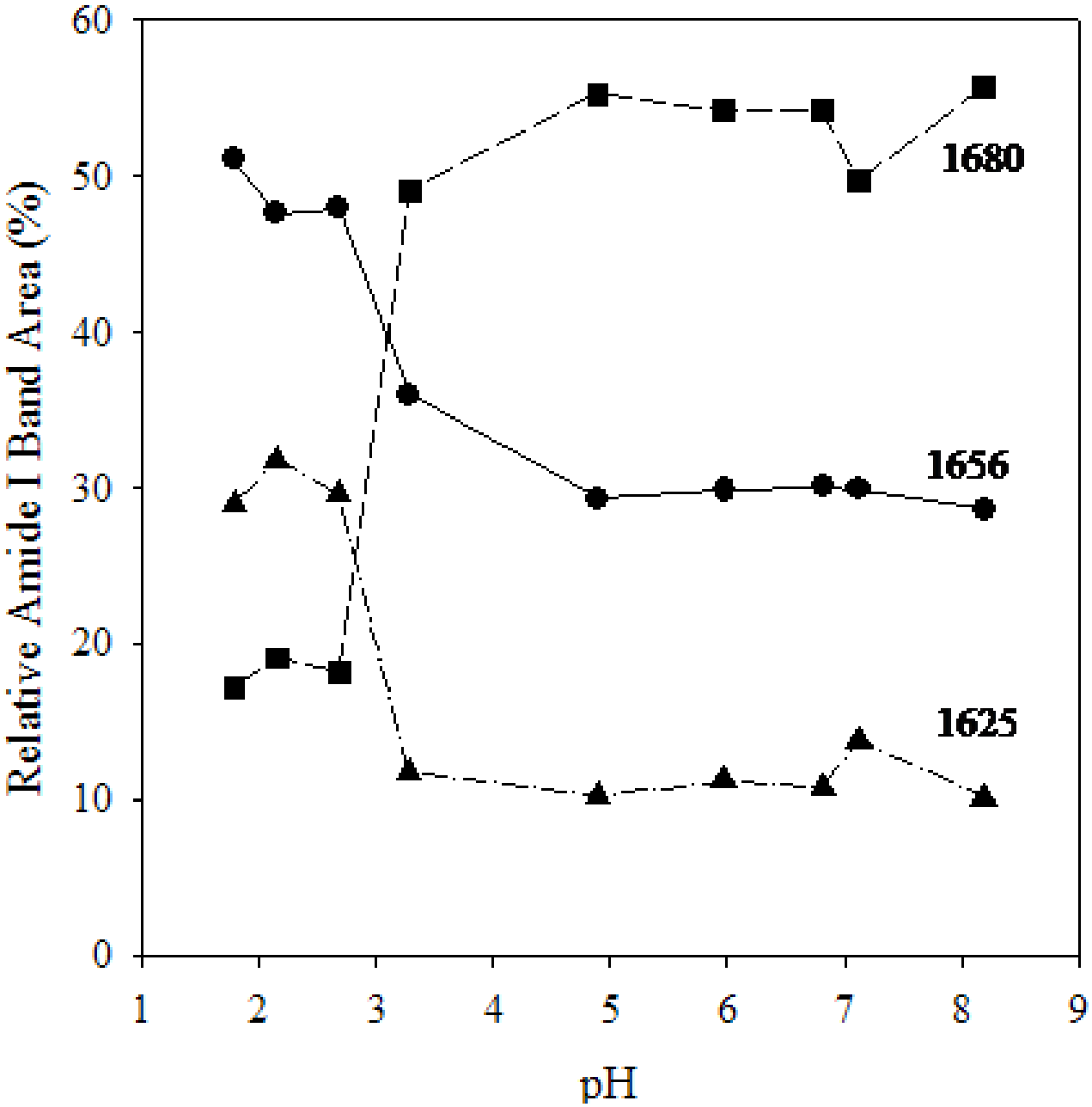
Relative Amide I Band Area (%)
60
50
40
30
20
10
0
1
2
3
4
5
6
7
8
9
pH
1680
1656
1625

intensity centered in that band. However, the residual α-helix and aggregation peaks are still present in substantial amounts at neutral pH, contributing ~30% and 10%, respectively, to the overall amide I band intensity.

We have also investigated the reversibility of the helix-to-amyloid dSP-C conformational transition. Beginning with the dSP-C solution at low pH (1.8), the pH of sample was gradually neutralized by titration with 0.01 N NaOH, as described above and as seen in Figure 4.3. The pH of the sample was then lowered by titration with 0.01 N HCl. In this case, aliquots of the sample solution were removed for IR analysis at specific pH values as the pH was lowered. Figure 4.5 illustrates the effect of reversing the sample pH on peptide conformation. The upper spectrum (Figure 4.5A) was obtained at pH 4.5 and shows a broad amide I band with a main peak at 1679 cm^{-1} along with a shoulder at 1656 cm^{-1}. The presence of these two bands indicates that as the pH is being lowered, the α-helix conformation begins to re-emerge alongside the amyloid β-structure. The lower spectrum (Figure 4.5B) demonstrates that when the pH is lowered to 1.5, the α-helix is the only conformation present for dSP-C. These spectra illustrate that the α-helix structure of dSP-C is fully recoverable from the amyloid β-type structure, and that a pH-dependent mechanism is responsible for the transition between the two forms.

The structure of dSP-C in the presence of lipids was further investigated by transmission IR spectroscopy. For these samples, stock lipid solutions of DPPC and DPPG (~2.5 mg/ml in $CHCl_3$:MeOH) were prepared. An organic solution containing 7:3 DPPC:DPPG along with ~20 wt% dSP-C was prepared by mixing the appropriate amounts of the phospholipid stock solution together with an aliquot from the stock solution of dSP-C that had been neutralized to pH ~7. This organic solution was placed on a CaF_2 disk and the solvent allowed to dry, similar to the samples in Figures 4.3 and 4.5. The result is shown in the upper spectrum (A) of Figure 4.6.

Figure 4.5 Transmission IR spectra of dSP-C in the amide I spectral region. Samples were prepared by titration of stock dSP-C sample (dissolved in 7:1 MeOH:CHCl3 + 5% 0.1N HCl). The sample was first titrated to neutral pH with 0.01 N NaOH, followed by reverse titration to acid pH's with 0.01 N HCl. Aliquots were obtained at the pH values indicated in the figure and placed on CaF2 windows. Spectra were obtained after solvent evaporation. (A) Upper spectrum. Sample obtained at pH 4.5. (B) Lower spectrum. Sample obtained at pH 1.5.

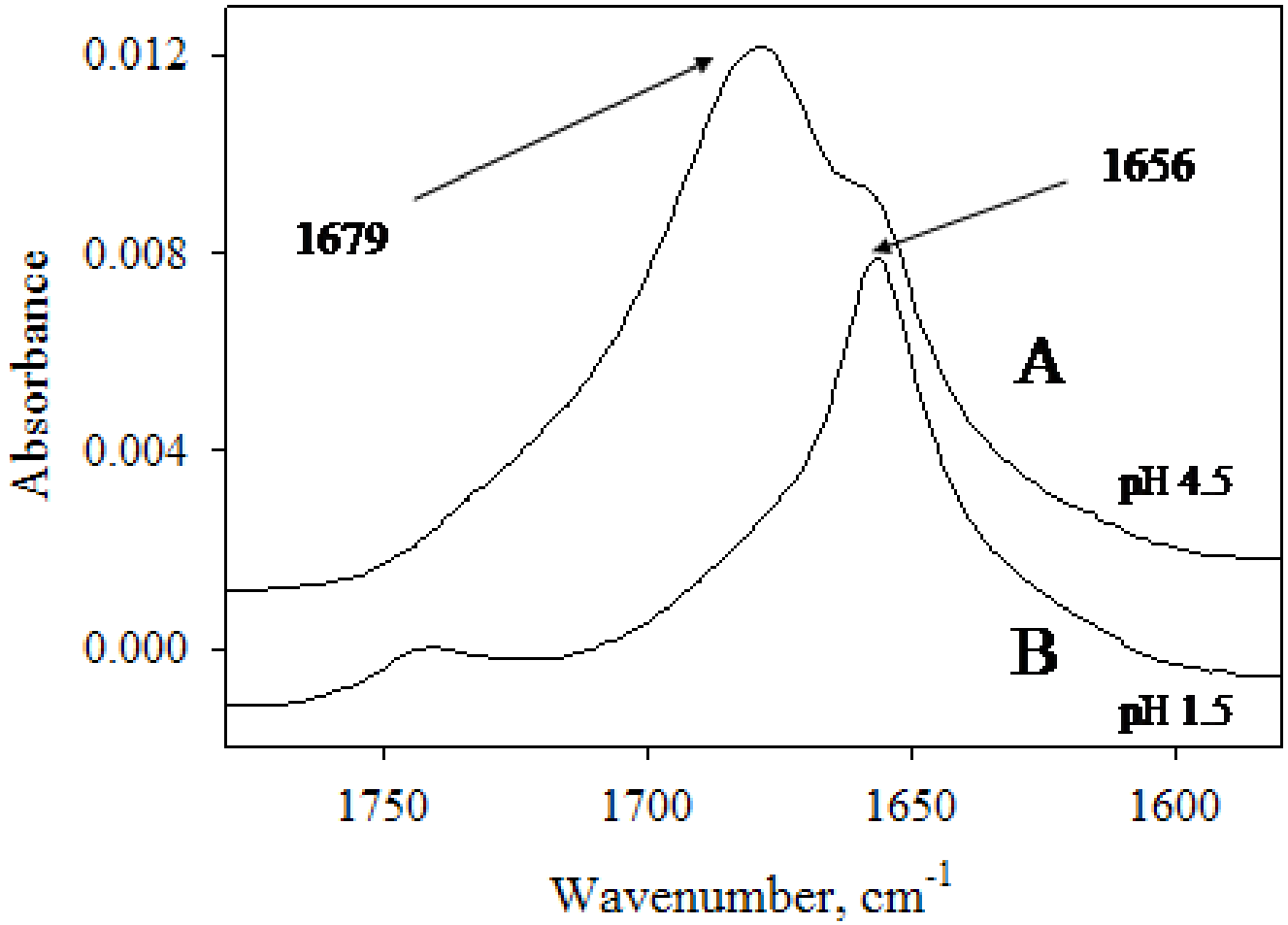
0.012
0.008
0.004
0.000
Absorbance
1679
1656
A
pH 4.5
B
pH 1.5
1750
1700
1650
1600
Wavenumber, cm-1

Two major bands are seen in this spectrum, one at ~1740 cm^{-1} due to the lipid carbonyl groups, and one at 1682 cm^{-1} due to the β-sheet structure. Clearly, dSP-C at neutral pH retains its amyloid fibril conformation when co-deposited from organic solution as a mixed lipid-protein complex.

Aqueous multi-lamellar lipid-protein vesicles of DPPC:DPPG/dSP-C were also formed by drying the co-solubilized lipid-protein organic solution in a N_2 stream, after which the lipid-protein film was rehydrated, followed by several cycles of heating and cooling above the lipid T_m. D_2O was used as the rehydration solvent rather than H_2O in order to avoid interference from the large δ(H-O-H) deformation vibration at ~1640 cm^{-1} that hinders quantitative subtracting of the H_2O background and complicates the analysis of the protein amide I vibration [51]. The use of D_2O results in a δ(D-O-D) deformation vibration in a region separate from the amide I vibration, but it also results in a slight shift of the protein amide I vibrations to lower wavenumber (termed amide I'), due to H → D exchange. Transmission IR spectroscopy of the aqueous DPPC:DPPG/dSP-C multilayers containing neutral dSP-C was performed using CaF_2 windows and a 6 micrometer pathlength spacer. The results are shown as the lower spectrum (B) in Figure 4.6. The main amide I' protein vibration at 1672 cm^{-1} indicates that dSP-C has undergone an unknown amount of H → D exchange. However, the presence of a single amide I' peak slightly shifted from the amide I peak of the original lipid-protein film indicates that the amyloid fibril structure of dSP-C is retained when it is incorporated into lipid-protein multilayers in aqueous suspension.

Figure 4.6 Transmission IR spectra of dSP-C in the amide I spectral region. Samples were prepared as lipid-protein complexes by co-solubilization in CHCl3:MeOH of DPPC: DPPG (7:3) with 20 wt% dSP-C. Prior to mixture with lipids, dSP-C was first adjusted to neutral pH. (A) Upper spectrum. Lipid-protein complex co-deposited from organic solution on CaF2 disk. Spectrum obtained after solvent evaporation. (B) Lower spectrum. Multilamellar lipid-protein vesicles prepared from D2O solution. Spectrum obtained using 20 micrometer pathlength cell with CaF2 windows.

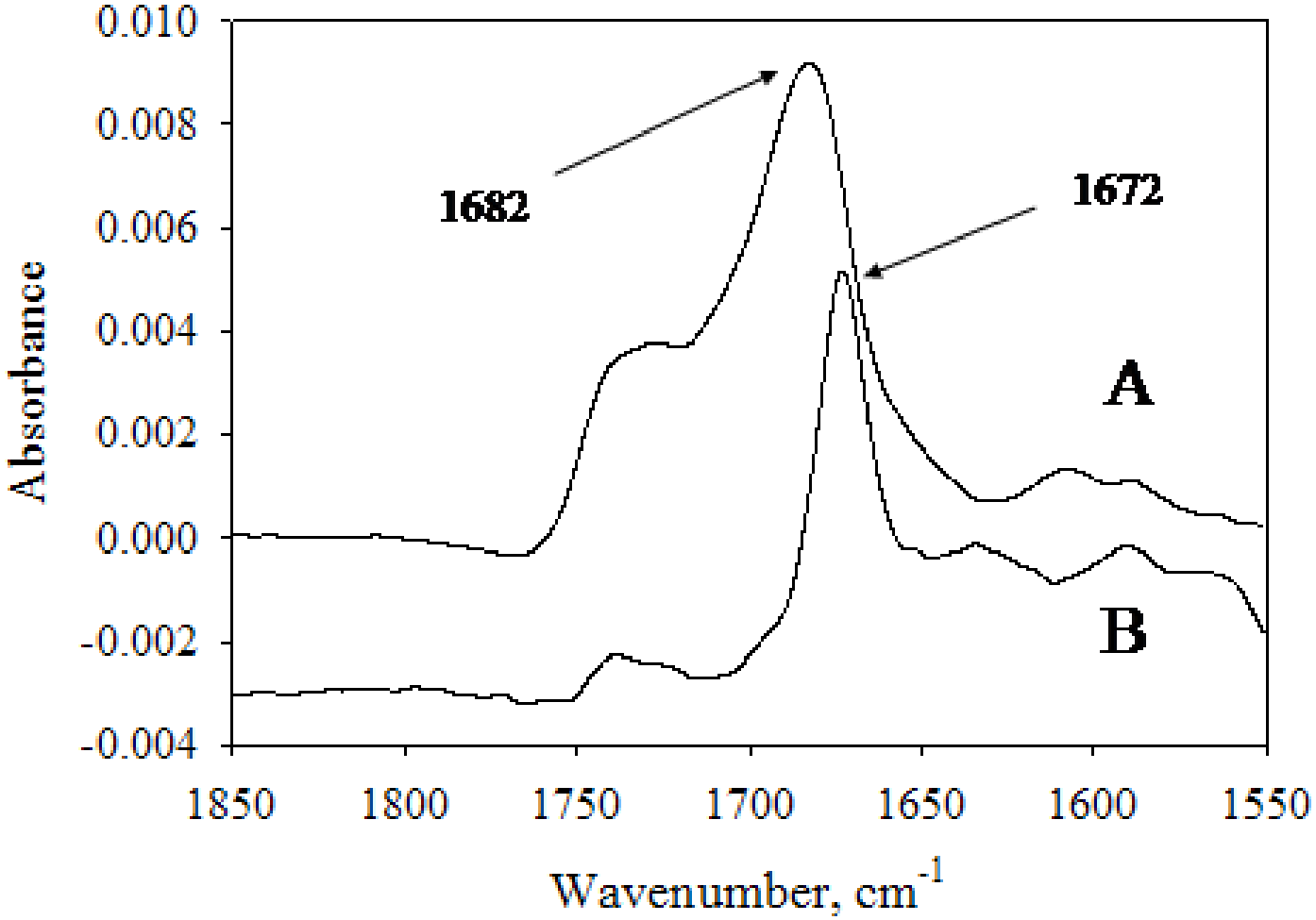
0.010
0.008
0.006
0.004
0.002
0.000
-0.002
-0.004
Absorbance
1682
1672
A
B
1850
1800
1750
1700
1650
1600
1550
Wavenumber, cm-1

dSP-C Secondary Structure in Transferred Langmuir-Blodgett Films

In addition to looking at the solution phase structure of dSP-C, we have also obtained the IR attenuated total reflectance (ATR) spectra of lipid-protein monolayers transferred to Ge ATR crystals from the A/W interface *via* the Langmuir-Blodgett method. Samples for ATR transfer were prepared similarly to the lipid-protein samples used for the solution studies described above (Figure 4.6). An organic solution containing 7:3 DPPC:DPPG along with ~10 wt% dSP-C was prepared by mixing the appropriate amounts of the phospholipid stock solution together with an aliquot from the stock solution of dSP-C that had been neutralized to pH ~7. Figure 4.7 illustrates the transmission IR spectrum of the DPPC:DPPG/dSP-C spreading solution used for L-B film transfer. In this Figure, the lipid-protein organic solution was placed on a CaF_2 disk and the solvent allowed to dry prior to acquiring the IR spectrum, similar to the samples in Figures 4.3 and 4.5. The single amide I vibration at 1680 cm^{-1} indicates that dSP-C is in the amyloid β-structure conformation in the spreading solution.

An aliquot from the 10 wt% DPPC:DPPG/dSP-C spreading solution was placed at the A/W interface of a LB film balance. The monomolecular film was compressed to the desired surface pressure and subsequently transferred to Ge ATR crystals as described in the Materials and Methods section. The resulting ATR-IR spectra of the 10 wt% PC:PG/dSP-C sample transferred at 30, 45 and 60 mN/m are shown in Figure 4.8A.

It is immediately clear from Figure 4.8A that the IR spectrum of the amide I region of the transferred L-B film of 10 wt% DPPC:DPPG/dSP-C does not match that of the spreading solution shown in Figure 4.7. Two differences are readily apparent. First, the amide I band at 1680 cm^{-1} corresponding to the amyloid fibril β-strand conformation is absent in the IR spectrum of the L-B film. Instead, a broad amide I band exists that has its maximum peak position at

Figure 4.7 Transmission IR spectroscopy of lipid-protein spreading solution used for Langmuir-Blodgett transfers. The solution were prepared by co-solubilization of DPPC: DPPG (7:3) in CHCl3:MeOH (1:1) with 10 wt% dSP-C. Prior to mixture with lipids, the dSP-C solution was first adjusted to neutral pH. Spectrum was obtained after solvent evaporation.

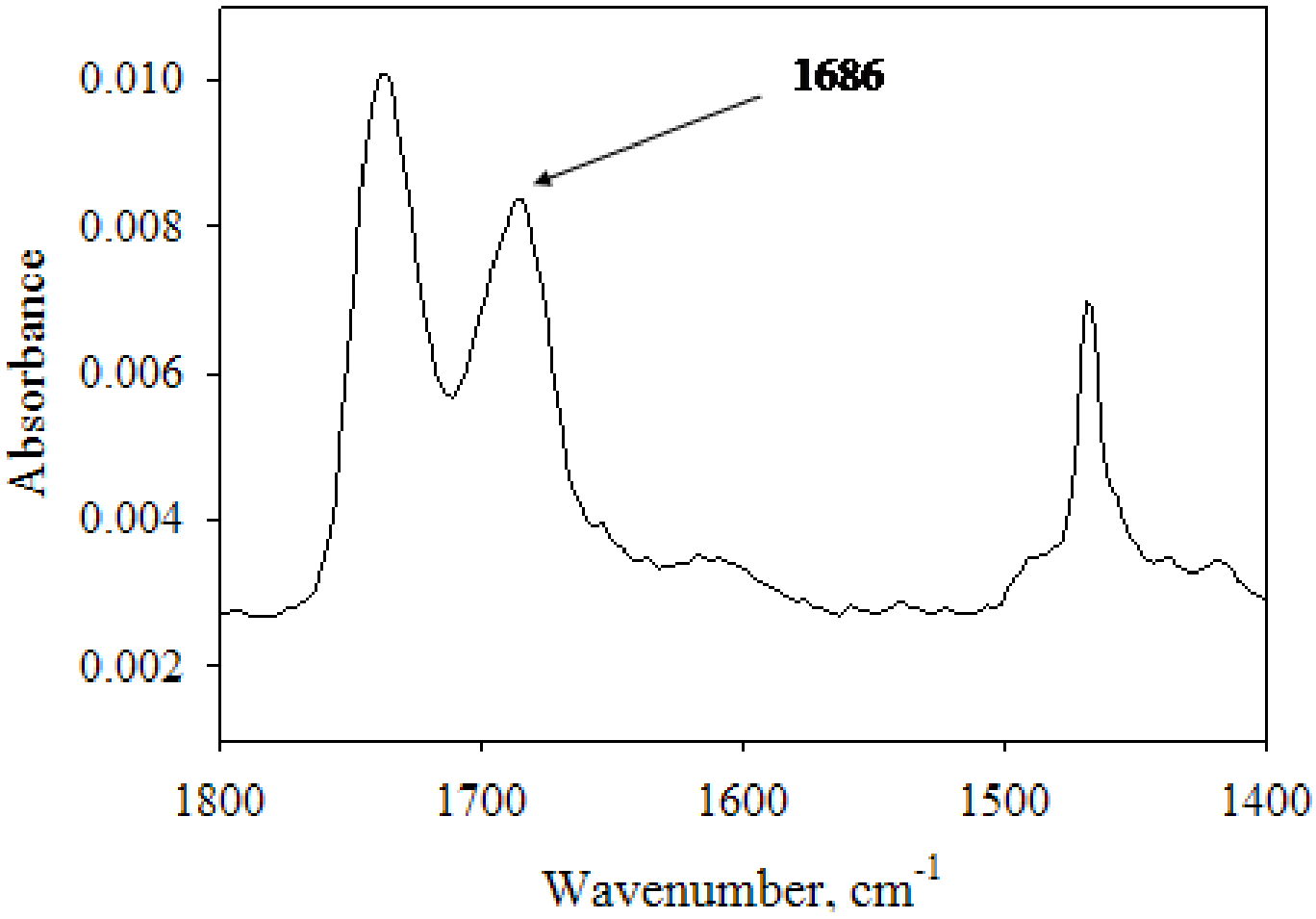
1686
0.010
0.008
0.006
0.004
0.002
Absorbance
1800
1700
1600
1500
1400
Wavenumber, cm-1

Figure 4.8 Attenuated total reflectance IR spectra of Langmuir-Blodgett monolayer films transferred to Ge ATR crystals. Samples were prepared as lipid-protein complexes by co-solubilization in CHCl3:MeOH of DPPC: DPPG (7:3) with a dSP-C solution that was first adjusted to neutral pH. The monomolecular film was transferred to the Ge crystal at the indicated surface pressures. ATR-IR spectra of transferred monolayer film of: (A) DPPC:DPPG (7:3) plus 10 wt% dSP-C. (B) DPPC:DPPG (7:3) plus 5 wt% dSP-C.

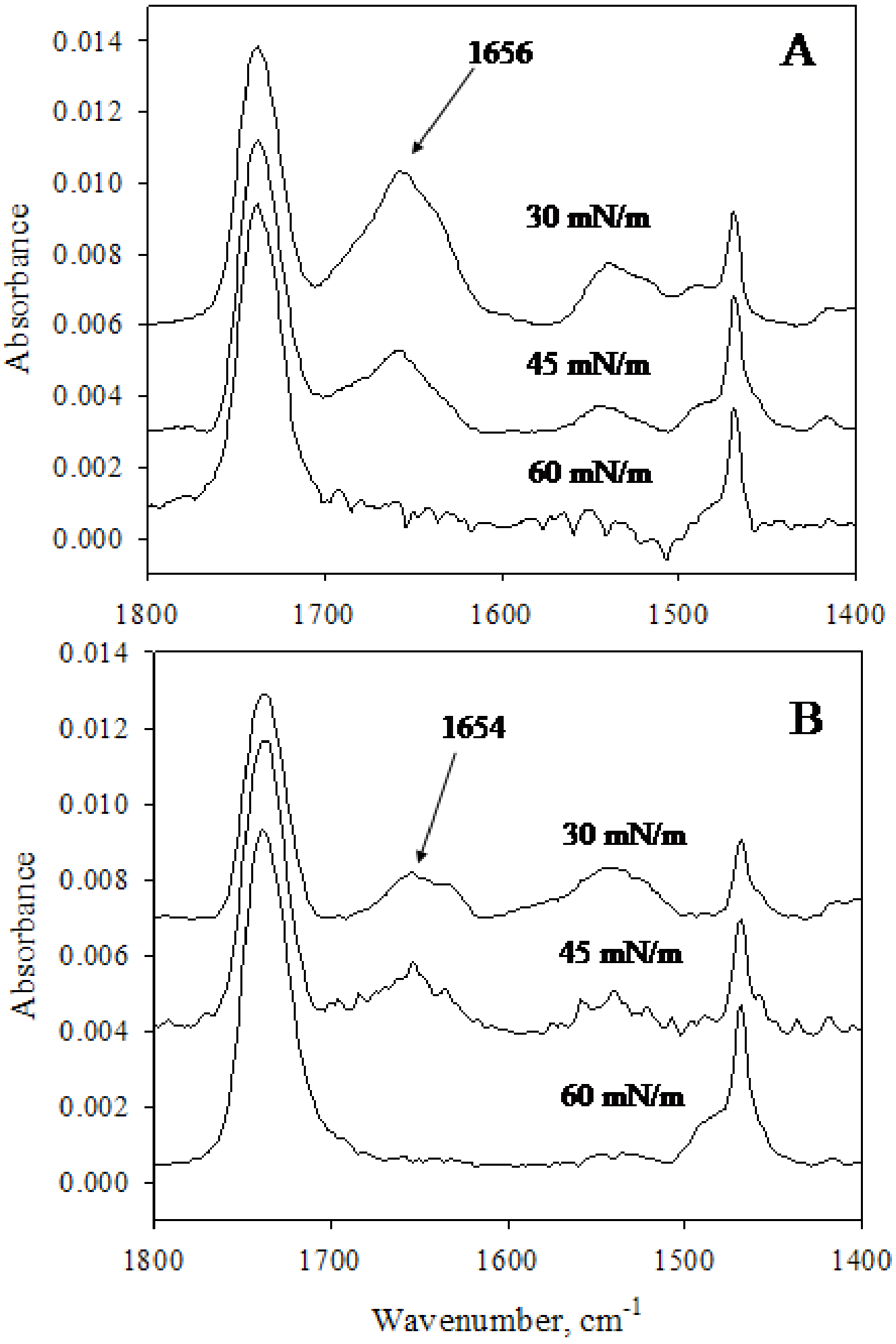
A
1656
30 mN/m
45 mN/m
60 mN/m
Absorbance
0.014
0.012
0.010
0.008
0.006
0.004
0.002
0.000
1800
1700
1600
1500
1400
B
1654
30 mN/m
45 mN/m
60 mN/m
Absorbance
0.014
0.012
0.010
0.008
0.006
0.004
0.002
0.000
1800
1700
1600
1500
1400
Wavenumber, cm-1

~1656 cm^{-1}, indicating an α-helical secondary structure, albeit one that also has some contribution from β-sheet conformation. In particular, the L-B film transferred at 30 mN/m in Figure 4.8A shows a shoulder at ~1634 cm^{-1} as well as a broad underlying IR intensity in the range of 1660 – 1690 cm^{-1}. Both these spectral features indicate the involvement of β structure in the transferred film.

The second difference between the IR spectra of the DPPC:DPPG/dSP-C lipid-protein complex in solution and in L-B transferred films is the fact that dSP-C is not membrane-associated at higher surface pressures. It is obvious from Figure 4.8A that increasing the surface pressure results in a progressive dissociation of 10 wt% dSP-C from the monolayer film, with all of the protein being lost from the surface by 60 mN/m. In fact, an examination of the integrated intensities of the protein amide vibration *vs*. the lipid carbonyl band shows that even at 30 mN/m, dSP-C has been partially desorbed from the surface. In Figure 4.7, the ratio of the integrated intensity of the protein amide I vibration to that of the lipid carbonyl in the spreading solution, *i.e.* $\frac{I_{protein}}{I_{lipid}}$, equals 0.74. In Figure 4.8A, this same ratio is 0.53 for the L-B film transferred at 30 mN/m, 0.28 for the L-B film transferred at 45 mN/m and 0 for the L-B film transferred at 60 mN/m.

The same situation holds for other DPPC:DPPG/dSP-C samples prepared at different lipid-protein ratios. Figure 4.8B presents the ATR-IR spectra of L-B monolayers containing 7:3 DPPC:DPPG plus 5 wt% dSP-C transferred at different surface pressures. The DPPC:DPPG/dSP-C sample with 5 wt% dSP-C (Figure 4.8B) behaves identically to the DPPC:DPPG/dSP-C sample containing 10 wt% dSP-C (Figure 4.8A). That is, 5 wt% dSP-C is progressively excluded from the lipid monolayer as the surface pressure increases (30 and 45

mN/m), and is completely absent from the membrane interface when the surface pressure reaches 60 mN/m.

Several possible explanations may account for the differences between the solution IR spectra of dSP-C (Figures 4.3-4.7) and the interfacial IR spectra of the same protein (Figure 4.8). First, the absence of amyloid β-structure at the A/W interface is likely due to the solubility of smaller dSP-C oligomers. It has been postulated that the formation of insoluble fibril plaques of dSP-C proceeds through the intermediate formation of smaller, soluble aggregates [52]. A previous study using electrospray ionization mass spectrometry indicated that centrifugation at 20,000 × *g* was needed to pellet larger dSP-C fibrils while pre-fibrillar aggregates or oligomers of dSP-C remained soluble in solution [31]. The lack of a large aggregation band at ~1620 cm^{-1} suggests that we do not have large, higher-order, insoluble, aggregated plaques of dSP-C present in our samples. It is therefore quite likely that smaller dSP-C β-strands, whose presence is indicated by the 1680 cm^{-1} band in solution, would be soluble and not surface-associated.

Secondly, the ATR-IR spectra of the transferred films seen in Figure 4.8 may be explained by the residual helical forms of dSP-C. A previous study reported that delipidation of SP-C reduces, but does not eliminate, the helical content of the deacylated protein [53]. This is also the behavior that we observe in the pH-dependent IR transmission spectra of dSP-C, where at neutral pH, the residual α-helical content of the protein is approximately 30% (Figures 4.3 and 4.4).

While deacylation of SP-C results in a coexistence of α and β structures, we find that it is the helical form of dSP-C that remains membrane-associated at the A/W interface, likely due to the hydrophobic alignment of the protein's α-helix with the hydrocarbon chains of the surrounding phospholipid molecules. However, probably due to the absence of the palmitoyl chains that

serve to anchor acylated SP-C to the membrane, increasing surface pressure is sufficient to exclude the deacylated α-helical dSP-C from the membrane interface (Figure 4.8). It is also possible that increasing lateral surface pressure drives dSP-C from a metastable α-helical into a β-strand conformation, thereby increasing the solubility of the protein and eliminating it from the membrane surface. However, we have not been able to experimentally confirm this.

A previous reflectance IR study of deacylated SP-C at the A/W interface showed no change in secondary structure between deacylated and dipalmitoylated SP-C [22]. These authors found that the α-helix secondary structure and tilt angle of SP-C remain unaffected by deacylation. In fact, our current results are not inconsistent with the conclusions of that study. The previous study only examined the IR spectra of deacylated SP-C in a DPPC monolayer at one surface pressure, ~28 mN/m. As seen in Figure 4.8, our ATR-IR spectra of 10 wt% dSP-C in a lipid monolayer at ~30 mN/m (Figure 4.8A) would also be consistent with an interpretation of a primarily helical protein at the A/W interface. Only further examination of dSP-C at additional surface pressures and in additional environments revealed: 1) the presence of a unique β-structure for the deacylated, amyloid form of this protein, and 2) that dSP-C is excluded from the membrane surface at high surface pressures.

dSP-C Secondary Structure at the A/W Interface

We have also used polarization-modulation infrared reflectance spectroscopy (PM-IRRAS) to study the structure of dSP-C and DPPC:DPPG/dSP-C monolayers *in-situ* at the A/W interface. PM-IRRAS has several advantages over conventional polarized IR reflectance spectroscopy for the study of monolayer films at the A/W interface, specifically the ability to discriminate against isotropic water and water vapor absorptions, and the ability to analyze the resulting spectra directly for the orientation and conformation of the interfacial monolayer [40]. However, PM-

IRRAS does have potential shortcomings when applied to monomolecular films. Because PM-IRRAS is based on the rapid modulation of polarized electromagnetic radiation reflected from the interface, one disadvantage of the technique is that the absence of a signal does not necessarily indicate the absence of a monolayer at the surface. Rather, the absence of a signal could indicate either an isotropic monomolecular film or a preferred monolayer orientation in which the transition dipole moment is oriented such that co-existing positive and negative signal contributions cancel one another [40]. Therefore, interpretation of PM-IRRAS spectra is best accomplished in conjunction with other information.

Figure 4.9 illustrates the amide I and amide II regions in PM-IRRAS spectra of dSP-C protein monolayers at the A/W interface acquired at different surface pressures. In the spectra shown in Figure 4.9A, the dSP-C protein was applied to the A/W interface at low surface pressure as an acidic solution of pH 1.8; spectra were acquired during compression of the monolayer to higher surface pressures. The subphase was 120 mM NaCl adjusted to pH 7. The most prominent band in this spectrum is the amide I vibration at 1656 cm^{-1}. As previously described, this wavenumber position corresponds to an α-helical conformation for the dSP-C monolayer, which also corresponds to the structure of dSP-C in solution at low pH (Figure 4.3). According to the PM-IRRAS "surface selection rule", strong positive bands in PM-IRRAS spectra indicate that the corresponding transition dipole moments are preferentially oriented in the plane of the surface [40]. If we assume that the protein's α-helix lies along the water surface, then (depending upon the choice made for the angle between the amide I transition moment and the long axis of the α-helix, see e.g. [54]), this implies that the dSP-C α-helix is oriented at a maximum angle of 29 – 38° from the interface.

Figure 4.9 PM-IRRAS spectra of dSP-C protein monolayers at the A/W interface. The dSP-C protein was applied in organic solution to the A/W interface at low surface pressure. Spectra were acquired at the indicated surface pressures during compression of the monolayer. The subphase was 120 mM NaCl adjusted to pH 7. (A) Spectra of dSP-C with spreading solution adjusted to pH 1.8. (B) Spectra of dSP-C with spreading solution adjusted to pH 7.

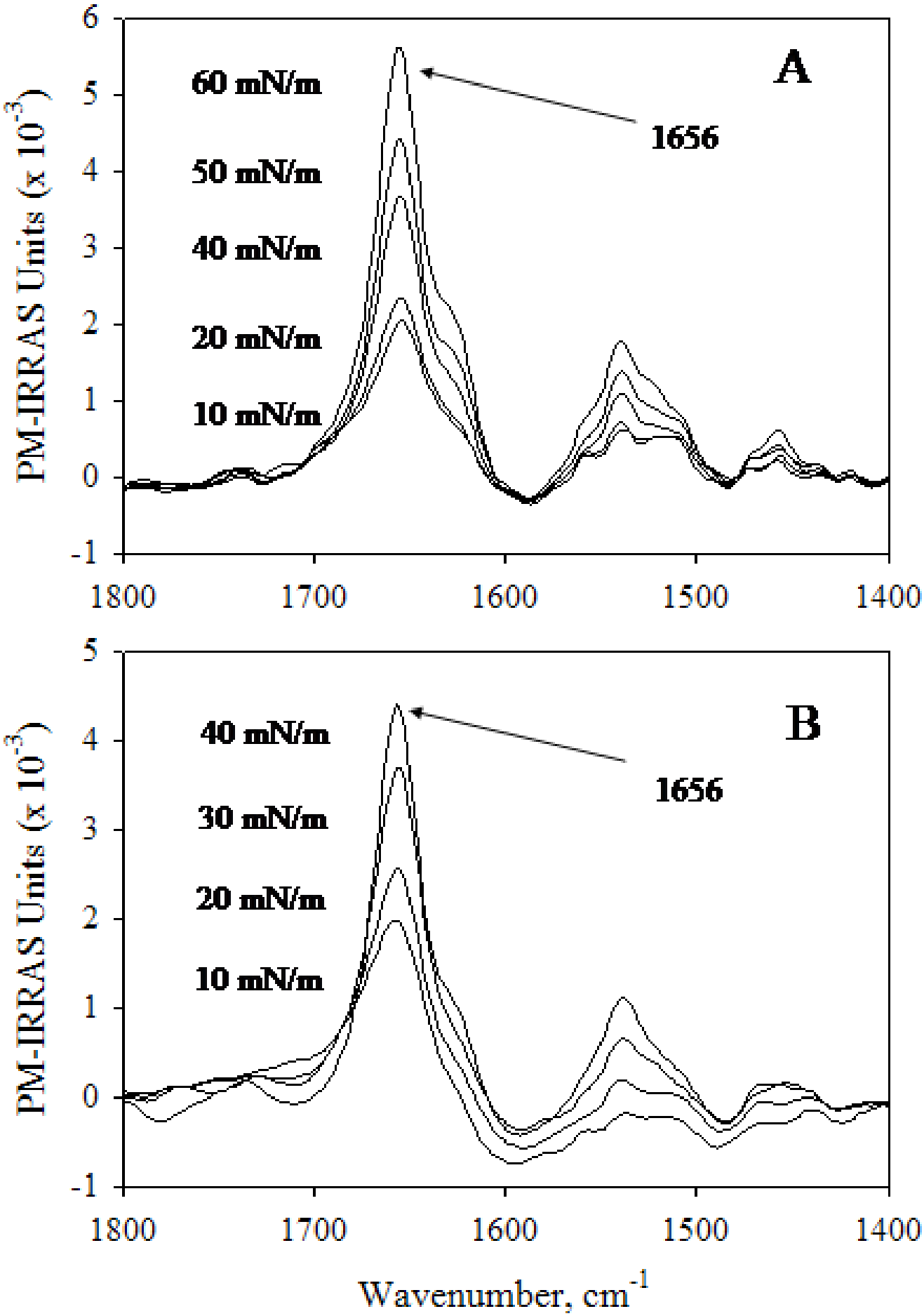
A
60 mN/m
50 mN/m
40 mN/m
20 mN/m
10 mN/m
1656
PM-IRRAS Units (x 10-3)
6
5
4
3
2
1
0
-1
1800
1700
1600
1500
1400
B
40 mN/m
30 mN/m
20 mN/m
10 mN/m
1656
PM-IRRAS Units (x 10-3)
5
4
3
2
1
0
-1
1800
1700
1600
1500
1400
Wavenumber, cm-1

Figure 4.9B presents PM-IRRAS spectra for dSP-C protein monolayers in which the dSP-C spreading solution was first neutralized to pH 7 before spreading at the A/W interface. Surprisingly, the PM-IRRAS spectra of a dSP-C monolayer spread from a neutral solution are indistinguishable from that of the dSP-C monolayer in acid form (Figure 4.9A), even though the same neutral dSP-C solution produced a transmission IR spectrum of a β-strand (Figure 4.3).

The helix-like PM-IRRAS spectra of a neutral dSP-C monolayer seen in Figure 4.9B are explainable if one assumes that the interfacial pH is significantly more acidic than the subphase pH. This may, in fact, be the case. Many previous surface chemistry publications have postulated that the pH of the water surface should be different than the bulk pH of the water subphase, although direct proof of such a difference is difficult to obtain; see, *e.g.* refs. cited in [55]. Two recent vibrational spectroscopy papers have offered new data to suggest that a ΔpH between bulk and interface does exist and that this pH difference depends upon the counterions present in solution [55, 56]. Using PM-IRRAS and sum frequency generation of fatty acid monolayers at the A/W interface, it was shown that the pH dependence of the acid dissociation reaction is strongly influenced by the subphase counterion. Specifically, with Na^+ ions, deprotonation of the fatty acid was very difficult to achieve, and required a pH of ~10 for half-neutralization of the fatty acid. This is 3 – 4 pH units greater than was the case with ions such as Cd^{2+} or Ca^{2+} and leads to an estimate that the H_3O^+ concentration at the interface could be on the order of 1,000 – 10,000 times greater than in the bulk [55]. Given the very sensitive pH dependence of the metastable α helix → β strand → α helix transition for dSP-C in solution that we demonstrated in Figures 4.3 and 4.5, it is possible that a highly acidic interfacial pH caused a conformational rearrangement of the neutral dSP-C from the β strand → α helix form. If this

can be confirmed, this would suggest a potential mechanism for the formation of amyloid SP-C fibrils at the alveolar interface in disease states such as PAP.

We have also used PM-IRRAS to investigate the structure of DPPC:DPPG/dSP-C lipid-protein monolayers at the A/W interface. Samples for study at the A/W interface were prepared identically to the lipid-protein samples described above for the solution studies (Figure 4.6) and ATR transfer studies (Figure 4.8). Figure 4.10 presents PM-IRRAS spectra for two types of lipid protein monolayers. Figure 4.10A shows the spectra of 10 wt% DPPC/DPPG/dSP-C in which the dSP-C stock solution was pH 1.8, while Figure 4.10B shows the spectra of 10 wt% DPPC/DPPG/dSP-C monolayers in which the dSP-C stock solution was first adjusted to pH 7 before preparing the sample. In Figure 4.10, a PM-IRRAS spectrum is presented for both types of lipid-protein monolayers at a low surface pressure (~5 mN/m) and at a high surface pressure (~40 mN/m).

As seen in both Figure 4.10A and 10B, the most prominent peak in the PM-IRRAS spectra of DPPC/DPPG/dSP-C monolayers is the lipid carbonyl band at ~1740 cm^{-1}. The strong downward sloping baseline between 1700 – 1650 cm^{-1} is due to the anomalous dispersion of the real part of the refractive index of water in this region, arising from the δ(H-O-H) deformation vibration of liquid water [40].

The most noticeable aspect of the amide I vibrations in the range 1700 – 1600 cm^{-1} for both types of DPPC/DPPG/dSP-C monolayers is the fact that they are extremely weak or non-existent. At low surface pressures (~5 mN/m), small positive PM-IRRAS signals in the range 1670 – 1660 cm^{-1} indicate a small amount of β-strand structure is present, as was also noticed in the ATR transferred films for these monolayers (Figure 4.8). However, no dominant amide I

Figure 4.10 PM-IRRAS spectra of dSP-C lipid-protein monolayers at the A/W interface. The monolayer was applied in organic solution to the A/W interface at low surface pressure. Spectra were acquired at the indicated surface pressures during compression of the monolayer. The lipid-protein film used was DPPC:DPPG (7:3) plus 10 wt% dSP-C. The subphase was 120 mM NaCl adjusted to pH 7. (A) Spectra of DPPC/DPPG/dSP-C with dSPC spreading solution adjusted to pH 1.8. (B) Spectra of DPPC/DPPG/dSP-C with dSP-C spreading solution adjusted to pH 7.

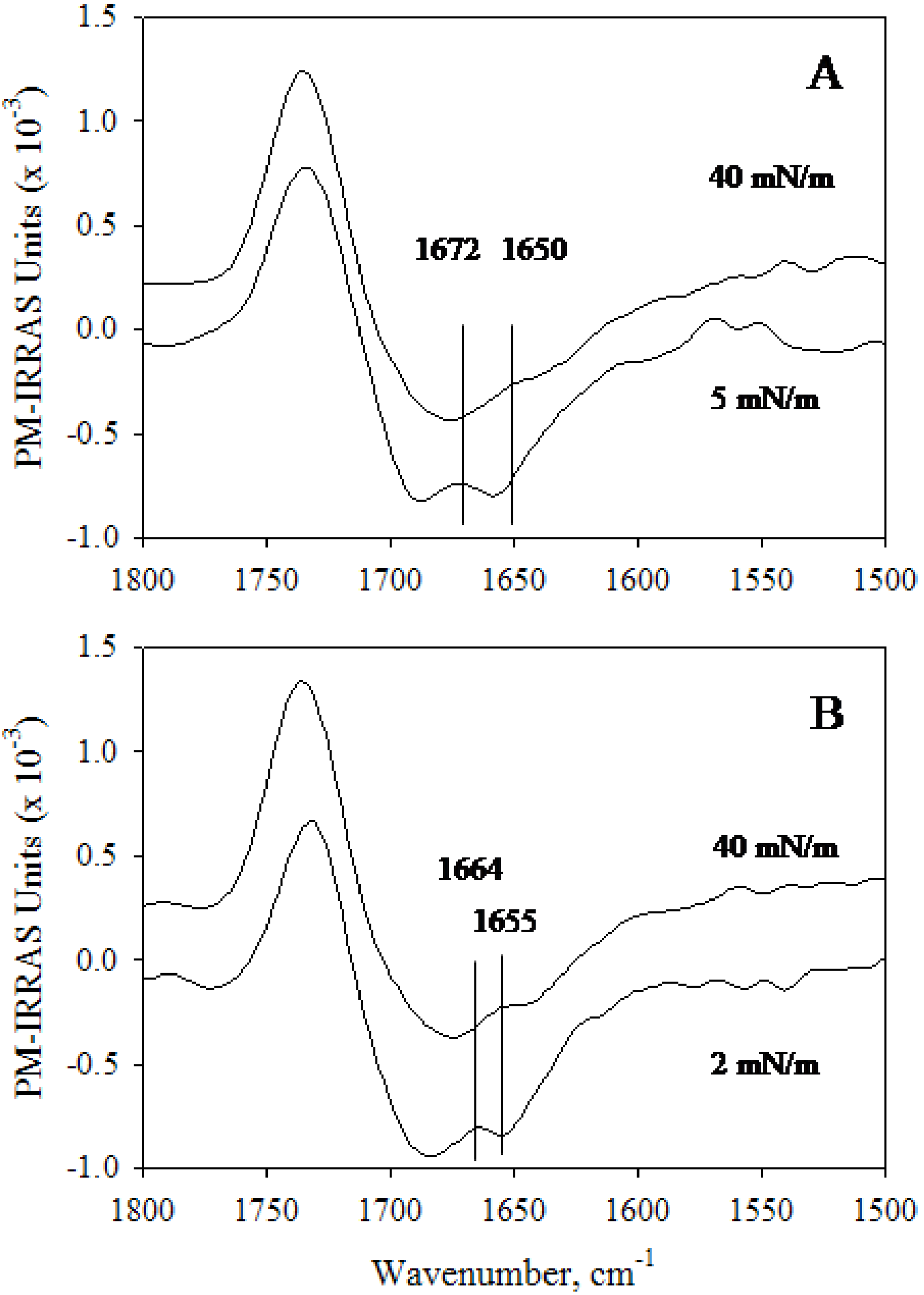
A
40 mN/m
5 mN/m
1672
1650
PM-IRRAS Units (x 10-3)
1.5
1.0
0.5
0.0
-0.5
-1.0
1800
1750
1700
1650
1600
1550
1500
B
40 mN/m
2 mN/m
1664
1655
PM-IRRAS Units (x 10-3)
Wavenumber, cm-1

vibration due to an α-helix conformation is seen in these spectra at either low or high surface pressures.

The most likely explanation for the absence of PM-IRRAS bands due to the α-helix in these spectra is that no preferential orientation exists for the helix fraction of dSP-C. While a defined orientation has been established for the fully acylated form of SP-C [23], we have shown that: 1) dSP-C in lipid-protein monolayers exists as a mixture of soluble β-strand and membrane-associated α-helix conformations, and 2) that the membrane-associated α-helix dissociates from the membrane or enters the subphase as a function of applied surface pressure. Since dSP-C readily dissociates from the interface (unlike fully acylated SP-C) it is unlikely to have a defined orientation in its membrane-associated form. A random or isotropic orientation of dSP-C would not produce a detectable PM-IRRAS signal.

Conclusions

We employed IR spectroscopy to study the pH dependence of the conformation of deacylated SP-C (dSP-C), which was observed to aggregate and form amyloid fibrils in solution. Several different IR techniques were used to study the structure of dSP-C in various environments. 1) Transmission IR spectroscopy was used to study the conformation of dSP-C in solutions and bulk liposomes. 2) Attenuated total reflectance (ATR) spectroscopy was used to study the structure of dSP-C in monomolecular films transferred onto solid substrates. 3) Photoelastic modulation IR reflection absorption spectroscopy (PM-IRRAS) was used to study the structure of dSP-C monolayers *in-situ* at the A/W interface. This work identified pH as a specific cause of conformational changes in dSP-C, and a possible contributor to amyloid fibril formation in pulmonary alveolar proteinosis. Our detailed conclusions are as follows.

- The formation of amyloid fibrils from dSP-C may be observed in solution using visible light microscopy. The visible images of the fibrils produced from dSP-C isolated in our laboratory are consistent with previously published images of amyloid fibrils isolated from the bronchoalveolar lavage of a clinical patient suffering from pulmonary alveolar proteinosis (PAP) and attributed to deacylated SP-C. Mass spectrometry (MALDI-TOF) confirmed that the dSP-C protein used in these experiments was in the deacylated forms.

- Solution phase IR spectra of dSP-C demonstrated that the deacylated protein at low pH primarily adopts an α-helical secondary structure similar to that of the fully acylated protein at neutral pH. However, as the pH is raised, an α-helix → β-strand conformational change occurs in dSP-C. The IR spectrum of dSP-C at neutral pH is consistent with a main conformation of short segments of twisted or coiled β-sheet strands or β-hairpins in an amyloid fibril structure. Deacylation of SP-C reduced, but did not eliminate, the helical content of the deacylated protein; residual α-helix structure was also present in dSP-C at neutral pH. The full α-helix structure of dSP-C is recoverable from the amyloid β-structure when the pH is lowered. When mixed with lipids in solution, dSP-C at neutral pH retains its amyloid fibril β-strand conformation when deposited from organic solution as a lipid-protein complex. In addition, the amyloid fibril structure of dSP-C is retained when it is incorporated into lipid-protein multilayers in aqueous solution.

- ATR-IR spectra of Langmuir-Blodgett monolayer films transferred to solid substrates demonstrated that the amyloid fibril β-strand conformation was absent in the IR spectrum of the L-B film. The absence of amyloid β-structure at the A/W interface

and in the L-B monolayers is likely due to the solubility of smaller dSP-C oligomers. A broad amide I contour centered at 1656 cm^{-1} indicated that an α-helical secondary structure was the primary conformation present in the L-B transferred films. However, the residual dSP-C α-helix was not strongly membrane-associated, as increasing the monolayer lateral surface pressure to 60 mN/m was sufficient to exclude all the remaining protein from the membrane interface.

- PM-IRRAS spectra of dSP-C protein monolayers *in-situ* at the A/W interface demonstrated that dSP-C exists as an α-helix oriented at a maximum of 29° - 38° from the interface when spread from a pH-adjusted, neutral solution, even though the same neutral dSP-C solution produced a transmission IR spectrum of a β-strand. We established that the dSP-C α-helix is metastable and pH-sensitive in solution; therefore, it is likely that a surface-specific mechanism caused a conformational rearrangement of the neutral dSP-C from the β strand → α helix form. The most probable explanation is that an increased concentration of H_3O^+ ion exists at the A/W interface and contributes to an effective low interfacial pH. If this can be confirmed, this would suggest a potential mechanism for the formation of amyloid SP-C fibrils at the alveolar interface in disease states such as PAP. PM-IRRAS was also used to study lipid-protein monolayers containing dSP-C *in-situ* at the A/W interface, but showed no discernable amide I band that could be attributed to an α-helix, suggesting that the residual dSP-C helix conformation seen in the ATR-IR spectra of transferred films is randomly or isotropically oriented prior to exclusion from the membrane interface.

Acknowledgements

The work described here was supported by the U.S. Public Health Service through National Institutes of Health grant EB001956 (R.A.D.). We thank Dr. Dennis Phillips of the Chemical and Biological Mass Spectrometry Facility at the University of Georgia for his help with the MALDI-TOF studies of dSP-C.

References

1. Notter, R.H., *Lung surfactants: basic science and clinical applications*. 2000, New York: Marcel Dekker, Inc.
2. Creuwels, L.A.J.M., L.M.G. van Golde, and H.P. Haagsman, *The pulmonary surfactant system: biochemical and clinical aspects.* Lung, 1997. **175**: p. 1-39.
3. Hunt, A.N., F.J. Kelly, and A.D. Postle, *Developmental variation in whole human lung phosphatidylcholine molecular species: a comparision of guinea pig and rat.* Early Hum. Develop., 1991. **25**: p. 157-171.
4. Kahn, M.C., et al., *Phosphotidylcholine molecular species of calf lung surfactant.* Am. J. Physiol., 1995. **13**: p. L567-L573.
5. Holm, B.A., et al., *Content of dipalmitoyl phosphatidylcholine in lung surfactant: ramifications for surface activity.* Pediatr. Res., 1996. **39**: p. 805-811.
6. Hawgood, S. and K. Schiffer, *Structures and properties of the surfactant-associated proteins.* Annu. Rev. Physiol., 1991. **53**: p. 375-394.
7. Johansson, J., T. Curstedt, and B. Robertson, *The proteins of the surfactant system.* Eur. Respir. J., 1994. **7**: p. 372-391.
8. Avery, M.E. and J. Mead, *Surface properties in relation to atelectasis and hyaline memrane disease.* Am. J. Dis. Child., 1959. **97**: p. 517-523.
9. Pison, U., et al., *Surfactant abnormalities in patients with respiratory failure after multiple trauma.* Am. Rev. Respir. Dis., 1989. **140**: p. 1033-1039.
10. Notter, R.H. and Z. Wang, *Pulmonary surfactant: physical chemistry, physiology and replacement.* Rev. Chem. Eng., 1997. **13**: p. 1-118.

11. Lewis, J.F. and A.H. Jobe, *Surfactant and the adult respiratory distress syndrome.* Am. Rev. Respir. Dis., 1993. **147**: p. 218-233.

12. Johansson, J., et al., *The NMR structure of the pulmonary surfactant-associated polypeptide SP-C in an apolar solvent contains a valyl-rich a-helix.* Biochemistry, 1994. **33**: p. 6015-6023.

13. Amrein, M., A. von Nahmen, and M. Sieber, *A scanning force and fluorescence light microscopy study of the structure and function of a model pulmonary surfactant.* Eur. Biophys. J., 1997. **26**: p. 349-357.

14. von Nahmen, A., et al., *The structure of a model pulmonary surfactant as revealed by scanning force microscopy.* Biophys. J., 1997. **72**: p. 463-469.

15. Kramer, A., et al., *Distribution of the surfactant-associated protein C within a lung surfactant model film investigated by near-field optical microscopy.* Biophys. J., 2000. **78**(1): p. 458-465.

16. Galla, H.J., et al., *The role of pulmonary surfactant protein C during the breathing cycle.* Thin Solid Films, 1998. **329**: p. 632-635.

17. Krüger, P., et al., *Effect of hydrophobic surfactant peptides SP-B and SP-C on Binary Phospholipid Monolayers. I. Fluorescence and dark-field microscopy.* Biophys. J., 1999. **77**: p. 903-914.

18. Krüger, P., et al., *Effect of the hydrophobic peptide SP-C on binary phospholipid monolayers. Molecular machinery at the air/water interface.* Biophys. Chem., 2002: p. In press.

19. Dluhy, R.A., *Infrared spectroscopy of biophysical monolayer filims at interfaces. Theory and applications*, in *Physical Chemistry of Biological Interfaces*, A. Baszkin and W. Norde, Editors. 2000, Marcel Deker: New York. p. 711-747.

20. Mendelsohn, R., J.W. Brauner, and A. Gericke, *External infrared reflection-absorption spectrometry. Monolayer films at the air-water interface.* Ann. Rev. Phys. Chem., 1995. **46**: p. 305-334.

21. Dluhy, R.A., et al., *Infrared spectroscopic investigations of pulmonary surfactant. Surface film transitions at the air-water interface and bulk phase thermotropism.* Biophys. J., 1989. **56**(6): p. 1173-1181.

22. Flach, C.R., et al., *Palmitoylation of lung surfactant protein SP-C alters surface thermodynamics, but not protein secondary structure or orientation in 1,2-dipalmitoylphosphatidylcholine Langmuir films.* Biochim. Biophys. Acta, 1999. **1416**(1-2): p. 11-20.

23. Gericke, A., C.R. Flach, and R. Mendelsohn, *Structure and orientation of lung surfactant SP-C and L-a-dipalmitoylphosphatidylcholine in aqueous monolayers.* Biophys. J., 1997. **73**(1): p. 492-499.

24. Pastrana-Rios, B., et al., *External reflection absorption infrared spectroscopy study of lung surfactant proteins SP-B and SP-C in phospholipid monolayers at the air/water interface.* Biophys. J., 1995. **69**(6): p. 2531-2540.

25. Bi, X., et al., *Secondary structure and lipid interactions of the N-terminal segment of pulmonary surfactant SP-C in Langmuir filims: IR reflection-absorption spectroscopy and surface pressure studies.* Biochemistry, 2002. **41**: p. 8385-8395.

26. Brockman, J.M., et al., *Effect of hydrophobic surfactant proteins SP-B and SP-C on binary phospholipid monolayers. II. Infrared external reflectance-absorption spectroscopy.* Biophys. J., 2002: p. In Press.

27. Shanmukh, S., et al., *Effect of hydrophobic surfactant proteins SP-B and SP-C on phospholipid monolayers. Protein structure studied using 2D IR and bn correlation analysis.* Biophys. J., 2002. **83**: p. 2126-2141.

28. Szyperski, T., et al., *Pulmonary surfactant-associated polypeptide C in a mixed organic solvent transforms from a monomeric alpha-helical state into insoluble beta-sheet aggregates.* Protein Science, 1998. **7**(12): p. 2533-2540.

29. Gustafsson, M., et al., *Amyloid fibril formation by pulmonary surfactant protein C.* FEBS Letters, 1999. **464**: p. 138-142.

30. Seymour, J.F. and J.J. Presneill, *Pulmonary alveolar proteinosis. Progress in the first 44 years.* Am J. Respir. Crit. Care Med., 2002. **166**: p. 215-235.

31. Gustafsson, M., et al., *The palmitoyl groups of lung surfactant protein C reduce unfolding into a fibrillogenic intermediate.* J. Mol. Biol., 2001. **310**: p. 937-950.

32. Kallberg, Y., et al., *Prediction of amyloid fibril-forming proteins.* J. Biol. Chem., 2001. **276**: p. 12945-12950.

33. Vandenbussche, G., et al., *Structure and orientation of the surfactant-associated protein C in a lipid bilayer.* Eur. J. Biochem., 1992. **203**: p. 201-209.

34. Wang, Z., et al., *Acylation of pulmonary surfactant protein-C is required for its optimal surface active interations with phospholipids.* J. Biol. Chem., 1996. **271**(32): p. 19104-19108.

35. Baatz, J.E., et al., *High yield purification of lung surfactant proteins SP-B and SP-C and the effects on surface activity.* Protein Express. Purificat., 2001. **23**(1): p. 180-190.

36. Shin, Y.S., *Spectrophotometric ultramicrodetermination of inorganic phosphorus and lipid phosphorus in serum.* Anal. Chem., 1962. **34**(9): p. 1164-1166.

37. Morrissey, J.H., *Silver stain for proteins in polyacrylamide gels: a modified procedure with enhanced uniform sensitivity.* Anal. Biochem., 1981. **117**: p. 307-310.

38. Cameron, D.G., J.K. Kauppinen, and D. Moffatt, *Precision in condensed phase vibrational spectroscopy.* Appl. Spectrosc., 1982. **36**(3): p. 245-50.

39. Blaudez, D., et al., *Polarization-modulated FT-IR spectroscopy of a spread monolayer at the air/water interface.* Appl. Spectrosc., 1993. **47**(7): p. 869-74.

40. Blaudez, D., et al., *Investigations at the air/water interface using polarization modulation IR spectroscopy.* J. Chem. Soc., Faraday Trans., 1996. **92**(4): p. 525-30.

41. Buffeteau, T. and M. Pezolet, *In situ study of photoinduced orientation in azopolymers by time-dependent polarization modulation infrared spectroscopy.* Appl. Spectrosc., 1996. **50**(7): p. 948-955.

42. Buffeteau, T., et al., *Orientational studies of polymers using polarization modulation IR linear dichroism: experimental procedure and quantitative analysis.* J. Chim. Phys. Phys.-Chim. Biol., 1993. **90**(7-8): p. 1467-89.

43. Goormaghtigh, E., V. Cabiaux, and J.-M. Ruysschaert, *Determination of soluble and membrane protein structure by Fourier transform infrared spectroscopy. I. Assignments and model compounds*, in *Physiochemical Methods in the Study of Biomembranes*, H.J. Hilderson and G.B. Ralston, Editors. 1994, Plenum Press: New York. p. 329-362.

44. Jackson, M. and H.H. Mantsch, *Biomembrane structure from FT-IR spectroscopy.* Spectrochim. Acta Rev., 1993. **15**: p. 53-69.

45. Kubelka, J. and T.A. Keiderling, *Differentiation of b-sheet forming structures: ab initio-based simulations of IR absorption and vibrational CD for model and protein b-sheets.* J. Am. Chem. Soc., 2001. **123**: p. 12048-12058.

46. Krimm, S. and J. Bandekar, *Vibrational spectroscopy and conformation of peptides, polypeptides, and proteins.* Adv. Prot. Chem., 1986. **38**: p. 181-364.

47. Harris, P.I., *Fourier transform infrared spectroscopic studies of peptides: potentials and pitfalls*, in *Infrared analysis of peptides and proteins: principles and applications*, B. Ram Singh, Editor. 2000, American Chemical Society: Washington, D.C. p. 54-95.

48. Silva, R.A.G.D., et al., *Folding studies on the human chorionic gonadatropin b-subunit using optical spectroscopy of peptide fragments.* J. Am.Chem.Soc., 2000. **122**: p. 8623-8630.

49. Kubelka, J. and T.A. Keiderling, *The anomalous infrared amide I intensity distribution in ^{13}C isotopically labelled peptide b-sheets comes from extended, multiple-stranded structures. An ab initio study.* J. Am.Chem.Soc., 2001. **123**: p. 6142-6150.

50. Koppaka, V. and P.H. Axelsen, *Accelerated accumulation of amyloid beta proteins on oxidatively damaged lipid membranes.* Biochemistry, 2000. **39**(32): p. 10011-10016.

51. Parker, F.S., *Applications of Infrared, Raman, and Resonance Raman Spectroscopy in Biochemistry*. 1983, New York: Plenum Press.

52. Johansson, J., *Membrane properties and amyloid fibril formation of lung surfactant protein.* Biochemical Society Transactions, 2001. **29**: p. 601-606.

53. Johansson, J., et al., *Secondary structure and biophysical activity of synthetic analogues of the pulmonary surfactant polypeptide SP-C.* Biochem. J., 1995. **307**: p. 535-541.

54. Buffeteau, T., et al., *Anisotropic optical constants of alpha-helix and beta-sheet secondary structures in the infrared.* Journal of Physical Chemistry B, 2000. **104**(18): p. 4537-4544.

55. Le Calvez, E., et al., *Effect of cations on the dissociation of arachidic acid monolayers on water studied by polarization-modulated infrared reflection-absorption spectroscopy.* Langmuir, 2001. **17**(3): p. 670-674.

56. Miranda, P.B., Q. Du, and Y.R. Shen, *Interaction of water with a fatty acid Langmuir film.* Chem. Phys. Lett., 1998. **286**: p. 1-8.

CHAPTER 5

kv CORRELATION ANALYSIS: A QUANTITATIVE TWO-DIMENSIONAL IR CORRELATION METHOD FOR ANALYSIS OF RATE PROCESSES WITH EXPONENTIAL FUNCTIONS.[1]

[1]Reproduced with permission from "Shanmukh, S. and Dluhy, R.A. Journal of Physical Chemistry 2004"
© 2005 American Chemical Society

Abstract

A modified two-dimensional infrared correlation technique called $k\nu$ correlation analysis is introduced. In this method, an asynchronous cross-correlation is performed between a set of N infrared spectra undergoing a dynamic intensity variation against a set of exponential functions that encompass a user-defined range of rate constants. The observed correlation intensities are a function of the rate constant of the exponential function and the spectral frequency. The $k\nu$ correlation plots reveal the rate relationships between different molecular groups in terms of a quantitative and tangible parameter, k, which is the rate constant of the exponential function used in the correlation. A new parameter, the effective rate constant, k_{eff}, is defined as the point of maximum correlation intensity at particular frequencies in the plot of k *vs.* ν. The calculated values of k_{eff} represent the relative rates at which the intensities of the spectral bands change during the course of the dynamic experiment. As a result, these k_{eff} values are comparable and can be used to assign quantitative rate relationships.

Using simulated IR spectra, it was shown that the k_{eff} parameter is sensitive to the relative order in which the intensity change occurs, while the size of the correlation peaks gives an indication of the magnitude of the intensity change. Spectral bands that vary the rate at which their intensity changes in a dynamic data set can be distinguished based on the signs of their peaks in the $k\nu$ correlation plots. We applied the $k\nu$ correlation analysis method to the time-dependent IR spectra of the photo-initiated polymerization reaction of ethyl 2-cyanoacrylate. Analysis of the k_{eff} effective rate constants showed that vibrational modes corresponding to the monomeric and polymeric cyanoacrylate molecules react differently depending on whether an inhibitor is present.

Introduction

Two dimensional infrared correlation spectroscopy (2D-IR) has proven to be a valuable tool due to its ability to enhance spectral resolution and identify overlapped spectral features[1-3]. Two-dimensional IR spectroscopy is based on the correlation of dynamic spectral variations induced by an external sample perturbation. The effect of these perturbation-induced changes in the local molecular environment is manifested as either time or external physical variable dependent changes in IR spectral parameters. These resulting dynamic spectra are subject to a cross-correlation analysis that produces two-dimensional maps that can enhance spectral information by spreading out the IR band intensities along two orthogonal axes. Two-dimensional spectroscopy has particular advantages in simplifying complex spectra, identifying inter- and intramolecular interactions, and facilitating band assignments[4].

Literature references to 2D IR correlation analysis have predominately been in the area of polymer structure, an application for which the method was first developed[5]. However, the last few years has seen increasing application of this methodology to other scientific areas, including biochemistry[6-8] and surface monomolecular films[9-12]. Studies using 2D hetero-spectral correlations have appeared that enable comparisons to be made among a number of spectral techniques[13, 14].

Standard 2D IR methods have been most successfully employed in simplifying complex spectra and facilitating band assignments through resolution enhancement[15]. In addition to these uses, 2D IR can also be used to determine the temporal order of events that occur in a set of dynamically varying spectra upon sample perturbation. The basis for this determination is the relative signs of the synchronous and asynchronous cross-peak at coordinate (ν_1, ν_2) in the 2D correlation plots[2].

Although standard 2D IR methods may be used to determine the relative sequence of molecular events, this procedure tends to be difficult to implement for highly overlapped spectra and may lead to uncertainties while comparing the signs of the numerous cross peaks in the synchronous and asynchronous correlation plots. In order to more quantitatively describe the degree of coherence between spectral intensity changes and the sequence of molecular events in a set of dynamic spectra, we previously developed a new approach that utilizes defined mathematical models as complementary functions to experimental data sets in the correlation algorithm[16]. This approach makes use of the fact that infrared intensity variations can take the shape of or can be approximated by common mathematical functions. By correlating such functional forms against experimental spectra, it is possible to obtain quantitative information about phase relationships. The first method developed under this approach was $\beta\nu$ correlation analysis, which makes use of sinusoidal curves that vary in their phase angles[16]. An asynchronous correlation was performed between the sinusoidal curves and the experimental data set and a new parameter called the effective phase angle, β_e, was used to describe the relative relationship between the signal variations. Bands with larger β_e values were shown to undergo changes earlier than bands with smaller β_e values. We have applied $\beta\nu$ correlation analysis to changes in the IR spectra of surface monolayers and showed how the relative rates of acyl chain and methyl group reorientation could be quantitatively determined[11], and have also applied this method in probing the conformational states and relative reorientation rates of proteins at surfaces[12].

In the current article we report on a new model-based approach to 2D correlation analysis that substitutes a different mathematical function for the sine function used in the $\beta\nu$ method. The selection of a particular model correlation function is dictated by the similarity of the

function waveform with common infrared intensity variation profiles that are applicable to molecular systems; in the present case this is an exponential function. A new model-based 2D correlation method called *kv correlation analysis* is introduced in which a set of dynamic spectra are correlated against a set of exponential curves that differ in their rate constants. As in the previously described *βv* correlation method, *kv* correlation analysis employs an asynchronous cross correlation since this calculation is more sensitive to intensity changes and spectral resolution enhancement than is the synchronous correlation. A quantitative parameter, the *effective rate constant*, k_{eff}, is defined and used to establish relative rate relationships between spectral intensity variations. Different intensity variation models composed of simulated spectra are used to illustrate the ability of the *k*v correlation method in distinguishing between processes occurring with different rates of change. This method as well as the βv correlation method can be applied to spectroscopic methods such as Raman and Near Infrared spectroscopy to obtain information about relative rates. To demonstrate the utility of the *kv* method, we studied the anionic polymerization of cyanoacrylate using the classic metallocene ruthenocene as a photoinitiator. This reaction was monitored using ATR-IR spectroscopy and *k*v correlation analysis was applied to the time-dependent spectra to elucidate the rates of intensity change in the different vibrational modes attributable to the monomeric and the polymeric cyanoacrylate species.

Materials and Methods

Reagents.

Ruthenocene ($RuCp_2$; CP_2 is η^5-C_5H_5) was obtained from Sigma-Aldrich (St. Louis, MO) at 97% purity and was further purified by vacuum sublimation. High purity ethyl 2-cyanoacrylate (CA) was obtained from Loctite Corp. (Rocky Hill, CT) at 99.9% purity and was used as

received; the colorless liquid monomer contained trace amounts of hydroquinone and methane sulfonic acid as scavengers for adventitious radical and basic impurities, respectively. Tetrohydrofuran (THF) was obtained from Fisher Scientific (Fairlawn, NJ) and used without further purification.

IR Spectroscopy.

Attenuated total reflectance infrared (ATR-IR) spectra were acquired using a BioRad/Digilab (Cambridge, MA) FTS-60 FT-IR spectrometer equipped with a LN_2-cooled, narrow band HgCdTe detector. Kinetic IR studies of the rate of photo-initiated polymerization of ethyl 2-cyanoacrylate were conducted on freshly prepared solution of CA containing the ruthenocene photoinitiator. A solution of CA in THF (2:3 v:v) was prepared to which $RuCp_2$ was added at a concentration of 12 mM. A small volume (~0.3 mL) of this sample solution was placed on a germanium ATR crystal mounted in a horizontal ATR accessory (CIC Photonics, Albuquerque, NM) within the sample chamber of the spectrometer. Polymerization of the CA sample commenced upon irradiating the sample with the polychromatic output of a mercury-arc lamp at 110 mW. Incident light intensity at the sample was measured with a Coherent (Santa Clara, CA) Model 10 power meter. ATR-IR spectra were collected every 1.5 s using the following parameters: one co-added scan, triangular apodization with one level of zero-filling, and 4 cm^{-1} resolution. Spectra were analyzed with the GRAMS 32/AI spectra software package (Ver. 6.0, Galactic Industries, Salem, NH).

Calculation of 2D IR Correlation Spectra.

The 2D IR synchronous spectrum, $\Phi(\nu_1,\nu_2)$, and the asynchronous spectrum, $\Psi(\nu_1,\nu_2)$, were calculated as previously described[11, 12, 16]. These algorithms use the most recent mathematical formulation in which a Hilbert transform is utilized for calculating the

asynchronous spectrum rather than the more commonly employed Fourier transform[17]. In all cases the average spectrum was subtracted from each time-dependent, sequentially obtained ATR-IR spectrum to produce a set of dynamic IR spectra. The resulting dynamic spectra were then used in the correlation analysis. Before 2D correlation analysis, the dynamic spectra were baseline corrected using the GRAMS/AI spectral software package.

The asynchronous 2D plots presented in this article were calculated using 2D IR correlation analysis algorithms written in our laboratory using the MATLAB programming environment (Version 6, The MathWorks, Inc., Natick, MA).

Simulated Spectra.

Computer-generated simulated IR spectra were calculated using an Array Basic program written in our laboratory for the Grams/AI environment (R. Dluhy, unpublished). All synthetic spectra were calculated using Lorentzian band shapes with a resolution of 1.0 cm^{-1}. Full widths at half-maximal peak intensity for the simulated band shapes were 10.0 cm^{-1}. No additional noise was added to the simulated spectra.

Results and Discussion

I. $k\nu$ Correlation Analysis: A modified 2D IR Method for Calculating Exponential Correlations.

In previous work, we introduced a modified two-dimensional infrared correlation method, called $\beta\nu$ correlation analysis, for quantitatively determining the relative rates of intensity change and the degree of coherence between intensity variations in a discrete set of dynamic spectra[16]. In this method, a cross correlation is performed between a set of spectra undergoing some dynamic variation against a simple mathematical function, which we chose to be a sine function. In $\beta\nu$ correlation analysis, the calculated correlation intensities are a function of the phase angle (β) of the sinusoidal function and the spectral frequency (ν). The maximum positive correlation

intensity will be observed at one point in the (β, ν) correlation plot. This point is used to define a new parameter, the effective phase angle, β_e , of $f(\nu, n)$ – where, for the range $360^o \geq \beta \geq 0^o$, β_e is simply equal to $\beta + 90^o$. We have applied classical 2D IR as well as $\beta\nu$ correlation spectroscopy to several model systems, including the *in-situ* IR spectroscopy of monomolecular films [11, 12]. The $\beta\nu$ method enabled us to identify specific molecular conformations and to follow the reorientation of these molecular groups as a function of an external perturbation. In a related work Eads et al applied the generalized 2D IR correlation technique to NMR spectra using both experimental cross correlation as well as model based correlation analyses in order to obtain quantitative diffusion coefficients[18]. The model data set used for the analysis comprised of a set of Gaussian curves generated with logarithmically spaced diffusion coefficients.

In the current work, we have expanded the scope of this modified 2D IR method by replacing the mathematical function used in the correlation analysis. The new method assumes an exponential relationship between spectral intensities in the dynamic data set. In this updated approach, a mathematical asynchronous cross-correlation is performed between a set of N infrared spectra undergoing a dynamic intensity variation against a set of exponential functions that encompass a range of rate constants. In keeping with the terminology introduced with the $\beta\nu$ method, we call this new method $k\nu$ correlation analysis, since the calculated correlation intensities are a function of the rate constant (k) of the exponential function and the spectral frequency (ν). The $k\nu$ two-dimensional correlation plots reveal rate relationships between different molecular events in terms of a quantitative and tangible parameter, k, which is the rate constant of the exponential function used in the correlation. As such, it is a model-dependent 2D IR correlation method analogous to the $\beta\nu$ correlation analysis described in our earlier papers.

An asychronous *kv* correlation analysis is mathematically described in Equation 1. The correlation intensity Ψ at some point (ν, *k*) represents the correlation of the measured IR spectral intensity $y(\nu, n_j)$ with the mathematical function *exp(-kt+R)*. In Equation 1, *y* is the spectral intensity; ν is the frequency or wavenumber; n_j is the number of the spectrum in the ordered sequence where the first spectrum number is zero; *k* is the rate constant of the exponential curve; *N* is the total number of spectra used in the calculation; *R* is a constant matrix, and M_{jk} is the Hilbert-Noda transform matrix[17] defined in Equation 2.

$$\Psi(\nu,k) = \frac{1}{N-1}\sum_{j=0}^{N-1} y(\nu,n_j)\cdot\sum_{k=0}^{N-1} M_{jk}\cdot\exp(-kt+R) \tag{1}$$

$$M_{jk} = \begin{cases} 0 & \text{if } j = k \\ 1/\pi(k-j) & \text{otherwise} \end{cases} \tag{2}$$

The asynchronous *kv* correlation intensity can be either positive or negative depending on the direction and magnitude of intensity change. Based on studies done on simulated spectra, which are described below, positive peaks are observed when the rate of intensity variation increases and negative peaks are observed when the rate of intensity variation decreases. In the cases of bands where the direction of intensity change alters during the course of the experiment, or when the rate of intensity change varies, both positive and negative correlation peaks may be observed for a single spectral band.

A new parameter, the *effective rate constant*, k_{eff}, is defined from the *kv* correlation plot. This k_{eff} parameter is defined as the point of maximum correlation intensity in the plot of *k vs.* ν. The range of values that k_{eff} can take may be arbitrarily set and is between 1 and 7 in the current work. The calculated values of k_{eff} are representative of the rates at which the intensities of the

spectral bands change during the course of the dynamic experiment. These k_{eff} values are not the actual kinetic rate constants *per se*, but are instead the *relative differences* of the rates defined by the rate constants used in the 2D correlation calculation. As a result, these k_{eff} values are comparable and can be used to assign quantitative rate relationships. Events at frequencies with a larger k_{eff} value occur earlier than events at frequencies with smaller k_{eff} values. Positive and negative k_{eff} values are comparable and hence no manipulation of the spectra or the correlation plots is required to compare increasing and decreasing bands.

The $k\nu$ plots of effective rate constants *vs.* wavenumber were calculated using $k\nu$ correlation analysis algorithms written in our laboratory using the MATLAB programming environment. As is the case with the traditional 2D IR correlation plots, the spectra used in the $k\nu$ plots were baseline corrected before calculation using the GRAMS/AI spectral software package.

II. Simulated Spectral Models Used to Illustrate the $k\nu$ Method.

In this section we explore how specific mathematical forms of spectral intensity variation affect the calculated k_{eff} values. Within each model, we describe several different possible paths of intensity variation for an absorption band in a set of dynamic spectra. Each model system can then be used to explore how the calculated k_{eff} values respond to the specific forms of intensity variation. In doing this, we can establish a relationship between the calculated k_{eff} values and the relative rates of intensity change for the time-resolved absorption bands in a dynamic data set.

Model A.

The first model that we consider for the application of the exponential correlation method consists of four spectral bands that exhibit linear increases in intensity through the data set (Figure 5.1A). In Model A, three of the four spectral bands increase in intensity, but in a two-stage increment in which there is a delay in the response of the individual features to the external

perturbation. Figure 5.1B illustrates the variation of the band intensity for the four peaks in Model A through the data set. From the intensity changes seen in Figure 5.1B, the sequence of spectral events can be summarized as $\nu_2 \rightarrow \nu_3 \rightarrow \nu_1 \rightarrow \nu_4$ where the symbol "→" means "occurs before". A set of dynamic spectra was generated from the spectra in Figure 5.1A by subtracting the reference (average) spectrum from each individual spectrum. When calculating $k\nu$ correlations for synthetic spectra, we used the average spectrum in the dynamic data set as the reference spectrum. Both the average spectrum and the zero spectrum were tried as references, however the average spectrum was found to give more accurate results with these intensity models.

An asynchronous $k\nu$ correlation was performed between the dynamic spectra generated from Figure 5.1A and a set of exponential curves that differed in their rate constants. The resulting $k\nu$ correlation plot is shown in Figure 5.1C. In this plot, each of the four simulated peaks contain positive k_{eff} values, which is expected since all the spectral intensities increase during the course of the data set. The k_{eff} values corresponding to the four spectral bands are shown in Table 5.1 and can be used to determine the relative rates of intensity change in the four peaks in the model described previously. The k_{eff}^{+} values $0.82 > 0.5 > 0.35 > 0.27$ indicate the order of change in spectral intensities to be $\nu_2 \rightarrow \nu_3 \rightarrow \nu_1 \rightarrow \nu_4$, as was defined in the model. This result clearly demonstrates that k_{eff} values can be used to establish the relative rates of change in the band intensities of a set of time-resolved spectra whose intensities change in a defined fashion.

Figure 5.1C also shows that the ν_2 band at 2050 cm^{-1} has a negative k_{eff} value ($k_{eff}^{-} = 0.13$) associated with it. The negative peak in the $k\nu$ plot is explained by the nature of the intensity variation for this band. As seen in Figure 5.1B, the 2050 cm^{-1} band intensity varies as a two-

Figure 5.1 Simulated spectral model 'A' with multi-step linear intensity changes. (A) Simulated infrared spectrum with bands at ν_1 = 2000 cm^{-1}, ν_2 = 2050 cm^{-1}, ν_3 = 2100 cm^{-1} and ν_4 = 2150 cm^{-1}. (B) Spectral intensity profile for the spectral bands. (C) *kv* correlation plot of the above model.

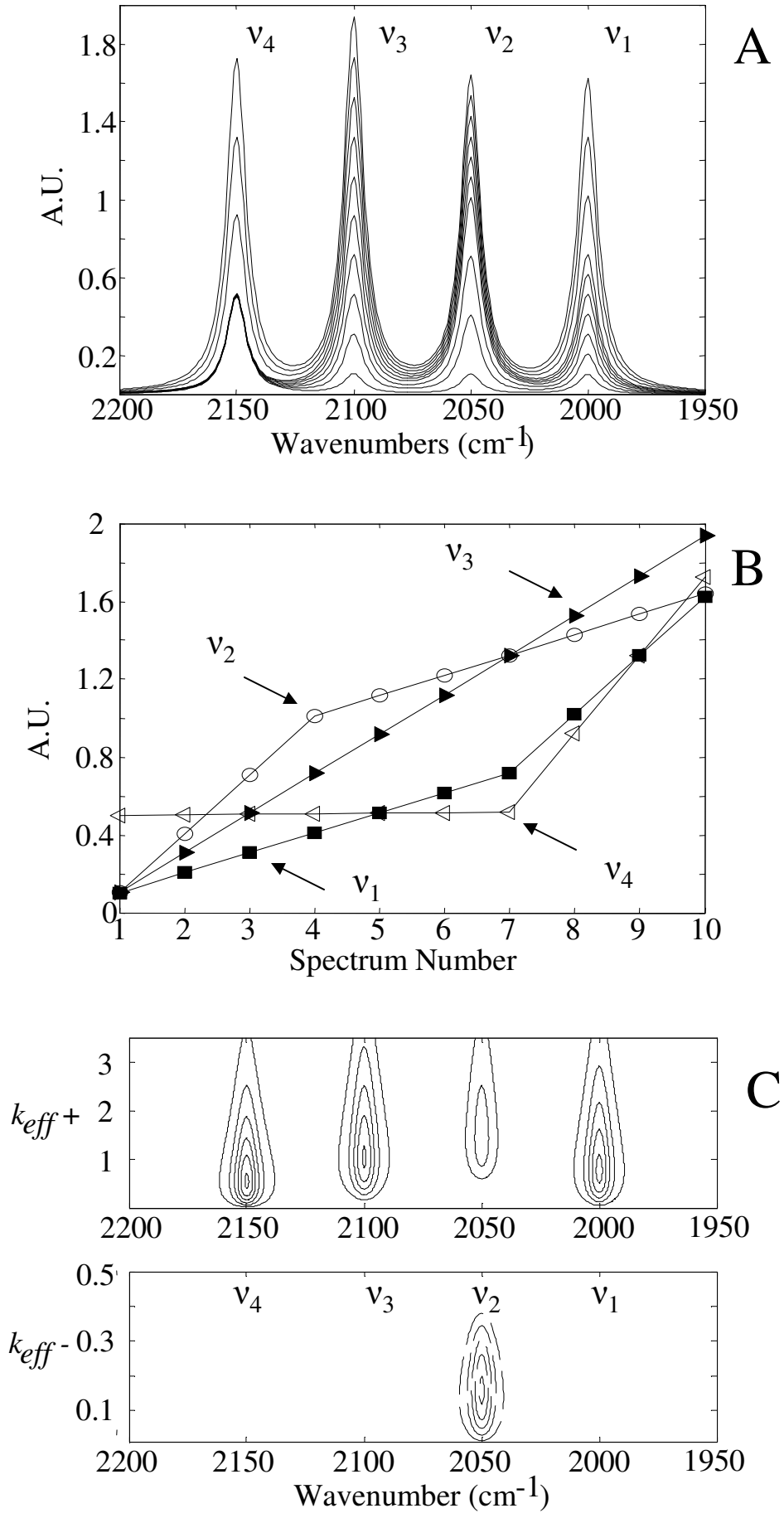
A
ν4
ν3
ν2
ν1
A.U.
1.8
1.4
1
0.6
0.2
2200
2150
2100
2050
2000
1950
Wavenumbers (cm-1)
B
ν3
ν2
ν4
ν1
A.U.
2
1.6
1.2
0.8
0.4
0
1
2
3
4
5
6
7
8
9
10
Spectrum Number
C
keff +
3
2
1
2200
2150
2100
2050
2000
1950
keff -
0.5
0.3
0.1
ν4
ν3
ν2
ν1
2200
2150
2100
2050
2000
1950
Wavenumber (cm-1)

Table 5.1

Values of the effective rate constants k_{eff}^{+} and k_{eff}^{-}, obtained from the $k\nu$ correlation plot in Figure 5.1. These effective rate constants were obtained from the simulated IR spectra in Model A that represents a two-step linear intensity change.

Band Assignment	Wavenumber (cm^{-1})	k_{eff}^{+}	k_{eff}^{-}
ν_1	2000	0.35	-
ν_2	2050	0.82	0.13
ν_3	2100	0.50	-
ν_4	2150	0.27	-

stage linear function – initially with a large positive slope, and then with a smaller positive slope (*i.e.* the rate of change decreases). The $k\nu$ correlation method calculates the decrease in the rate of intensity change as a negative k_{eff} value since the rate of change decreased relative to the initial rate. The presence of a negative correlation peak for the 2050 cm^{-1} band illustrates that the $k\nu$ correlation method is sensitive to the <u>*change*</u> in the relative rates of the band intensities through the dynamic data set. This is an advantage of the $k\nu$ method over the previously published $\beta\nu$ correlation analysis method.

<u>*Model B*</u>.

This model, illustrated in Figure 5.2A, contains four simulated bands in which the band intensities increase in a two-stage linear fashion. In this case, all band intensities increase linearly after an initial lag period that differs for each band. The model was constructed such that the intensity of the band at ν_1 at 2000 cm^{-1} begins to increase before the ν_2 band at 2050 cm^{-1} increases, followed by the intensity increases of ν_3 (2100 cm^{-1}) and ν_4 (2150 cm^{-1}). The sequence of spectral events in Figures 2A and 2B can be summarized as $\nu_1 \rightarrow \nu_2 \rightarrow \nu_3 \rightarrow \nu_4$. A $k\nu$ correlation was performed on the dynamic spectra generated from the spectral set. The resulting plot is presented in Figure 5.2C and the corresponding k_{eff} values are listed in Table 5.2. Four positive peaks were generated in the corresponding $k\nu$ plot shown in Figure 5.2C. From the k_{eff} values the following order of relative rates can be determined; ν_1 ($k_{eff}^{+} = 0.45$) $\rightarrow$ ν_2 ($k_{eff}^{+} = 0.39$) $\rightarrow$ ν_3 ($k_{eff}^{+} = 0.35$) $\rightarrow$ ν_4 ($k_{eff}^{+} = 0.30$). This corresponds to the order that was built into this intensity change model. This particular model indicates that the k_{eff} values are sensitive to the <u>*order*</u> in which the intensity change occurs, while the magnitude of the bands in the $k\nu$ plot reflects the <u>*degree*</u> of the spectral intensity variation.

Figure 5.2 Simulated spectral model 'B' with multi-step linear intensity changes. (A) Simulated infrared spectrum with bands at ν_1 = 2000 cm-1, ν_2 = 2050 cm-1, ν_3 = 2100 cm-1 and ν_4 = 2150 cm-1. (B) Spectral intensity profile for the spectral bands. (C) kν correlation plot of the above model.

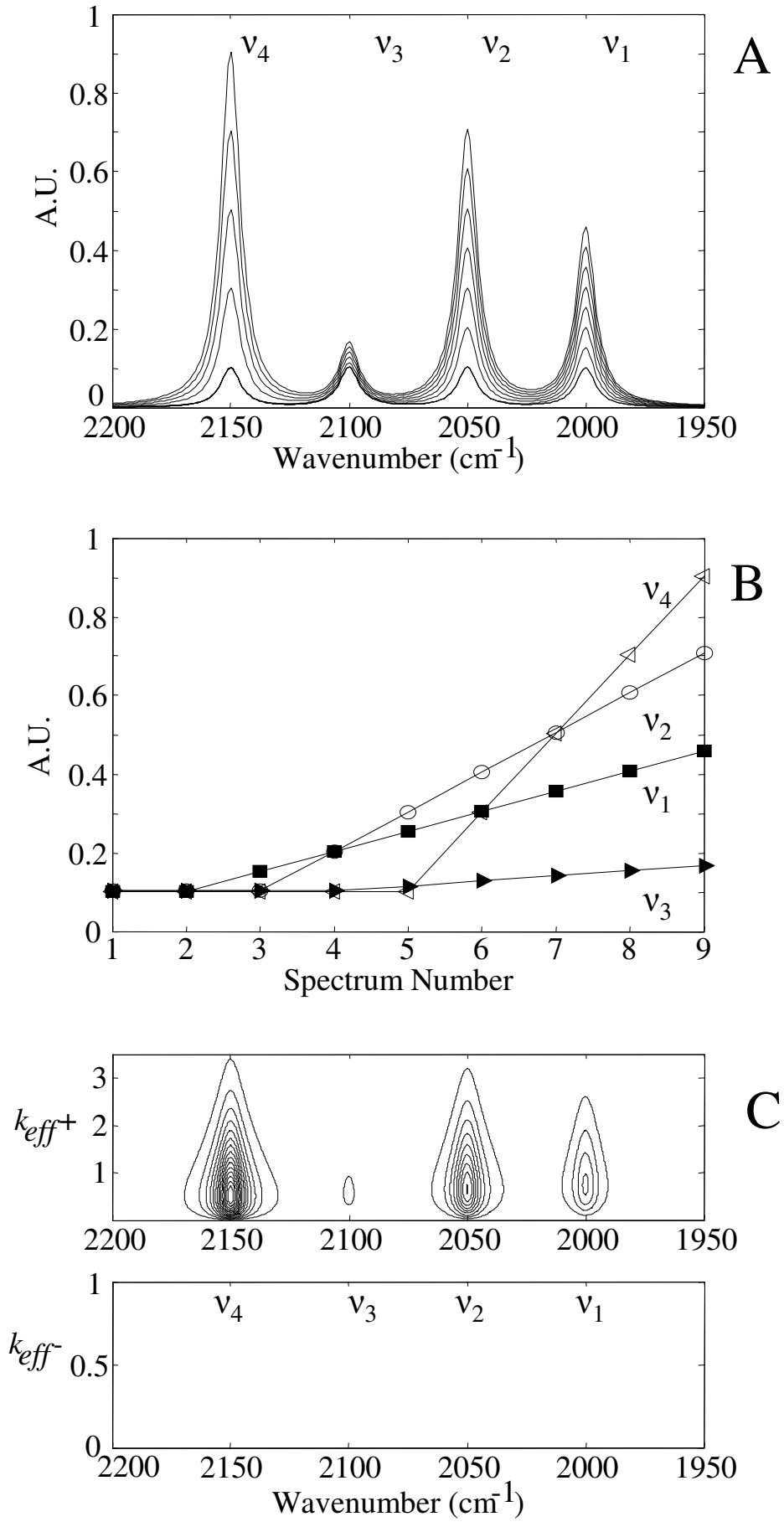
A
ν4
ν3
ν2
ν1
A.U.
Wavenumber (cm-1)
B
Spectrum Number
C
keff+
keff-

Table 5.2

Values of the effective rate constants k_{eff}^{+} and k_{eff}^{-}, obtained from the $k\nu$ correlation plot in Figure 5.2. These effective rate constants were obtained from the simulated IR spectra in Model B that represents a delayed linear intensity change.

Band Assignment	Wavenumber (cm^{-1})	k_{eff}^{+}	k_{eff}^{-}
ν_1	2000	0.45	-
ν_2	2050	0.39	-
ν_3	2100	0.35	-
ν_4	2150	0.30	-

Model C.

As seen in Figures 3A & 3B, this model consists of four spectral bands whose intensities increase exponentially with different rate constants. A $k\nu$ correlation was performed on the dynamic spectra generated from the spectral set and the resulting correlation plot is presented in Figure 5.3C with the corresponding k_{eff} values listed in Table 5.3. The k_{eff} values for all four bands are positive since the bands are exponentially increasing in intensity in the positive direction. In addition, all the bands in the simulated spectrum have approximately the same k_{eff}^{+} value of 0.8, which means that there is no asynchronicity between the rates of intensity change in these bands.

Model D.

The final model in the analysis, shown in Figures 4A and 4B, consists of four simulated spectral bands whose intensities decrease exponentially with different rate constants. In terms of 2D correlation spectroscopy, an exponential decrease in band intensity can be understood as a delay in the response of the individual features to the external perturbation. A $k\nu$ correlation was performed between the dynamic data set calculated from the spectra in Figure 5.4A and a set of decreasing exponential curves that differed in their rate constants. The resulting $k\nu$ plot is presented in Figure 5.4C and the corresponding k_{eff} values for the observed peaks are listed in Table 5.4. As seen in Figure 5.4C, the $k\nu$ correlation plot for this model has negative peaks at all frequencies denoting a decrease in band intensity through the data set. However the different k values calculated for each band denote the difference in the rate of decrease of the individual band intensities. From the negative k_{eff} values it can be seen that the ν_1 band at 2000 cm^{-1} (k_{eff}^{-} = 2.2) has a higher rate of intensity change than do than the bands at ν_2 (2050 cm^{-1}, k_{eff}^{-} = 1.8), ν_3

Figure 5.3 Simulated spectral model 'C' with bands whose intensities increase exponentially. (A) Simulated infrared spectrum with bands at ν_1 = 2000 cm^{-1}, ν_2 = 2050 cm^{-1}, ν_3 = 2100 cm^{-1} and ν_4 = 2150 cm^{-1}. (B) Spectral intensity profile for the spectral bands. (C) *kv* correlation plot of the above model.

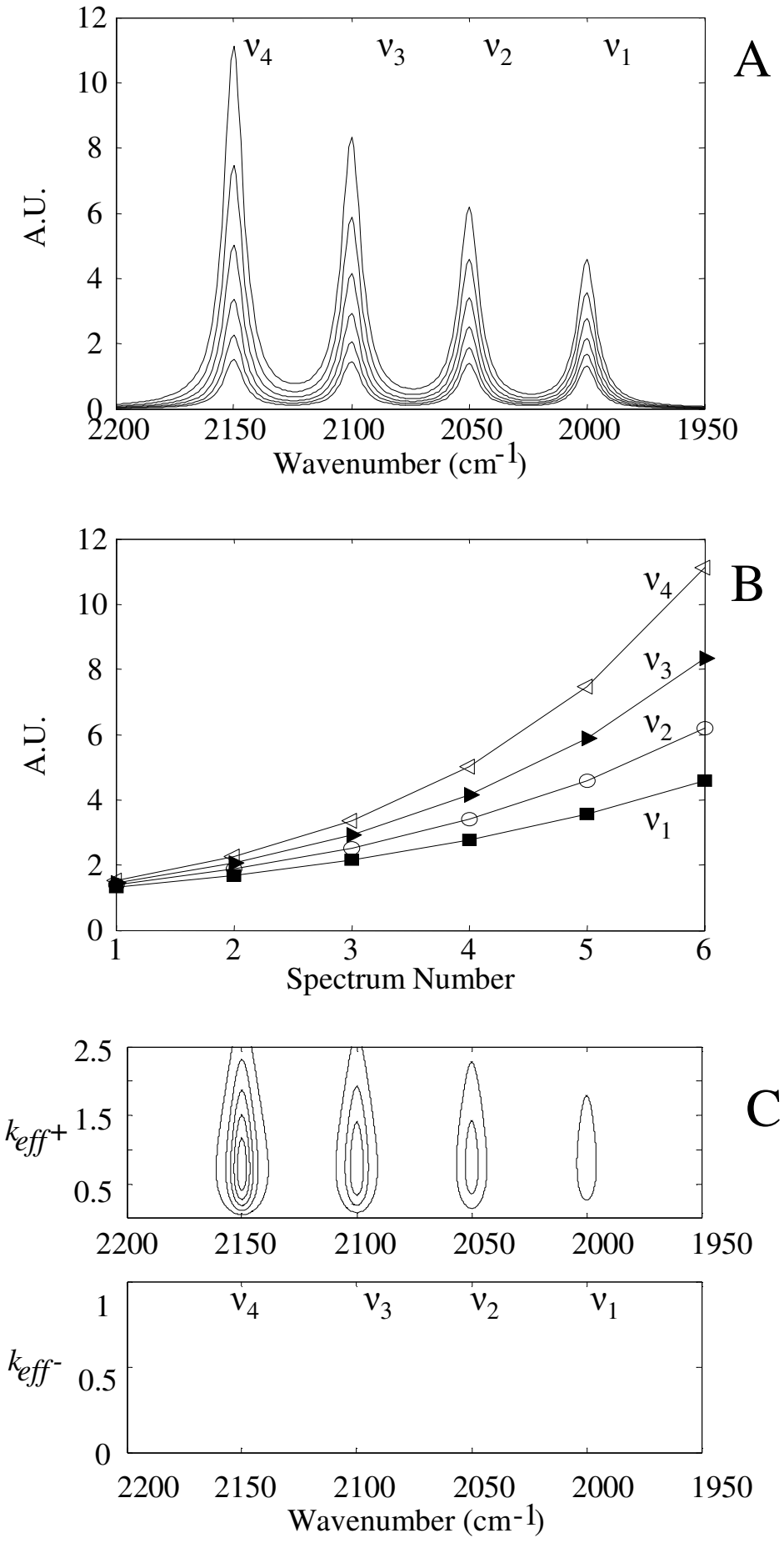
A
A.U.
Wavenumber (cm-1)
ν4
ν3
ν2
ν1
B
A.U.
Spectrum Number
C
keff+
keff-

Table 5.3

Values of the effective rate constants k_{eff}^{+} and k_{eff}^{-}, obtained from the $k\nu$ correlation plot in Figure 5.3. These effective rate constants were obtained from the simulated IR spectra in Model C that represents an increasing exponential intensity change.

Band Assignment	Wavenumber (cm^{-1})	k_{eff}^{+}	k_{eff}^{-}
ν_1	2000	0.7	-
ν_2	2050	0.8	-
ν_3	2100	0.8	-
ν_4	2150	0.8	-

Figure 5.4 Simulated spectral model 'D' with bands whose intensities decrease exponentially. (A) Simulated infrared spectrum with bands at ν_1 = 2000 cm^{-1}, ν_2 = 2050 cm^{-1}, ν_3 = 2100 cm^{-1} and ν_4 = 2150 cm^{-1}. (B) Spectral intensity profile for the spectral bands. (C) *kv* correlation plot of the above model.

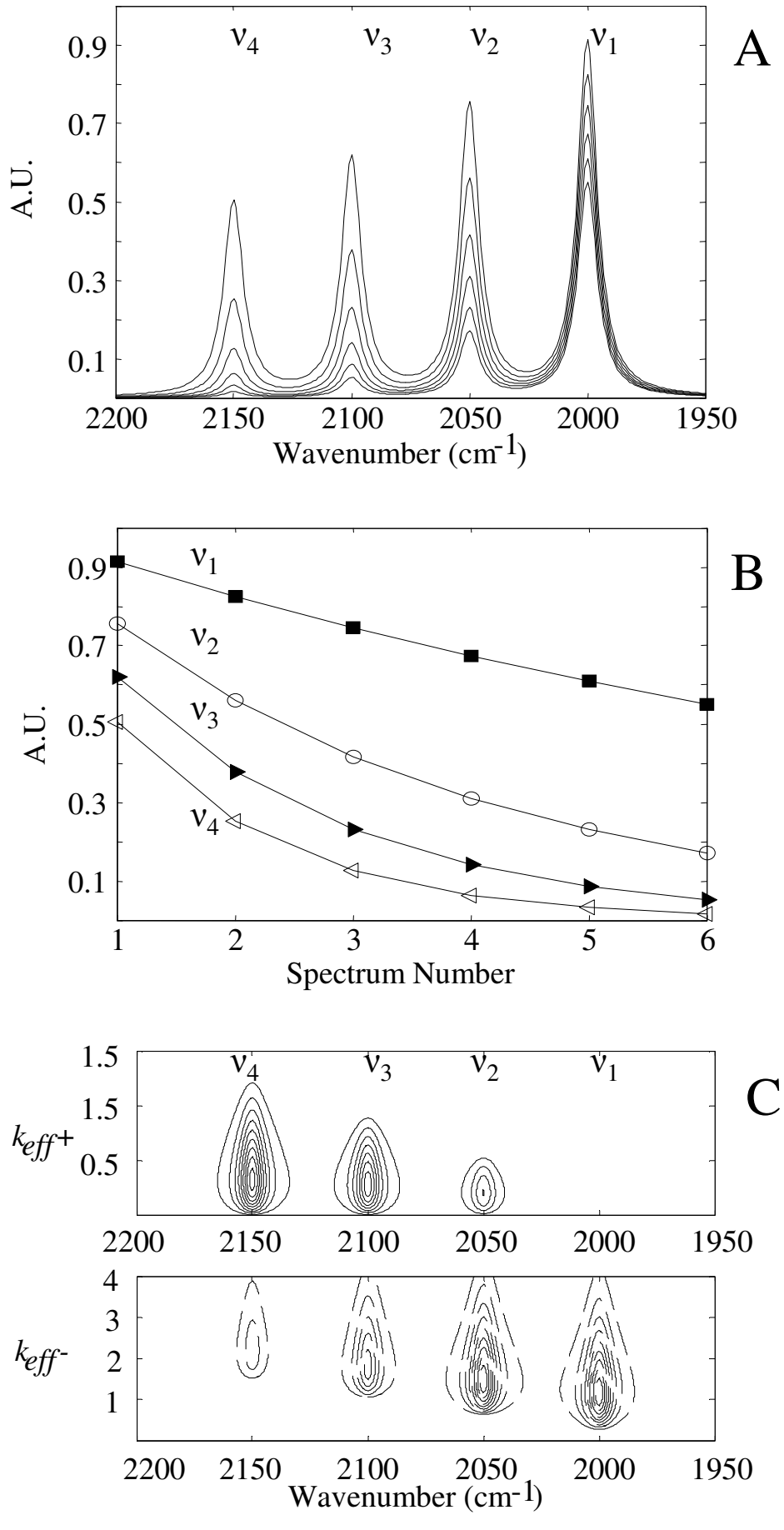
A
ν4
ν3
ν2
ν1
A.U.
0.9
0.7
0.5
0.3
0.1
2200
2150
2100
2050
2000
1950
Wavenumber (cm-1)
B
ν1
ν2
ν3
ν4
A.U.
0.9
0.7
0.5
0.3
0.1
1
2
3
4
5
6
Spectrum Number
C
keff+
1.5
1.5
0.5
keff-
4
3
2
1
2200
2150
2100
2050
2000
1950
Wavenumber (cm-1)

Table 5.4

Values of the effective rate constants k_{eff}^{+} and k_{eff}^{-}, obtained from the $k\nu$ correlation plot in Figure 5.4. These effective rate constants were obtained from the simulated IR spectra in Model D that represents a decreasing exponential intensity change.

Band Assignment	Wavenumber (cm^{-1})	k_{eff}^{+}	k_{eff}^{-}
ν_1	2000	-	1.1
ν_2	2050	0.2	1.4
ν_3	2100	0.2	1.8
ν_4	2150	0.3	2.2

(2100 cm^{-1}, k_{eff}^{-} = 1.4) and ν_4 (2150 cm^{-1}, k_{eff}^{-} = 1.1). The different k_{eff}^{-} values represents the different rates at which the intensities of the respective bands change.

Figure 5.4C also shows that the band at 2150, 2100 and 2050 cm^{-1} have positive k_{eff} value associated with them: ν_4 (2150 cm^{-1}, k_{eff}^{+} = 0.30), ν_3 (2100 cm^{-1}, k_{eff}^{+} = 0.20), and ν_2 (2050 cm^{-1}, k_{eff}^{+} = 0.20). The positive peaks in the $k\nu$ plot for this model are explained by the nature of the intensity decreases for these bands. The intensities for these three bands vary in a two-step process – initially with a large negative slope, and then with a smaller negative slope (*i.e.* the rate of decrease slows). The $k\nu$ correlation method calculates the decrease in the rate of intensity change as a positive k_{eff} value since the rate of change increased relative to the initial rate. Similar to the case described above in Model A, the presence of positive and negative correlation peaks for an absorption band illustrates that the $k\nu$ correlation method is sensitive to the <u>*change*</u> in the relative rates of the band intensities through the dynamic data set.

III. Application of the kν Method: Anionic Photopolymerization of Cyanoacrylate.

Classical metallocenes such as ferrocene and ruthenocene ($FeCp_2$ and $RuCp_2$, where Cp_2 is η^5-C_5H_5) can be used as anionic photoinitiators for polymerization reactions. These metallocenes dissolve readily in a wide range of nonaqueous solvents, exhibit good thermal stability and are photolytically inert in solution[19]. It has been shown that $FeCp_2$ and $RuCp_2$ form ground state donor-acceptor (D-A) complexes with electron accepting solvents that are characterized by a charge-transfer-to-solvent (CTTS) absorption band in the near-UV region. Irradiation into this band causes the one-electron oxidation of the metallocenes to the corresponding metallocenium cation accompanied by reduction of the solvent to its radical anion[20-23]. Metallocene photo-oxidation also occurs in neat ethyl 2-cyanoacrylate (CA) to produce an initiating species for anionic polymerization[24].

Photo-initiated polymerization of CA is characterized by an induction period followed by a rapid acceleration of the polymerization reaction that finally reaches a limiting value at ~80-90% conversion. The induction period is attributed to the presence of methane sulfonic acid (MSA), which serves as a scavenger for adventitious traces of basic impurities in the commercial monomer. Polymerization is inhibited until sufficient anionic species are photochemically generated to neutralize this acid, whereupon rapid consumption of monomer commences. Not surprisingly, addition of extra MSA to a sample lengthens the induction period and slows the ensuing anionic polymerization.

We previously showed that the rate of photo-initiated polymerization in CA could be quantitative characterized by attenuated total reflectance infrared spectroscopy (ATR-IR)[24]. This technique allows continuous monitoring of the polymerization occurring in a 2-3 μm layer of monomer immediately adjacent to the surface of the ATR crystal. In the current work we have taken the time-dependent ATR-IR spectra of the photo-initiated polymerization of CA and subjected them to generalized 2D IR as well as *kv* correlation analysis in order to elucidate the rate relationships between the different spectral features.

The ATR-IR spectra of the CA polymerization reaction are shown in Figure 5.5. Several vibrational modes are observed in the IR spectrum that are correlated with molecular changes occurring during polymerization[25]. For example: 1) The bands at 1190 cm^{-1} and 1290 cm^{-1} are due to the stretching vibrations of the C–O bond of the ester that is conjugated to the C=C of the monomer. These two bands have approximately the same intensity and are characteristic of α, β-unsaturated esters. As the polymerization reaction proceeds and conjugation decreases, the infrared intensities of these bands decrease. 2) The band at 1250 cm^{-1} that is due the C–O ester stretch of the polymeric cyanoacrylate molecule. This band increases in intensity during the

polymerization process. 3) The band at 1616 cm^{-1} is due to the C=C stretch of the cyanoacrylate monomer molecule and decreases with time as the polymerization reaction proceeds. 4) The vibrational frequency of the C=O group increases from 1735 cm^{-1} for the conjugated ester to 1752 cm^{-1} for the saturated ester.

Figure 5.6A illustrates the time-dependence of the intensity profiles of these vibrational modes for the case of the polymerization of CA in the absence of inhibitor, while Figure 5.6B illustrates the same data for the polymerization of CA in the presence of inhibitor. From Figure 5.6 the time regimes corresponding to maximal spectral intensity changes may be identified. We used the spectra between 20 – 42 s (16 spectra total) to characterize the polymerization reaction in the absence of inhibitor (Figure 5.6A) and the spectra between 94 – 191 s (65 spectra total) to characterize the reaction in the presence of inhibitor (Figure 5.6B).

The spectra in these time domains were analyzed using conventional two-dimensional infrared correlation spectroscopy and *kv* correlation analysis to determine the relative rate relationships and degree of coherence among the molecular groups of CA during the photo-initiated polymerization process. The vibrational modes studied were 1190 cm^{-1} (conjugated carbonyl ester C–O stretch), 1250 cm^{-1} (saturated carbonyl ester C–O stretch), 1290 cm^{-1} (conjugated carbonyl ester C–O stretch), 1616 cm^{-1} (C=C stretch), 1732 cm^{-1} (conjugated carbonyl ester C=O stretch) and 1753 cm^{-1} (saturated carbonyl ester C=O stretch).

Figure 5.5 Time-dependent ATR-IR spectra of the ruthenocene-initiated polymerization reaction of cyanoacrylate collected over 300 seconds. Arrows designate the direction of increase or decrease in intensity for the indicated bands over the course of the polymerization reaction. (A) Spectral region showing the carbonyl (C=O) bands and the C=C band at 1616 cm^{-1}. (B) Spectral region showing the ester C–O bands due to the monomeric cyanoacrylate molecule at 1190 cm^{-1} and 1290 cm^{-1} as well as the ester C-O band for the polymer at 1250 cm^{-1}.

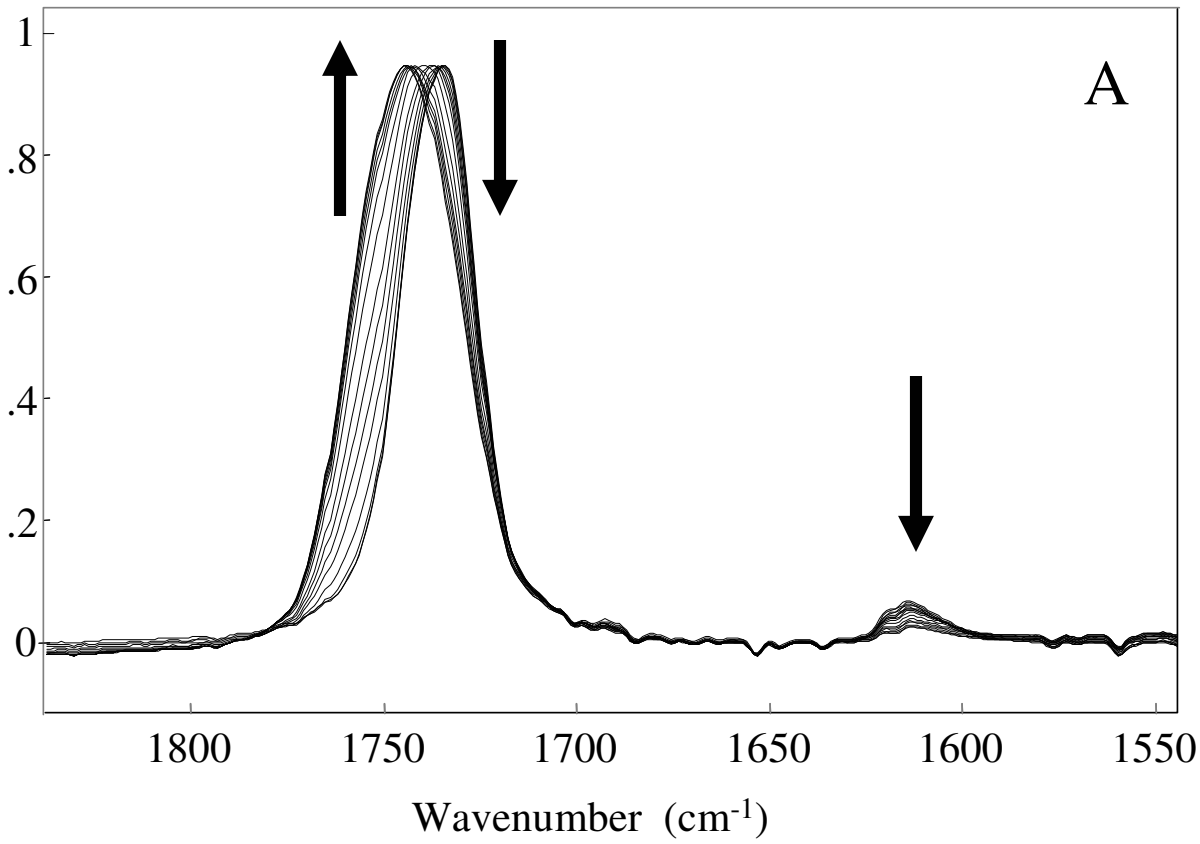
A
1
.8
.6
.4
.2
0
1800
1750
1700
1650
1600
1550
Wavenumber (cm-1)

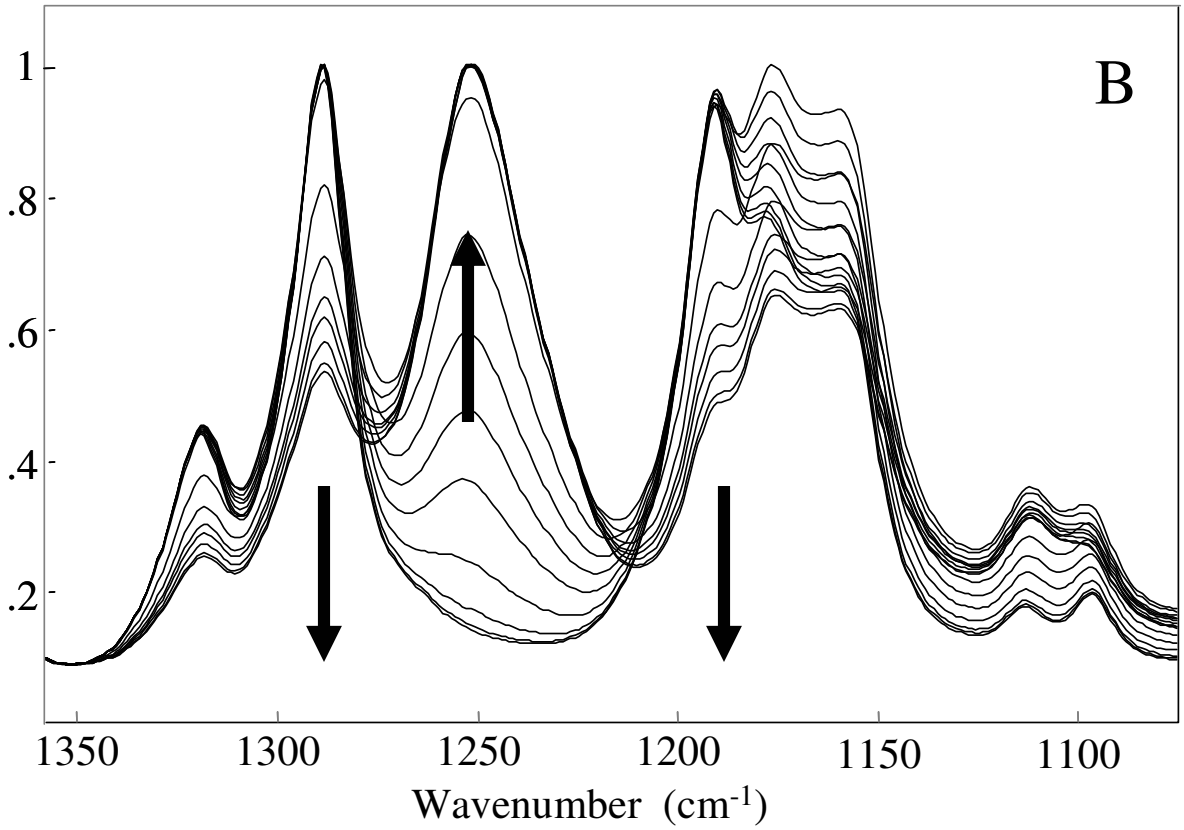
B
1
.8
.6
.4
.2
1350
1300
1250
1200
1150
1100
Wavenumber (cm-1)

Figure 5.6 Spectral intensity profiles for the spectral bands shown in Figure 5.5 over the time course of the ruthenocene-initiated photo-polymerization reaction of CA. The different bands shown are 1190 cm^{-1} (■), 1250 cm^{-1} (●), 1290 cm^{-1} (Δ), 1616 cm^{-1} (○), 1734 cm^{-1} (□), and 1754 cm^{-1} (◇). (A) Intensity profiles for the CA bands during the polymerization reaction in the absence of an inhibitor. (B) Intensity profiles for the CA bands during the polymerization reaction in the presence of the inhibitor MSA.

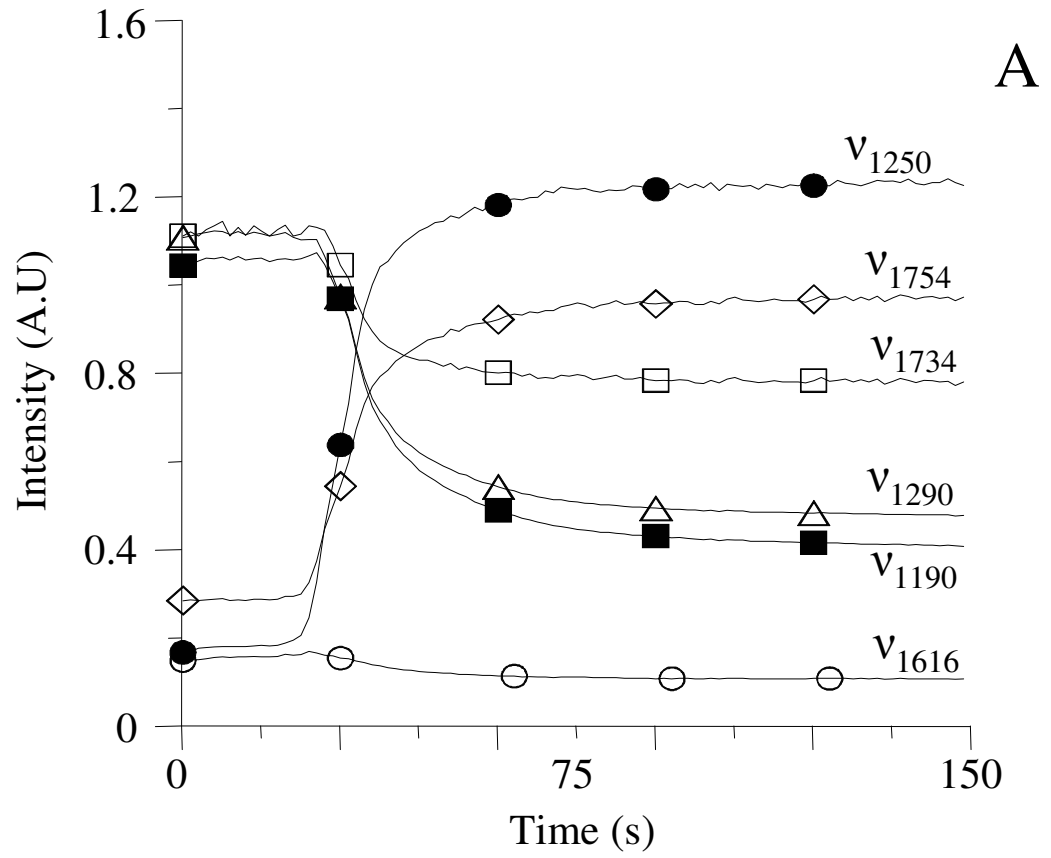
A
1.6
1.2
0.8
0.4
0
Intensity (A.U)
0
75
150
Time (s)
ν1250
ν1754
ν1734
ν1290
ν1190
ν1616

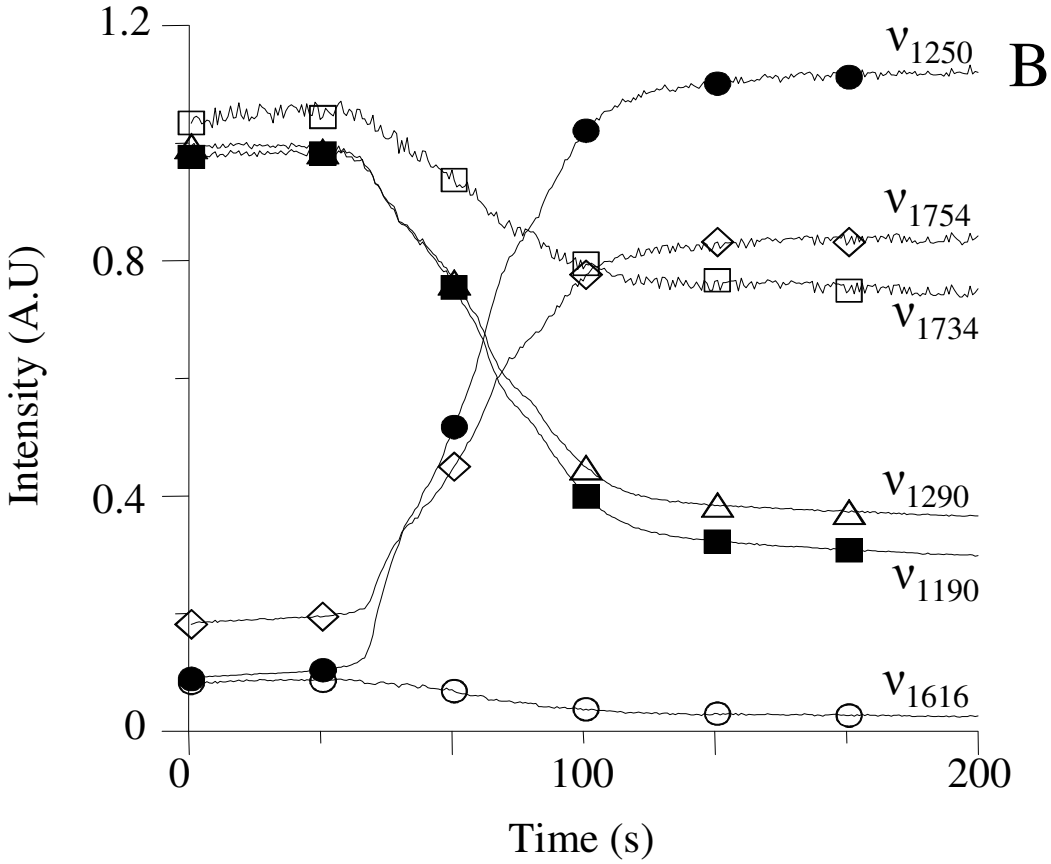
B
1.2
0.8
0.4
0
Intensity (A.U)
0
100
200
Time (s)
ν1250
ν1754
ν1734
ν1290
ν1190
ν1616

III A. 2D IR Analysis of CA Photopolymerization

Asynchronous 2D IR Correlation

Asynchronous 2D IR correlation plots calculated from the ATR–IR spectra of the polymerization reaction in the absence of inhibitor are shown in Figure 5.7. In all the 2D IR and $k\nu$ correlation plots presented here, positive peaks are represented by solid contour lines and negative peaks are represented by dashed contour lines. The signs of the asynchronous peaks indicate whether the intensity change at a particular frequency leads or lags when compared to other frequencies. The asynchronous map in Figure 5.7A shows the correlation of the spectral region between 1700 cm^{-1} and 1800 cm^{-1} which contain the carbonyl stretching bands of the monomeric and the polymeric cyanoacrylate. A negative asynchronous doublet peak is observed between 1734 cm^{-1} and 1754 cm^{-1}, which is a manifestation of the asynchronous relationship between the intensity changes of the two carbonyl bands. We have previously showed that an asynchronous cross peak doublet is characteristic of two overlapped bands where the underlying sub-bands are changing intensity[9]. Figure 5.7B shows the asynchronous correlation between the regions 1700 cm^{-1} – 1800 cm^{-1} and 1150 cm^{-1} – 1300 cm^{-1}. The latter region comprises the bands due to the ester C=O stretching and the ester C–O stretching vibrations. Positive cross peaks are observed between 1754 cm^{-1} *vs.* 1285 cm^{-1}, 1754 cm^{-1} *vs.* 1188 cm^{-1}, while a negative cross peak is observed between 1734 cm^{-1} and 1250 cm^{-1}. Of note is the absence of an asynchronous cross peak between the band at 1754 cm^{-1} (due to the carbonyl stretch of the saturated polymeric CA) and the band at 1250 cm^{-1} (due to the C–O ester stretch of the saturated polymeric CA); this implies that the intensity changes of these modes proceed at a similar rate. Also, the absence of pronounced asynchronous cross peaks between the band at 1734 cm^{-1} (due to the carbonyl stretch of the conjugated monomeric CA) and the bands at 1190 cm^{-1} and 1290

cm^{-1} (due to the C–O ester stretching vibrations of the conjugated monomeric CA) also implies that the intensity changes of these modes proceed at similar rates.

kv Correlation Analysis

The *kv* correlation plots calculated from the ATR–IR spectra of the CA polymerization reaction in the absence of inhibitor are shown in Figure 5.8. The *kv* correlation map of the spectral region between 1700 cm^{-1} – 1800 cm^{-1} is displayed in Figure 5.8A. A positive peak is seen at 1754 cm^{-1} with a k_{eff}^{+} value of 0.656. Negative peaks occur at 1754 cm^{-1} and 1734 cm^{-1} with k_{eff}^{-} values of 0.05 and 0.55 respectively. The small negative peak at 1754 cm^{-1} appears since the rate of increase in intensity of this band decreases towards the end of the time interval chosen for the correlation. Figure 5.8B shows the *kv* correlation plot of the spectral region 1150 cm^{-1} – 1300 cm^{-1}. A positive peak at 1250 cm^{-1} with a k_{eff}^{+} value of 0.68 and negative peaks at 1190 cm^{-1}, 1250 cm^{-1} and 1290 cm^{-1} with k_{eff}^{-} values 0.51, 0.05 and 0.53 respectively. The bands that are characteristic of the polymeric cyanoacrylate molecule (1754 cm^{-1} and 1251 cm^{-1}) have very similar k_{eff}^{+} and k_{eff}^{-} values, as seen in Table 5.5, implying that the on-going polymerization reaction affects these bands simultaneously. This is logical, since both bands arise from the carbonyl ester group in the saturated polymeric cyanoacrylate molecule. The bands characteristic of the monomeric CA at 1190 cm^{-1}, 1290 cm^{-1} and 1734 cm^{-1} have negative bands with similar k_{eff}^{-} values indicating similar decreasing rates of intensity change. A comparison of the absolute k_{eff} values for the monomeric and polymeric vibrational modes indicates that polymeric bands both have k_{eff}^{+} values (~0.66-0.68) that are larger than the k_{eff}^{-} values of the monomeric modes (~0.48-0.55). This difference indicates the increase in intensity

Figure 5.7 Asynchronous 2D IR correlation plots calculated from the time-dependent ATR-IR spectra of the ruthenocene-initiated photo-polymerization reaction of CA in the absence of any inhibitor. Solid lines indicate regions of positive correlation intensity; dashed lines indicate regions of negative correlation intensity. The one-dimensional spectrum shown on the top and side of the 2D plots is the calculated average of the spectra used in the 2D analysis. (A) Auto-correlation within the 1700 cm^{-1} – 1800 cm^{-1} spectral region. (B) Correlation between the 1700 cm^{-1} – 1800 cm^{-1} and 1150 cm^{-1} – 1300 cm^{-1} spectral regions.

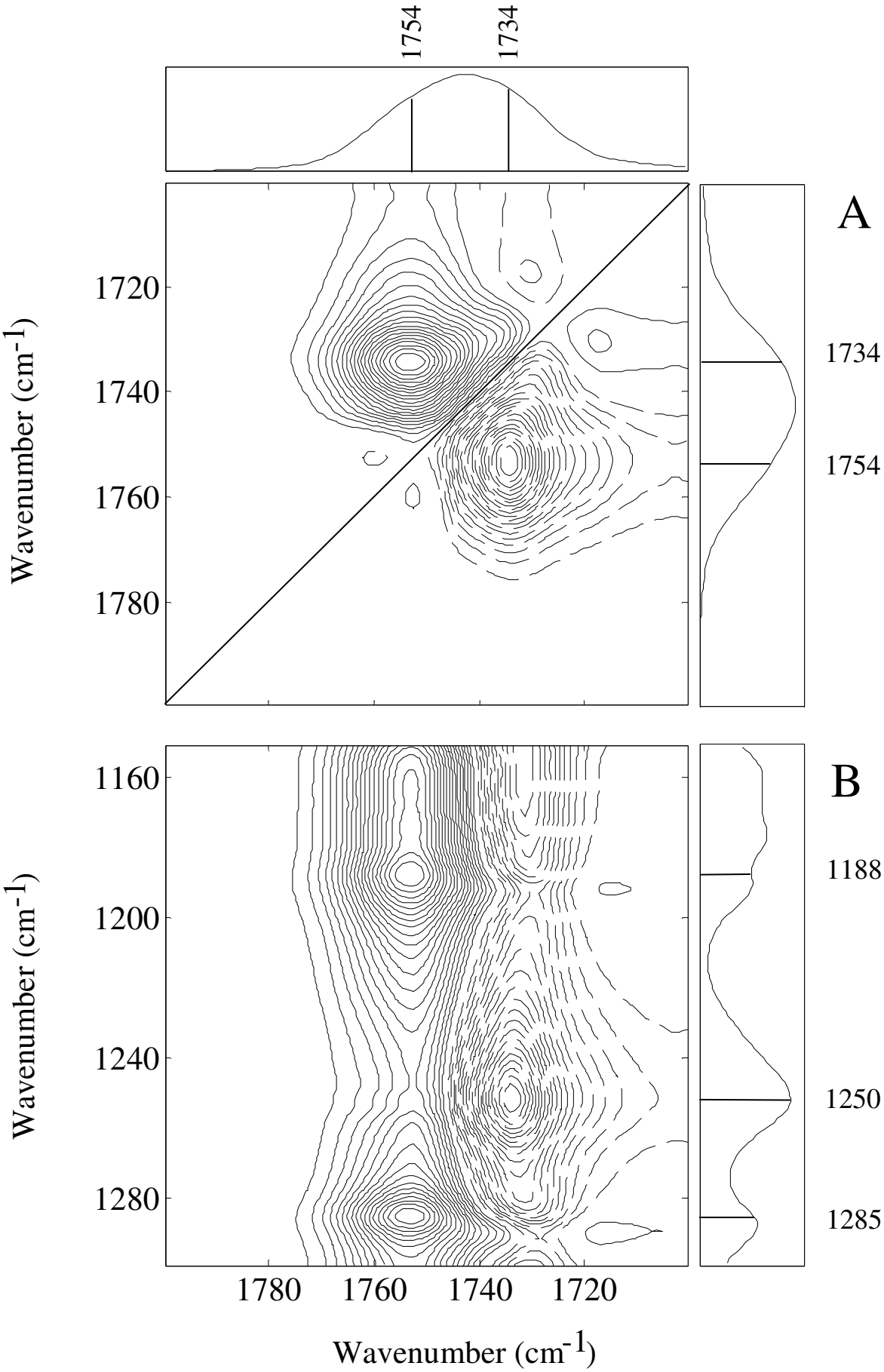
1754
1734
A
1720
1740
1760
1780
Wavenumber (cm-1)
1734
1754
B
1160
1200
1240
1280
Wavenumber (cm-1)
1188
1250
1285
1780
1760
1740
1720
Wavenumber (cm-1)

Figure 5.8 *kv* correlation plots calculated from the time-dependent ATR-IR spectra of the ruthenocene-initiated photo-polymerization reaction of CA in the absence of any inhibitor. Solid lines indicate regions of positive correlation intensity; dashed lines indicate regions of negative correlation intensity. The one-dimensional spectrum shown on the top is the calculated average of the spectra used in the *kv* analysis. Within each *kv* correlation plot, the top half indicates positive exponential correlation values (k_{eff}^{+}) while the bottom half indicates negative exponential correlation values (k_{eff}^{-}). (A) *kv* correlation plot in the region 1700 cm^{-1} – 1800 cm^{-1}. (B) *kv* correlation plot in the region 1150 cm^{-1} – 1300 cm^{-1}.

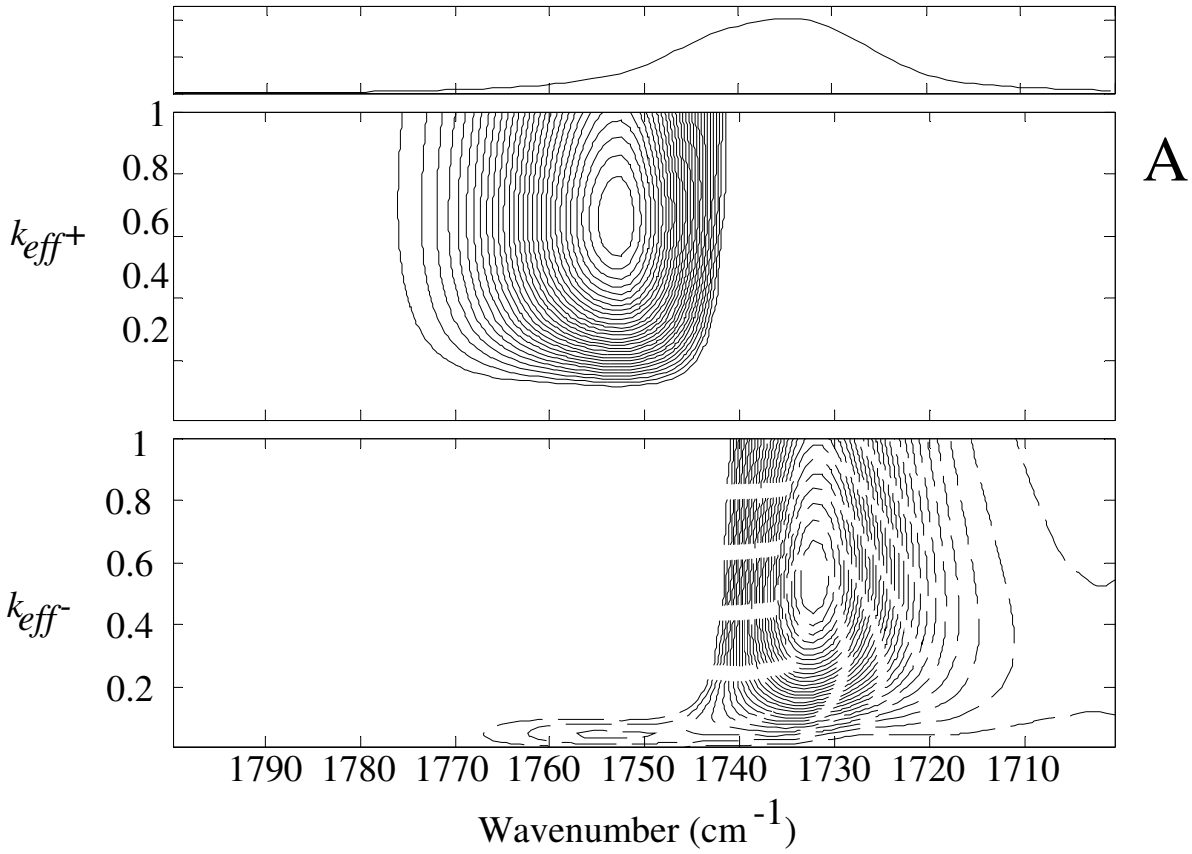
A
k_{eff}+
k_{eff}-
1
0.8
0.6
0.4
0.2
1790 1780 1770 1760 1750 1740 1730 1720 1710
Wavenumber (cm -1)

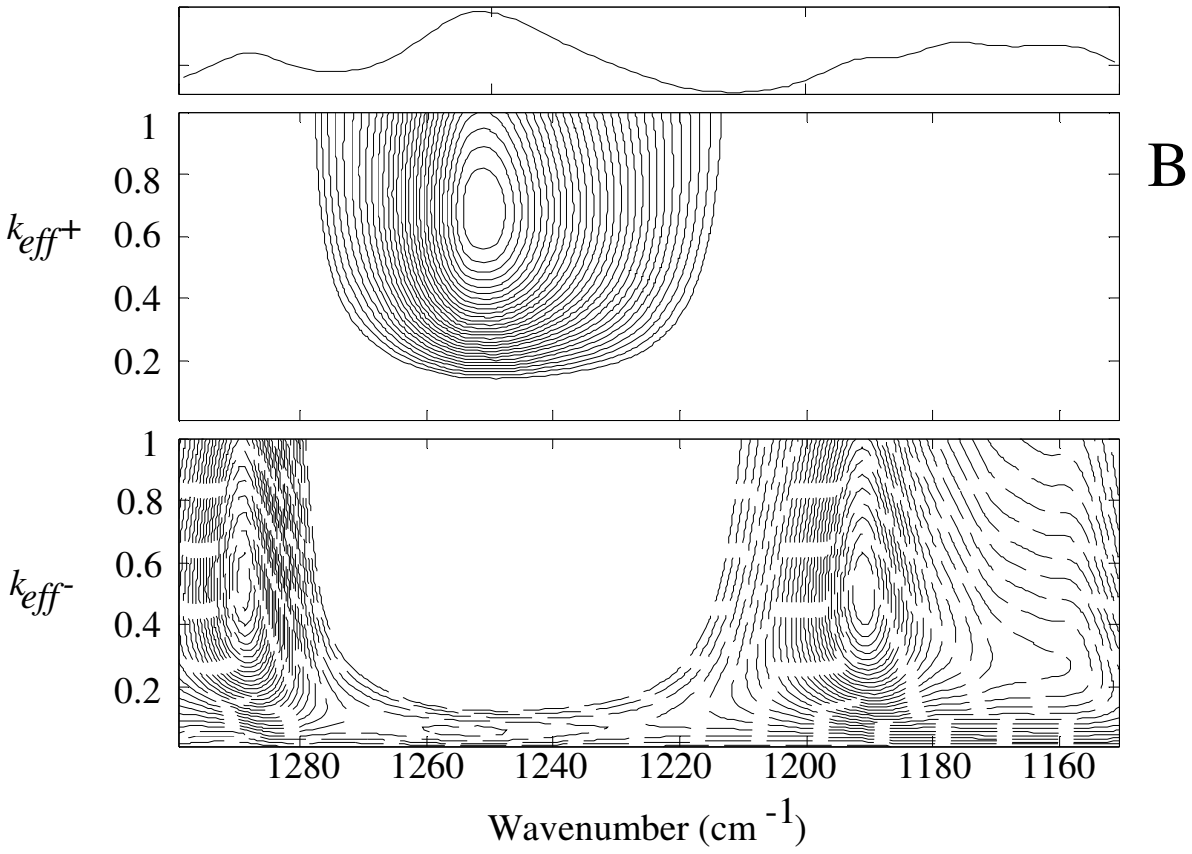
B
k_{eff}+
k_{eff}-
1
0.8
0.6
0.4
0.2
1280 1260 1240 1220 1200 1180 1160
Wavenumber (cm -1)

Table 5.5

Values of the effective rate constants k_{eff}^{+} and k_{eff}^{-}, obtained from the $k\nu$ correlation plot in Figure 5.8. These effective rate constants were obtained from the time-dependent ATR-IR spectra of the $RuCp_2$ photo-initiated polymerization of CA in the absence of an inhibitor.

Wavenumber (cm^{-1})	Band Assignment	k_{eff}^{+}	k_{eff}^{-}
1753	Polymeric Ester C = O	0.66	0.05
1732	Monomeric Ester C = O	-	0.55
1616	Monomeric C = C	-	0.48
1251	Polymeric Ester C - O	0.68	0.05
1290	Monomeric Ester C - O	-	0.53
1190	Monomeric Ester C - O	-	0.51

of the saturated polymeric CA begins earlier than the decrease in intensity of the bands due to the conjugated monomeric CA, and that the polymerization reaction is slightly out-of-phase with depletion of the monomer.

III B. 2D IR Analysis of CA Photopolymerization in Presence of Inhibitor

Asynchronous 2D IR Correlation

Asynchronous 2D IR correlation plots calculated from the ATR–IR spectra of the polymerization reaction in the presence of the reaction inhibitor methane sulfonic acid (MSA) are shown in Figure 5.9. The region between 1700 cm^{-1} – 1800 cm^{-1} that is indicative of the carbonyl stretching bands of the monomeric and the polymeric cyanoacrylate is shown in Figure 5.9A. There are significant differences between the 2D IR correlation maps of CA in the presence of the MSA inhibitor (Figure 5.9A) and in the absence of the inhibitor (Figure 5.7A). Positive cross peaks are observed at 1742 cm^{-1} *vs.*1754 cm^{-1} and 1730 cm^{-1} *vs.* 1754 cm^{-1} in the asynchronous map (Figure 5.9A). In addition, a negative asynchronous peak is now observed at 1730 cm^{-1} *vs.* 1740 cm^{-1}, resulting in an elongated quartet of cross peaks. We have previously showed that an elongated asynchronous cross peak quartet is characteristic of a single band undergoing a frequency shift[9]. Therefore, the presence of the MSA inhibitor appears to change the underlying polymerization mechanism as it affects the C=O band. Figure 5.9B shows the asynchronous correlation plot between the 1700 cm^{-1} – 1800 cm^{-1} and the 1150 cm^{-1} – 1300 cm^{-1} regions. In this plot, cross peaks are observed between vibrational modes attributable to the CA polymer and monomer, e.g. positive cross peaks at 1754 cm^{-1} *vs.* 1285 cm^{-1} and 1754 cm^{-1} *vs.* 1188 cm^{-1}, and negative cross peaks at 1730 cm^{-1} *vs.* 1251 cm^{-1} and 1733 cm^{-1} *vs.* 1190 cm^{-1}. The presence of asynchronicity between polymer and monomer modes indicates the mutually independent reorientation of the two types of CA molecules during the polymerization reaction.

kν Correlation Analysis

The *kν* correlation plots of the ATR-IR spectra of the ruthenocene-mediated polymerization reaction in the presence of the MSA inhibitor are displayed in Figure 5.10. The *kν* correlation map of the C=O spectral region between 1700 cm^{-1} – 1800 cm^{-1} is displayed in Figure 5.10A. A positive $k\nu$ correlation peak is seen at 1754 cm^{-1} with a k_{eff}^{+} value of 0.15 while a negative peak is observed at 1734 cm^{-1} with a k_{eff}^{-} value of 0.15. Figure 5.10B shows the *kν* correlation plot of the spectral region 1150 cm^{-1} – 1300 cm^{-1} where a positive peak at 1251 cm^{-1} (k_{eff}^{+} = 0.16) and negative peaks at 1190 cm^{-1} (k_{eff}^{-} = 0.14) and 1290 cm^{-1} (k_{eff}^{-} = 0.15) are observed. A comparison of the absolute k_{eff} values for the monomeric and polymeric vibrational modes in Table 5.6 indicates that both polymeric modes have k_{eff}^{+} values (~0.15-0.16) that are virtually the same as the k_{eff}^{-} values of the monomeric modes (~0.14-0.15). This indicates the increase in intensity of the saturated polymeric CA begins in concert with the decrease in intensity of the bands due to the conjugated monomeric CA and that the polymerization reaction is in-phase with depletion of the monomer. This differs from the case of CA polymerization in the absence of additional MSA inhibitor (Figure 5.8 and Table 5.5). The $k\nu$ correlation method was thus able to show how the polymerization behavior of CA in the presence of inhibitor differed from that of CA in the absence of inhibitor.

Conclusions

Our laboratory has previously developed an approach called $\beta\nu$ correlation analysis to quantitatively describe the degree of coherence between spectral intensity changes and the sequence of molecular events in a set of dynamic spectra[16]. This method utilizes defined mathematical models as complementary functions to experimental data sets in the correlation algorithm. In the work described in this article, we have expanded the scope of this method to

encompass exponential relationships between spectral intensities using a technique called $k\nu$ correlation analysis.

A $k\nu$ correlation analysis is an asynchronous cross correlation performed between a set of N spectra undergoing some dynamic intensity variation against a set of exponential functions with a user-defined range of rate constants. As such, it is a model-dependent 2D IR correlation method analogous to the $\beta\nu$ method previously described. In $k\nu$ correlation analysis, the observed correlation intensities are a function of the rate constant of the exponential function and the spectral frequency. The 2D correlation plots reveal rate relationships between different molecular events in terms of a quantitative and tangible parameter, k, which is the rate constant of the exponential function used in the correlation. A new parameter, the effective rate constant, k_{eff}, is defined as the point of maximum correlation intensity at particular frequencies in the plot of k *vs.* ν. The calculated values of k_{eff} represent the rates at which the intensities of the spectral bands change during the course of the dynamic experiment. As a result, these k_{eff} values are comparable and can be used to assign quantitative rate relationships. Events at frequencies with a larger k_{eff} value occur earlier than events at frequencies with smaller k_{eff} values. Positive and negative k_{eff} values are comparable and hence no manipulation of the spectra or the correlation plots is required to compare bands with increasing and decreasing intensities.

Using simulated IR spectra, we applied $k\nu$ correlation analysis to several intensity variation models. Based on these results, we showed that $k\nu$ correlation methods are sensitive to the <u>*relative change*</u> in the rates of the band intensities through the dynamic data set. The k_{eff} values are not the actual kinetic rate constants *per se*, but are instead the <u>*relative differences*</u> of the rates defined by the rate constants used in the correlation calculation. The k_{eff} parameter is sensitive to

Figure 5.9 Asynchronous 2D IR correlation plots calculated from the time-dependent ATR-IR spectra of the ruthenocene-initiated photo-polymerization reaction of CA in the presence of the inhibitor MSA. Solid lines indicate regions of positive correlation intensity; dashed lines indicate regions of negative correlation intensity. The one-dimensional spectrum shown on the top and side of the 2D plots is the calculated average of the spectra used in the 2D analysis. (A) Auto-correlation within the 1700 cm^{-1} – 1800 cm^{-1} spectral region. (B) Correlation between the 1700 cm^{-1} – 1800 cm^{-1} and 1150 cm^{-1} – 1300 cm^{-1} spectral regions.

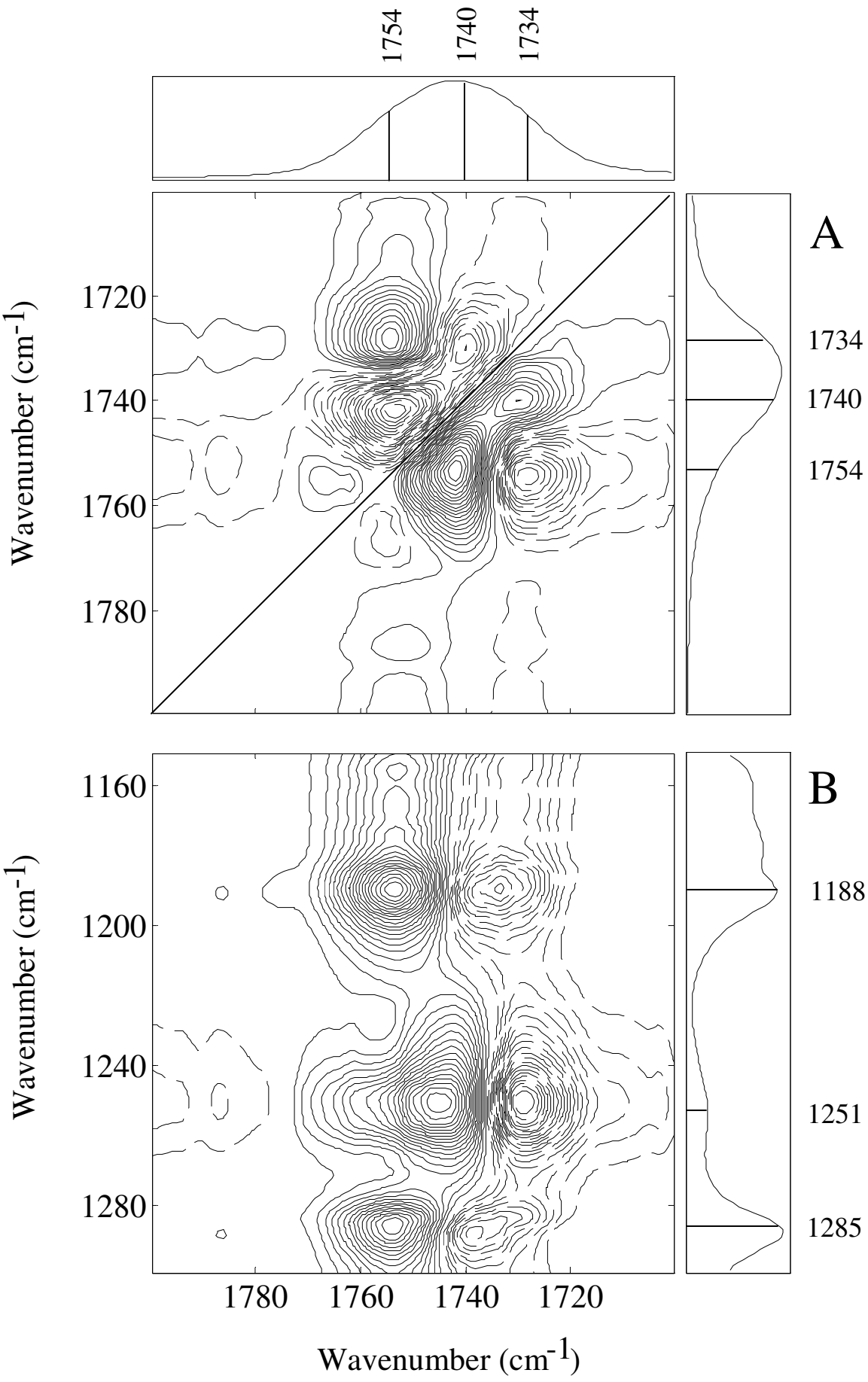
1754
1740
1734
A
1720
1740
1760
1780
Wavenumber (cm-1)
1734
1740
1754
B
1160
1200
1240
1280
Wavenumber (cm-1)
1188
1251
1285
1780
1760
1740
1720
Wavenumber (cm-1)

Figure 5.10 *kv* correlation plots calculated from the time-dependent ATR-IR spectra of the ruthenocene-initiated photo-polymerization reaction of CA in the presence of the MSA inhibitor. Solid lines indicate regions of positive correlation intensity; dashed lines indicate regions of negative correlation intensity. The one-dimensional spectrum shown on the top is the calculated average of the spectra used in the *kv* analysis. Within each *kv* correlation plot, the top half indicates positive exponential correlation values (k_{eff}^{+}) while the bottom half indicates negative exponential correlation values (k_{eff}^{-}). (A) *kv* correlation plot in the region 1700 cm^{-1} – 1800 cm^{-1}. (B) *kv* correlation plot in the region 1150 cm^{-1} – 1300 cm^{-1}.

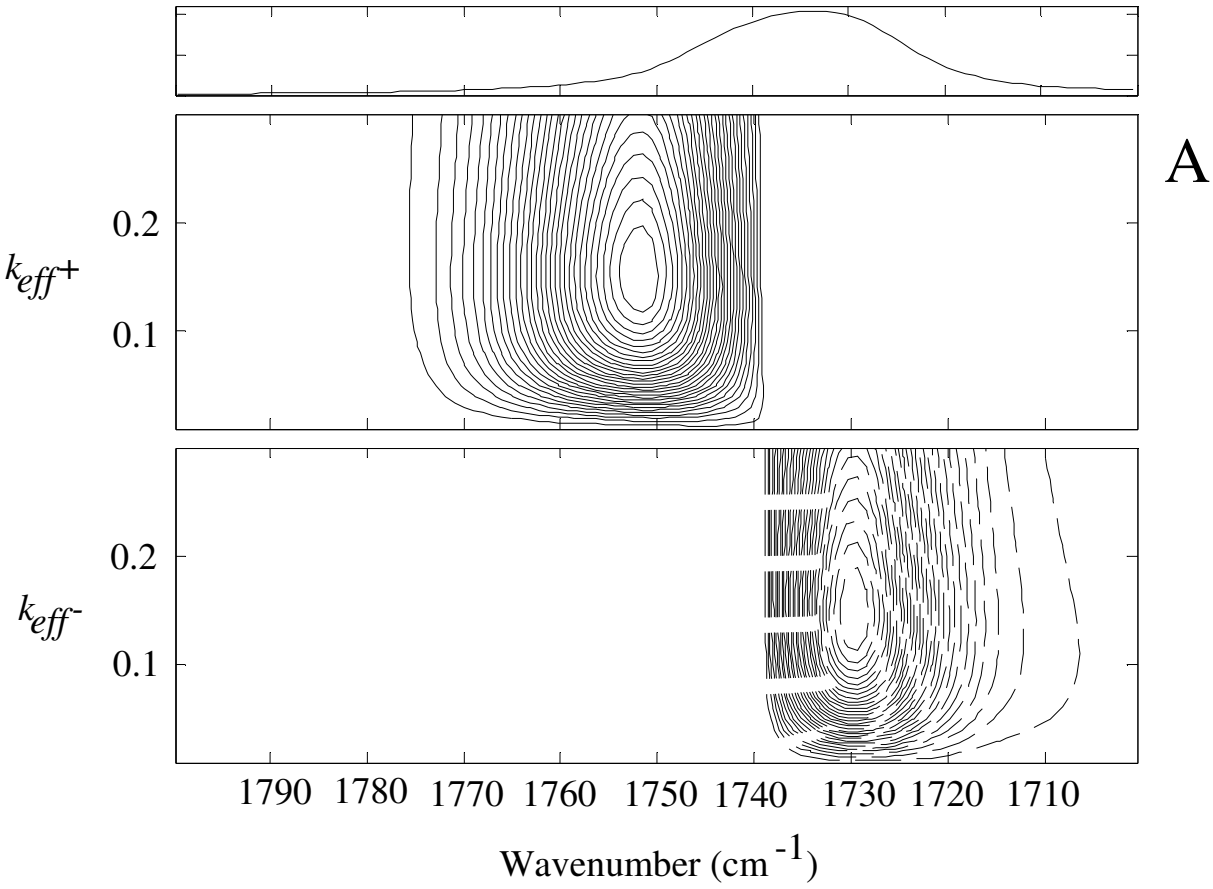
A
0.2
k_{eff}+
0.1
0.2
k_{eff}-
0.1
1790 1780 1770 1760 1750 1740 1730 1720 1710
Wavenumber (cm -1)

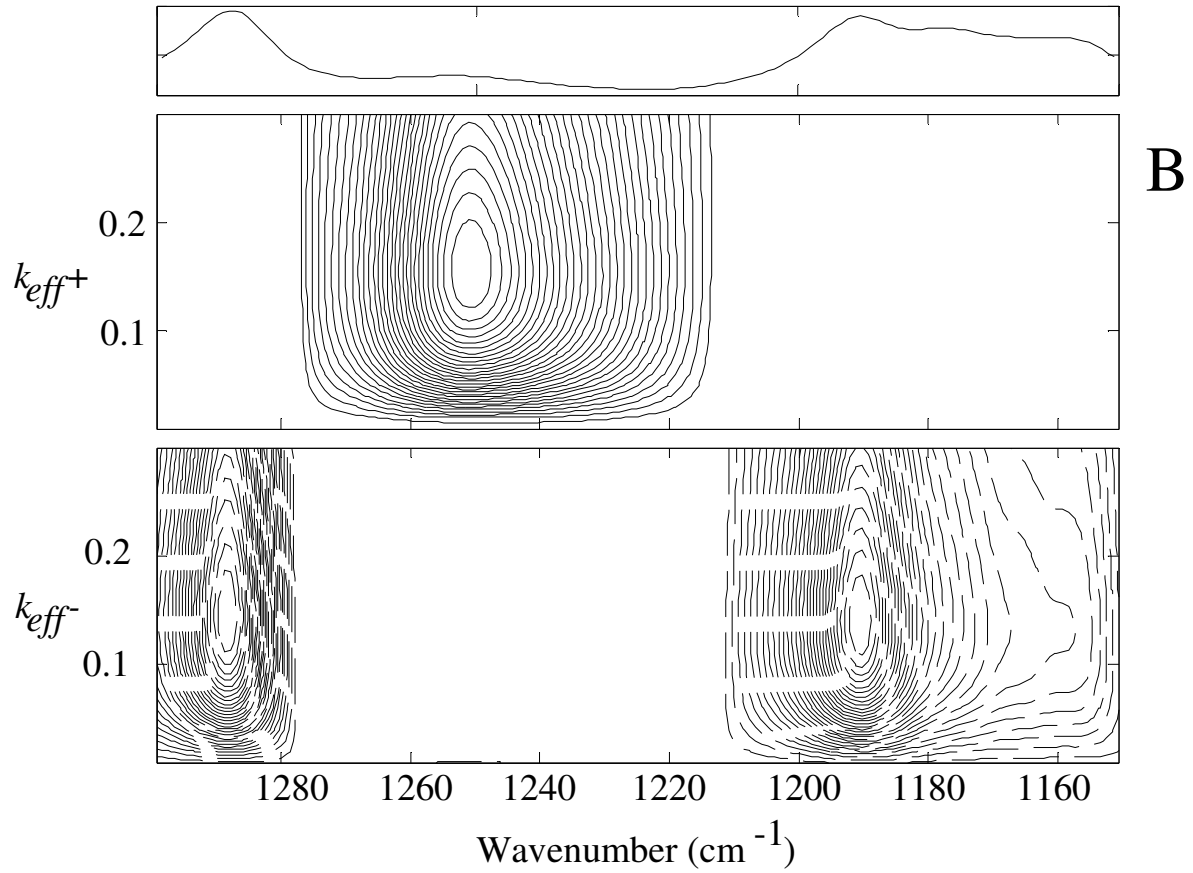
B
0.2
k_{eff}+
0.1
0.2
k_{eff}-
0.1
1280 1260 1240 1220 1200 1180 1160
Wavenumber (cm -1)

Table 5.6

Values of the effective rate constants k_{eff}^{+} and k_{eff}^{-}, obtained from the $k\nu$ correlation plot in Figure 5.10. These effective rate constants were obtained from the time-dependent ATR-IR spectra of the $RuCp_2$ photo-initiated polymerization of CA in the presence of MSA as an inhibitor.

Wavenumber (cm^{-1})	Band Assignment	k_{eff}^{+}	k_{eff}^{-}
1753	Polymeric Ester C = O	0.15	-
1732	Monomeric Ester C = O	-	0.15
1616	Monomeric C = C	-	0.14
1251	Polymeric Ester C - O	0.16	-
1290	Monomeric Ester C - O	-	0.15
1190	Monomeric Ester C - O	-	0.14

the *relative order* in which the intensity change occurs, while the size of the correlation peaks gives an indication of the *magnitude* of the intensity change. Spectral bands that vary the rate at which their intensity changes in a dynamic data set can be distinguished based on the signs of the peaks in the $k\nu$ correlation plots, thereby doing away with the necessity to modify the phase parameter, as in the case of the $\beta\nu$ correlation method.

We applied the $k\nu$ correlation analysis method to the photo-initiated polymerization reaction of 2 ethyl-cyanoacrylate. ATR-IR spectra of the anionic polymerization reaction of CA using ruthenocene as a photoinitiator were collected both in the presence and absence of an inhibitor (methane sulfonic acid). The resulting time-dependent IR spectra were analyzed using the $k\nu$ correlation method. Analysis of the k_{eff} effective rate constants showed that, in the absence of the inhibitor, the vibrational modes corresponding to the polymeric CA molecule react earlier in the polymerization process than do the vibrational modes attributable to the monomeric CA molecule. When an inhibitor is present, both monomer and polymer modes undergo intensity changes at approximately the same rate.

Acknowledgements

The work described here was supported by the U.S. Public Health Service through National Institutes of Health grant EB001956 (R.A.D.).

References

1. Noda, I., *Two-dimensional infrared (2D IR) spectroscopy: theory and applications.* Appl. Spectrosc., 1990. **44**: p. 550-554.
2. Noda, I., *Generalized two-dimensional correlation method applicable to infrared, Raman, and other types of spectroscopy.* Appl. Spectrosc., 1993. **47**: p. 1329-1336.
3. Harrington, P.d.B., A. Urbas, and P.J. Tandler, *Two-dimensional correlation analysis.* Chemometrics and Intelligent Laboratory Systems, 2000. **50**(2): p. 149-174.
4. Noda, I., et al., *Generalized two-dimensional correlation spectroscopy.* Appl. Spectrosc., 2000. **54**(7): p. 236A-248A.
5. Noda, I., G.M. Story, and C. Marcott, *Pressure-induced transitions of polyethylene studied by two-dimensional infrared correlation spectroscopy.* Vib. Spectrosc., 1999. **19**(2): p. 461-465.
6. Filosa, A., et al., *Two-dimensional infrared correlation spectroscopy as a probe of sequential events in the thermal unfolding of cytochromes c.* Biochemistry, 2001. **40**: p. 8256-8263.
7. Paquet, M.-J., et al., *Two-dimensional infrared correlation spectroscopy study of the aggregation of cytochrome c in the presence of dimyristoylphosphatidylglycerol.* Biophys. J., 2001. **81**: p. 305-312.
8. Graff, D.K., et al., *The effects of chain length and thermal denaturation on helix-forming peptides: a mode-specific analysis using 2D FT-IR.* J. Am. Chem. Soc., 1997. **119**: p. 11282-11294.

9. Elmore, D.L. and R.A. Dluhy, *Application of 2D IR correlation analysis to phase transitions in Langmuir monolayer films.* Colloids and Surfaces A, 2000. **171**(1-3): p. 225-239.

10. Elmore, D.L. and R.A. Dluhy, *Pressure-dependent changes in the infrared C-H vibrations of monolayer films at the air/water interface revealed by two- dimensional infrared correlation spectroscopy.* Appl. Spectrosc., 2000. **54**(7): p. 956-962.

11. Elmore, D.L., S. Shanmukh, and R.A. Dluhy, *A study of binary phospholipid mixtures at the air-water interface using infrared reflection-absorption spectroscopy and 2D-IR βν correlation analysis.* J. Phys. Chem. A, 2002. **106**: p. 3420-3428.

12. Shanmukh, S., et al., *Effect of hydrophobic surfactant proteins SP-B and SP-C on phospholipid monolayers. Protein structure studied using 2D IR and βν correlation analysis.* Biophys. J., 2002. **83**: p. 2126-2141.

13. Pancoska, P., J. Kubelka, and T.A. Keiderling, *Novel use of a static modification of two-dimensional correlation analysis. Part I. Comparision of the secondary structure sensitivity of electronic circular dichroism, FT-IR, and Raman spectra of proteins.* Appl. Spectrosc., 1999. **53**(6): p. 655-665.

14. Kubelka, J., P. Pancoska, and T.A. Keiderling, *Novel use of a static modification of two-dimensional correlation analysis. Part II: Hetero-spectral correlations of protein Raman, FT-IR and circular dichroism spectra.* Appl. Spectrosc., 1999. **53**: p. 666-671.

15. Ozaki, Y. and I. Noda, *Two-Dimensional Correlation Spectroscopy.* 2000.

16. Elmore, D.L. and R.A. Dluhy, *βν correlation analysis: a modified two-dimensional infrared correlation method for determining relative rates of intensity change.* J. Phys. Chem. B, 2001. **105**: p. 11377-11386.

17. Noda, I., *Determination of two-dimensional correlation spectra using the Hilbert Transform.* Appl. Spectrosc., 2000. **54**(7): p. 994-999.

18. Eads, C.D. and I. Noda, *Generalized correlation NMR spectroscopy.* Journal of the American Chemical Society, 2002. **124**(6): p. 1111-1118.

19. Geoffroy, G.L., Wrighton, M.S., in *Organometallic Photchemistry*. 1979, Academic Press: New York.

20. Akiyama, T., et al., *Photochemical Substitution of Ferrocene in Halogenated Hydrocarbon-Ethanol Solutions.* Bulletin of the Chemical Society of Japan, 1973. **46**(6): p. 1851-1854.

21. Borrell, P. and E. Henderson, *Photochemistry of Charge-Transfer Complex between Ruthenocene and Carbon-Tetrachloride.* Journal of the Chemical Society-Dalton Transactions, 1975(5): p. 432-438.

22. Granifo, J. and G. Ferraudi, *Mechanistic Organometallic Photochemistry - Observation of Metastable Ruthenocenium in Photolysis of Ruthenocene.* Inorganic Chemistry, 1984. **23**(14): p. 2210-2212.

23. Bergamini, P., et al., *Radical-Forming Electron-Transfer - Photoreactions Involving Iron Group Metallocenes.* Journal of Organometallic Chemistry, 1989. **365**(3): p. 341-346.

24. Sanderson, C.T., et al., *Classical metallocenes as photoinitiators for the anionic polymerization of an alkyl 2-cyanoacrylate.* Macromolecules, 2002. **35**(26): p. 9648-9652.

25. Lin-Vien, D., et al., *The Handbook of Infrared and Raman Characteristic Frequencies of Organic Molecules.* 1991.

CHAPTER 6

2D IR ANALYSES OF RATE PROCESSES IN LIPID-ANTIBIOTIC MONOMOLECULAR FILMS.[1]

[1] Shanmukh, S. and Dluhy, R.A. 2004. *Vibrational Spectroscopy*. 36(2): 167-177
Reprinted here with the permission of the publisher

Abstract

Polarization modulation infrared reflection spectra of a 1,2-dipalmitoyl-sn-glycero-3-phosphatidic acid (DPPA) monolayer on a subphase containing 5mM tetracycline hydrochloride (TC) were collected under varying surface pressures at the air-water interface. Statistical correlation spectroscopy using 2D IR, $\beta\nu$ and $k\nu$ correlation analyses were performed on these spectra to gain a better understanding of the surface pressure-induced effects on the interaction between the phospholipid and antibiotic. Conventional 2D IR correlation maps revealed strong correlation behavior between the vibrational modes of the lipid and antibiotic. $\beta\nu$ correlation plots provided information about the relative rates of occurrence of the coupled responses noted in the conventional 2D IR plots. These calculations indicated that molecular reorientation occurs at lower surface pressures for the modes in Ring A than for the modes in Ring C. A new model-dependent two-dimensional correlation method, exponential $k\nu$ correlation analysis, confirmed the results from the previous correlation methods and confirmed that the lipid-antibiotic interactions occurred in a bimodal fashion, depending upon surface pressure. The conclusions of the correlation analysis of the surface-pressure induced changes in the DPPA – TC monolayer system lead to the following model for lipid – antibiotic interaction. Initial interaction between the tetracycline molecule and the DPPA molecule occurs at low surface pressures primarily between Ring A of the tetracycline molecule and the lipid headgroup region. However, with increasing surface pressure, the mode of interaction changes, and the strongest interaction at high surface pressures occurs between Ring C of tetracycline and the DPPA headgroup.

Introduction

Two dimensional infrared correlation spectroscopy (2D IR) has proven to be a valuable tool due to its ability to enhance spectral resolution and identify overlapped spectral features [1]. This

has proven especially valuable in infrared spectroscopic studies of biomolecules, as this enables one, for example, to identify discrete and unique protein secondary structure conformations as well as interconversion of one form to another as a result of changes in external environment [2-7]. Two-dimensional IR correlation analysis has also been used to analyze structure in monomolecular films. The phase behavior of phospholipid monolayers have been studied using 2D IR and it was shown how these methods could distinguish bands due to co-existing phases in a disorder-order phase transition in the monolayer [8, 9].

Standard 2D IR methods have been most successfully employed in simplifying complex spectra and facilitating band assignments through resolution enhancement [10]. In addition to these uses, 2D IR can also be used to determine the temporal order of events that occur in a set of dynamically varying spectra upon sample perturbation. The basis for this determination is the relative signs of the synchronous and asynchronous cross-peak at coordinate (ν_1, ν_2) in the 2D correlation plots [11].

While it is certainly possible to determine the relative sequence of molecular events based on standard 2D IR methods, this procedure tends to be difficult to implement for highly overlapped spectra and may lead to uncertainties. In order to more quantitatively describe the degree of coherence between spectral intensity changes and the sequence of molecular events in a set of dynamic spectra, we have recently developed a modified 2D IR correlation method called βv correlation analysis [12]. This method is a variation of asynchronous cross-correlation, in which dynamically varying spectra are correlated against a mathematical function with a varying phase angle. We recently applied βv correlation analysis to surface pressure-induced changes in the IRRAS spectra of phospholipid monolayers at the A/W interface, and showed how the relative rates of acyl chain and methyl group reorientation could be quantitatively determined [13] and

have also applied this analysis in the study of conformational changes and relative reorientation rates of hydrophobic surfactant proteins SP-B and SP-C at the A/W interface [14].

Our current objective is to use polarization-modulation infrared reflection absorption spectroscopy (PM-IRRAS) to study the interactions of the antibiotic tetracycline with a phospholipid monolayer at the air-water interface. It has been shown that tetracycline induces significant changes on phospholipid monolayers and the strongest interactions are observed for the DPPA system due to specific dipole-dipole interactions [15, 16]. The aim of the current study is to unambiguously identifying the specific regions of interaction between the two molecules at the air-water interface.

To accomplish this aim, we use both conventional 2D IR and βv correlation analysis to analyze the PM-IRRAS spectra obtained from the lipid-antibiotic interactions. In addition, we introduce a new model-dependent 2D correlation method, kv correlation analysis. Our results are able to clearly identify the functional groups involved in this lipid-antibiotic interaction and the order in which their respective functional groups reorient upon increasing monolayer surface pressure.

Experimental

Materials

Tetracycline hydrochloride (TC) was obtained from Sigma (St. Louis, MO, purity > 99%) while 1,2-dipalmitoyl-*sn*-glycero-3-phosphatidic acid (DPPA) (>99%) was obtained from Avanti Polar Lipids (Alabaster, AL). The chemical structures of tetracycline hydrochloride and DPPA are shown in Figure 6.1. HPLC grade chloroform (J.T. Baker, Phillipsburg, NJ) was used as the spreading solvent and typical DPPA concentrations of 1 mg/mL were used for making the spreading solutions. Ultrapure H_2O obtained from a Barnstead (Dubuque, IA) ROpure/Nanopure

Figure 6.1 (A) Structure of 1,2-dipalmitoyl-*sn*-glycero-3-phosphatidic acid (DPPA). (B) Structure of tetracycline hydrochloride (TC). The rings of TC are denoted as indicated in the figure.

A

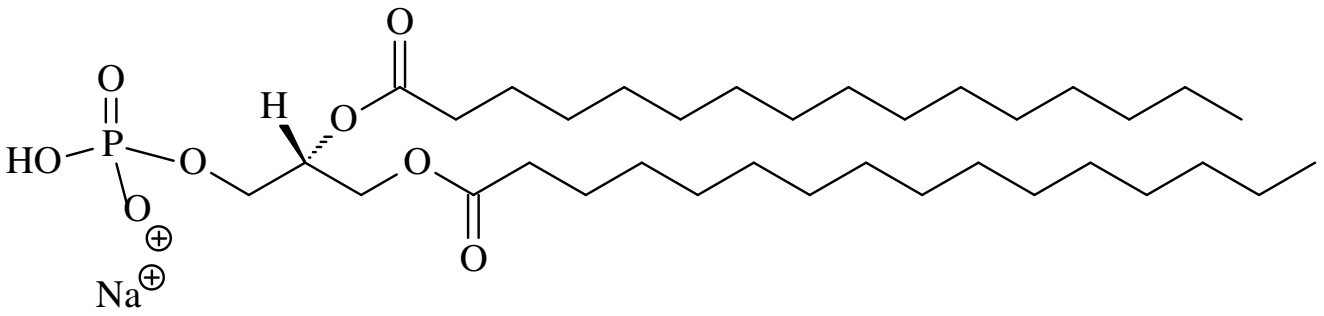

D C B A

B

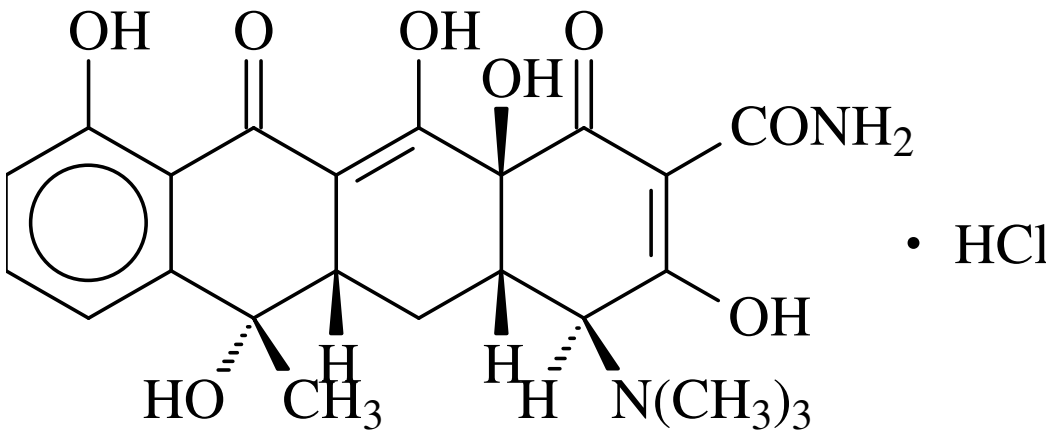

reverse osmosis/deionization system was used for making the subphase and had a nominal resistivity of 18.3 MΩ cm. The concentration of tetracycline in the subphase was 5 mM.

PM-IRRAS Measurements

Polarization-modulation IR reflection-absorption (PM-IRRAS) measurements at the A/W interface were performed using a Bruker Instruments (Billerica, MA) Equinox 55 Fourier transform infrared spectrometer optically interfaced to a variable angle external reflection accessory (Bruker model XA511-A). The external reflection accessory was equipped with a custom-designed Langmuir trough (Riegler & Kirstein, Berlin, Germany) containing a micro-balance Wilhelmy sensor for surface pressure readings.

PM-IRRAS measurements were performed using previously described protocols [17-20], with changes adapted for our particular experimental design. The IR beam from the interferometer was directed through its external beam port and steered using mirrors into the excitation arm of the reflectance accessory. The excitation arm of the external reflection accessory was rotated using computer-driven stepper motors to achieve an angle of incidence of 74 degrees. Before reflection from the A/W interface, a wire grid polarizer (IGP225, Molectron Detector, Portland, OR) passed *p*-polarized light through a ZnSe photoelastic modulator (PEM-90, Hinds Instruments, Hillsboro, OR) operating at its resonance frequency f_m of 50 kHz. After reflection from the A/W interface, the doubly modulated IR radiation was collected by an *f*/1 ZnSe lens and focused onto the 1 mm^2 sensing chip of a liquid N_2-cooled photovoltaic HgCdTe detector (KMPV11, Kolmar Technologies, Newburyport, MA). The signal from the HgCdTe detector preamplifier may be separated into sum (I_{dc} – resulting from the IR spectrometer) and difference (I_{ac} – resulting from PEM modulation) components using dual-channel electronics with lock-in detection, as previously described [17, 19]. PM-IRRAS spectra were recorded at a

resolution of 4 cm^{-1} using a scan speed/sampling frequency of 13 kHz. The total acquisition time for each spectrum was 15min, resulting in 1500 interferograms per spectrum. Further details of the procedure used in our laboratory for collection of PM-IRRAS spectra have been previously reported [21],

Calculation of 2D IR Correlation Spectra

The 2D IR synchronous spectrum, $\Phi(\nu_1,\nu_2)$, and the asynchronous spectrum, $\Psi(\nu_1,\nu_2)$, were calculated as previously described [12, 14]. In all cases the average spectrum was subtracted from each sequentially obtained surface pressure-dependent IRRAS spectrum to produce a set of dynamic IR spectra. The resulting dynamic spectra were then used in the correlation analysis.

The 2D plots presented in this article were calculated using 2D IR correlation analysis algorithms written in our laboratory using the MATLAB programming environment (Version 6, The MathWorks, Inc., Natick, MA). These algorithms incorporate the most recent mathematical formalism in which a Hilbert transform is utilized for calculating the asynchronous spectrum rather than the more commonly employed Fourier transform [22].

$\beta\nu$ Correlation Analysis

A $\beta\nu$ correlation analysis is a mathematical asynchronous cross correlation performed on a set of dynamically varying IR spectra against a set of sinusoidal functions that differ only by their phase angle β. A full description of the details of the $\beta\nu$ correlation analysis has been presented elsewhere [12], as well as the application of $\beta\nu$ correlation analysis to conformational analysis of monolayer films [13, 14]. In this study the $\beta\nu$ correlations were performed with ϕ = 10^o, so that sin($k10° + \beta$) describes approximately ¼ of the cycle of a sine function, or the approximate form of a commonly observed variation in spectral band intensities upon sample

perturbation. Only the asynchronous correlation algorithm is used in the $\beta\nu$ correlation analysis presented here, since asynchronous 2D IR correlations are more sensitive to differences in the form of the signal variation than are synchronous correlations [23].

As previously described, the $\beta\nu$ correlation analysis calculates an effective phase angle, β_e [12]. The effective phase angle β_e is the point of maximum positive correlation intensity in the plot of β *vs.* ν and quantitatively defines the relative rates of reorientation of molecular groups in the set of dynamic spectra.

The $\beta\nu$ plots of effective phase angles *vs.* wavenumber were calculated using $\beta\nu$ correlation analysis algorithms written in our laboratory using the MATLAB programming environment. The computational algorithm for the $\beta\nu$ correlation analysis incorporates the Hilbert transform for calculating the asynchronous spectrum [22].

Exponential 2D IR Correlation – $k\nu$ Correlation Analysis

A $k\nu$ correlation analysis is a mathematical cross correlation performed between a set of N spectra undergoing some dynamic intensity variation against a set of decreasing exponential functions that are varying in their rate constants [24]. As such, it is a model-dependent 2D IR correlation method analogous to the $\beta\nu$ correlation analysis described above.

A $k\nu$ correlation analysis is mathematically described as shown in Equation 1. The correlation intensity Ψ at some point (ν, k) represents the correlation of the measured IR spectral intensity $y(\nu, n_j)$ with the mathematical function $exp(-kt + R)$. In Equation 1, y is the IR intensity; ν is the frequency or wavenumber; n_j is the number of the spectrum in the ordered sequence where the first spectrum number is zero; k is the rate constant of the exponential curve; N is the total number of spectra used in the calculation; R is a constant matrix, and M_{jk} is the Hilbert-Noda transform matrix previously defined [12, 22].

$$\Psi(\nu,k)=\frac{1}{N-1}\sum_{j=0}^{N-1}y(\nu,n_j)\cdot\sum_{k=0}^{N-1}M_{jk}\cdot\exp(-k\,t+R) \qquad (1)$$

The asynchronous $k\nu$ correlation intensity can be either positive or negative depending on the direction and magnitude of intensity change. Based on studies done on simulated spectra, positive peaks are observed when intensities increase and negative peaks are observed when intensities decrease. In the cases of bands where the direction of intensity change varies during the course of the experiment, or when the rate of intensity change decreases, both positive and negative correlation peaks may be observed. A full description of the details of the $k\nu$ correlation analysis has been presented elsewhere [24].

In a $k\nu$ correlation analysis, a new parameter, k_{eff}, is defined from the $k\nu$ correlation plots that is the point of maximum correlation intensity in the plot of k vs. ν. The range of values that k_{eff} can take may be arbitrarily set and are between 1 and 7 in this article. The calculated values of k_{eff} are representative of the rates at which the different molecular processes occur. These values are not actual rate constants, per se, but are instead the *relative differences* of the rates defined by the rate constants used in the 2D correlation calculation. As a result, these k_{eff} values are comparable and can be used to assign quantitative rate relationships. Events at spectral frequencies with a larger k_{eff} value occur earlier than events at spectral frequencies at smaller k_{eff} values. Positive and negative k_{eff} values are comparable and hence no manipulation of the spectra is required to compare increasing and decreasing bands. As in the case of the conventional 2D IR correlation analysis, frequency shifts in band positions affect the shapes of the correlation peaks observed, however the effects are not as pronounced. Analysis of simulated frequency-shifted spectral models can identify the cause of the observed frequency shifting in the correlation plots [8]. In the case of spectral bands that give both positive and negative

correlation peaks in the *kv* correlation plot, the frequency at which the one correlation peak occurs would be slightly shifted relative to the other correlation peak [24].

In this current, article, $k\nu$ correlation analyses were performed on PM-IRRAS spectra of lipid-antibiotic mixtures at the A/W interface. Before correlation, the spectra were normalized for changes in surface density, baseline corrected using the GRAMS/AI spectral software package (Galactic, Nashua, NH) and the resulting spectra were smoothed using a 2nd degree Savitsky-Golay polynomial. The $k\nu$ plots of effective rate constants *vs.* wavenumber were calculated using $k\nu$ correlation analysis algorithms written in our laboratory using the MATLAB programming environment.

Results and Discussion

Monolayer IR Spectroscopy

Previous research using monomolecular films of DPPA on a tetracycline-containing subphase has indicated that specific inter-molecular interactions may occur between the polar head groups of the phospholipid in the condensed phase and the tetracycline molecules dissolved in the subphase [15, 16]. In order to test this hypothesis, we employed polarization-modulation infrared reflectance-absorption spectroscopy (PM-IRRAS) and obtained IRRAS spectra at the air-water (A/W) interface for monolayer films of DPPA on a tetracycline-containing subphase. These lipid-antibiotic spectra are shown in Figure 6.2; the PM-IRRAS spectra in this Figure have been normalized to account for changes in trough area. Normalization refers to the adjustment of monolayer IR spectral intensities to take into account changes in surface density as the trough area available to the monomolecular film decreases during compression. Intensity changes in area-normalized monolayer spectra more accurately reflect conformational changes in the monolayer, as apposed to merely reflecting an increase in number density of molecules in the

focus of the IR beam. We have previously shown that intensity normalization is important for understanding 2D IR correlation maps calculated from IRRAS monolayer spectra [9].

The IR spectra presented in Figure 6.2 were acquired while the monolayer was held at specific surface pressure values from 2.0 – 40.0 mN/m. The main spectral features apparent in the PM-IRRAS spectrum in Figure 6.2 are: 1) the C=O band of DPPA at 1737 cm^{-1}, 2) the Amide I mode of the amide group in Ring A of TC at 1660 cm^{-1}, 3) the C=O band in Ring A of TC at 1616 cm^{-1}, and 4) the C=O band in Ring C of TC at 1579 cm^{-1} [15]. As the surface pressure is increased (Figure 6.2a-2f) the bands at 1660 cm^{-1}, 1616 cm^{-1} and 1579 cm^{-1} rapidly decrease in intensity. This decrease in intensity is attributed to the nature of interaction of the tetracycline molecule present in the subphase with the lipid monolayer. Based on studies of the pressure-area isotherms of this system it has been observed that the greatest degree of insertion occurs at lower surface pressures since the lipid monolayer is less tightly packed [15]. Furthermore, the weak intensities of the tetracycline bands are attributed to the sub-monolayer nature of the antibiotic interaction with the lipid in which the bulk of the antibiotic molecules are present in the subphase [15].

The panel on the right of Figure 6.2 shows the following low-frequency IR bands: 5) the antisymmetric PO_4^{2-} stretching vibration of DPPA at 1227 cm^{-1}, 6) the antisymmetric C-O-C stretching vibration of DPPA at 1180 cm^{-1}, 7) the symmetric PO_4^{2-} stretching vibration of DPPA at 1103 cm^{-1}, and 8) the symmetric C-O-C stretching vibration of DPPA at 1058 cm^{-1}. Two-dimensional IR, $\beta\nu$ and $k\nu$ correlation analyses were performed on these PM-IRRAS spectra to gain a better understanding of the surface pressure-induced effects on the interaction between the phospholipid and antibiotic.

Figure 6.2 PM-IRRAS spectra of a DPPA monolayer on a subphase containing 5mM tetracycline hydrochloride at the air-water interface. The monolayer was applied in organic solution to the A/W interface at low surface pressure. The spectra displayed were acquired at: a) 3.0 mN/m, b) 5.0 mN/m, c) 10.0 mN/m, d) 20.0 mN/m, e) 30.0 mN/m, and f) 40.0 mN/m. In the panel on the left, the band caused by the dispersion of the refractive index of water a ~1640 cm^{-1} has been subtracted out using a fitted Lorentzian curve. The resulting subtracted spectra are presented here. The panel on the left shows the spectral region between 1800 cm^{-1} and 1550 cm^{-1} containing: 1) the lipid C=O band at 1737 cm^{-1}, 2) the amide band in ring A at 1660 cm^{-1}, 3) the C=O in ring A at 1616 cm^{-1} and 4) the C=O in ring C. The panel on the right shows the spectral region between 1250 cm^{-1} and 1000 cm^{-1} containing: 5) ν_{as} PO_4^{2-} of DPPA at 1227 cm^{-1}, 6) ν_{as} C-O-C of DPPA at 1180 cm^{-1}, 7) ν_s PO_4^{2-} of DPPA at 1103 cm^{-1} and 8) ν_s C-O-C of DPPA at 1058 cm^{-1}.

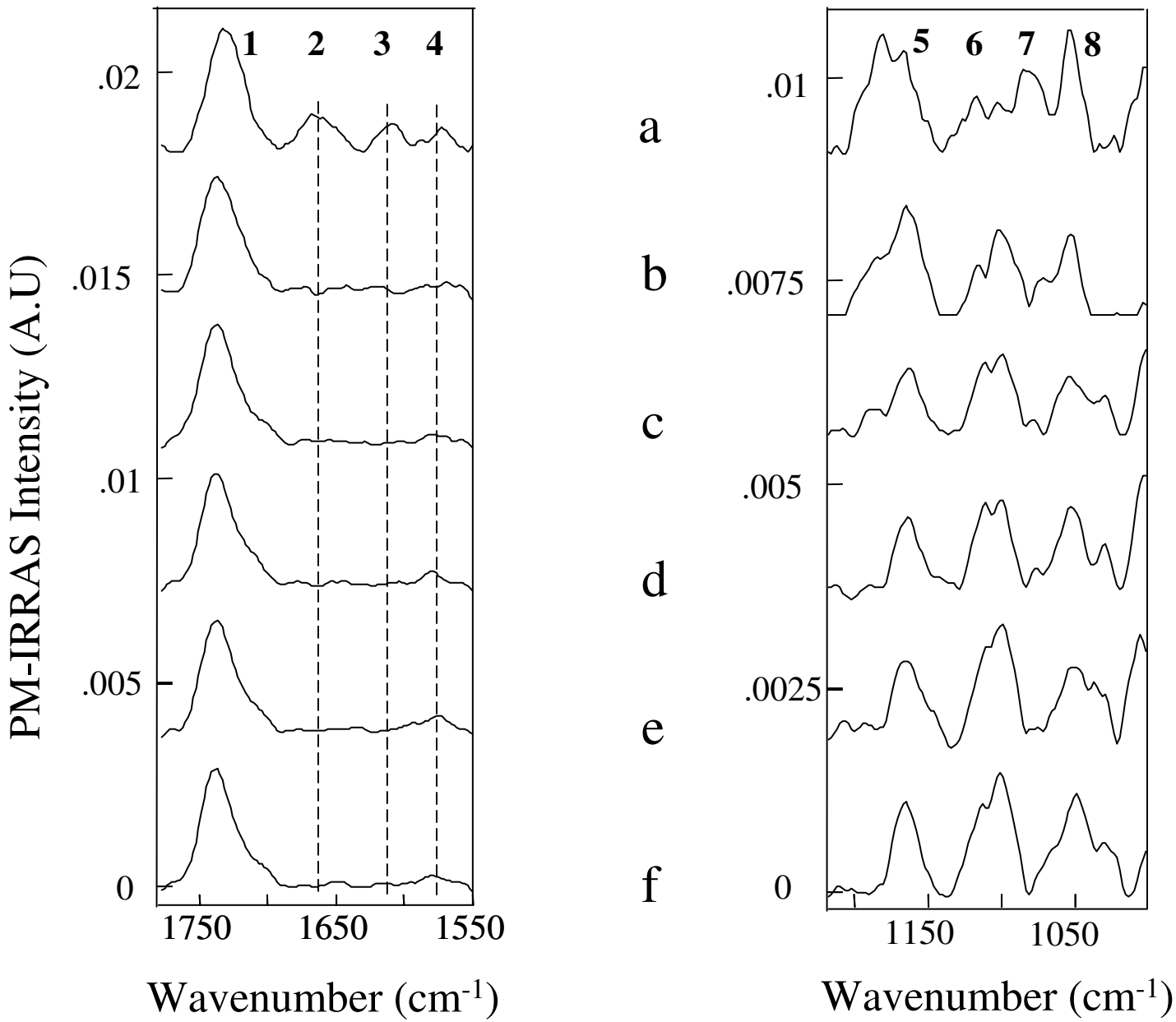
PM-IRRAS Intensity (A.U)
1
2
3
4
.02
.015
.01
.005
0
1750
1650
1550
Wavenumber (cm-1)
a
b
c
d
e
f
5
6
7
8
.01
.0075
.005
.0025
0
1150
1050
Wavenumber (cm-1)

2D-IR Correlation Analysis

Conventional two-dimensional infrared correlation spectroscopy was applied to the dynamic set of PM-IRRAS DPPA – TC spectra in order to analyze the different spectral features obtained from the 2D synchronous, $\Phi(\nu_1,\nu_2)$, and asynchronous, $\Psi(\nu_1,\nu_2)$, maps. The 2D correlation maps were calculated as previously described [12, 14].

Figure 6.3A shows the 2D synchronous correlation map of the PM-IRRAS spectra of the DPPA monolayer on the TC subphase. A strong autopeak is observed at 1737 cm^{-1} corresponding to the carbonyl stretching vibration due to the carbonyl group present in the headgroup of the lipid. A weakly intense autopeak is observed at 1572 cm^{-1} corresponding to the C=O vibration of the carbonyl group present in Ring C of the TC molecule. A positive cross peak is observed between 1572 cm^{-1} and 1737 cm^{-1}. Positive synchronous cross peaks indicate a coordinated spectral response in which the functional groups are reorienting in the same direction. Negative cross peaks are observed at 1657 cm^{-1} *vs*. 1737 cm^{-1}, 1610 cm^{-1} *vs*. 1737 cm^{-1} and 1572 cm^{-1} *vs*. 1657 cm^{-1}. Negative synchronous cross peaks indicate significantly coupled molecular reorientation, albeit one where the spectral intensity of one component increases while the second decreases. The bands corresponding to the amide vibrational mode (1657 cm^{-1}) and the C=O stretching mode of the carbonyl group in Ring A (1610 cm^{-1}) of the tetracycline, both give negative peaks with the carbonyl band of the DPPA molecule, indicating a coupled (negative) response between the two with respect to the carbonyl of the phospholipid. The positive cross peak between the carbonyl group at Ring C and the lipid carbonyl indicates a different (positive) response from the groups in Ring A.

The asynchronous 2D IR correlation plot of the experimental PM-IRRAS spectra is displayed in Figure 6.3B. Asynchronous 2D spectra are antisymmetric with respect to the diagonal in the

Figure 6.3 2D IR correlation plots of the 1800 cm^{-1} – 1550 cm^{-1} region of the PM-IRRAS spectra of DPPA on the subphase containing 5mM tetracycline hydrochloride shown in Figure 6.2. Solid lines indicate regions of positive correlation intensity, while dashed lines indicate regions of negative correlation intensity. (A) Synchronous 2D correlation plot. (B) Asynchronous 2D correlation plot. In both (A) and (B), the topmost panel illustrates the average spectrum in the dynamic spectral data set used in the correlation calculations.

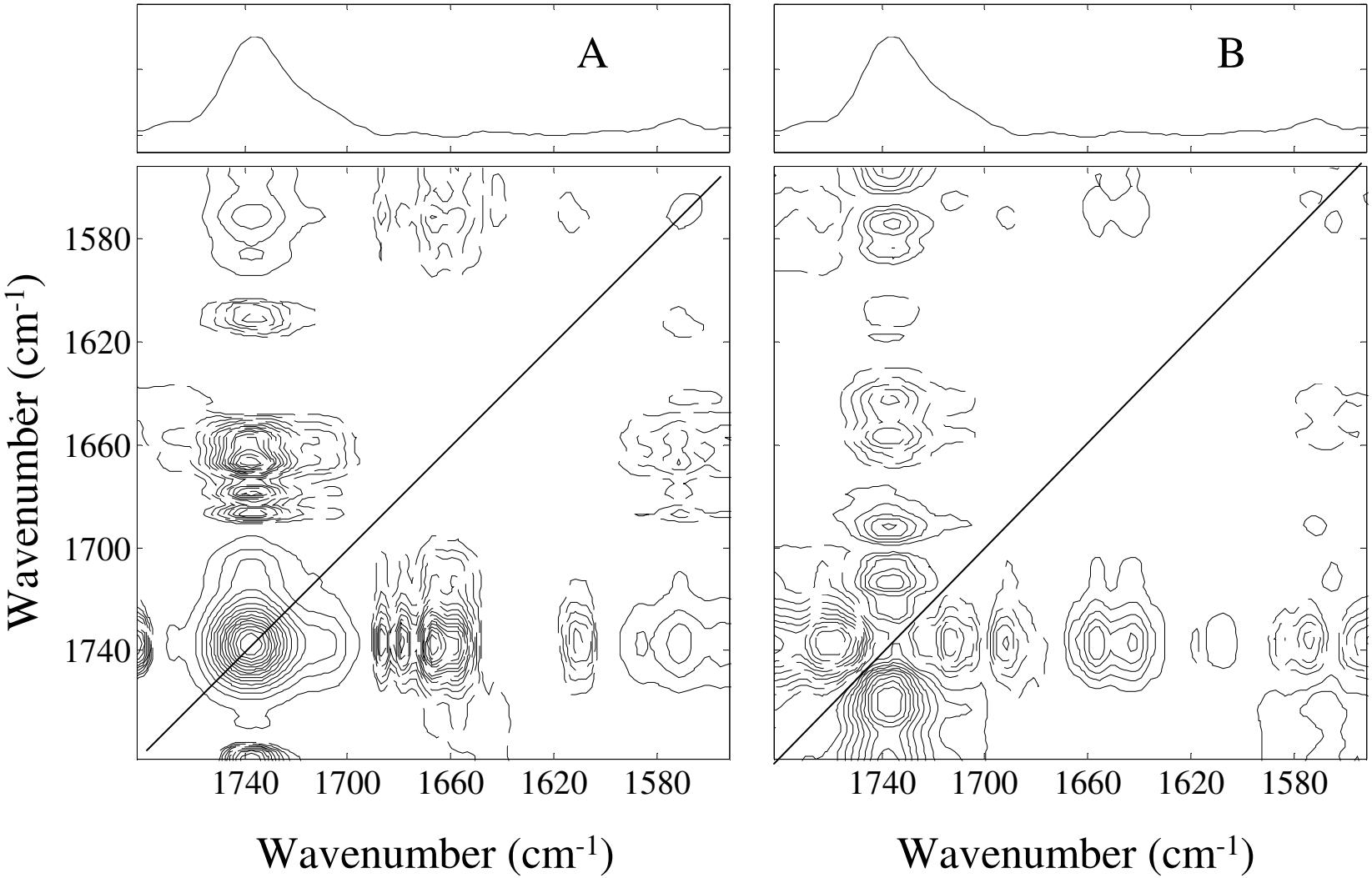
A
B
1580
1620
1660
1700
1740
Wavenumber (cm-1)
1740
1700
1660
1620
1580
Wavenumber (cm-1)
1740
1700
1660
1620
1580
Wavenumber (cm-1)

correlation map and contain no auto peaks; the spectrum consists only of off-diagonal cross peaks with two intensity maxima – one positive and one negative. Peaks appear in asynchronous 2D correlation maps if the transition dipole moments are significantly decoupled, or if the dipole moments reorient out-of-phase or at different rates in response to the external perturbation. This attribute is used to unmask the differential response of functional groups in the molecule, and makes asynchronous 2D correlation plots particularly useful for resolution enhancement [11]. Prominent cross peaks are observed at 1737 cm^{-1} *vs*. 1761 cm^{-1} (-), 1657cm^{-1} *vs*. 1737 cm^{-1} (-), 1607 cm^{-1} *vs*. 1737 cm^{-1} (-), 1713 cm^{-1} *vs*. 1735cm^{-1} (+), 1691cm^{-1} *vs*. 1735 cm^{-1} (+) and 1574 cm^{-1} *vs*. 1737cm^{-1} (+).

Figure 6.4A shows the 2D synchronous correlation map between the low-frequency region (1250 cm^{-1} – 1020 cm^{-1}) and the region containing the carbonyl vibrations of the PM-IRRAS spectra of the DPPA monolayer on the TC subphase. Since this is a hetero-spectral correlation between different regions of the spectrum, no autopeaks will be observed. Positive cross peaks are observed at 1737 cm^{-1} *vs*. 1048 cm^{-1}, 1737 cm^{-1} *vs*. 1103 cm^{-1}, 1578 cm^{-1} *vs*. 1048 cm^{-1} and 1578 cm^{-1} *vs*. 1103 cm^{-1}. Negative cross peaks are observed at 1737 cm^{-1} *vs*. 1184 cm^{-1} and 1580 cm^{-1} *vs*. 1184 cm^{-1}. The cross peaks due to the amide band at 1657 cm^{-1} and the carbonyl in Ring A at 1616 cm^{-1} are very weak in intensity. The presence of strong cross peaks between the carbonyl ester and phosphate vibrations with the C=O mode in Ring C (1578 cm^{-1}) indicate a coupled response between these modes. Furthermore, both the C=O of the lipid (1737 cm^{-1}) and the C=O of Ring C give negative cross peaks with the antisymmetric ester vibration at 1180 cm^{-1} indicating similar reorientation behavior of the two carbonyl modes. A close-up of the region of the map showing the synchronous correlation between the C=O band in Ring C versus the ester and PO_4^{2-} vibrations is shown in Figure 6.5. It is quite clear from this plot that there is a strong

Figure 6.4 2D IR hetero-spectral correlation plots between the regions 1250 cm^{-1} – 1020 cm^{-1} and the 1800 cm^{-1} – 1550 cm^{-1}. Solid lines indicate regions of positive correlation intensity, while dashed lines indicate regions of negative correlation intensity. (A) Synchronous 2D correlation plot. (B) Asynchronous 2D correlation plot. In both (A) and (B), the topmost panel illustrates the average spectrum in the dynamic spectral data set used in the correlation calculations.

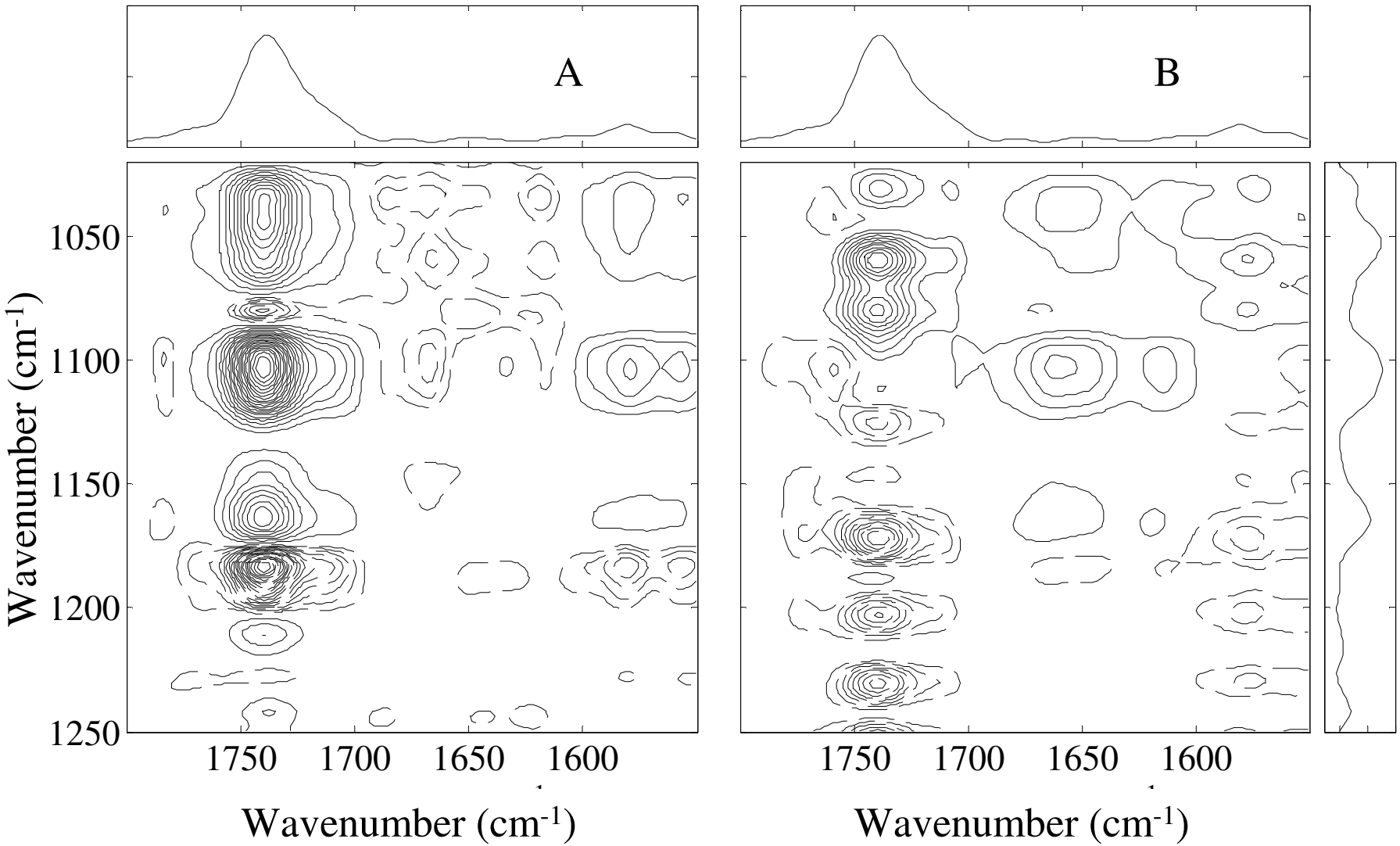
A
B
1050
1100
1150
1200
1250
Wavenumber (cm-1)
1750
1700
1650
1600
Wavenumber (cm-1)
1750
1700
1650
1600
Wavenumber (cm-1)

Figure 6.5 2D IR hetero-spectral synchronous correlation plot between the regions 1250 cm^{-1} – 1020 cm^{-1} and 1600 cm^{-1} – 1550 cm^{-1} illustrating the cross peaks between the C=O band in Ring C at 1572 cm^{-1} and the phosphate and ester bands in the lipid headgroup region.

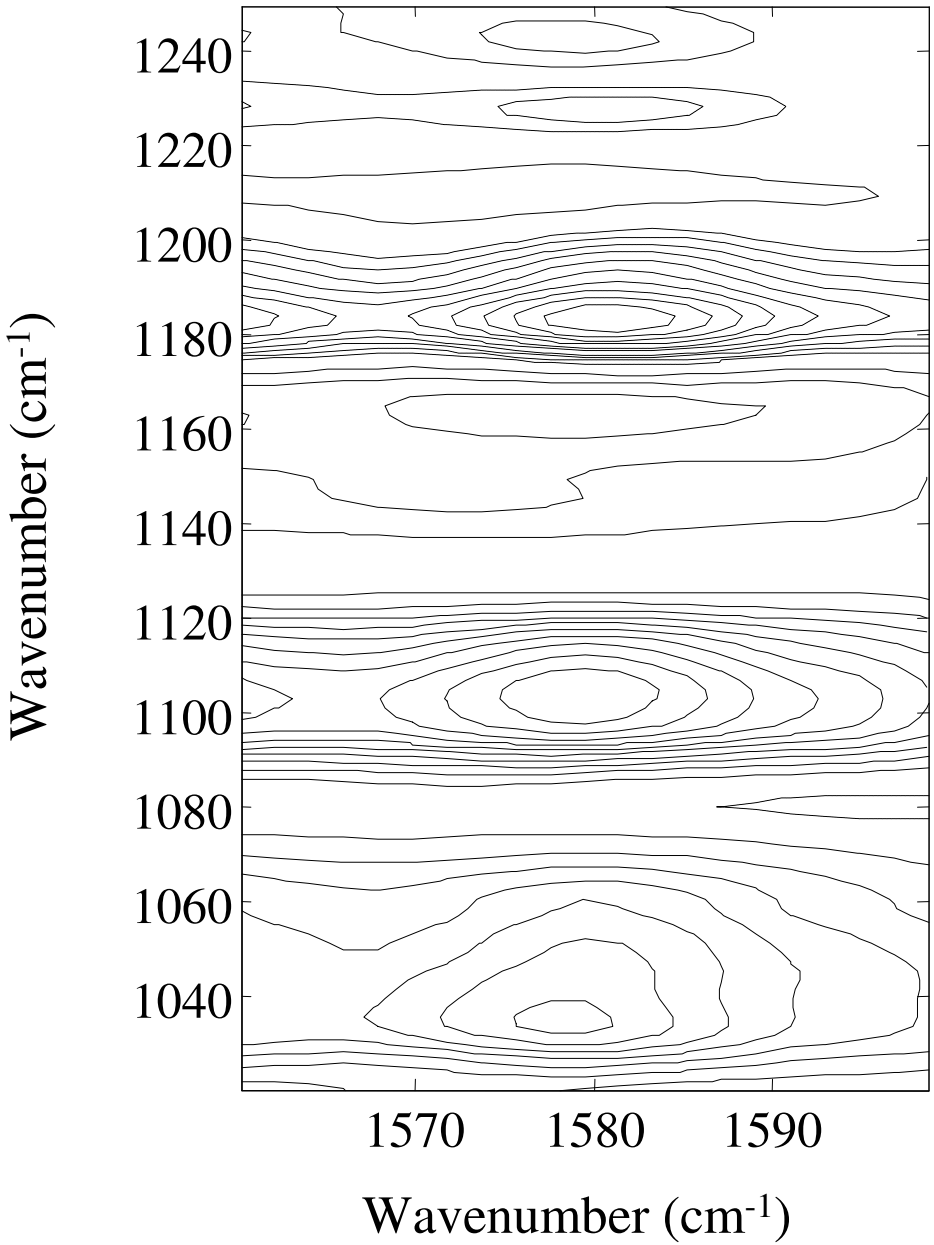
1240
1220
1200
1180
1160
1140
1120
1100
1080
1060
1040
Wavenumber (cm-1)
1570
1580
1590
Wavenumber (cm-1)

interaction between Ring C of the tetracycline molecule and the headgroup region of the phospholipid.

The asynchronous 2D IR correlation plot of the same region is displayed in Figure 6.4B. Prominent cross peaks are observed at 1737 cm^{-1} *vs*. 1171 cm^{-1} (-), 1737cm^{-1} *vs*. 1231 cm^{-1} (-), 1578 cm^{-1} *vs*. 1173 cm^{-1} (-), 1576 cm^{-1} *vs*. 1229 cm^{-1} (-), 1739 cm^{-1} *vs*. 1061 cm^{-1} (+) and 1576 cm^{-1} *vs*. 1059 cm^{-1} (+), while weak cross peaks are observed at 1658 cm^{-1} *vs*. 1103 cm^{-1} (+) and 1615 cm^{-1} *vs*. 1103 cm^{-1} (+). The presence of negative peaks between the bands in Ring A and the symmetric stretch of the PO_4^{2-} group indicates an out-of-phase behavior between these bands. This will be discussed further in the sections describing the $\beta\nu$ and $k\nu$ correlation analyses.

$\beta\nu$ Correlation Analysis

In addition its use in studying structural changes and making band assignments, 2D IR correlation spectroscopy has also been used to determine the temporal order of events that occur during the external sample perturbation. The basis for this determination is the relative signs of the asynchronous and synchronous cross peaks [11]. A positive asynchronous cross peak at (ν_1, ν_2) indicates that the intensity change at ν_1 occurs before ν_2; a negative cross peak at ν_1 is observed if the change occurs after ν_2. This rule, however, is reversed if the corresponding synchronous peak at (ν_1, ν_2) has a negative sign, *i.e.* $\Phi(\nu_1,\nu_2) < 0$. While it is possible to determine the relative sequence of molecular rearrangements based on comparison of the signs of the cross peaks in the asynchronous *vs.* synchronous correlation maps, this procedure is somewhat cumbersome, inherently qualitative in nature and leads to uncertainties for highly overlapped spectra. In order to more quantitatively describe the degree of coherence between the observed spectral intensity changes and the sequence of molecular events in a discrete set of dynamic spectra, we have developed modified 2D IR methods that utilize well-known

mathematical functional forms to simulate experimental IR intensity variations. One such method is $\beta\nu$ correlation analysis, in which an asynchronous cross-correlation is performed using a set of dynamically varying spectra, *i.e.* $y(\nu, n_j)$, against a sine function of the form $\sin(k\phi + \beta)$ [12]. The resulting correlation intensities are a function of the spectral frequency (ν) and the phase angle (β) of the mathematical function. The maximum correlation intensity will be observed at one point (ν,β) in the correlation plot for the range $360 > \beta > 0$. This point is used to define a new parameter – the effective phase angle β_e of $f(\nu,\beta)$. The β_ε value quantitatively reveals the degree of coherence between the experimental intensities and the sequence of molecular events in a discrete set of dynamic spectra. We recently applied $\beta\nu$ correlation analysis to surface pressure-induced changes in the IRRAS spectra of phospholipid monolayers at the A/W interface, and showed how the relative rates of acyl chain and methyl group reorientation could be quantitatively determined [13]. We have also applied this method to surface pressure induced conformational changes in the secondary structure of hydrophobic surfactant proteins SP-B and SP-C at the air-water interface [14].

We have applied $\beta\nu$ correlation analysis to the PM-IRRAS spectra of the DPPA monolayer on the tetracycline containing subphase. The $\beta\nu$ correlation plot for of these spectra is shown in Figure 6.6. In addition, the values for the effective phase angle (β_e) and the band assignments for the peaks in this plot are presented in Table 6.1. It is immediately obvious from Figure 6.6 that the most intense peak in the $\beta\nu$ plot is observed at 1737 cm^{-1} corresponding to the carbonyl group in the phospholipid headgroup. Peaks at 1657 cm^{-1}, 1616 cm^{-1} and 1579 cm^{-1} corresponding to the Amide band in Ring A, C=O group in Ring A and the C=O group in Ring C of the tetracycline molecule respectively. From the β_e values in Table 6.1, it is apparent that there are two distinct groups of β_e values. The modes in Ring A have β_e values of 242.1 and

Figure 6.6 2D $\beta\nu$ phase angle correlation plots calculated in the 1800 cm^{-1} – 1550 cm^{-1} region of the monolayer PM-IRRAS spectra of DPPA on the subphase containing 5mM tetracycline hydrochloride shown in Figure 6.2. The topmost panel illustrates the average spectrum in the dynamic spectral data set used in the correlation calculations.

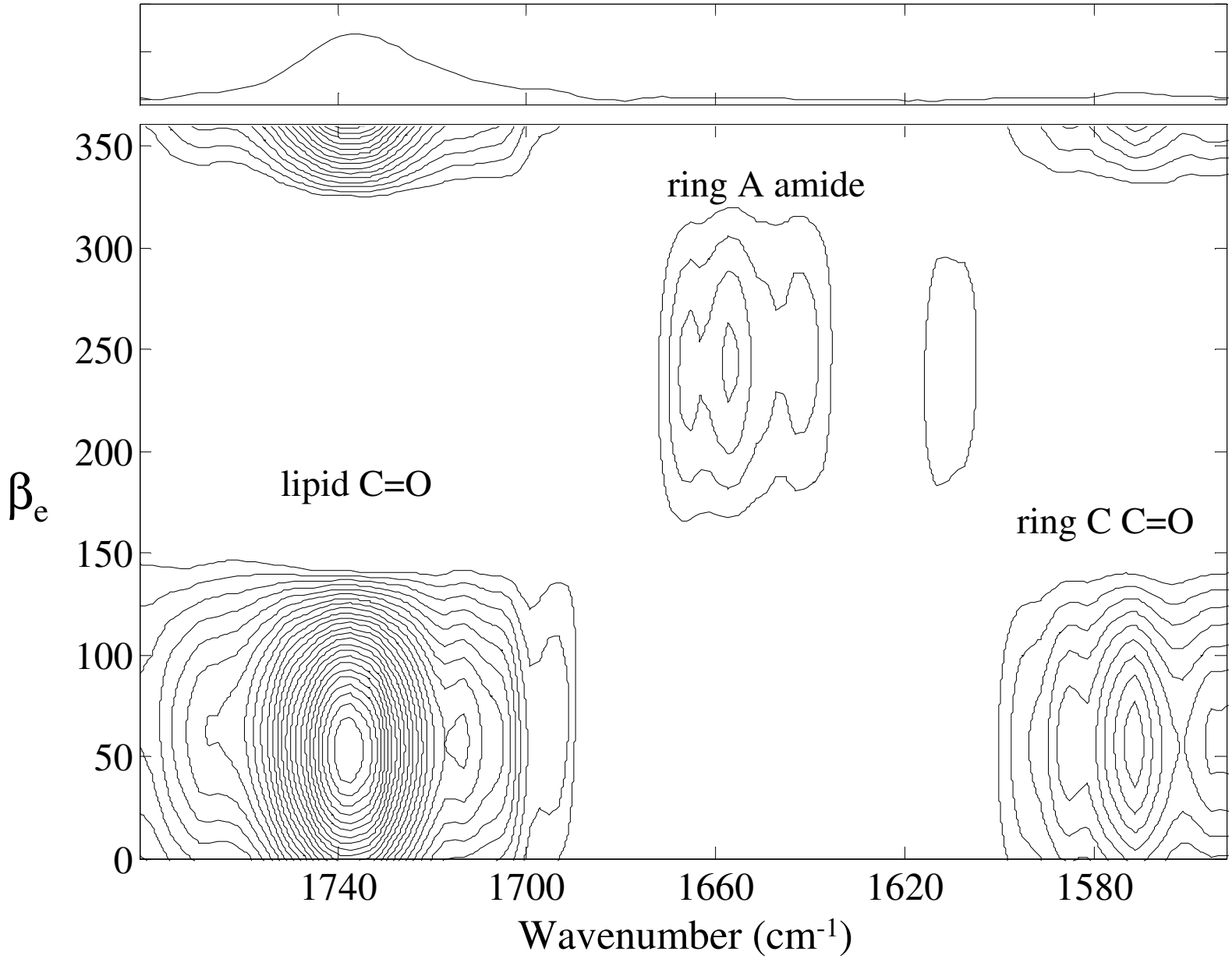
ring A amide
lipid C=O
ring C C=O
β_e
350
300
250
200
150
100
50
0
1740
1700
1660
1620
1580
Wavenumber (cm^{-1})

Table 6.1

Values of the effective phase angle, β_e, obtained from the $\beta\nu$ plots in Figures 6 and 7

Observed cm^{-1} Value	Assignment	β_e
1737	C=O of DPPA	51.8
1657	Amide group	242.1
1616	C=O of Ring A	240.1
1579	C=O of Ring C	55
1227	Asym. PO_4^{2-}	241.9
1180	Asym. C-O-C	241.1
1103	Sym. PO_4^{2-}	51.7
1058	Sym. C-O-C	62.3

Figure 6.7 2D βν phase angle correlation plots calculated in the region 1250 cm-1 – 1020 cm-1 using the monolayer PM-IRRAS spectra of DPPA / 5mM tetracycline hydrochloride shown in Figure 6.2. The topmost panel illustrates the average spectrum in the dynamic spectral data set used in the correlation calculations.

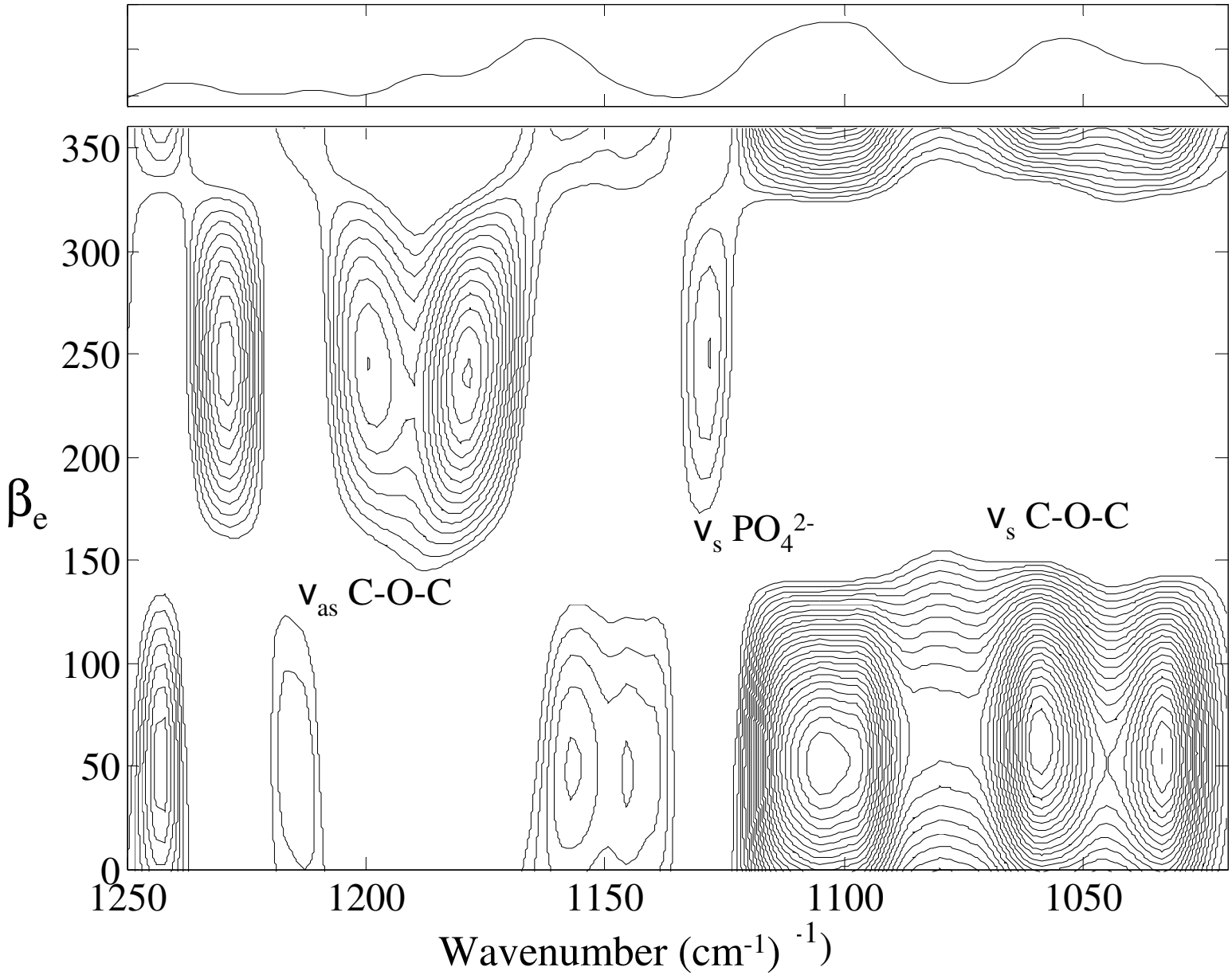
350
300
250
200
150
100
50
0
β_e
ν_{as} C-O-C
ν_s PO_4^{2-}
ν_s C-O-C
1250
1200
1150
1100
1050
Wavenumber (cm^{-1}) $^{-1}$)

240.1, while the C=O mode in Ring C has a β_e value of 55.0, indicating that the vibrational modes attributed to Ring A reorient simultaneously and earlier than do the modes from Ring C. The presence of peaks at these wavenumber values also confirms their presence in the 2D-IR synchronous and asynchronous maps.

$\beta\nu$ correlation analysis was also applied to the region of the PM-IRRAS spectra containing the vibrations of the headgroup carbonyl ester and phosphate groups (1250 – 1020 cm^{-1}); this correlation plot is displayed in Figure 6.7. In addition, the values for the effective phase angle (β_e) and the band assignments for the peaks in this plot are included in Table 6.1. Intense peaks in the $\beta\nu$ plot are observed at 1227 cm^{-1} , due to the asymmetric PO_4^{2-} stretch, 1180 cm^{-1}, corresponding to the antisymmetric stretch of the carbonyl esters, 1103 cm^{-1}, due to the symmetric stretch of the PO_4^{2-} group and at 1058 cm^{-1} corresponding to the symmetric carbonyl ester stretching vibration. From the β_e values in Table 6.1, it is apparent that the symmetric stretching modes of the ester (51.7) and the phosphate group (62.3) have similar β_e values to the C=O group in the lipid (51.8) and the C=O group in Ring C (55), indicating a similar reorientation response to increasing monolayer surface pressure. The asymmetric stretching modes of the C-O-C and PO42- groups have similar β_e values (241.9 and 241.1, respectively) to the amide I and C=O vibrations of Ring A (242.1 and 240.1), indicating a simultaneous reorientation of this portion of the lipid along with this region of the antibiotic that occurs early in the monolayer compression.

kν Correlation Analysis

We have also investigated the suitability of additional mathematical functions for use in model-dependent 2D IR correlation analysis. This article describes the application of one such function, *i.e.* an exponential function, as a mathematical waveform that simulates IR intensity variations. We have calculated the asynchronous correlations between the dynamically varying experimental PM-IRRAS spectra and a simulated exponential data set of the form $exp(-kt + R)$. The resulting correlation intensities are a function of the spectral frequency (ν) and the rate constant (k) of the exponential function. A maximum or minimum correlation intensity will be observed at one point (ν, k) in the correlation plot. A new parameter, k_{eff}, is defined from the $k\nu$ correlation plots that is the point of maximum correlation intensity in the plot of k vs. ν. Both positive and negative correlation intensities are plotted since they represent the differences in the rate of intensity change of individual spectral bands from those of the exponential curves used in the correlation. Correlation maxima are observed at a point ($\nu, k+$) when there is an increase in the infrared intensity in the positive direction and correlation minima are observed at ($\nu, k-$) when there is an increase in the intensity in the negative direction. The *'k'* values quantitatively reveal the degree of coherence between the experimental intensities and the sequence of molecular events in a discrete set of dynamic spectra. Since positive and negative *'k'* values can be directly compared, assignment of the event sequence can be achieved intuitively, and without any modification to the correlation results. Application of this correlation method to models of simulated IR spectra has shown that this is indeed a robust method and can be used to deduce quantitative temporal relationships between molecular events. A detailed description of this technique will be presented elsewhere.

We have applied the $k\nu$ exponential correlation analysis method to the PM-IRRAS spectra of the DPPA monolayer on the subphase containing tetracycline. The $k\nu$ correlation plots for this system are shown in Figures 6.8 and 6.9. The upper panel represents the region of positive correlation intensity and the lower panel represents the region of negative correlation intensity. The values for the effective rate constant (k_{eff}) and the respective band assignments are presented in Table 6.2. For the high frequency region, the $k\nu$ correlation maps reveal peaks at 1736 cm^{-1}, 1657 cm^{-1}, 1616 cm^{-1} and 1579 cm^{-1} (Figure 6.8). The correlation peaks observed in the $k\nu$ plot (Table 6.2) are identical to those observed in the $\beta\nu$ correlation plots (Table 6.1).

Based on the signs of the correlation peaks and the values of the effective rate constants the following inferences can be made. It is immediately apparent from Figure 6.8 that the band at 1736 cm^{-1}, due to the lipid carbonyl group, has both positive and negative correlation peaks. Since the k_{eff} + value of the 1736 cm^{-1} peak (2.44**)**, is significantly larger than the k_{eff} – value (-0.36**)**, it can be concluded that the intensity of the carbonyl group increases substantially as the monolayer is initially compressed. However, as the monolayer reaches higher surface pressures, the rate of intensity increase declines. Since dipole moments reorienting similarly have the same sign for the correlation intensity, it can be said that the bands due to Ring A of the TC molecule at 1616 cm^{-1} (k_{eff} + = 0.41) and 1657 cm^{-1} (k_{eff} + = 0.48) reorient similarly at nearly identical rates. The band at 1572 cm^{-1}, corresponding to the C=O in Ring C, has a negative correlation peak at (k_{eff} – = -0.37**)**, indicating a substantially different reorientation behavior than the groups in Ring A.

We have also applied $k\nu$ exponential correlation analysis to the low-frequency region of the PM-IRRAS spectra containing the bands due to the phosphate and carbonyl ester groups in the lipid headgroup (1250 – 1000 cm^{-1}). The $k\nu$ correlation plot is shown in Figure 6.9; the

Figure 6.8 2D $k\nu$ exponential correlation plots calculated in the region 1800 cm^{-1} – 1550 cm^{-1} using the monolayer PM-IRRAS spectra of DPPA / 5mM tetracycline hydrochloride shown in Figure 6.2. The topmost panel illustrates the average spectrum in the dynamic spectral data set used in the correlation calculations. The center panel illustrates positive $k\nu$ correlation intensities (i.e. k_{eff} +), while the lower panel illustrates negative $k\nu$ correlation intensities (i.e. k_{eff} –).

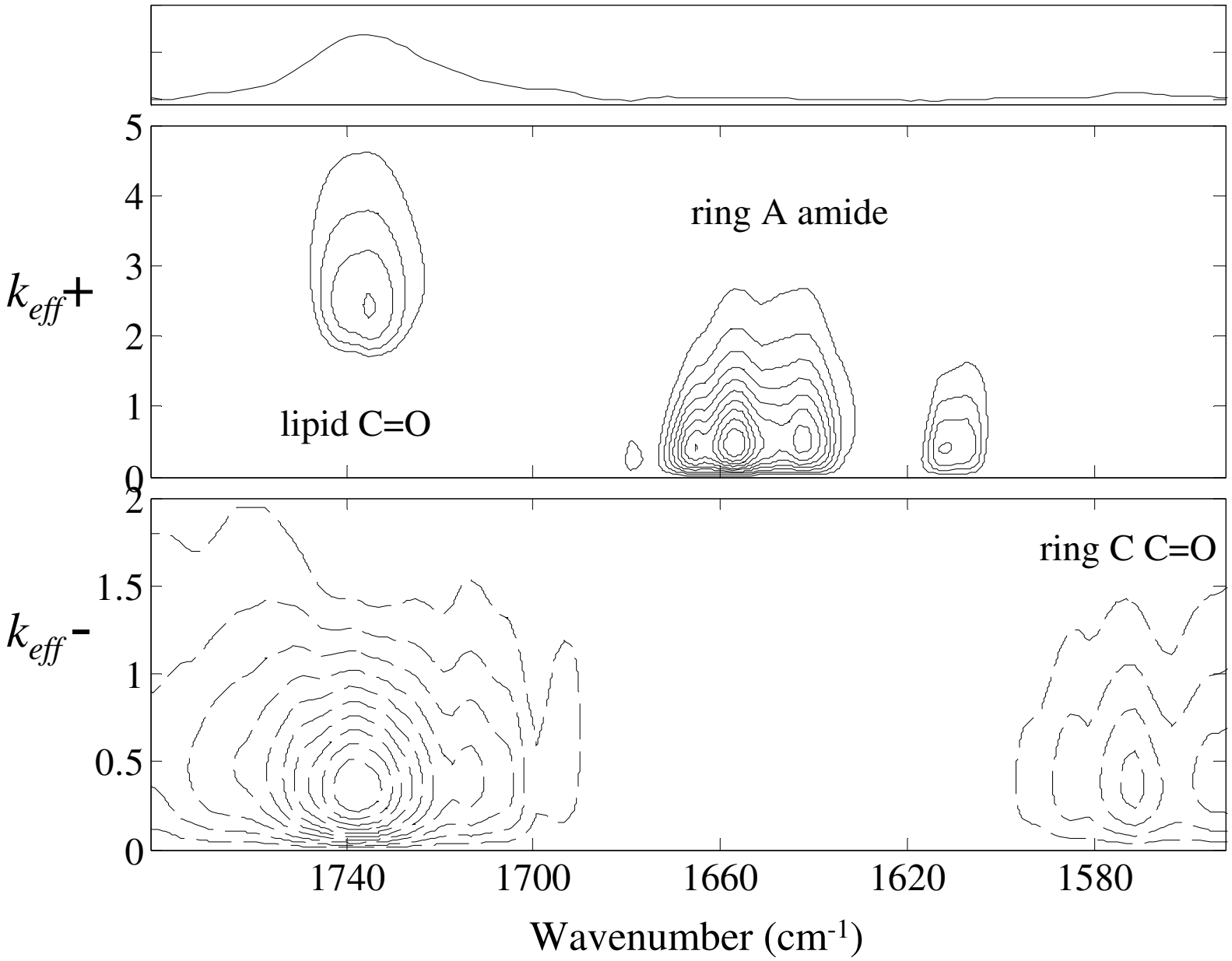
5
4
3
2
1
0
k_{eff}+
ring A amide
lipid C=O
2
1.5
1
0.5
0
k_{eff}-
ring C C=O
1740
1700
1660
1620
1580
Wavenumber (cm-1)

Figure 6.9 2D *kv* exponential correlation plots calculated in the region 1250 cm-1 – 1020 cm-1 using the monolayer PM-IRRAS spectra of DPPA / 5mM tetracycline hydrochloride shown in Figure 6.2. The topmost panel illustrates the average spectrum in the dynamic spectral data set used in the correlation calculations. The center panel illustrates positive *kv* correlation intensities (i.e. k_{eff} +), while the lower panel illustrates negative *kv* correlation intensities (i.e. k_{eff} –).

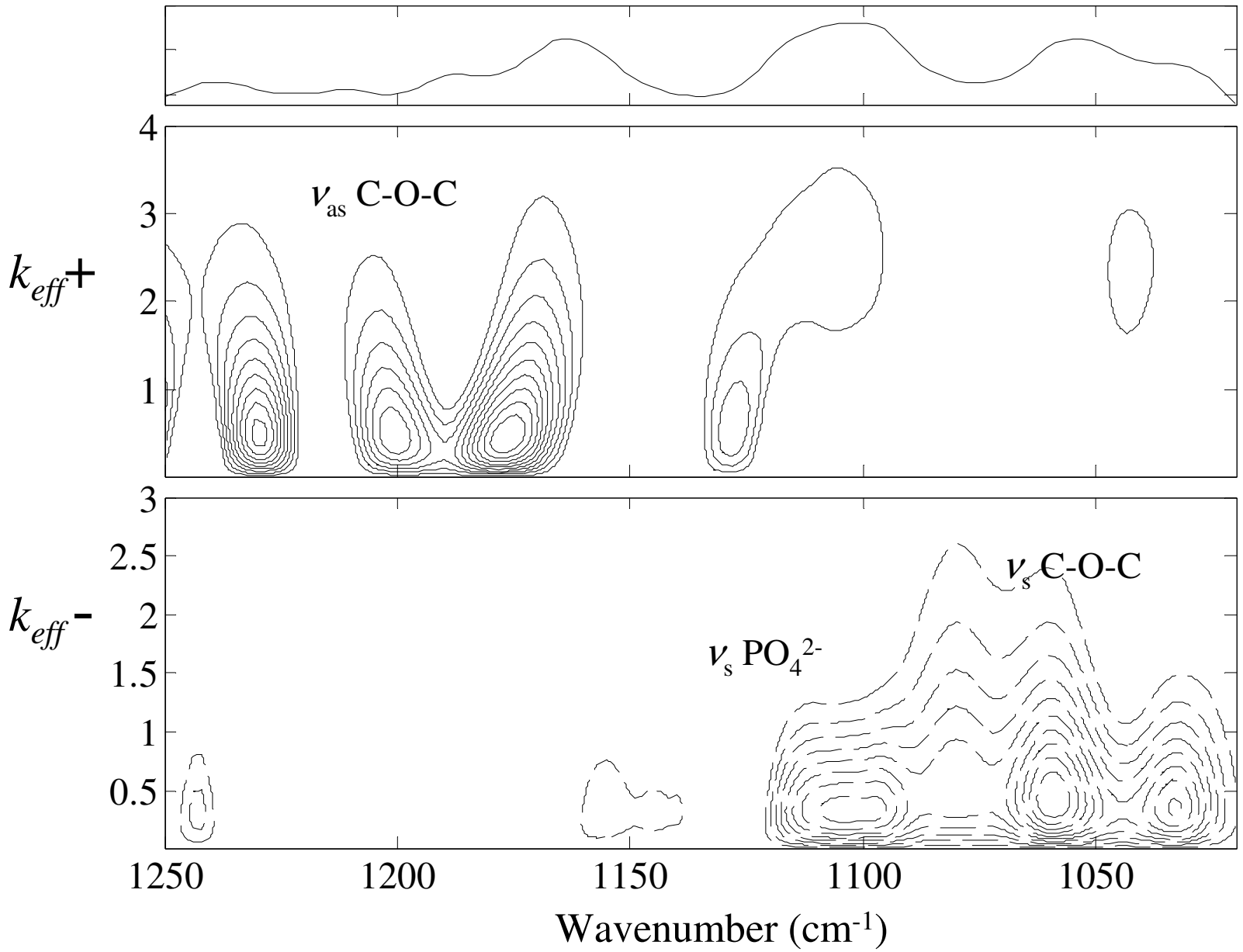
k_{eff}+
k_{eff}-
ν_{as} C-O-C
ν_s C-O-C
ν_s PO_4^{2-}
4
3
2
1
3
2.5
2
1.5
1
0.5
1250
1200
1150
1100
1050
Wavenumber (cm^{-1})

Table 6.2

Values of the effective rate constants, $k_{eff}+$ and $k_{eff}-$ obtained from the $k\nu$ plots in Figures 8 and 9

Observed cm^{-1} Value	Assignment	$k_{eff}+$	$k_{eff}-$
1737	C=O of DPPA	2.44	0.36
1657	Amide group	0.48	-
1616	C=O of Ring A	0.41	-
1579	C=O of Ring C	-	0.36
1227	Asym. PO_4^{2-}	0.49	-
1180	Asym. C-O-C	0.47	-
1103	Sym. PO_4^{2-}	-	0.30
1058	Sym. C-O-C	-	0.41

calculated values for the effective rate constant (k_{eff}) and the respective band assignments are presented in Table 6.2. The $k\nu$ correlation maps reveal peaks at 1227 cm^{-1}, 1180 cm^{-1}, 1103 cm^{-1} and 1058 cm^{-1} (Figure 6.9). Using arguments similar to those discussed above, Figure 6.9 indicates that the PO_4^{2-} group (k_{eff} + = 0.49) and the carbonyl ester (k_{eff} + = 0.47) reorient at nearly identical rates. It is apparent from Table 6.2 that these k_{eff} values are similar to the k_{eff} values for the modes in Ring A, indicating a similar rate of reorientation. From Figure 6.9, it is observed that the correlation peaks due to the symmetric stretches of the PO_4^{2-} group and the carbonyl esters at 1103 cm^{-1} (k_{eff} – = -0.3) and 1058 cm^{-1} (k_{eff} – = -0.41) respectively have similar k_{eff} values. These k_{eff} values are almost identical to those of the C=O band present in Ring C of the tetracycline molecule (k_{eff} – = -0.37**)** and the C=O band of the lipid at higher pressures (k_{eff} – = -0.36**)**. It can be concluded based on the signs and the values of the k_{eff} values that the symmetric stretching modes of the phosphate and the ester groups in the lipid headgroup have a strong interaction with the Ring C carbonyl mode and reorient at a similar rate.

We propose the following conclusions based on the k_{eff} values taken from the $k\nu$ correlation plots of the DPPA – TC monolayer. Previous studies have postulated a specific "electrostatic" interaction between the tetracycline molecule and the head group of phospholipids and that this interaction is most significant for the acid head group in DPPA [16]. Previous UV-VIS and FTIR/ATR spectra suggested intermolecular interactions occur between the TC amide group and DPPA [15]. From the current study, the β_e and k_{eff} values demonstrate that the molecular groups in Ring A of the TC molecule undergo reorientational changes at identical rates and in the same direction as does the DPPA headgroup carbonyl. These data indicate a specific inter-molecular interaction between Ring A of the tetracycline and the headgroup of the phospholipid occurs at low surface pressures. However, at higher surface pressures, reorientation of the

carbonyl group of Ring C occurs in concert with the lipid carbonyl and headgroups. Therefore, Region C of the antibiotic interacts more strongly with the lipid at high surface pressures.

Conclusions

Polarization modulation infrared reflection spectra of a dipalmitoyl phosphatidic acid monolayer on a subphase containing 5mM tetracycline hydrochloride were collected under varying surface pressures. Two-dimensional IR, $\beta\nu$ and $k\nu$ correlation analyses were performed on these PM-IRRAS spectra to gain a better understanding of the surface pressure-induced effects on the interaction between the phospholipid and antibiotic.

The synchronous 2D IR correlation map reveal strong correlation behavior between the C=O of the DPPA, the amide and C=O mode of Ring A, the C=O mode of Ring C, as well additional lipid headgroup modes (Figures 3 – 5). The presence of cross peaks in the synchronous correlation indicates the presence of a coupled response in the reorientation of the dipole moments of the modes from the lipid and antibiotic, but complete information about how that reorientation occurs is not available.

The $\beta\nu$ correlation plots (Figures 6 and 7) help to provide information about the relative rates of occurrence of the coupled responses noted in the conventional 2D IR plots. From the β_e values of the different correlation peaks listed in Table 6.1, it can be seen that the peaks due to the bands in Ring A have a greater β_e value than either the peaks due to the carbonyl in Ring C or the peak due to the lipid carbonyl band. This indicates that the reorientation occurs earlier for the modes in Ring A, *i.e.* at lower pressures, than the mode in Ring C. This is also supported by the rapid decrease in intensity of the absorption bands corresponding to the amide group and the carbonyl in Ring A in the one-dimensional PM-IRRAS spectrum, as the surface pressure of the monolayer is increased.

A new model-dependent two-dimensional correlation method, exponential $k\nu$ correlation analysis, provided further insights into the rates of reorganization of different monolayer components upon increasing surface pressure (Figures 8 and 9). For example, the lipid carbonyl band at 1736 cm^{-1} shows both positive and negative values for its effective rate constant, k_{eff}. The bimodal distribution of the k_{eff} value for the 1736 cm^{-1} band is reflected in the vibrational modes arising from the tetracycline antibiotic. First, the amide I vibration and the C=O vibration from Ring A of the TC molecule both have positive k_{eff} values nearly identical to several lipid headgroup bands. This relationship is also revealed in the $\beta\nu$ correlation plots, indicating that the Ring A vibrational modes reorient early and in concert with phospholipid headgroup. Secondly, the C=O vibration from Ring C of the TC molecule has a negative k_{eff} value identical to that of the lipid carbonyl band. These data indicate there is a strong interaction between the lipid and antibiotic and that they reorient simultaneously at high surface pressures.

A consideration of the 2D IR correlation analysis of the surface-pressure induced changes in the DPPA – TC monolayer system leads to the following model for lipid – antibiotic interaction. Initial interaction between the tetracycline molecule and the DPPA molecule occurs at low surface pressures primarily between Ring A of the tetracycline molecule and the lipid headgroup region. However, with increasing surface pressure, the mode of interaction changes, and the strongest inter-molecular interactions at high surface pressures occurs between Ring C of tetracycline and the DPPA headgroup.

Acknowledgements

The work described here was supported by the U.S. Public Health Service through National Institutes of Health grant EB001956 (R.A.D.).

References

1. Noda, I., et al., *Generalized two-dimensional correlation spectroscopy.* Appl. Spectrosc., 2000. **54**(7): p. 236A-248A.
2. Filosa, A., et al., *Two-dimensional infrared correlation spectroscopy as a probe of sequential events in the thermal unfolding of cytochromes c.* Biochemistry, 2001. **40**: p. 8256-8263.
3. Paquet, M.-J., et al., *Two-dimensional infrared correlation spectroscopy study of the aggregation of cytochrome c in the presence of dimyristoylphosphatidylglycerol.* Biophys. J., 2001. **81**: p. 305-312.
4. Schultz, C.P., O. Barzu, and H.H. Mantsch, *Two-dimensional infrared correlation analysis of protein unfolding: use of spectral simulations to validate structural changes during thermal denaturation of bacterial CMP kinases.* Appl. Spectrosc., 2000. **54**: p. 931-938.
5. Sefara, N., N.P. Magtoto, and H.H. Richardson, *Structural characterization of β-lactoglobulin in solution using two-dimensional FT mid-infrared and FT near-infrared correlation spectroscopy.* Appl. Spectrosc., 1997. **51**(4): p. 536-540.
6. Ismoyo, F., Y. Wang, and A.A. Ismail, *Examination of the effect of heating on the secondary structure of avidin and avidin-biotin complex by resolution-enhanced two-dimensional infrared correlation spectroscopy.* Appl. Spectrosc., 2000. **54**: p. 939-947.
7. Graff, D.K., et al., *The effects of chain length and thermal denaturation on helix-forming peptides: a mode-specific analysis using 2D FT-IR.* J. Am. Chem. Soc., 1997. **119**: p. 11282-11294.

8. Elmore, D.L. and R.A. Dluhy, *Application of 2D IR correlation analysis to phase transitions in Langmuir monolayer films.* Colloids and Surfaces A, 2000. **171**(1-3): p. 225-239.

9. Elmore, D.L. and R.A. Dluhy, *Pressure-dependent changes in the infrared C-H vibrations of monolayer films at the air/water interface revealed by two- dimensional infrared correlation spectroscopy.* Appl. Spectrosc., 2000. **54**(7): p. 956-962.

10. Ozaki, Y. and I. Noda, eds. *Two-Dimensional Correlation Spectroscopy*. 2000, American Institute of Physics: New York.

11. Noda, I., *Generalized two-dimensional correlation method applicable to infrared, Raman, and other types of spectroscopy.* Appl. Spectrosc., 1993. **47**: p. 1329-1336.

12. Elmore, D.L. and R.A. Dluhy, *$\beta\nu$ correlation analysis: a modified two-dimensional infrared correlation method for determining relative rates of intensity change.* J. Phys. Chem. B, 2001. **105**: p. 11377-11386.

13. Elmore, D.L., S. Shanmukh, and R.A. Dluhy, *A study of binary phospholipid mixtures at the air-water interface using infrared reflection-absorption spectroscopy and 2D-IR $\beta\nu$ correlation analysis.* J. Phys. Chem. A, 2002. **106**: p. 3420-3428.

14. Shanmukh, S., et al., *Effect of hydrophobic surfactant proteins SP-B and SP-C on phospholipid monolayers. Protein structure studied using 2D IR and $\beta\nu$ correlation analysis.* Biophys. J., 2002. **83**: p. 2126-2141.

15. Caminati, G., et al., *Spectroscopic investigation of tetracycline interaction with phospholipid Langmuir-Blodgett films.* Mat. Sci. & Eng. C, 2002. **22**(2): p. 301-305.

16. Gambinossi, F., et al., *Antibiotic interaction with phospholipid monolayers.* Mat. Sci. & Eng. C, 2002. **22**(2): p. 283-288.

17. Blaudez, D., et al., *Polarization-modulated FT-IR spectroscopy of a spread monolayer at the air/water interface.* Appl. Spectrosc., 1993. **47**(7): p. 869-74.

18. Blaudez, D., et al., *Investigations at the air/water interface using polarization modulation IR spectroscopy.* J. Chem. Soc., Faraday Trans., 1996. **92**(4): p. 525-30.

19. Buffeteau, T. and M. Pezolet, *In situ study of photoinduced orientation in azopolymers by time-dependent polarization modulation infrared spectroscopy.* Appl. Spectrosc., 1996. **50**(7): p. 948-955.

20. Buffeteau, T., et al., *Orientational studies of polymers using polarization modulation IR linear dichroism: experimental procedure and quantitative analysis.* J. Chim. Phys. Phys.-Chim. Biol., 1993. **90**(7-8): p. 1467-89.

21. Dluhy, R.A., et al., *Deacylated pulmonary surfactant protein SP-C transforms from α-helical to amyloid fibril structure via a pH-dependent mechanism: an infrared structural investigation.* Biophys. J., 2003. **85**: p. 2417-2429.

22. Noda, I., *Determination of two-dimensional correlation spectra using the Hilbert Transform.* Appl. Spectrosc., 2000. **54**(7): p. 994-999.

23. Noda, I., *Two-dimensional infrared (2D IR) spectroscopy: theory and applications.* Appl. Spectrosc., 1990. **44**: p. 550-554.

24. Shanmukh, S. and R.A. Dluhy, *kn Correlation analysis. A quantitative two-dimensional IR coorelation method for analysis of rate processes using exponential functions.* J. Phys. Chem. A, 2004: p. In press.

CHAPTER 7

STRUCTURE AND PROPERTIES OF PHOSPHOLIPID-PEPTIDE MONOLAYERS CONTAINING MONOMERIC SP-B_{1-25}. PEPTIDE CONFORMATION BY INFRARED SPECTROSCOPY.[1]

[1] Shanmukh, S., Biswas, N., Waring, A.J., Walther, F.J., Wang, Z., Chang, Y., Notter, R.H. and Dluhy, R.A. 2005. *Biophysical Chemistry*. 113(3):233-244

Reprinted here with the permission of the publisher

Abstract

The conformation and orientation of synthetic monomeric human-sequence SP-B_{1-25} (mSP-B_{1-25}) was studied in films with phospholipids at the air-water (A/W) interface by polarization modulation infrared reflectance absorption spectroscopy (PM-IRRAS). Modified two dimensional infrared (2D IR) correlation analysis was applied to PM-IRRAS spectra to define changes in the secondary structure and rates of reorientation of mSP-B_{1-25} in the monolayer during compression. PM-IRRAS spectra and 2D IR correlation analysis showed that in pure films, mSP-B_{1-25} had a major α–helical conformation plus regions of β-sheet structure. These α-helical regions reoriented later during film compression than β structural regions, and became oriented normal to the A/W interface as surface pressure increased. In mixed films with 4:1 mol:mol perdeuterated dipalmitoyl phosphatidylcholine:dioleoyl phosphatidylglycerol (DPPC-d_{62} :DOPG), the IR spectra of mSP-B_{1-25} showed that a significant, concentration-dependent conformational change occurred when mSP-B_{1-25} was incorporated into a DPPC-d_{62} :DOPG monolayer. At an mSP-B_{1-25} concentration of 10 wt%, the peptide assumed a predominately β-sheet conformation with no contribution from α-helical structures. At lower, more physiological peptide concentrations, 2D IR correlation analysis showed that the propensity of mSP-B_{1-25} to form α-helical structures was increased. In phospholipid films containing 5 wt% mSP-B_{1-25}, a substantial α-helical peptide structural component was observed, but regions of α and β structure reoriented together rather than independently during compression. In films containing 1 wt% mSP-B_{1-25}, peptide conformation was predominantly α-helical and the helical regions reoriented later during compression than remaining β structural components. The increased α-helical structure of mSP-B_{1-25} demonstrated here by PM-IRRAS and 2D IR correlation analysis in monolayers of 4:1 DPPC:DOPG containing 1 wt% (and to a lesser extent 5 wt%) peptide may be

relevant for the formation of the intermediate order 'dendritic' surface phase observed in similar surface films by epi-fluorescence.

Introduction

SP-B is a highly-active component of endogenous lung surfactant, with an amphipathic molecular structure capable of interacting strongly with both hydrophobic and hydrophilic regions on phospholipids to increase adsorption and overall dynamic surface tension lowering, [1-5]. SP-B is also a functionally-crucial constituent in clinical exogenous surfactants used to treat diseases of surfactant deficiency or dysfunction such as the neonatal respiratory distress syndrome (RDS), clinical acute lung injury (ALI), and the acute respiratory distress syndrome (ARDS) [1, 6]. Because of the functional importance of SP-B in endogenous and exogenous surfactants, its molecular biophysical behavior has been of significant research interest. Although a good deal is now known about the structure and activity of SP-B, its specific interactions and molecular orientations directly in interfacial films with phospholipids are not yet completely defined. The full length SP-B protein is thought to have at least five to six distinct domains [7-10], including an N-terminal region with a short insertion sequence that can assume an extended β–sheet conformation and is adjacent to a stable amphipathic helix.

One approach to elucidating the contributions to activity of different structural regions of SP-B involves the study of synthetic peptides such as SP-B_{1-25}, which incorporates the 25 amino acids in the important N-terminal region of the native protein [11-16]. In a companion study, we have used epi-fluorescence techniques to investigate the morphology and phase behavior of compressed interfacial films containing human sequence monomeric SP-B_{1-25} (mSP-B_{1-25}) plus 4:1 mol:mol dipalmitoyl phosphatidylcholine (DPPC):dioleoyl phosphatidylglycerol (DOPG) [17]. The present paper examines the molecular behavior of mSP-B_{1-25} in films with 4:1

perdeuterated DPPC-d_{62}:DOPG at the air-water (A/W) interface using polarization-modulation IR reflection-absorption (PM-IRRAS). PM-IRRAS has several advantages over conventional polarized IR reflectance spectroscopy for studying molecular properties in films at the A/W interface. These include the ability to discriminate isotropic water and water vapor absorptions, as well as to analyze spectra directly for molecular orientations and conformations in the interfacial film *in situ* [18].

We have previously used conventional monolayer IR spectroscopy as well as PM-IRRAS to examine the molecular interactions of bovine SP-B/C in monolayers with synthetic phospholipids at the A/W interface [19, 20]. In addition, the conformation of SP-B_{1-25} has been investigated in experimental studies [13, 14] and in computer simulations [15, 16]. However, there is little or no information on the orientation and conformation of this peptide in interfacial monolayers containing DPPC plus an unsaturated anionic component (DOPG) as occurs in native lung surfactant. The results presented here provide the first direct spectroscopic analyses of the structure and orientation of mSP-B_{1-25} in a phospholipid matrix at the A/W interface. They also complement epi-fluorescence experiments carried out in a companion study on morphological and phase changes in monolayers of 4:1 DPPC:DOPG with 1, 5, and 10 wt% mSP-B_{1-25} [17].

Materials and Methods

Synthetic materials

The synthetic acyl chain perdeuterated phospholipid 1,2-dipalmitoyl-*sn*-glycero-3-phosphocholine (DPPC-d_{62}) as well as 1,2-dioleoyl-*sn*-glycero-3-phosphoglycerol (DOPG) were purchased from Avanti Polar Lipids (Alabaster, AL). These lipids were specified as >99% pure, and were used as supplied. ACS grade NaCl and high-performance liquid chromatography

(HPLC) grade methanol and chloroform were obtained from J.T. Baker (Phillipsburg, NJ). Ultrapure H_2O used for film balance subphases and in all cleaning procedures was obtained from a Barnstead (Dubuque, IA) ROpure/Nanopure reverse osmosis/deionization system, and had a nominal resistivity of 18.3 MΩ cm. Film balance subphases in all experiments were 120 mM NaCl adjusted to pH 7 with a phosphate buffer.

Peptide synthesis and purification

SP-$B_{1\text{-}25}$ (NH_2-FPIPLPYCWLCRALIKRIQAMIPKG-COOH) was made by solid-phase peptide synthesis employing O-fluorenylmethyl-oxycarbonyl (Fmoc) chemistry. Fmoc amino acids and coupling agents were from AnaSpec (San Jose, CA). Solvents and other reagents used for peptide synthesis and purification were HPLC grade or better (Fisher Scientific, Tustin, CA; Aldrich Chemical, Milwaukee, WI). The peptide was synthesized on an 0.25 mmole scale with an ABI 431A peptide synthesizer configured for FastMoc™ double coupling cycles [21] utilizing a pre-derivatized N–α-Fmoc-glycine HMP resin (AnaSpec, San Jose, CA). Deprotection and cleavage of the peptide from the resin was carried out using TFA/thioanisol/EDT/phenol/water (10:0.5:0.25:0.5:0.5 by vol.) for two hours followed by precipitation cold with t-butyl ether. The crude product was then purified by preparative reverse phase HPLC with a Vydac C-18 column and a water/acetonitrile linear gradient with 0.1% trifluoroacetic acid as described previously [22]. The molecular weight of the peptide was determined by fast atom bombardment and/or MALDI-TOF mass spectrometry, and purity of >95% was confirmed by analytical HPLC and capillary electrophoresis.

Preparation of lipid-peptide mixtures

Stock phospholipid solutions of DPPC-d_{62} and DOPG (~1 mg/ml) were prepared in 3:1 $CHCl_3$:MeOH. For the phospholipid-peptide mixtures, the required volume of mSP-$B_{1\text{-}25}$ in 1:1

$CHCl_3$:MeOH was evaporated with N_2 for ~30 min to ensure complete solvent evaporation. The dried protein film was then dissolved in a volume of 2,2,2-trifluoroethanol (TFE). An appropriate volume of the DPPC-d_{62}:DOPG stock phospholipid solution was then added to the protein solution in TFE. The resultant phospholipid-protein solution was evaporated for ~45 min with N_2, and left overnight in a vacuum desiccator for complete elimination of solvent. The dried lipid-protein sample was then dissolved in 3:1 $CHCl_3$:MeOH for use in the monolayer IR studies.

Polarization Modulation IR Reflection-Absorption Spectroscopy (PM-IRRAS)

Spectroscopic measurements of lipid-peptide monolayers at the A/W interface were performed using a Bruker Instruments (Billerica, MA) Equinox 55 Fourier transform infrared spectrometer optically interfaced to a variable angle external reflection accessory (Bruker model XA511-A). The external reflection accessory was equipped with a custom-designed Langmuir trough (Riegler & Kirstein, Berlin, Germany) containing a micro-balance Wilhelmy sensor for surface pressure readings. Films were spread dropwise from a $CHCl_3$:MeOH solution at the A/W interface, and surface spectra were acquired at 22±0.3 ^{o}C. PM-IRRAS measurements were performed using previously described protocols adapted for our experimental design [23].

The IR beam from the interferometer was directed through its external beam port and steered using mirrors into the excitation arm of the reflectance accessory. This IR beam was singly modulated at frequencies $f = 2V\tilde{\nu}$, where V is the scan speed of the interferometer and $\tilde{\nu}$ is the wavenumber of the IR radiation, resulting in a spectral bandwidth of approximately 0.4 – 6.5 kHz. The excitation arm of the external reflection accessory was rotated using computer-driven stepper motors to achieve an angle of incidence of 74 degrees. Before reflection from the A/W interface, a wire grid polarizer (IGP225, Molectron Detector, Portland, OR) passed *p*-polarized

light through a ZnSe photoelastic modulator (PEM-90, Hinds Instruments, Hillsboro, OR) operating at its resonance frequency f_m of 50 kHz. The application of a sinusoidal input voltage to the PEM crystal induced a linear modulation of the IR beam between *p*- and *s*-polarization states at a 2 f_m frequency of 100 kHz, resulting in a second, high frequency modulation of the IR radiation. After reflection from the A/W interface, the doubly modulated IR radiation was collected by an *f*/1 ZnSe lens and focused onto the 1 mm^2 sensing chip of a liquid N_2-cooled photovoltaic HgCdTe detector (KMPV11, Kolmar Technologies, Newburyport, MA).

Due to the fact that the spectral frequencies from the interferometer were more than an order of magnitude removed from the modulation frequencies added by the PEM, the signal from the HgCdTe detector preamplifier was separated into sum (I_{dc} – resulting from the IR spectrometer) and difference (I_{ac} – resulting from PEM modulation) components using dual-channel electronics with lock-in detection, as previously described [24]. The I_{ac} difference signal was demodulated at 2 f_m with a digital lock-in amplifier (Stanford Research Systems, Model SR830) using a 100 μs time constant. The I_{ac} difference signal from the output of the lock-in, as well as the I_{dc} sum signal, was filtered using low-pass filters; electronic filtering was achieved using dual-channel electronics (Stanford Research System, Model SR650). At the output of the electronic filters, both I_{ac} and I_{dc} signals were combined using a multiplexer and sent to the 16-bit ADC of the Bruker IR spectrometer. The combined signal was deconstructed and Fourier-transformed using spectrometer software. The ratio of the resulting I_{ac} and I_{dc} single beam spectra provides the PM-IRRAS signal *S*.

$$S = \frac{I_{ac}}{I_{dc}} = C\,\frac{J_2(\phi)\left(R_p - R_s\right)}{\left(R_p + R_s\right) + J_0(\phi)\left(R_p - R_s\right)} \tag{1}$$

In this equation C is a constant that is the ratio of the slightly different electronic amplification of the two signal channels, and $J_n(\phi_0)$ is the n^{th} – order Bessel function of maximum dephasing ϕ_0 introduced by the PEM (set here to introduce maximum dephasing, $\phi_0 = \pi$, at 2000 cm^{-1}). PM-IRRAS spectra were normalized as difference spectra, with ΔS defined as the difference in signal intensity between the film-covered surface (S) and the bare water surface (S_0):

$$\Delta S = \frac{S - S_0}{S_0} \tag{2}$$

Spectra were recorded at a resolution of 4 cm^{-1} using a scan speed/sampling frequency of 13 kHz. The total acquisition time for each spectrum was 20 minutes, resulting in 1500 interferograms per spectrum.

Calculation of Exponential 2D IR Correlations – $k\nu$ Correlation Analysis

A $k.\nu$ correlation analysis is a mathematical cross correlation performed between a set of N spectra undergoing some dynamic intensity variation against a set of decreasing exponential functions that are varying in their rate constants [25]. As such, it is a model-dependent 2D IR correlation method analogous to the $\beta\nu$ correlation analysis method that we have previously described and applied to biophysical monolayer systems [19, 26]. The $k.\nu$ correlation analysis used here is mathematically described as shown in Equation 3. The asynchronous correlation intensity Ψ at some point (ν, k) represents the correlation of the measured IR spectral intensity $y(\nu, n_j)$ with the mathematical function $\exp(-kt+R)$. In Equation (3), y is the IR intensity; ν is the frequency or wavenumber; n_j is the number of the spectrum in the ordered sequence where the first spectrum number is zero; k is the rate constant of the exponential curve; N is the total

number of spectra used in the calculation; R is a constant matrix, and M_{jk} is the Hilbert-Noda transform which is defined in Equation (4).

$$\Psi(\nu,k)=\frac{1}{N-1}\sum_{j=0}^{N-1}y(\nu,n_j)\cdot\sum_{k=0}^{N-1}M_{jk}\cdot\exp(-kt+R) \tag{3}$$

$$M_{jk}=\begin{cases}0 & \text{if } j=k\\ 1/\pi(k-j) & \text{otherwise}\end{cases} \tag{4}$$

Only the asynchronous correlation algorithm is used in the $k\nu$ correlation analyses presented in this study, since asynchronous 2D IR correlations are more sensitive to differences in the form of the signal variation than are synchronous correlations [27]. The computational algorithm for the $k\nu$ correlation analysis uses the most recent mathematical formalism in which a Hilbert transform is used for calculating the asynchronous spectrum rather than the more computationally cumbersome Fourier transform [28].

Two-dimensional $k\nu$ correlation analyses were performed on monolayer PM-IRRAS spectra. Before correlation, these spectra were normalized for changes in surface density as previously described [19, 29] and baseline corrected using the GRAMS/AI spectral software package (Galactic, Nashua, NH). Special considerations were made for baseline correction in the amide I spectral region between 1600 – 1700 cm^{-1}. Details of the procedures used in this region are presented in the Appendix. The 2D plots presented in this article were calculated using two-dimensional $k\nu$ correlation analysis algorithms written in our laboratory for the MATLAB programming environment (Version 6, The MathWorks, Inc., Natick, MA).

Results and Discussion

1. Pure mSP-B_{1-25} peptide monolayers

We have used polarization modulation infrared reflectance spectroscopy (PM-IRRAS) to study the structure and orientation of the mSP-B_{1-25} peptide as an individual monolayer film at the A/W interface as well as when inserted in 4:1 DPPC-d_{62}:DOPG monolayers at different concentrations (10, 5 and 1 wt%). PM-IRRAS has several advantages over conventional polarized IR reflectance spectroscopy for the study of monolayer films at the A/W interface, specifically the ability to discriminate against isotropic water and water vapor absorptions and the ability to analyze the resulting spectra directly for the orientation and conformation of the interfacial monolayer [18].

Figure 7.1 shows the amide I region in the PM-IRRAS spectrum of a monomolecular film containing only mSP-B_{1-25} on a 120 mM NaCl subphase. The spectra were collected at increasing surface pressures between 1 mN/m – 25 mN/m. The predominant intensity of the broad amide band is seen at 1658 cm^{-1}, corresponding to an α-helical component of peptide structure. The surface selection rules of the PM-IRRAS experiment at the air-water interface specify that strong positive absorption bands in the spectrum indicate IR transition dipole moments that are aligned parallel to the interface [24]. If it is assumed that the amide I dipole moment of the peptide is oriented in the plane of the surface, this implies that the mSP-B_{1-25} peptide is oriented approximately 29-38° from the interface (depending on the choice of the angle between the amide I transition moment and the long axis of the α-helix, *e.g.* Buffeteau, *et al*., 2000). An orientation angle of 29-38° from the horizontal is consistent with the tilt angle for SP-B_{1-25} (56° from the normal to the interface) calculated from x-ray scattering [13]. The

Figure 7.1 PM-IRRAS spectra of a monomolecular film of mSP–$B_{1\text{-}25}$ at the A/W interface. Spectra were collected at surface pressures ranging between 1 – 25 mN/m as the monolayer was compressed. The spectral region between 1730 cm^{-1} – 1580 cm^{-1} showing the peptide amide I band is displayed. The direction of the arrow indicates a decrease of spectral intensity in the amide I band upon monolayer compression. Monolayers were studied at 22 ± 0.3^{o}C at the A/W interface on a subphase containing 120 mM NaCl

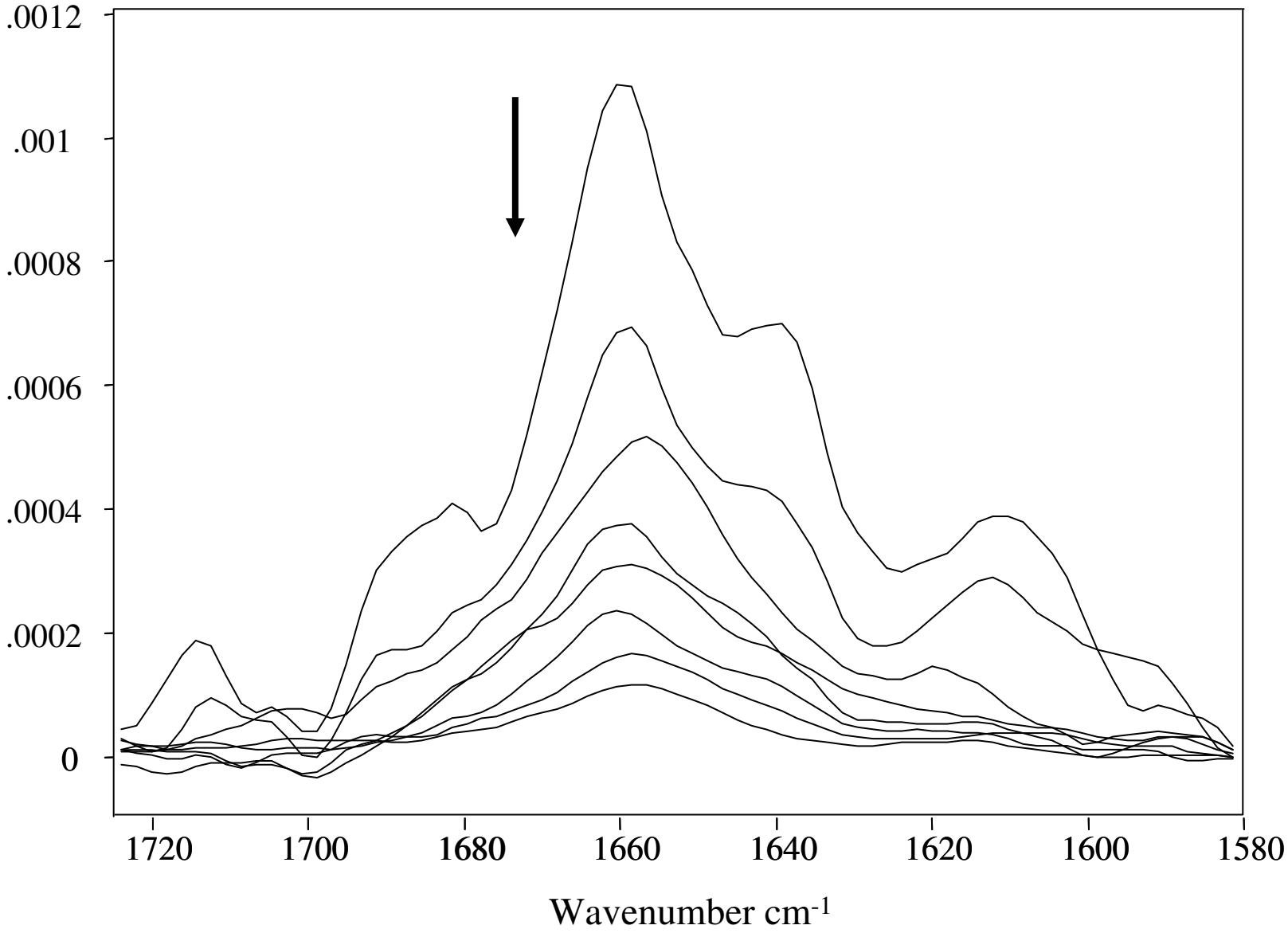
.0012
.001
.0008
.0006
.0004
.0002
0
1720
1700
1680
1660
1640
1620
1600
1580
Wavenumber cm-1

intensity of the amide I band in the IRRAS spectra for the mSP-B_{1-25} peptide monolayer in Figure 7.1 decreases with increasing surface pressure, indicating that the orientation of the dipole moment changes from parallel to perpendicular to the interface.

An earlier IRRAS study of a shorter SP-B_{1-20} monolayer on a D_2O subphase has reported an amide I band frequency at 1642 cm^{-1} indicative of a solvent-exposed α–helical or random coil structure [30]. Based on the broadness of the amide I band, the authors also suggested a small degree of β-sheet structure or surface aggregation in the peptide monolayer. A reversible surface-pressure induced β-sheet structure has also been reported for an SP-B_{9-36} peptide [10, 30]. In order to address the secondary structure of mSP-B_{1-25} at the A/W interface more quantitatively, we applied $k\nu$ correlation analysis to the measured PM-IRRAS spectra. (Note: A detailed description of the data analysis methods we used to process the PM-IRRAS spectra, including an explanation of the $k\nu$ correlation analysis technique, is provided in the Appendix.)

Figure 7.2 shows the *kν* correlation plot calculated from PM-IRRAS spectra for an mSP–B_{1-25} monolayer as a function of surface pressure. The peaks in the upper panel reflect correlations having a positive intensity, and those in the lower panel correspond to negative correlation intensity. The peaks in the *kν* correlation plot in Figure 7.2 confirm that mSP-B_{1-25} has heterogeneous structural regions during compression. Specific band assignments and calculated k_{eff} values from the spectra in Figure 7.2 are given in Table 7.1. Positive correlation peaks are observed at 1688.7 cm^{-1} (β-sheet), 1660.2 cm^{-1} (α-helix), 1637.6 cm^{-1} (β-turn) and 1608 cm^{-1} (side chain). Negative correlation peaks are observed at 1688.7 cm^{-1} (β-sheet), 1674.2 cm^{-1} (β-turn), 1656 cm^{-1} (α-helix) and 1617 cm^{-1} (β-sheet). The positive peak at 1660 cm^{-1} is assumed to reflect α-helical structure, but shifted somewhat in frequency due to changes in peptide orientation during monolayer compression. Based on the above, the secondary structure of pure

Figure 7.2 *kv* correlation plots calculated from the PM-IRRAS spectra of a monolayer of mSP–$B_{1\text{-}25}$ displayed in Figure 7.1. Solid lines indicate regions of positive correlation intensity; dashed lines indicate regions of negative correlation intensity. The one-dimensional spectrum shown on the top is a representative spectrum taken from the data set used in the *kv* analysis. Upper panel represents positive exponential correlation values (k_{eff}^{+}) while the lower panel indicates negative exponential correlation values (k_{eff}^{-}).

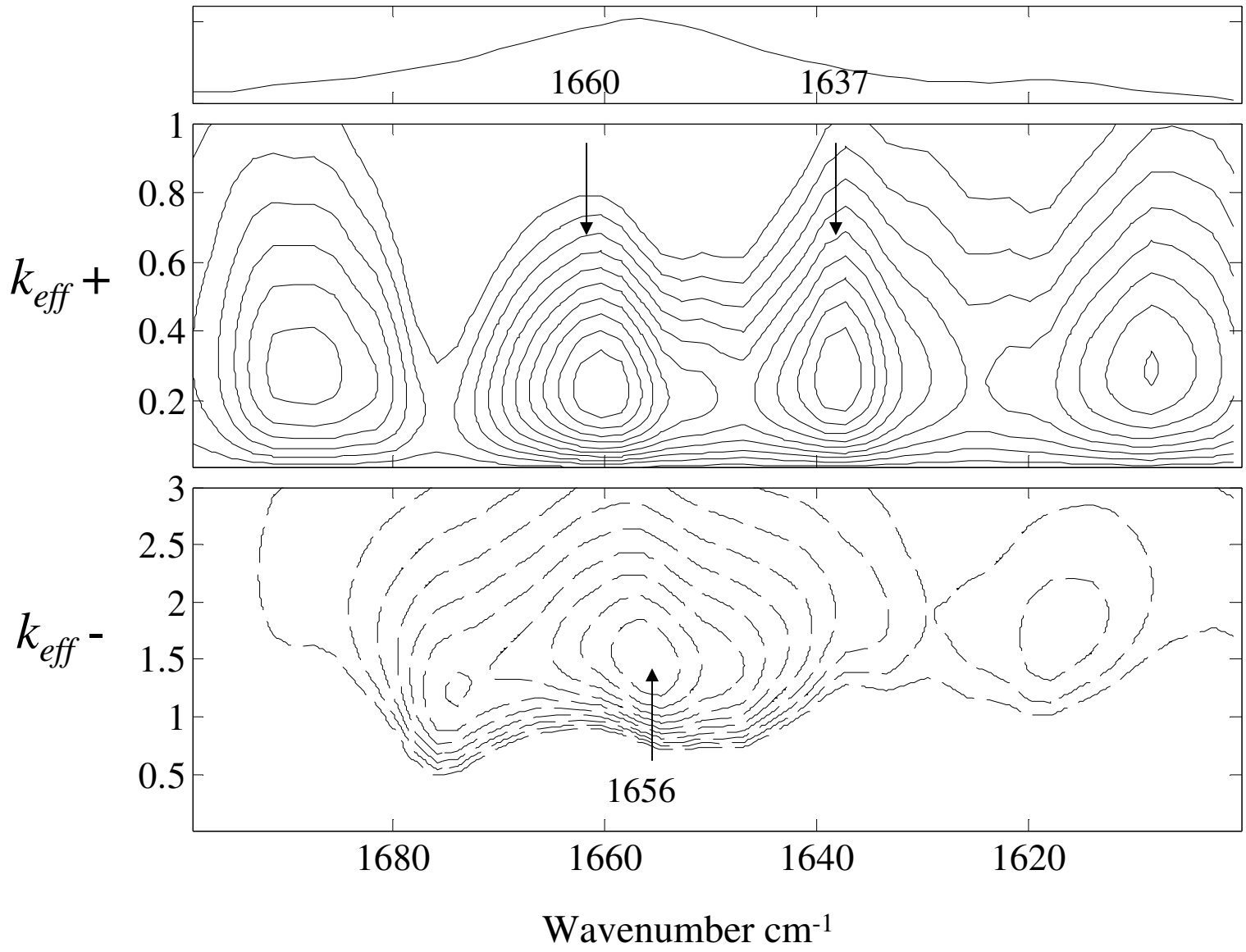
1660
1637
1
0.8
0.6
0.4
0.2
k_{eff} +
3
2.5
2
1.5
1
0.5
k_{eff} -
1656
1680
1660
1640
1620
Wavenumber cm-1

Table 7.1

Band assignments and values of effective rate constants (k_{eff}) for monolayers of pure mSP-B_{1-25} at the A/W interface.

Wavenumber, cm^{-1}	Assignment	k_{eff}^{+}	k_{eff}^{-}
1688.7	β – sheet	0.28	2.23
1674.2	β – turn	-	1.22
1660.2	α – helix	0.23	-
1656.0	α – helix	-	1.49
1637.6	β – turn	0.28	-
1617.1	β – sheet	-	1.78
1608.0	Side Chain	0.30	-

mSP-B_{1-25} at the A/W interface contains a substantial component of α-helix together with regions of β-sheet.

In addition to identifying specific structural components in the amide band contour, *kv* correlation analysis also assesses the rate at which these components change relative to one another as surface pressure increases during compression [25]. For the mSP-B_{1-25} peptide at the A/W interface, the values of k_{eff} in Table 7.1 show that vibrations attributed to regions of β structure have larger k_{eff} values and hence reorient earlier during compression than the α-helical portion of the peptide.

2. Monolayers containing DPPC-d_{62} : DOPG + 10 wt% mSP–B_{1-25}

PM-IRRAS spectra for monolayers containing 4:1 DPPC-d_{62}:DOPG plus 10 wt% mSP-B_{1-25} are shown in Figure 7.3. The spectra were collected at increasing surface pressures between 1 – 25 mN/m during monolayer compression. The bands that are most prominent in the spectrum in Figure 7.3A are at 1737 cm^{-1} (C=O stretching vibration of the DPPC-d_{62} and DOPG carbonyl bands), 1658 cm^{-1} (amide I band of the mSP-B_{1-25} peptide), 1265 cm^{-1} (asymmetric PO_4^{2-} stretching vibration of the phospholipids), 1220 cm^{-1} (asymmetric PO_4^{2-} stretching vibration of the phospholipids), 1085 cm^{-1} (combination of the symmetric PO_4^{2-} stretching vibration of phospholipids and the CD_2 scissoring mode of DPPC-d_{62}) and 1053 cm^{-1} (asymmetric carbonyl ester stretch due to the phospholipids). Figure 7.3B shows only those vibrations due to the carbonyl group of the phospholipids and the amide I band of the peptide in the 1820 cm^{-1} – 1550 cm^{-1} spectral region. The positive PM-IRRAS absorption bands of the amide I and carbonyl bands indicate that their transition dipole moments are aligned parallel to the interface [24]. The intensity of the amide I band is also seen to decrease with increasing surface pressure, indicating

Figure 7.3 PM-IRRAS spectra of a monolayer of 4:1 DPPC-d_{62}:DOPG containing 10% mSP–$B_{1\text{-}25}$ at the A/W interface. Spectra were collected at surface pressures ranging between 1 – 25 mN/m as the monolayer was compressed at 22 ± 0.3 ^{o}C at the A/W interface on a subphase of 120 mM NaCl. (A) Spectral region between 1800 cm^{-1} – 1000 cm^{-1}. (B) Spectral region between 1820 cm^{-1} – 1550 cm^{-1} that incorporates the lipid carbonyl C=O stretching band (~1740 cm^{-1}) and the peptide amide I band (~1650 cm^{-1}). The direction of the arrow indicates a decrease in the spectral intensity of the amide I band upon monolayer compression.

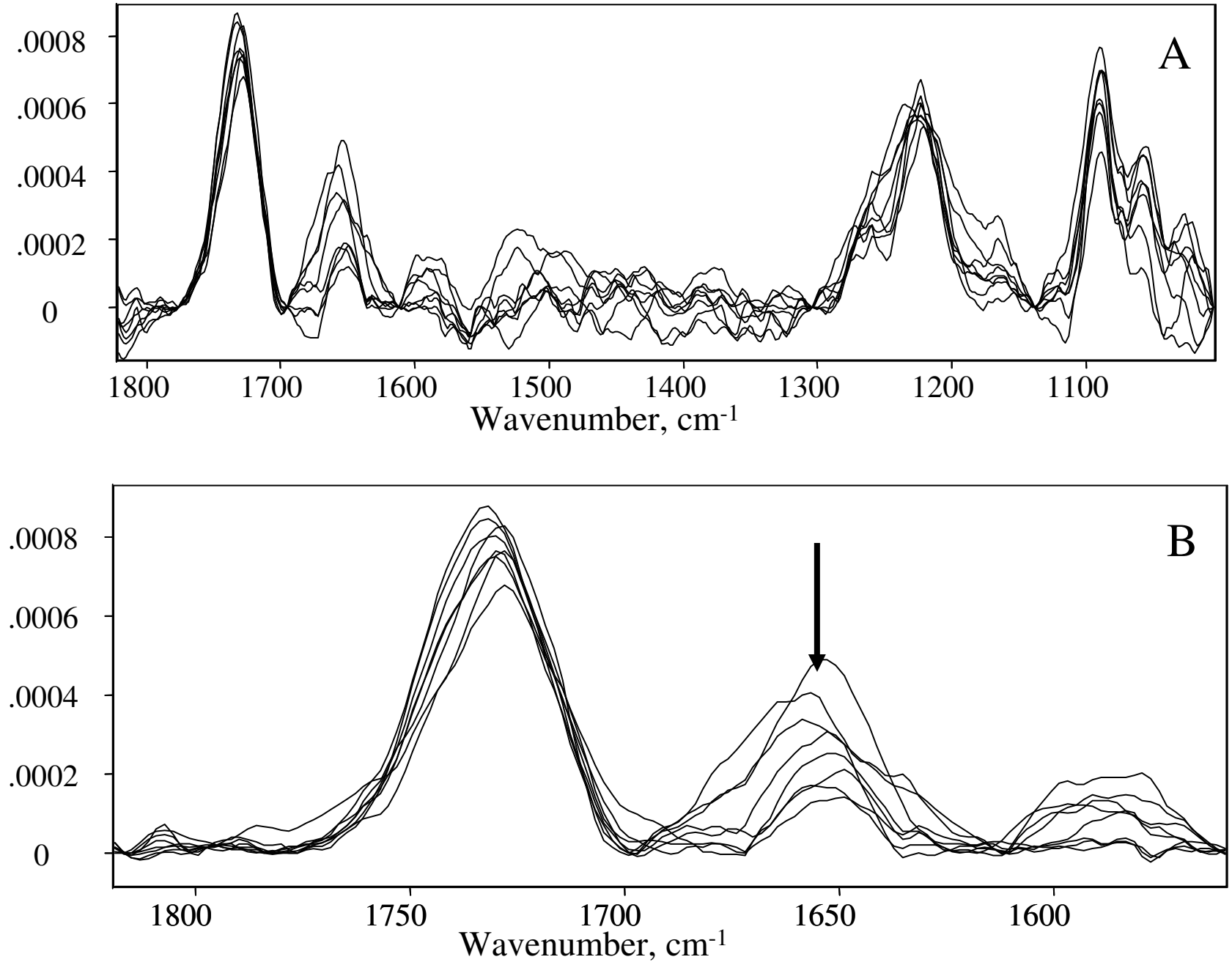
A
.0008
.0006
.0004
.0002
0
1800
1700
1600
1500
1400
1300
1200
1100
Wavenumber, cm-1
B
.0008
.0006
.0004
.0002
0
1800
1750
1700
1650
1600
Wavenumber, cm-1

Figure 7.4 *kv* correlation plots calculated from the PM-IRRAS spectra of a monolayer of 10 wt% mSP–$B_{1\text{-}25}$ displayed in Figure 7.3. Solid lines indicate regions of positive correlation intensity; dashed lines indicate regions of negative correlation intensity. The one-dimensional spectrum shown on the top is a representative spectrum taken from the data set used in the *kv* analysis. Upper panel represents positive exponential correlation values (k_{eff}^{+}) while the lower panel indicates negative exponential correlation values (k_{eff}^{-}).

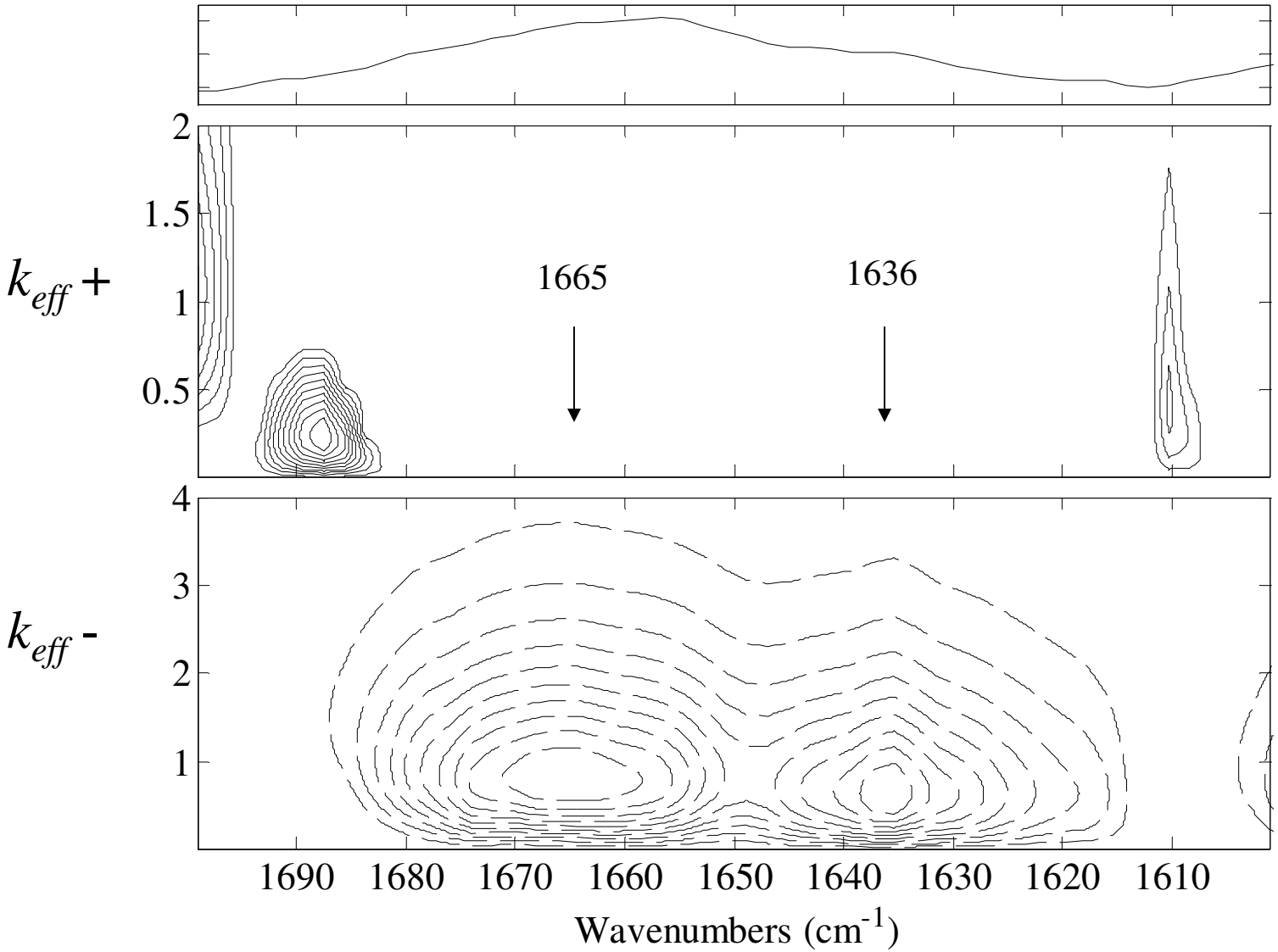
k_{eff} +
k_{eff} -
2
1.5
1
0.5
4
3
2
1
1665
1636
1690
1680
1670
1660
1650
1640
1630
1620
1610
Wavenumbers (cm^{-1})

Table 7.2

Band assignments and values of effective rate constants (k_{eff}) for monolayers of 4:1 DPPC-d_{62}:DOPG containing 10 wt% mSP-B_{1-25} at the A/W interface

Wavenumber, cm^{-1}	Assignment	k_{eff}^{+}	k_{eff}^{-}
1687.6	β – sheet	0.24	-
1665.1	β – turn	-	0.78
1635.8	β – turn	-	0.62
1610.1	Side chain	0.41	-

that the orientation of the dipole moment changes from parallel to perpendicular to the interface during compression.

Figure 7.4 shows the *kv* correlation plot of the PM-IRRAS spectra for the 10 wt% mSP-B_{1-25} mixture, while Table 7.2 gives band assignments and k_{eff} values for the correlation peaks. Intense negative correlation peaks were observed at 1665.1 cm^{-1} (β-turn) and 1635.8 cm^{-1} (β-turn) and positive correlation peaks are observed at 1687.6 cm^{-1} (β-sheet) and 1610.1 cm^{-1} (side chain). The most striking difference between the *kv* correlation plots of mSP-B_{1-25} alone (Figure 7.2) and in the presence of 4:1 DPPC:DOPG (Figure 7.4) is the lack of any significant correlation peak around 1655-60 cm^{-1}, wavenumbers corresponding to an α-helix. Combining 10 wt% mSP-B_{1-25} in a film with 4:1 DPPC:DOPG thus appears to induce an α-helix → β-sheet conformational change in the peptide at the A/W interface. Upon increasing surface pressure, all the secondary structural components reorient away from the interface in a coherent manner during compression.

3. Monolayers containing DPPC-d_{62} : DOPG + 5 wt% mSP – B_{1-25}

The PM-IRRAS spectra of mixed monolayers of 4:1 DPPC-d_{62}:DOPG + 5 wt% mSP-B_{1-25} are presented in Figure 7.5. The spectral region consisting of the amide I band (~ 1655 cm^{-1}) and the carbonyl band (1737 cm^{-1}) due to the phospholipids are the main bands shown. The amide I band decreased in intensity as surface pressure increased, indicating a reorientation of the dipole moment of the peptide away from the interface and towards the surface normal. The *kv* correlation plot calculated from the PM-IRRAS spectra for the DPPC-d_{62}:DOPG/5 wt% mSP-B_{1-25} monolayer is shown in Figure 7.6, with band assignments and corresponding k_{eff} values in Table 7.3. Positive correlation peaks were observed at 1641.3 cm^{-1} (β-turn), 1618.5 cm^{-1} (β-sheet) and 1609.4 cm^{-1} (side chain) and negative correlation peaks were observed at 1680.3 cm^{-1}

Figure 7.5 PM-IRRAS spectra of a monolayer of 4:1 DPPC-d_{62}:DOPG containing 5 wt% mSP–$B_{1\text{-}25}$ at the A/W interface. Spectra were collected at surface pressures ranging between 1 – 25 mN/m as the monolayer was compressed at 22 ± 0.3 ^{o}C at the A/W interface on a subphase of 120 mM NaCl. Spectral region between 1820 cm^{-1} – 1550 cm^{-1} includes the lipid carbonyl C=O stretching band (~1740 cm^{-1}) and the peptide amide I band (~1650 cm^{-1}). The direction of the arrow indicates decreased spectral intensity in the amide I band upon monolayer compression.

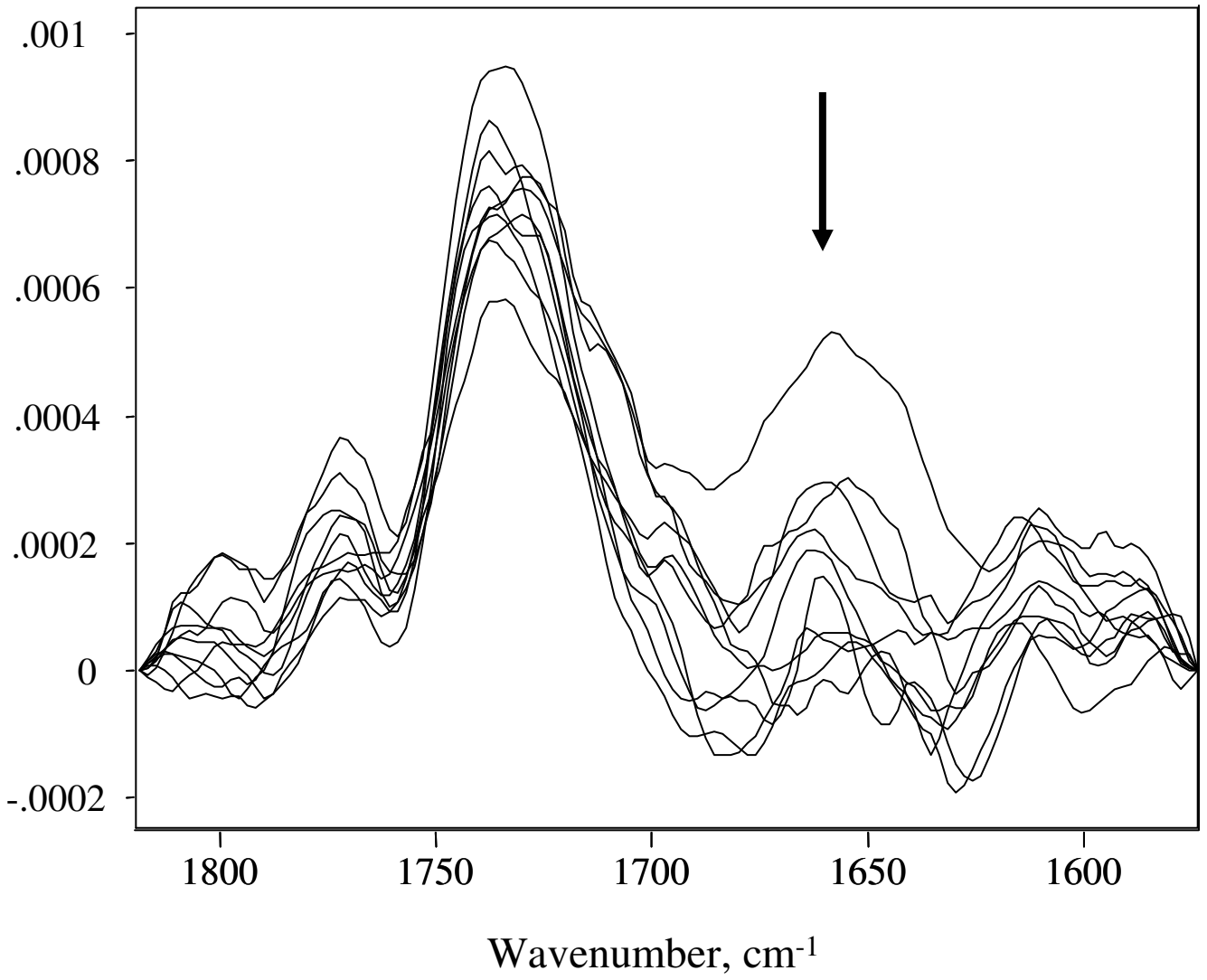
.001
.0008
.0006
.0004
.0002
0
-.0002
1800
1750
1700
1650
1600
Wavenumber, cm-1

Figure 7.6 *kv* correlation plots calculated from the PM-IRRAS spectra of a monolayer of 5 wt% mSP–$B_{1\text{-}25}$ displayed in Figure 7.5. Solid lines indicate regions of positive correlation intensity; dashed lines indicate regions of negative correlation intensity. The one-dimensional spectrum shown on the top is a representative spectrum taken from the data set used in the *kv* analysis. Upper panel represents positive exponential correlation values (k_{eff}^{+}) while the lower panel indicates negative exponential correlation values (k_{eff}^{-}).

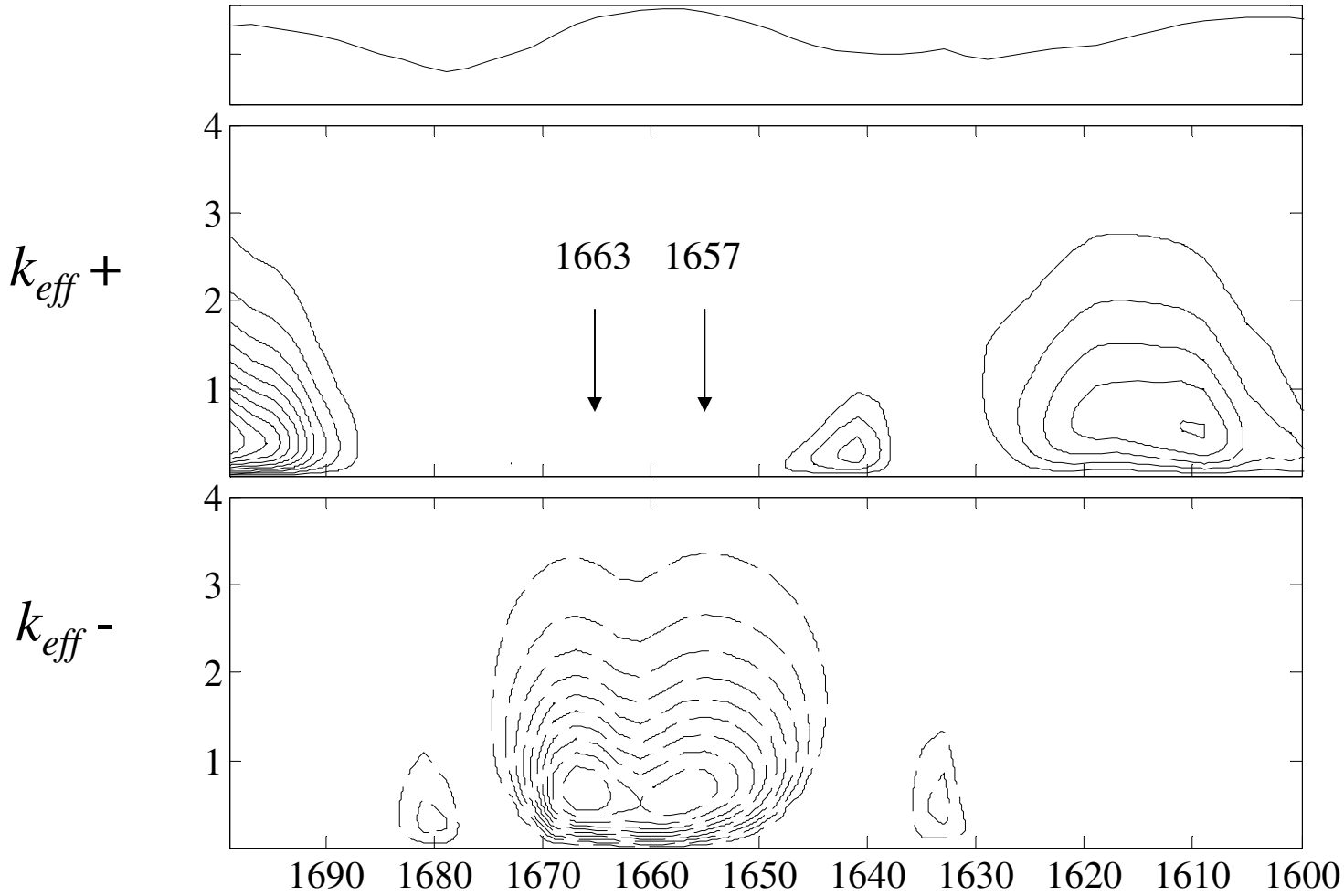
k_{eff} +
k_{eff} -
1663
1657
4
3
2
1
1690
1680
1670
1660
1650
1640
1630
1620
1610
1600
Wavenumber cm-1

Table 7.3

Band assignments and values of effective rate constants (k_{eff}) for monolayers of 4:1 DPPC-d_{62}:DOPG containing 5 wt% mSP-B_{1-25} at the A/W interface

Wavenumber, cm^{-1}	Assignment	k_{eff}^{+}	k_{eff}^{-}
1680.3	β – sheet	-	0.31
1666.3	β – turn	-	0.65
1657.0	α - helix	-	0.60
1641.3	β – turn	0.28	-
1633.3	β – sheet	-	0.52
1618.5	β – sheet	0.65	-
1609.4	Side chain	0.55	-

(β-sheet), 1666.3 cm^{-1} (β-turn), 1657.0 cm^{-1} (α-helix) and 1633.3 cm^{-1} (β-sheet). Unlike the 10 wt% mSP–B_{1-25} mixture above, a correlation cross peak at 1657 cm^{-1} was found to be present (Figure 7.6), indicating that a significant segment of the peptide was in an α-helical conformation.

Calculated k_{eff} values for DPPC-d_{62}:DOPG/5 wt% mSP-B_{1-25} monolayers indicated that both the β-sheet and α-helix components have very similar rate constants (k_{eff} ~0.60 – 0.65) (Table 7.3). This implies little or no preferential reorientation of mSP–B_{1-25} structural components during compression, with the peptide as a whole reorienting toward the surface normal as surface pressure increases. This behavior is different from that found in 10 wt% peptide films, and reinforces the understanding that the molecular structure of SP-B can vary depending on the lipid environment, the lipid-protein ratio, the extent of film compression, and other factors [19, 31-33].

4. Monolayers containing $DPPC_{d62}$: DOPG + 1 wt% mSP – B_{1-25}

Figure 7.7A shows PM-IRRAS spectra for monolayers containing 4:1 DPPC-d_{62}:DOPG + 1 wt% mSP-B_{1-25} on a subphase of 120 mM NaCl. As in the more concentrated peptide films above, the intensity of the amide band decreased with increasing surface pressure, indicating an overall reorientation of the dipole moment of the peptide towards the surface normal. Figure 7.8 shows the *kv* correlation plot calculated from the PM-IRRAS spectra for the 4:1 DPPC-d_{62}-:DOPG/1 wt% mSP-B_{1-25} monolayer, and Table 7.4 shows the band assignments and corresponding k_{eff} values. Positive correlation peaks were found at 1686.9 cm^{-1} (β-sheet), 1678.2 cm^{-1} (β-turn) and 1652.6 cm^{-1} (α-helix), while negative correlation peaks were present at 1696.8 cm^{-1} (side chain), 1686.9 cm^{-1} (β-sheet), 1668.5 cm^{-1} (β-turn), 1637.4 cm^{-1} (β-turn), 1630.5 cm^{-1} (β-sheet), 1621.3 cm^{-1} (β-sheet) and 1602.4 cm^{-1} (side chain). The most notable aspect of the

correlation analysis in Figure 7.8 is the intense correlation peak at 1652.6 cm^{-1} with k_{eff} = +0.31, indicating a strong positive correlation for an α-helical peptide conformation in the 1 wt% mSP-B_{1-25} monolayer. The 2D IR correlation analyses in Figures 7.4, 7.6, and 7.8 unambiguously show that the conformation of mSP-B_{1-25} in monolayers with 4:1 DPPC-d_{62}:DOPG is concentration-dependent. At higher peptide levels (10 wt%), the predominant secondary structural peptide conformation is β-sheet. As the concentration of the peptide decreases towards physiological values of 1 wt%, the mSP-B_{1-25} peptide adopts a much more markedly α-helical conformation within the surface film.

The calculated k_{eff} values for DPPC-d_{62}:DOPG/1 wt% mSP-B_{1-25} monolayers also show that the different secondary structural components of the peptide have divergent rate constants as a function of surface pressure (Table 7.4). This behavior differs from the data for monolayers containing 5 wt% mSP-B_{1-25} (Table 7.3), and indicates that the α and β peptide structural components in 1 wt% monolayers reorient independently during compression. The β structural components have consistently larger k_{eff} values (0.95 – 0.17) than the α-helical structures (k_{eff} ~0.31), indicating an initial reorientation of β secondary structure with increasing surface pressure, followed by a slower reorientation of α-helix.

A recent fluorescence quenching study on the topographical organization of the mSP-B_{1-25} peptide incorporated in DPPC liposomes has proposed that the α-helical peptide regions are aligned parallel to the water-lipid interface [34], although earlier physical [12, 22] and computational studies [15] have postulated a tilted peptide model. The data presented here indicate that for all concentrations tested, the mSP-B_{1-25} peptide is oriented in the plane of the interface only at low surface pressures, and becomes increasingly upright and oriented away from the interface with increasing surface pressure.

Figure 7.7 PM-IRRAS spectra of a monolayer of 4:1 DPPC-d_{62}:DOPG containing 1% mSP–$B_{1\text{-}25}$ at the A/W interface. Spectra were collected at surface pressures ranging between 1 – 25 mN/m as the monolayer was compressed at 22 ± 0.3 ^{o}C. The spectral region between 1820 cm^{-1} – 1550 cm^{-1} shows the lipid carbonyl C=O stretching band (~1740 cm^{-1}) and the peptide amide I band (~1650 cm^{-1}). (A) Monolayer on a subphase containing 120 mM NaCl. (B) Monolayer on a subphase containing 120 mM NaCl plus 2 mM $CaCl_2$. Direction of the arrow in (A) indicates a decrease of spectral intensity for the amide I band upon monolayer compression.

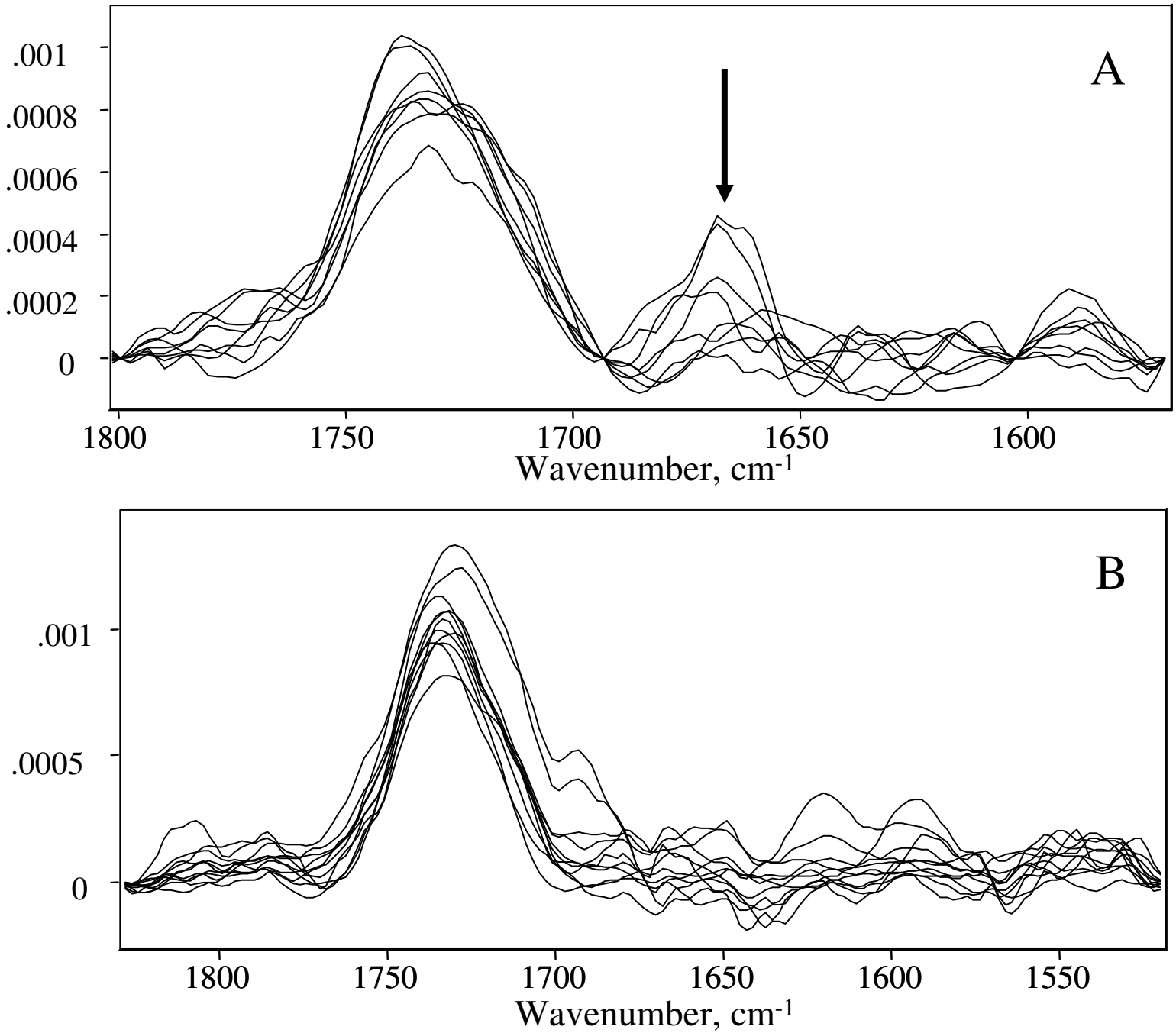
A
.001
.0008
.0006
.0004
.0002
0
1800
1750
1700
1650
1600
Wavenumber, cm-1
B
.001
.0005
0
1800
1750
1700
1650
1600
1550
Wavenumber, cm-1

Figure 7.8 *kv* correlation plots calculated from the PM-IRRAS spectra of a monolayer of 1 wt% mSP–$B_{1\text{-}25}$ displayed in Figure 7.7 (A). The solid lines indicate regions of positive correlation intensity; and the dashed lines indicate regions of negative correlation intensity. The one-dimensional spectrum shown at the top is representative of the data used in *kv* analysis. The upper panel represents positive exponential correlation values (k_{eff}^{+}) while the lower panel indicates negative exponential correlation values (k_{eff}^{-}).

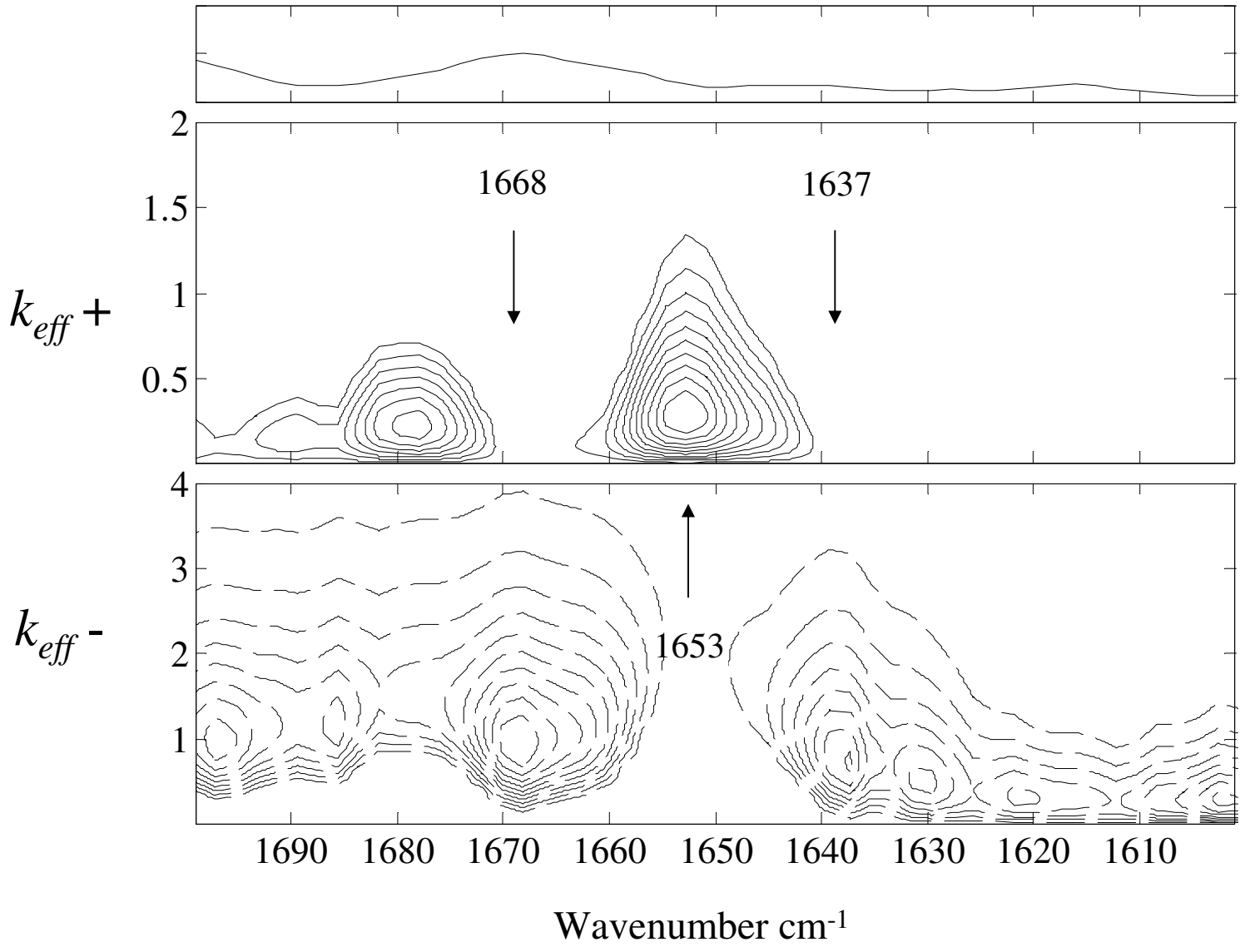
2
1.5
1
0.5
k_{eff} +
1668
1637
4
3
2
1
k_{eff} -
1653
1690
1680
1670
1660
1650
1640
1630
1620
1610
Wavenumber cm^{-1}

Table 7.4

Band assignments and values of effective rate constants (k_{eff}) for monolayers of 4:1 DPPC-d_{62}:DOPG containing 1 wt% mSP-B_{1-25} at the A/W interface

Wavenumber, cm^{-1}	Assignment	k_{eff}^{+}	k_{eff}^{-}
1696.8	Side chain		1.03
1686.9	β – sheet	0.18	1.17
1678.2	β – sheet	0.23	-
1668.5	β – turn	-	0.95
1652.6	α – helix	0.31	-
1637.4	β – turn	-	0.76
1630.5	β – sheet	-	0.50
1621.3	β – sheet	-	0.31
1602.4	Side chain	-	0.31

5. Monolayers containing $DPPC_{d62}$: DOPG + 1 wt% mSP-B_{1-25} on 2 mM $CaCl_2$

The presence of 2 mM Ca^{2+} was found to have little or no effect on the PM-IRRAS spectra or *kv* correlation plots of pure films of mSP-B_{1-25} or films containing 4:1 DPPC-d_{62}:DOPG plus 10 wt% or 5 wt% peptide. However, this was not true for monolayers of 4:1 DPPC-d_{62}:DOPG plus 1 wt% mSP-B_{1-25} (Figure 7.7B). For this mixture, the only major band observed in the PM-IRRAS spectrum in the presence of Ca^{2+} is the C=O stretching vibration at 1737 cm^{-1} due to the phospholipids (Figure 7.7B). The prominent amide I band in Figure 7.7A on a subphase containing only 120 mM NaCl is notably absent in Figure 7.7B. The absence of the amide signal in the Ca^{2+}-containing system is consistent with either an isotropic monomolecular film or a preferred peptide orientation in which the transition dipole moment has co-existing positive and negative signal contributions that cancel each other [18]. Moreover, the DPPC-d_{62}:DOPG/1 wt% mSP-B_{1-25} film in Figure 7.7B exhibits no discernable change in amide I band intensity as surface pressure increases, indicating that Ca^{2+} has locked the peptide α-helix into an immobile conformation that resists reorientation. The calcium-dependent IR behavior of 4:1 DPPC:DOPG monolayers containing 1 wt% mSP-B_{1-25} is consistent with the finding that these monolayers display differing fluorescence images when studied on subphases with and without 2 mM Ca^{2+} [17].

Conclusions

Research over the past several decades has examined and established the functional importance of lung surfactant proteins *in vivo* and in clinical exogenous surfactants. Only a portion of the molecular structure of full length SP-B is reflected in the mSP-B_{1-25} peptide studied here. Each monomer of the complete native SP-B protein contains three intramolecular disulfide bridges that impart considerable structural rigidity. An intermolecular disulfide-linked

dimer form is also prevalent in humans and other animal species, and higher oligomers also exist including trimers and possibly even salt bridge-linked quaternary forms. However, despite containing only a portion of the structure of the native protein, monomer and dimer peptides incorporating the 25 N-terminal residues of human SP-B mimic many of its surface active and biophysical behaviors [35-43]. The results of the present study are consistent with and extend this prior work, demonstrating extensive structurally-relevant molecular interactions of mSP-B_{1-25} in mixed films with 4:1 DPPC:DOPG at the A/W interface.

To date, there have been relatively few spectroscopic studies that have directly addressed the conformation and configuration of SP-B in monolayers. One such study used grazing angle x-ray diffraction to examine mSP-B_{1-25} in fatty acid monolayers [13], and reported that the peptide was oriented at an angle of ~56° relative to the surface normal. However, the grazing angle x-ray approach only indirectly addresses protein conformation, as it monitors the ordered phase of the monolayer and implicitly describes peptide configuration based on the changes in order. IR spectroscopic methods can address the conformation of proteins in monomolecular films with more direct specificity. External reflectance IR spectroscopy was initially used to study molecular structure in films at the A/W interface in the mid-1980's, and progress in this field has recently been reviewed [44, 45]. The technique can also been extended by the use of polarization-source modulation using a photoelastic modulator [24]. IRRAS methodology has previously been applied to study surfactant films at the A/W interface, including studies on extracted lung surfactant [46]. More recently, IRRAS has been used to investigate the functional roles of the hydrophobic surfactant proteins SP-B and SP-C [20, 47-49]. PM-IRRAS and 2D IR correlation methods have recently been used to examine the molecular behavior of native SP-B and SP-C in monolayers, demonstrating that these proteins adopt a variety of conformations and

orientations during compression [19]. However, the present studies are the first to address specific conformations and orientations of the N-terminal region of human SP-B directly in compressed films with phospholipids at the A/W interface.

Several prior IR studies have investigated the secondary structure of N-terminal SP-B peptides. A bulk phase IR study of ^{13}C-labelled mSP-B_{1-25} indicated a predominately α–helical peptide structure in solution and in liposomes [11]. An earlier IRRAS study of an SP-B peptide fragment (SP-B_{1-20}) on a D_2O subphase observed the amide I band frequency at 1642 cm^{-1} indicative of a solvent-exposed α–helical or random coil structure [30]. Based on the broadness of the amide I band, the authors also suggested that a small degree of β-sheet structure or surface aggregation should also be present in the SP-B_{1-20} monolayer. In addition, they also examined an SP-B_{9-36} peptide and showed that it could undergo a reversible surface-pressure induced formation of β-sheet structure in the peptide monolayer. The reversible formation of β-sheet structure in an SP-B_{9-36} peptide has recently been confirmed using ^{13}C-labelling [10].

The current study has examined the conformation and orientation of mSP-B_{1-25} in monolayers at the A/W interface, both as a pure substance and in mixtures with 4:1 DPPC-d_{62}:DOPG containing peptide contents of 1 – 10 wt%. The lower 1 wt% concentration level closely mimics the physiological content of hydrophobic proteins in endogenous lung surfactant. The results here are the first to directly examine the conformation of mSP-B_{1-25} peptide in a DPPC:DOPG matrix at the A/W interface. A model-dependent 2D IR correlation analysis method ($k\nu$ correlation analysis) recently developed in our laboratory [25] was used to reveal rate relationships involving the molecular conformation and reorientation of mSP-B_{1-25} in compressed interfacial films. A different 2D IR correlation analysis method was previously been applied to the IRRAS spectra of full length SP-B and SP-C [19]. In the present study, a

combination of PM-IRRAS and $k\nu$ correlation analysis showed that in monolayers at the A/W interface, pure mSP-$B_{1\text{-}25}$ had a heterogeneous secondary structure dominated by α-helix but also containing β-sheet structure (Figures 7.1 and 7.2). Calculated values of k_{eff} for β-sheet structural regions in pure mSP-$B_{1\text{-}25}$ monolayers were larger than those of α-helical structural regions, indicating an earlier reorientation of the β structures with increasing surface pressure during compression.

Our results also show that the conformation and reorientation of mSP-$B_{1\text{-}25}$ was strongly affected by incorporation in a phospholipid matrix at the A/W interface. A comparison of $k\nu$ correlation analyses from Figures 7.4, 7.6 and 7.8 shows unambiguously that the conformation of the mSP-$B_{1\text{-}25}$ peptide in 4:1 DPPC-d_{62}:DOPG monolayers was concentration-dependent. In films of 4:1 DPPC:DOPG plus 10 wt% mSP-$B_{1\text{-}25}$, there was a lack of any significant correlation peak around 1655-60 cm^{-1} corresponding to an α-helix (compare Figures 7.2 and 7.4). During compression, all of the peptide secondary structural components in films containing 10 wt% mSP-$B_{1\text{-}25}$ became reoriented away from the interface in a coherent manner as surface pressure increased. The extent of peptide α-helical structures in surface films with 4:1 DPPC:DOPG became more substantial as mSP-$B_{1\text{-}25}$ content was reduced to physiological levels. At mSP–$B_{1\text{-}25}$ contents of 5 wt%, a correlation cross peak at 1657 cm^{-1} appeared in the $k\nu$ correlation analysis plot (Figure 7.6), indicating a substantial segment of the peptide in an α-helical conformation. However, k_{eff} rate constants for this film implied no preferential reorientation of secondary structure components as the peptide as a whole reoriented toward the surface normal with increasing surface pressure (Table 7.3). In phospholipid monolayers containing 1 wt% mSP-$B_{1\text{-}25}$, an intense correlation peak at 1652.6 cm^{-1} with k_{eff} = +0.31 indicated a very strong positive correlation for an α-helical conformation (Figure 7.8). Also in the 1 wt% film, divergent k_{eff}

values indicated that the structural components of the peptide reoriented independent of one another as surface pressure increased during compression (Table 7.4). Calculated k_{eff} values for 1 wt% peptide films were consistent with an initial reorientation of β-structure secondary structure with increasing surface pressure, followed by a slower reorientation of α-helical regions of peptide structure.

Acknowledgements

The financial support of the U.S. Public Health Service through National Institutes of Health (NIH) grants EB001956 (R.A.D.), HL56176 (R.H.N.) and HL55534 (F.J.W. and A.J.W.) is gratefully acknowledged.

Appendix

2D IR correlation analysis of PM-IRRAS spectra of peptides – data analysis methods

The analysis of PM-IRRAS spectra of peptides at the A/W interface requires careful spectral data processing. PM-IRRAS spectra possess a strong downward sloping baseline between 1700 – 1650 cm^{-1} due to the anomalous dispersion of the real part of the refractive index of water in this region, arising from the δ(H-O-H) deformation vibration of liquid water [18]. The intensity of this deformation vibration increases as the monolayer is compressed to higher surface pressures due to a change in the structure of the water molecules at the interface. In 2D IR correlation analysis, one of the requisite data pretreatment methods is to ensure a uniform baseline for all the spectra. Therefore, baseline correction of monolayer PM-IRRAS spectra, especially in the amide I region, is needed. We accomplished baseline correction for the amide I bands by fitting a Lorentzian curve to the δ(H-O-H) deformation band and subtracting this band from each of the experimentally acquired PM-IRRAS spectra. The full-width at half maximum of the Lorentzian band was varied depending on the surface tension and the resulting shape of the δ(H-O-H) spectral feature. The baseline-corrected PM-IRRAS spectra were then normalized for changes in surface density. These baseline-corrected and normalized spectra were used in the 2D IR correlation analyses described in this article to determine the structure and orientation of mSP-$B_{1\text{-}25}$ in a pure component film at the A/W interface as well as when inserted in 4:1 DPPC-d_{62}:DOPG monolayers at different concentrations (10, 5 and 1 wt%).

Two-dimensional infrared correlation spectroscopy (2D IR) has been shown to be a very effective technique in elucidating secondary structural information from infrared absorption spectra of proteins undergoing a dynamic perturbation [50-52]. This dynamic environmental perturbation could be the concentration of the protein, temperature, pH of the solvent or, as in the

current case, surface pressure. In a previous publication, we successfully applied both conventional and modified 2D IR to IRRAS spectra of surfactant protein (SP-C) monolayers. These methods allowed us to identify protein secondary structural components and assign relative rates of orientation as a function of monolayer compression for those components [19].

In the current analysis of the PM-IRRAS spectra of mSP-$B_{1\text{-}25}$ at the A/W interface we have used a method known as kv correlation analysis to evaluate the spectra. A kv correlation analysis is a mathematical asynchronous cross correlation performed between a set of N spectra undergoing some dynamic intensity variation against a set of exponential functions with a user-defined range of rate constants. Details of the kv correlation analysis method are presented elsewhere [25]. The kv correlation analysis method is a model-dependent 2D IR correlation method analogous to the $\beta\nu$ method we previously used to analyze monolayer IR spectra of the native SP-B and SP-C proteins [19]. In kv correlation analysis, the observed correlation intensities are a function of the rate constant of the exponential function and the spectral frequency. The 2D correlation plots reveal rate relationships between different molecular events in terms of a quantitative and tangible parameter, k, which is the rate constant of the exponential function used in the correlation. A new parameter, the effective rate constant, k_{eff}, is defined as the point of maximum correlation intensity at particular frequencies in the plot of k *vs.* ν. The calculated values of k_{eff} represent the rates at which the intensities of the spectral bands change during the course of the dynamic experiment. As a result, these k_{eff} values are comparable and can be used to assign quantitative rate relationships. Events at frequencies with a larger k_{eff} value occur earlier than events at frequencies with smaller k_{eff} values. Positive and negative k_{eff} values are comparable and hence no manipulation of the spectra or the correlation plots is required to compare bands with increasing and decreasing intensities.

We have shown that $k\nu$ correlation methods are sensitive to the relative change in the rates of the band intensities through a dynamic data set [25]. The k_{eff} values are not the actual kinetic rate constants *per se*, but instead the k_{eff} parameter is sensitive to the relative order in which the intensity change occurs, while the size of the correlation peaks gives an indication of the magnitude of the intensity change. Spectral bands whose rate of intensity change varies through a dynamic data set are distinguished by the presence of both positive and negative peaks in the $k\nu$ correlation plots.

The presence of both a positive and negative correlation peak at a particular frequency can be understood as a modulation in the rate of intensity change at that frequency. The decrease in intensity of the amide I band upon increasing surface pressure in the PM-IRRAS spectra of mSP-$B_{1\text{-}25}$ (Figure 7.7) suggest that the positive peaks in the correlation plot are due to a decreased rate of change in these bands with increasing surface pressure. Since the PM-IRRAS spectra used in the *kv* correlation analysis have already been normalized for changes in surface density, the correlation peak intensity can be taken as an indicator of the change in intensity as a result of change in orientation of the amide I band.

References

1. Notter, R.H., *Lung surfactants: basic science and clinical applications*. 2000, New York: Marcel Dekker, Inc.
2. Veldhuizen, R., et al., *The role of lipids in pulmonary surfactant.* Biochim. Biophys. Acta, 1998. **1408**: p. 90-108.
3. Tanaka, Y., et al., *Development of synthetic lung surfactants.* J. Lipid Res., 1986. **27**: p. 475-485.
4. Poulain, F.R. and J.A. Clements, *Pulmonary surfactant therapy.* West. J. Med., 1995. **162**: p. 43-50.
5. Hawgood, S., M. Derrick, and P. Poulain, *Structure and properties of surfactant protein B.* Biochim. Biophys. Acta, 1998. **1408**: p. 150-160.
6. Chess, P., et al., *Surfactant replacement therapy in lung injury*, in *Lung Injury: Mechanisms, Pathophysiology and Therapy*, R.H. Notter, J.N. Finkelstein, and B.A. Holm, Editors. 2004, Marcel Dekker: New York. p. In press.
7. Waring, A.J., et al., *Synthesis, secondary structure and folding of the bend region of lung surfactant protein B.* Pept. Res., 1996. **9**(1): p. 28-39.
8. Liepinsh, E., et al., *Saposin fold revealed by the NMR structure of NK-lysin.* Nat. Struct. Biol., 1997. **4**(10): p. 793-795.
9. Zaltash, S., et al., *Pulmonary surfactant protein B: a structural model and a functional analogue.* Biochim. Biophys. Acta, 2000. **1466**: p. 179-186.
10. Flach, C.R., et al., *Location of structural transitions in an isotopically labeled lung surfactant SP-B peptide by IRRAS.* Biophys. J., 2003. **85**: p. 340-349.

11. Gordon, L.M., et al., *Conformational mapping of the N-terminal segment of surfactant protein B in lipid using ^{13}C-enhanced Fourier transform infrared spectroscopy.* J. Peptide Res., 2000. **55**: p. 330-347.

12. Kurutz, J.W. and K.Y.C. Lee, *NMR structure of lung surfactant peptide SP-B_{11-25}.* Biochemistry, 2002. **41**: p. 9627-9636.

13. Lee, K.Y., et al., *Synchrotron X-ray study of lung surfactant-specific protein SP-B in lipid monolayers.* Biophys. J., 2001. **81**(1): p. 572-585.

14. Flanders, B.N., S.A. Vickery, and R.C. Dunn, *Imaging of monolayers composed of palmitic acid and lung surfactant protein B.* J. Microscopy, 2001. **202**: p. 379-385.

15. Kaznessis, Y.N., S. Kim, and R.G. Larson, *Specific mode of interaction between components of model pulmonary surfactants using computer simulations.* J. Mol. Biol., 2002. **322**: p. 569-582.

16. Freites, J.A., Y. Choi, and D.J. Tobias, *Molecular dynamics simulations of a pulmonary surfactant protein B peptide in a lipid monolayer.* Biophys. J., 2003. **84**: p. 2169-2180.

17. Biswas, N., et al., *Structure and properties of phospholipid-peptide monolayers containing monomeric SP-B1-25. I. Phases and morphology by epi-fluorescence microscopy.* Biophys. J., 2004: p. Submitted.

18. Blaudez, D., et al., *Investigations at the air/water interface using polarization modulation IR spectroscopy.* J. Chem. Soc., Faraday Trans., 1996. **92**(4): p. 525-30.

19. Shanmukh, S., et al., *Effect of hydrophobic surfactant proteins SP-B and SP-C on phospholipid monolayers. Protein structure studied using 2D IR and $\beta\nu$ correlation analysis.* Biophys. J., 2002. **83**: p. 2126-2141.

20. Brockman, J.M., et al., *Effect of hydrophobic surfactant proteins SP-B and SP-C on binary phospholipid monolayers. II. Infrared external reflectance-absorption spectroscopy.* Biophys. J., 2003. **84**: p. 326-340.

21. Fields, C.G., et al., *HBTU activation for automated Fmoc solid-phase peptide synthesis.* Peptide Res., 1991. **4**: p. 95-101.

22. Gordon, L.M., et al., *Conformation and molecular topography of the N-terminal segment of surfactant protein-B in structure-promoting environments.* Protein Science, 1996. **5**(8): p. 1662-1675.

23. Dluhy, R.A., et al., *Deacylated pulmonary surfactant protein SP-C transforms from α-helical to amyloid fibril structure via a pH-dependent mechanism: an infrared structural investigation.* Biophys. J., 2003. **85**: p. 2417-2429.

24. Blaudez, D., et al., *Polarization-modulated FT-IR spectroscopy of a spread monolayer at the air/water interface.* Appl. Spectrosc., 1993. **47**(7): p. 869-74.

25. Shanmukh, S. and R.A. Dluhy, *$k\nu$ correlation analysis. A quantitative two-dimensional IR correlation method for analysis of rate processes using exponential functions.* J. Phys. Chem. A, 2004: p. In Press.

26. Elmore, D.L. and R.A. Dluhy, *$\beta\nu$ correlation analysis: a modified two-dimensional infrared correlation method for determining relative rates of intensity change.* J. Phys. Chem. B, 2001. **105**: p. 11377-11386.

27. Noda, I., *Two-dimensional infrared (2D IR) spectroscopy: theory and applications.* Appl. Spectrosc., 1990. **44**: p. 550-554.

28. Noda, I., *Determination of two-dimensional correlation spectra using the Hilbert Transform.* Appl. Spectrosc., 2000. **54**(7): p. 994-999.

29. Elmore, D.L. and R.A. Dluhy, *Pressure-dependent changes in the infrared C-H vibrations of monolayer films at the air/water interface revealed by two- dimensional infrared correlation spectroscopy.* Appl. Spectrosc., 2000. **54**(7): p. 956-962.

30. Dieudonne, D., et al., *Secondary structure in lung surfactant SP-B peptides: IR and CD studies of bulk and monolayer phases.* Biochem. Biophys. Acta, 2001. **1511**: p. 99-112.

31. Cruz, A., C. Casals, and J. Perez-Gil, *Conformational flexibility of pulmonary surfactant proteins SP-B and SP-C studied in aqueous-organic solvents.* Biochem. Biophys. Acta, 1995. **1255**: p. 68-76.

32. Cruz, A., et al., *Different modes of interaction of pulmonary surfactant protein SP-B in phosphatidylcholine bilayers.* Biochemical Journal, 1997. **327**: p. 133-138.

33. Cruz, A., et al., *Depth profiles of pulmonary surfactant protein B in phosphatidylcholine bilayers, studied by fluorescence and electron spin resonance spectroscopy.* Biochemistry, 1998. **37**: p. 9488-9496.

34. Wang, Y.D., K.M.K. Rao, and E. Demchuk, *Topographical organization of the N-terminal segment of lung pulmonary surfactant protein B (SP-B1-25) in phospholipid bilayers.* Biochemistry, 2003. **42**(14): p. 4015-4027.

35. Lipp, M.M., et al., *Phase and morphology changes in lipid monolayers induced by SP-B protein and its amino-terminal peptide.* Science, 1996. **273**(5279): p. 1196-1199.

36. Longo, M.L., et al., *A function of lung surfactant protein SP-B.* Science, 1993. **261**(5120): p. 453-456.

37. Longo, M.L., et al., *A function of lung surfactant protein SP-B.* Science, 1993. **261**: p. 453-456.

38. Fan, B., et al., *Antibodies against synthetic amphipathic helical sequences of surfactant protein SP-B detect a conformational change in the native protein.* FEBS Letters, 1991. **282**: p. 220-224.

39. Veldhuizen, E.J.A., et al., *Dimeric N-terminal segment of human surfactant protein B (dSP-B1-25) has enhanced surface properties compared to monomeric SP-B1-25.* Biophys. J., 2000. **79**: p. 377-384.

40. Lipp, M.M., et al., *Phase and morphology changes in lipid monolayers induced by SP-B protein and its amino-terminal peptide.* Science, 1996. **273**: p. 1196-1199.

41. Lipp, M.M., et al., *Coexistence of buckled and flat monolayers.* Physical Rev. Lett., 1998. **81**(8): p. 1650-1653.

42. Diemel, R.V., et al., *Multilayer formation upon compression of surfactant monolayers depends on protein concentration as well as lipid composition: An atomic force microscopy study.* J. Biol. Chem., 2002. **277**: p. 21179-21188.

43. Ding, J., et al., *Nanostructure changes in lung surfactant monolayers induced by interactions between palmitoyloleoylphosphatidylglycerol and surfactant protein B.* Langmuir, 2003. **19**: p. 1539-1550.

44. Mendelsohn, R., J.W. Brauner, and A. Gericke, *External infrared reflection-absorption spectrometry. Monolayer films at the air-water interface.* Ann. Rev. Phys. Chem., 1995. **46**: p. 305-334.

45. Dluhy, R.A., *Infrared spectroscopy of biophysical monomolecular films at interfaces: Theory and applications.* Applied Spectroscopy Reviews, 2000. **35**(4): p. 315-351.

46. Dluhy, R.A., et al., *Infrared spectroscopic investigations of pulmonary surfactant. Surface film transitions at the air-water interface and bulk phase thermotropism.* Biophys. J., 1989. **56**(6): p. 1173-1181.

47. Pastrana-Rios, B., et al., *External reflection absorption infrared spectroscopy study of lung surfactant proteins SP-B and SP-C in phospholipid monolayers at the air/water interface.* Biophys. J., 1995. **69**(6): p. 2531-2540.

48. Gericke, A., C.R. Flach, and R. Mendelsohn, *Structure and orientation of lung surfactant SP-C and L-α-dipalmitoylphosphatidylcholine in aqueous monolayers.* Biophys. J., 1997. **73**(1): p. 492-499.

49. Flach, C.R., et al., *Palmitoylation of lung surfactant protein SP-C alters surface thermodynamics, but not protein secondary structure or orientation in 1,2-dipalmitoylphosphatidylcholine Langmuir films.* Biochim. Biophys. Acta, 1999. **1416**(1-2): p. 11-20.

50. Paquet, M.-J., et al., *Two-dimensional infrared correlation spectroscopy study of the aggregation of cytochrome c in the presence of dimyristoylphosphatidylglycerol.* Biophys. J., 2001. **81**: p. 305-312.

51. Schultz, C.P., O. Barzu, and H.H. Mantsch, *Two-dimensional infrared correlation analysis of protein unfolding: use of spectral simulations to validate structural changes during thermal denaturation of bacterial CMP kinases.* Appl. Spectrosc., 2000. **54**: p. 931-938.

52. Ismoyo, F., Y. Wang, and A.A. Ismail, *Examination of the effect of heating on the secondary structure of avidin and avidin-biotin complex by resolution-enhanced two-dimensional infrared correlation spectroscopy.* Appl. Spectrosc., 2000. **54**: p. 939-947.

CHAPTER 8

RANDOMLY ALIGNED SILVER NANOROD ARRAYS PRODUCE HIGH SENSITIVITY SERS SUBSTRATES.[1]

[1] Shanmukh, S. (co-author), Chaney, S.B., Zhao, Y.-P. and Dluhy, R.A. submitted to Advanced Physics Letters 2005

Abstract

Substrates consisting of silver nanorod arrays with varying rod lengths were fabricated by an oblique angle vapor deposition method. These arrays were evaluated as potential surface-enhanced Raman spectroscopy (SERS) substrates using trans-1,2-bis(4-pyridyl)ethane as a reporter molecule. SERS activity was shown to depend upon the length of the nanorods. The Ag nanorods with average lengths of 508.29 ± 44.86 nm, and having aspect ratios of 5.69 ± 1.49 exhibited the maximum SERS enhancement factors of greater than 10^8. Theoretical calculations indicate that this large SERS enhancement may be partially explained by the shape, density and lateral arrangement of the Ag nanorod arrays.

Introduction

Since its discovery in the late 1970s, Surface-enhanced Raman scattering (SERS) has emerged as a routine and powerful tool for the investigation and structural characterization of interfacial and thin-film systems. In spite of its recent popularity, SERS does have limitations, including strict requirements that must be met in order to achieve optimal enhancement. One of the critical aspects of the technique involves the need for producing an ideal surface morphology on the SERS substrate for maximum enhancement, a requirement that is predicted from long-range classical electromagnetic (EM) theory [1-3]. Experimentally, the challenge of achieving an ideal, reproducible surface morphology on a metal surface can be quite daunting. This fundamental limitation demonstrates the need for fabrication methods that produce reproducible and practical SERS-active substrates.

In recent years, vapor-deposited silver metal films and Ag nanoparticles have gained favor as SERS substrates.[4-8] Standard vapor deposition methods result in silver island films (AgIF) of discontinuous particles of ellipsoidal geometry that are more stable than metal sols and produce a

surface of particles that are more uniform in shape than the electrochemical method. Unfortunately, SERS enhancements obtained from these substrates tend to be lower than those obtained from colloidal aggregates. However, the combination of vapor deposition with nanosphere or e-beam lithographic procedures produces regular arrays of Ag nanoparticles that exhibit large SERS intensities. In addition, the size, shape and spacings of these Ag nanostructures can be controlled to tune the optical properties of the nanoparticle arrays.[8-10]

Research with nanoparticles has shown that that the size, shape and structural arrangement of the nanofabricated metallic particles are extremely important variables in achieving maximum SERS enhancement. For example, Au nanorods exhibited stronger SERS signals than Au nanoparticles[11], and an optimal nanorod aspect ratio was needed to reach the maximum enhancement.[12] Specially aligned nanorods have been shown to exhibit large SERS enhancement factors.[13] Unfortunately, many of the previous methods reported for preparing metallic nanoparticle arrays for high sensitivity SERS applications are expensive or time-consuming, and it is difficult to easily prepare reproducible metal-coated substrates of the correct surface morphology to provide maximum SERS enhancements.[14]

Based on these previous studies it appears that two major factors are necessary in order to achieve high SERS enhancements using nanoparticle arrays: a high aspect ratio nanorod and an optimized spatial arrangement of the nanoarray. In principle, then, by carefully tuning the size, shape and arrangement of these nanoparticle arrays, one may achieve a maximum enhanced EM field. We believe that a simple physical vapor deposition method, oblique angle vapor deposition, offers a flexible, easy and inexpensive method for fabrication of high aspect nanorod arrays for high sensitivity SERS applications.

Oblique angle deposition (OAD) is a physical vapor deposition technique[15] in which the substrate is rotated in the polar direction by a stepper motor, as shown in Figure 8.1. During deposition, the angle between the incoming vapor from the source and the surface normal of the substrate is set to be greater than 75^{o}. The main mechanisms that control the growth are the shadowing effect and surface diffusion. OAD is simple to implement, and any thin film physical vapor deposition system can be readily changed to an OAD system.

Materials and Methods

The Ag nanorod substrates used in this study were fabricated using a custom-designed electron beam/sputtering evaporation (E-beam) system (Torr International, New Windsor, NY). The substrate used in these experiments was a glass microscope slide with a typical dimension of 3" × 1"; the microscope slide was cleaned using standard RCA1 methods before loading into the substrate holder. The motion of the substrate holder was controlled by two vacuum stepper motors, one rotating in the polar direction and one rotating in the azimuthal direction, as shown in Figure 8.1. A custom-designed substrate shutter was used to selectively reveal increasing portions (predetermined) of the substrate during the deposition process, thereby forming a multi-region Ag nanorod sample with varying Ag rod lengths within a single deposition. These regions are denoted as A, B, C, D, E and F in Figure 8.1b. Typically, a base layer of a 50 nm Ag thin film was initially deposited at normal incidence, *i.e*. the substrate was face down to the evaporation source as shown in Figure 8.1(a). The substrate was then rotated to an incident angle of 86°, after which Ag nanorods were deposited in steps of ~200 nm by partially opening the shutter after each deposition. During deposition, the Ag thickness was checked by a film thickness monitor at normal incidence. Actual nanorod length for each deposition region was determined using a LEO 982 field emission scanning electron microscope (SEM) (LEO Electron

Figure 8.1. (a) Experimental setup for oblique angle deposition. A high vacuum motor was used to rotate the substrate in the polar direction. A manual shutter was used to continue to block the incoming vapor so that six different regions with different nanorod lengths can be formed. (b) A schematic diagram showing the six regions after deposition.

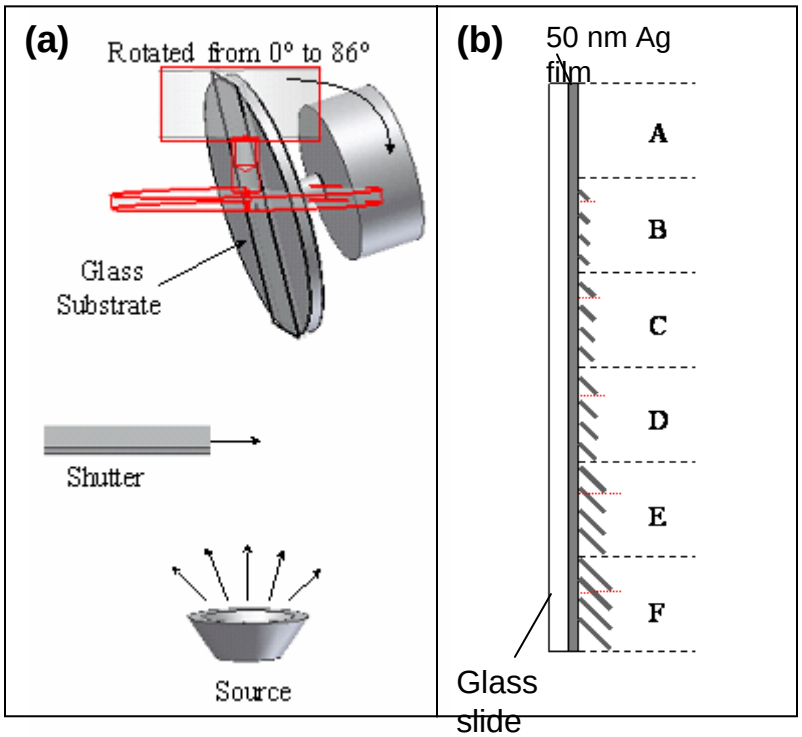
(a)
Rotated from 0° to 86°
Glass
Substrate
Shutter
Source
(b)
50 nm Ag
film
A
B
C
D
E
F
Glass
slide

Microscopy, Inc., Thornwood, NY). The average surface roughness and nanorod thickness was evaluated from atomic force microscopy (AFM) images using a DI NanoScope 3100 (Digital Instruments, Woodbury, NY)

Figure 8.2 shows six representative SEM images on different parts of the sample. For the 50 nm thick initial Ag deposition, Ag nanoparticles exist on the surface (Fig. 2A). With increasing deposition time, randomly distributed but aligned nanorod arrays are developed on the substrate (Fig. 2B-2F). The length of the nanorods increases monotonically as a function of deposition time, and the nanorods are titled with respect to the normal to the substrate surface. Previous results have shown that the tilt angle for these nanorods is between 50°- 60° with respect to the substrate normal. SEM images were used to determine that the six separate regions had nanorod lengths of l = 0, 190, 218, 300, 366, and 508 nm, respectively. The diameter of the Ag nanorods was estimated from AFM measurements to be ~80-90 nm, while the density of the nanorods was approximately 15-25 μm^{-2}.

These Ag nanorod arrays have been evaluated as surface enhanced Raman substrates. SERS spectra were acquired as a function of the length of the nanorod using a near-IR confocal Raman microscope (Hololab Series 5000, Kaiser Optical Systems, Inc., Ann Arbor, MI) at an excitation wavelength of 785 nm. The spectrograph used was a Kaiser Optical Systems Holospec *f*/1.8-NIR equipped with a LN_2-cooled CCD camera (1024EHRB, Princeton Instruments, Trenton, NJ). Laser illumination at 785 nm was supplied by a Coherent Radiation 899 Ti:Sapphire laser pumped by a Innova 300 Ar^+ ion laser (Coherent, Santa Clara, CA). The molecular probe used in this study was trans-1,2-bis(4-pyridyl)ethene (BPE, Aldrich, 99.9+%). BPE was chosen as the probe to calculate enhancement factors because of its high Raman scattering cross-section and its ability to adsorb strongly and irreversibly to a Ag substrate.[16] BPE solutions were prepared by

Figure 8.2. SEM images of the six different regions with Ag nanorod lengths of l = 0, 190, 218, 300, 366 and 508 nm, respectively. Since the SEM images for each individual region were obtained from smaller pieces cut from the original six-region substrate, the directions of the nanorods were not aligned during the measurement.

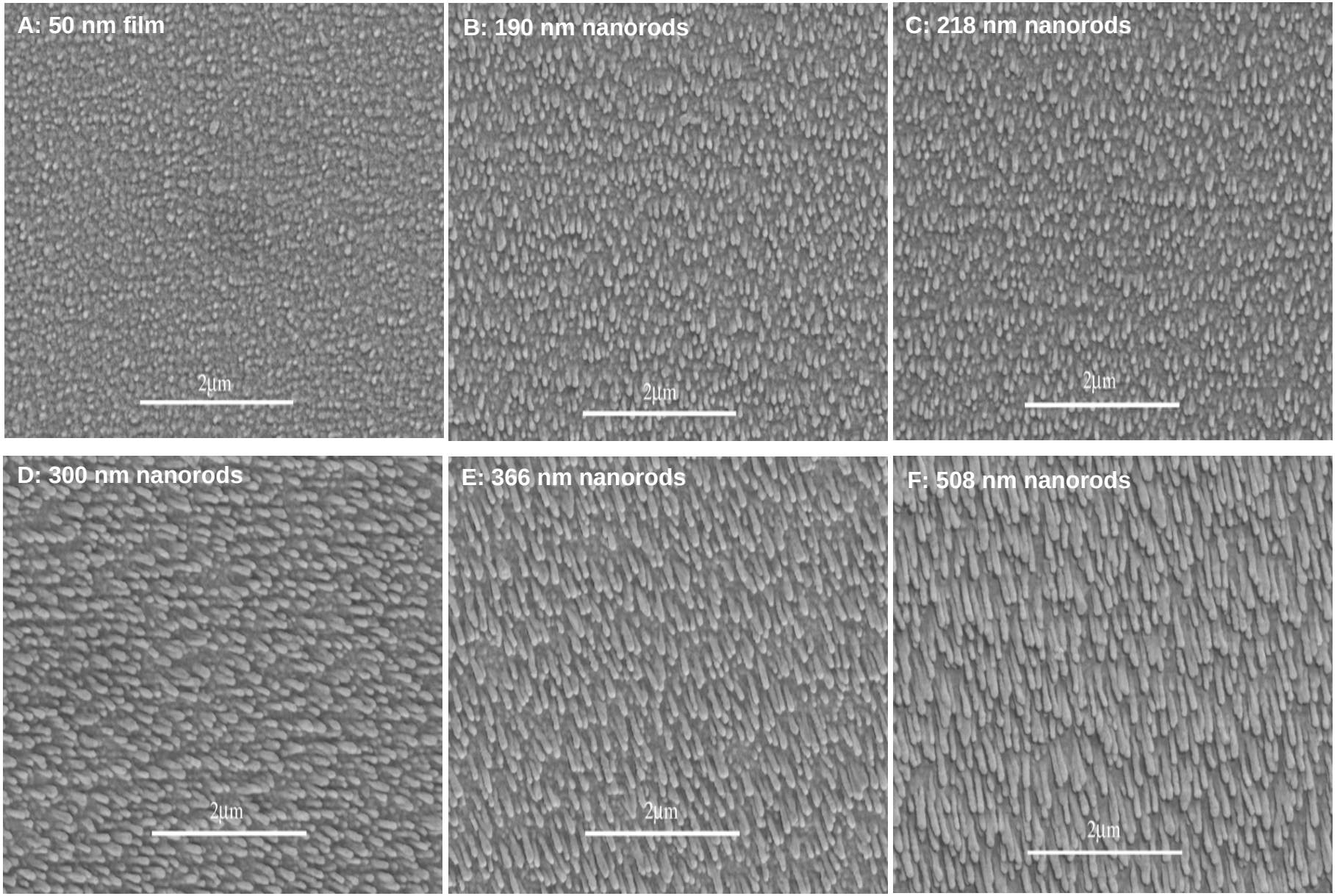
A: 50 nm film
2μm
B: 190 nm nanorods
2μm
C: 218 nm nanorods
2μm
D: 300 nm nanorods
2μm
E: 366 nm nanorods
2μm
F: 508 nm nanorods
2μm

sequential dilution in HPLC grade methanol (Aldrich). The concentration of the BPE and the volume applied were calculated to produce a surface coverage of ~0.21 monolayers to avoid self-quenching effects.[17, 18] A BPE solution was applied to each of the SERS substrates and allowed to dry before the acquisition of spectra. The 1200 cm^{-1} peak of BPE was chosen for the quantification because of its relative insensitivity to molecular orientation on a Ag surface. SERS spectra were collected at multiple locations on the sample for ~10 s each with ~20 mW laser power at the microscope objective.

Results and Discussion

Representative SERS spectra of BPE on Ag nanorod arrays with rod lengths of 508 nm, 300 nm, and 190 nm are presented in Figure 8.3(a). For comparison with the 508 nm spectrum, the spectra for the 190 nm and 300 nm rods have been enlarged by 200× and 10×, respectively. It is clear from Fig. 3(a) that the SERS intensity increases dramatically with nanorod length. The SERS Surface Enhancement Factor (SEF) was calculated for BPE on the stepped Ag nanorod samples according to the equation $SEF = \frac{I_{surf} / N_{surf}}{I_{bulk} / N_{bulk}}$. In this expression, I_{surf} and I_{bulk} denote the integrated intensities for the 1200 cm^{-1} band of the BPE adsorbed on the Ag surface and BPE in solution, respectively; whereas N_{surf} and N_{bulk} represent the corresponding number of BPE molecules excited by the laser beam.

Figure 8.3(b) illustrates the calculated SERS SEF plotted as a function of the length of the Ag nanorod. The SEF increased from almost zero for Region A (l = 0 nm), to over 10^5 for a very short Ag nanorod in Region B (l = 190 nm), and then increased another three orders of magnitude (10^8) for a nanorod in Region F (l = 508 nm). The intense SERS enhancement factors observed on these Ag nanorods (10^8) are orders of magnitude larger than those obtained from previously-published methods of forming nanoparticle arrays by vapor deposition (SEF

Figure 8.3. (a) The representative SERS spectra of BPE adsorbed onto Ag nanorods of length 190 nm, 300 nm, and 508 nm, repectively. The spectra for the 190 nm and 300 nm arrays were enlarged by a factor of 200 and 10, respectively. (b) The SERS enhancement factor calculated as a function of the Ag nanorod length. Experimentally determined SERS SEF (■), and SERS SEF theoretically calculated from the spheroid approximation (●).

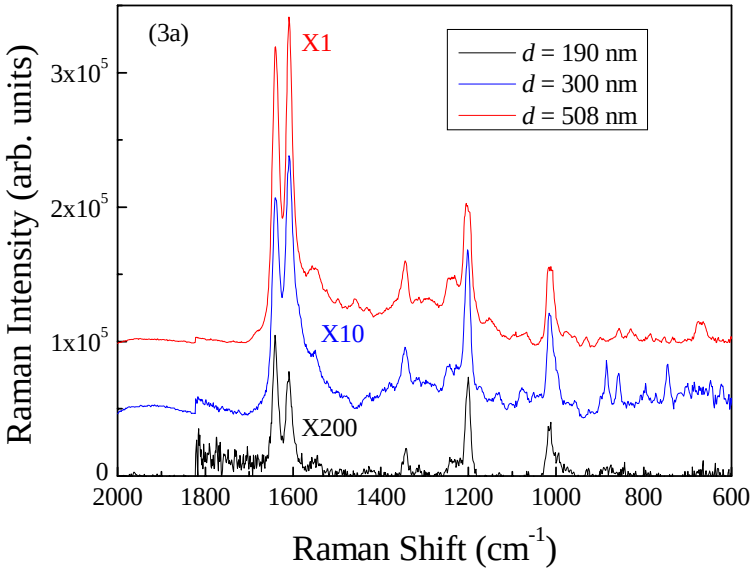
(3a)
X1
X10
X200
d = 190 nm
d = 300 nm
d = 508 nm
Raman Intensity (arb. units)
3x10^5
2x10^5
1x10^5
0
2000
1800
1600
1400
1200
1000
800
600
Raman Shift (cm^-1)

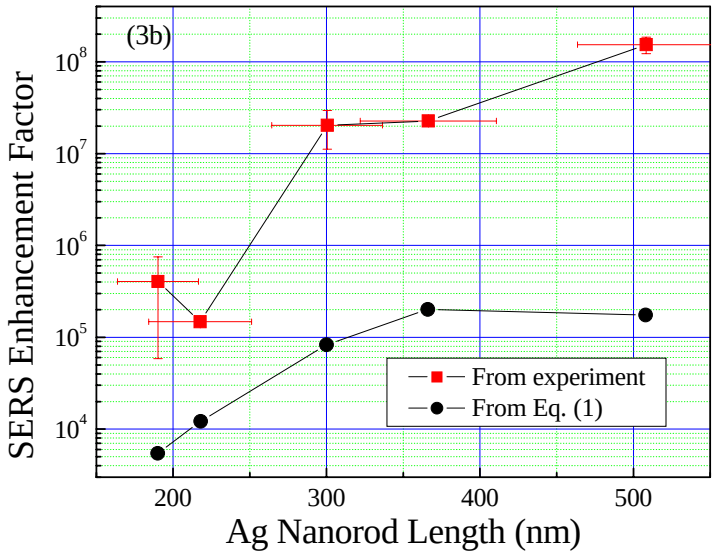
(3b)
SERS Enhancement Factor
10^8
10^7
10^6
10^5
10^4
From experiment
From Eq. (1)
200
300
400
500
Ag Nanorod Length (nm)

~10^4)[12, 19], and compare favorably to the best SERS enhancements reported using substrates prepared by elaborate nano-lithographic procedures (SEF ~10^8).[20] The maximum average SERS SEF calculated for multiple locations on a single substrate was 1.39 x 10^8 for a Ag nanorod array measured at 508 nm. The reproducibility of the SERS SEF and nanorod height measurements is given by the error bars in Figure 8.3(b). Only a very few experiments, including near-field SERS measurements (SEF ~10^{13})[21] and substrates with specifically engineered nm-scale "hot spots" (SEF ~10^{14})[22, 23], have demonstrated larger SERS enhancements than the Ag nanorod substrates described here.

It is likely that the large SERS enhancement factors for these substrates are due mainly to an electromagnetic dipole effect accentuated by the high aspect ratio of the Ag nanorods.[24] If we treat the Ag nanorods as prolate spheroid particles, the electric field at the tip of the spheroid is enhanced by a factor of $f(\omega)$ $\left(E_{out} = f(\omega)E_0\right)$. Under the modified long wavelength approximation (MLWA)[25], $f(\omega)$ is given by

$$\left|f(w)\right|^2 = \frac{\left|\varepsilon(\omega)\right|^2}{\left\{1-\left[1-\varepsilon_1(\omega)\right]L_j+\varepsilon_2\left(\frac{4\pi^2V}{3\lambda^3}\right)\right\}^2+\left\{\varepsilon_2 L_j+\left[1-\varepsilon_1(\omega)\right]\left(\frac{4\pi^2V}{3\lambda^3}\right)\right\}^2} \qquad (1)$$

where $\varepsilon(\omega)=\varepsilon_1(\omega)+i\varepsilon_2(\omega)$ is the wavelength-dependent dielectric constant of the spheroid, $V=\frac{4}{3}\pi b^2 a$ is the volume, and L_j is the depolarization factor, $L_j=\frac{1-e^2}{e^2}\left(-1+\frac{1}{2e}\ln\frac{1+e}{1-e}\right)$, where $e^2=1-\frac{b^2}{a^2}$. Both *a* and *b* are the radii of the principle axes of the spheroid ($a > b$). The Raman enhancement factor will be approximately proportional to

$\left|f(\omega)\right|^4$. Using the bulk dielectric constant of Ag at 785 nm[26], the calculated Raman enhancement factor is shown in Figure 8.3(b). Although the theoretical estimation of SEF as a function of nanorod length follows a similar trend to that of the experimental data, the estimated SEF is much lower than that obtained experimentally. This discrepancy increases with increasing nanorod length. When l < 300 nm, the discrepancy is less than two orders of magnitude, while when $l \geq 300$ nm, the discrepancy increases to over two orders of magnitude. The discrepancy between experimental and calculated SEF is consistent with the change in morphology of the Ag nanorods as seen in Figure.8.2. For l < 300 nm, there is no lateral overlap of the nanorods on the surface, while for $l \geq 300$ nm, lateral overlap exists between adjacent nanorods. Therefore, the enhanced electric field is not only determined by the aspect ratio of a single nanorod, but also the lateral arrangement of the nanorod arrays, *i.e*. the enhanced field also depends upon the radiation fields generated by nearest-neighbor nanorods, as has been previously demonstrated using nanoparticle arrays.[27]

In summary, we have created a novel Ag nanorod substrate that is fabricated utilizing a vapor deposition technique that is easily implemented in the laboratory. These substrates achieve SERS enhancement factors of approximately 10^8 for arrays of Ag rods having a length of 508 nm and a width of 80-90 nm. These substrates reproducibly produce SERS spectra with no discernable hot spots and show potential as high sensitivity substrates for SERS-based measurements.

Acknowledgements

SBC and YPZ thank the support from the National Science Foundation (ECS-0304340). SS and RAD are supported by the U.S. Public Health Service through National Institutes of Health grant EB001956.

References :

1. Gersten, J. and A. Nitzan, *Electromagnetic Theory: A Speheroidal Model*, in *Surface Enhanced Raman Scattering*, R.K. Chang and T.E. Furtak, Editors. 1982, Plenum: New York. p. 89-107.

2. Metiu, H. and P. Das, *The electromagnetic theory of surface enhanced spectroscopy.* Annu. Rev. Phys. Chem., 1984. **35**: p. 507-536.

3. Moskovits, M., *Surface enhanced spectroscopy.* Rev. Mod. Phys., 1985. **57**: p. 783-826.

4. Schlegel, V.L. and T.M. Cotton, *Silver island films as substrates for enhanced Raman scattering: effect of deposition rate on intensity.* Anal. Chem., 1991. **63**: p. 241-247.

5. Van Duyne, R.P., J.C. Hulteen, and D.A. Treichel, *Atomic force microscopy and surface-enhanced Raman spectroscopy. I. Ag island films and Ag film over polymer nanosphere surfaces supported on glass.* J. Chem. Phys., 1993. **99**(3): p. 2101-2115.

6. Semin, D.J. and K.L. Rowlen, *Influence of vapor deposition parameters on SERS active Ag film morphology and optical properties.* Anal. Chem., 1994. **66**(23): p. 4324-4331.

7. Roark, S.E. and K.L. Rowlen, *Thin silver films: influence of substrate and postdeposition treatment on morphology and optical properties.* Anal. Chem., 1994. **66**(2): p. 261-270.

8. Jensen, T.R., G.C. Schatz, and R.P. Van Duyne, *Nanosphere lithography: Surface plasmon resonance spectrum of a periodic array of silver nanoparticles by ultraviolet-visible extinction spectroscopy and electrodynamic modeling.* J. Phys. Chem. B, 1999. **103**(13): p. 2394-2401.

9. Jensen, T.R., et al., *Nanosphere lithography: Tunable localized surface plasmon resonance spectra of silver nanoparticles.* J. Phys. Chem. B, 2000. **104**(45): p. 10549-10556.

10. Felidj, N., et al., *Controlling the optical response of regular arrays of gold particles for surface-enhanced Raman scattering.* Phys. Rev. B, 2002. **65**: p. 075419.

11. Nikoobakht, B. and M.A. El-Sayed, *Surface-enhanced Raman scattering studies on aggregated gold nanorods.* J. Phys. Chem. A, 2003. **107**(18): p. 3372-3378.

12. Nikoobakht, B., J. Wang, and M.A. El-Sayed, *Surface-enhanced Raman scattering of molecules adsorbed on gold nanorods: off-surface plasmon resonance condition.* Chem. Phys. Lett., 2002. **366**: p. 17-23.

13. Tao, A., et al., *Langmuir-Blodgett silver nanowire monolayers for molecular sensing using surface-enhanced Raman spectroscopy.* Nano Letters, 2003. **3**: p. 1229-1233.

14. Tian, Z.Q., B. Ren, and D.Y. Wu, *Surface-enhanced Raman scattering: From noble to transition metals and from rough surfaces to ordered nanostructures.* J. Phys. Chem. B, 2002. **106**(37): p. 9463-9483.

15. Abelmann, L. and C. Lodder, *Oblique evaporation and surface diffusion.* Thin Solid Films, 1997. **305**(1-2): p. 1-21.

16. Norrod, K.L., et al., *Quantitative comparison of five SERS substrates: Sensitivity and limit of detection.* Appl. Spectros., 1997. **51**(7): p. 994-1001.

17. Yang, W.H., et al., *A surface-enhanced hyper-Raman and surface-enhanced Raman scattering study of trans-1,2-bis(4-pyridyl)ethylene adsorbed onto silver film over nanosphere electrodes. Vibrational assignments: experiment and theory.* J. Chem. Phys., 1996. **104**(11): p. 4313-4323.

18. Zeman, E.J., et al., *A surface enhanced resonance Raman study of cobalt phthalocyanine on rough Ag films - theory and experiment.* J. Chem. Phys., 1987. **87**(7): p. 4189-4200.

19. Mulvaney, S.P., et al., *Three-layer substrates for surface-enhanced Raman scattering: preparation and preliminary evaluation.* J. Raman Spectros., 2003. **34**: p. 163-171.

20. Green, M. and F.M. Liu, *SERS substrates fabricated by island lithography: the silver/pyridine system.* J. Phys. Chem. B, 2003. **107**(47): p. 13015-13021.

21. Stöckle, R.M., et al., *Sub-wavelength Raman spectroscopy on isolated silver islands.* Vib. Spectros., 2000. **22**: p. 39-48.

22. Nie, S.M. and S.R. Emery, *Probing single molecules and single nanoparticles by surface-enhanced Raman scattering.* Science, 1997. **275**(5303): p. 1102-1106.

23. Kneipp, K., et al., *Extremely large enhancement factors in surfce-enhanced Raman scattering for molecules on colloidal gold clusters.* Appl. Spectros., 1998. **52**: p. 1493-1497.

24. Wang, D.-S. and M. Kerker, *Enhanced Raman scattering by molecules adsorbed at the surface of colloidal spheroids.* Phys. Rev. B, 1981. **24**(4): p. 1777-1790.

25. Wokaun, A., J.P. Gordon, and P.F. Liao, *Radiation damping in surface enhanced Raman scattering.* Phys. Rev. Lett., 1982. **48**: p. 957-960.

26. Johnson, P.B. and R.W. Christy, *Optical constants of noble metals.* Phys. Rev. B, 1972. **6**: p. 4370-4379.

27. Zhao, L.L., K.L. Kelly, and G.C. Schatz, *The extinction spectra of silver nanoparticle arrays: Influence of array structure on plasmon resonance wavelength and width.* J. Phys. Chem. B, 2003. **107**: p. 7343-7350.

CHAPTER 9

CONCLUSIONS

From the data presented in the preceding chapters, the following conclusions can be drawn from the work presented in this dissertation. Majority of the work presented in this dissertation has involved the application of two dimensional infrared correlation methods to IRRAS and PM-IRRAS spectra of Langmuir monolayers of proteins and lipids at the air-water interface. A modified 2D IR method, *kv* correlation, has also been developed and applied to different molecular systems.

1. Using *in-situ* IR spectroscopy at the A/W interface and 2D IR and *βv* correlation, the conformational intermediates that exist in the hydrophobic surfactant proteins SP-B and SP-C in lipid-protein monolayers were investigated. The results described here have identified specific protein conformations and followed the reorientation of these protein conformations as a function of increasing surface pressure. The surface pressure regimes that encompassed the greatest variation in amide I spectral intensity were identified using a statistical approach based on a windowed autocorrelation method. SP-C was shown to comprise of a heterogeneous secondary structure, including α-helix, β-sheet, and an intermolecular aggregation of extended β-sheet structure and this is the first infrared spectroscopic evidence that multiple α-helix conformations as well as β-structure conformational intermediates exist for SP-C – containing monolayers at the A/W interface. A high α-helical content

for SP-B with contributions from β-sheet and unordered structure has been predicted based on the presence of cross peaks in the 2D maps. This is the first study to demonstrate the presence of two α-helical components of SP-B in monomolecular films in monomolecular films at the A/W interface. The conservation of protein secondary structure and in-phase reorientation of the entire protein throughout all surface pressures is likely due to the stabilization of the protein core by intramolecular disulfide bonds.

2. In Chapter 4, IR spectroscopy was employed to study the pH dependence of the conformation of deacylated SP-C (dSP-C), which was observed to aggregate and form amyloid fibrils in solution. Several different IR techniques were used to study the structure of dSP-C in various environments. 1) Transmission IR spectroscopy was used to study the conformation of dSP-C in solutions and bulk liposomes. 2) Attenuated total reflectance (ATR) spectroscopy was used to study the structure of dSP-C in monomolecular films transferred onto solid substrates. 3) Polarization modulation IR reflection absorption spectroscopy (PM-IRRAS) was used to study the structure of dSP-C monolayers *in-situ* at the A/W interface. This work identified pH as a specific cause of conformational changes in dSP-C, and a possible contributor to amyloid fibril formation in pulmonary alveolar proteinosis.

3. A new model-based approach to 2D correlation analysis called *kv correlation analysis* is introduced in Chapter 5 that substitutes a different mathematical function for the sine function used in the *βv* method. In this method a set of dynamic spectra are correlated against a set of exponential curves that differ in their rate constants. As in the

previously described βv correlation method, kv correlation analysis employs an asynchronous cross correlation since this calculation is more sensitive to intensity changes and spectral resolution enhancement than is the synchronous correlation. A quantitative parameter, the *effective rate constant*, k_{eff}, is defined and used to establish relative rate relationships between spectral intensity variations. Different intensity variation models composed of simulated spectra are used to illustrate the ability of the kv correlation method in distinguishing between processes occurring with different rates of change. To demonstrate the utility of the kv method, the anionic polymerization of cyanoacrylate using the classic metallocene ruthenocene as a photoinitiator was studied. This reaction was monitored using ATR-IR spectroscopy and kv correlation analysis was applied to the time-dependent spectra to elucidate the rates of intensity change in the different vibrational modes attributable to the monomeric and the polymeric cyanoacrylate species.

4. In Chapter 6, different 2D IR correlation analysis methods are applied to investigate the surface-pressure induced changes in the DPPA – TC monolayer system and propose a model for lipid – antibiotic interaction. Initial interaction between the tetracycline molecule and the DPPA molecule occurs at low surface pressures primarily between Ring A of the tetracycline molecule and the lipid headgroup region. However, with increasing surface pressure, the mode of interaction changes, and the strongest inter-molecular interactions at high surface pressures occurs between Ring C of tetracycline and the DPPA headgroup.

5. The conformation and orientation of synthetic monomeric human-sequence SP-B_{1-25} (mSP-B_{1-25}) was studied in films with phospholipids at the air-water (A/W) interface by polarization modulation infrared reflectance absorption spectroscopy (PM-IRRAS) in Chapter 7. Modified two dimensional infrared (2D IR) correlation analysis was applied to PM-IRRAS spectra to define changes in the secondary structure and rates of reorientation of mSP-B_{1-25} in the monolayer during compression. PM-IRRAS spectra and 2D IR correlation analysis showed that in pure films, mSP-B_{1-25} had a major α–helical conformation plus regions of β-sheet structure. These α-helical regions reoriented later during film compression than β structural regions, and became oriented normal to the A/W interface as surface pressure increased. In mixed films with 4:1 mol:mol perdeuterated dipalmitoyl phosphatidylcholine:dioleoyl phosphatidylglycerol (DPPC-d_{62} :DOPG), the IR spectra of mSP-B_{1-25} showed that a significant, concentration-dependent conformational change occurred when mSP-B_{1-25} was incorporated into a DPPC-d_{62} :DOPG monolayer. At an mSP-B_{1-25} concentration of 10 wt%, the peptide assumed a predominately β-sheet conformation with no contribution from α-helical structures. At lower, more physiological peptide concentrations, 2D IR correlation analysis showed that the propensity of mSP-B_{1-25} to form α-helical structures was increased. In phospholipid films containing 5 wt% mSP-B_{1-25}, a substantial α-helical peptide structural component was observed, but regions of α and β structure reoriented together rather than independently during compression. In films containing 1 wt% mSP-B_{1-25}, peptide conformation was predominantly α-helical and the helical regions reoriented later during compression than remaining β structural components.

6. In Chapter 8, substrates consisting of silver nanorod arrays with varying rod lengths were fabricated by an oblique angle vapor deposition method. These arrays were evaluated as potential surface-enhanced Raman spectroscopy (SERS) substrates using trans-1,2-bis(4-pyridyl)ethane as a reporter molecule. SERS activity was shown to depend upon the length of the nanorods. The Ag nanorods with average lengths of 508.29 ± 44.86 nm, and having aspect ratios of 5.69 ± 1.49 exhibited the maximum SERS enhancement factors of greater than 10^8. Theoretical calculations indicate that this large SERS enhancement may be partially explained by the shape, density and lateral arrangement of the Ag nanorod arrays.